THÈSE DE DOCTORAT

de l'Université de recherche Paris Sciences et Lettres
PSL Research University

Préparée à l'Observatoire de Paris

Observations Extragalactiques avec Optique Adaptative : Polarisation dans les Noyaux Actifs de Galaxie et Étude des Super Amas d'Étoiles

École doctorale n°127

ASTRONOMIE ET ASTROPHYSIQUE D'ÎLE-DE-FRANCE

Spécialité ASTRONOMIE ET ASTROPHYSIQUE

COMPOSITION DU JURY :

Mme. Catherine Boisson
Astronome, LUTH
Président

Mme. Almudena Alonso-Herrero
Senior Staff Scientist, CSIC
Rapporteur

M. Christopher Packham
Associate Professor, Univ. of Texas
Rapporteur

Mme. Annie Zavagno
Maître de Conférence, LAM
Membre du jury

M. Damien Gratadour
Maître de Conférence, LESIA
Directeur de thèse

M. Daniel Rouan
Professeur, LESIA
Directeur de thèse

Soutenue par **Lucas GROSSET**
le 15 Septembre 2017

Dirigée par **Damien GRATADOUR**
et **Daniel ROUAN**

Abstract

Extragalactic observations with Adaptive Optics: Polarisation in Active galactic Nuclei and Study of Super Stellar Clusters

Abstract:

Despite having strong theoretical models, the current limitation in our understanding of the small-scale structures of galaxies is linked to the lack of observational evidences. Many powerful telescopes and instruments have been developed in the last decades, however one of these strongest tools, namely Adaptive Optics (AO), can only be used on a very limited number of targets. Indeed, for AO to be efficient, a bright star is required close to the scientific target, typically under $30''$. This is mandatory for the AO systems to be able to measure the atmospheric turbulence and this condition is rarely satisfied for extended extragalactic targets such as galaxies. The main part of this thesis work consisted in going deeper in the analysis of the inner tens of parsecs of Active Nuclei (AGN) by combining different techniques to obtain and to interpret new data. In this context, we developed a new radiative transfer code to analyse the polarimetric data. A second part of my work was dedicated to a high angular resolution study of Super Star Clusters (SSC) in a new system, thanks to data obtained with the AO demonstrator CANARY instrument.

The unified model for AGN stats that Seyfert 1 or 2 types are the same type of object harbouring a luminous accretion disk surrounded by a thick torus, but seen under different viewing angles. This model has been successfully tested for many years by several observers, bringing some evolutions to the initial model, but on the torus, one of the most important pieces, we still lack information because of its limited extension and of the high contrast required. We took advantage of SPHERE's extreme contrast and high angular resolution to propose a near infrared (NIR) polarimetric observation of the archetypal Seyfert 2 galaxy NGC 1068 in H and Ks broad bands, revealing a clear double hourglass shape of centro-symmetric pattern and a central pattern diverging from these. We continued these measurements in narrow bands (in the NIR) and at shorter wavelengths (R band) in order to study the wavelength dependency of the measured polarisation, which we are currently analysing. If the features are wavelength-dependent, this will bring new constraints on the properties of scatterers.

Polarimetry is a powerful tool as it gives access to more information than spectroscopy or imaging alone. In particular, indications on the geometry of the scatterers, the orientation of the magnetic fields or the physical conditions of matter can be revealed thanks to the additional parameters measured (the polarisation degree and the polarisation position angle for linear polarisation). The counterpart of polarimetric measurements is that analyses of data is not straightforward. The use of numerical simulations, and especially radiative transfer codes, is necessary to fully understand the observations. I developed during the first part of my PhD a simulation of radiative

transfer code, MontAGN, with the aim of reproducing the features that we observed. This code allowed us to bring some constraining results on the optical depth of the structures. The torus' optical depth was constrained to 20 in the Ks band as a minimum. Our investigations on the densities in the ionisation cone are consistent with densities of 2.0×10^9 m^{-3}, in the range of previously estimated values for this AGN.

The last part of my PhD work was dedicated to SSC (also known as young massive clusters). These clusters correspond to the more massive example of star forming clusters, often about 10 Myr and still embedded in a dusty shell. These clusters exhibit extreme observed star formation rates. We took advantage of an instrumental run of the multi-object AO demonstrator CANARY instrument, installed at the William Hershel Telescope in 2013 to obtain images in H and Ks bands at higher resolution than previously achievable. Data on the galaxy IRAS 21101+5810 were reduced and analysed, constraining the age of the clusters between 10 and 100 Myr and the extinction to about $A_V \approx 3$. Photometry was obtained thanks to a new algorithm to estimate the galaxy background, bringing improvements on the fitting of the clusters' luminosity distributions.

Keywords: Galaxies: Seyfert, star clusters, Techniques: photometric, polarimetric, high angular resolution, Methods: observational, numerical, Radiative transfer.

Résumé

Observations Extragalactiques avec Optique Adaptative : Polarisation dans les Noyaux Actifs de Galaxie et Étude des Super Amas d'Étoiles

Abstract :

L'observation à haute résolution angulaire du centre des galaxies est l'un des défis les plus importants de l'astronomie moderne. Peu de galaxies sont en effet situées suffisamment proches de nous pour permettre une observation détaillée de leur structure et de leur différentes composantes. Un autre facteur limitant vient s'ajouter à travers le besoin critique d'une source de lumière ponctuelle à proximité de toute cible afin de rendre possible une correction par optique adaptative. Celle-ci est requise pour toute observation au sol sans laquelle la turbulence atmosphérique rendrait impossible une résolution meilleure que 0,5–1 seconde d'angle. Cette dernière restriction est relativement difficile à remplir dans le cadre de galaxies, à proximité de laquelle on ne trouve pas nécessairement d'étoile assez brillante, et la prochaine génération d'instruments a besoin de franchir ces limitations par des corrections plus vaste, plus ciblées ou applicables à un plus grand nombre de cibles.

L'observation des noyaux actifs de galaxie est particulièrement sensible à ces facteurs. Ne concernant qu'une fraction des galaxies observables et étant la partie centrale de ces galaxie, peu d'instruments permettent d'accéder à la structure interne de ces noyaux. En 1993, Antonnucci définit le modèle unifié des noyaux actifs, postulat stipulant que les différents types de noyaux actifs sont les mêmes objets intrinsèques, observés depuis différents angles de vue, suite à une observation en 1985 faite avec Miller de NGC 1068. Celle-ci est Depuis, de nombreuses études se sont portées sur les quelques principaux noyaux observables. Le tore de poussière, bloquant la lumière dans le plan équatorial de la galaxie et donc crucial pour ce modèle est néanmoins difficile à détecter du fait de sa taille relativement restreinte (autour de la dizaine à la centaine de parsecs) et du haut contraste requis pour séparer son signal de l'émission du centre du noyaux.

Cette thèse porte sur l'analyse d'observations en infrarouge proche de galaxies actives proches à l'aide d'optique adaptative afin d'accéder à une imagerie haute résolution angulaire de la région centrale de ces objets. Nous nous sommes ainsi appliqués à l'observation avec SPHERE du noyau actif NGC 1068, archétype de la galaxie à noyau actif (NAG) de type 2, très lumineuse et située relativement proche de la Terre, à 14 Mpc environ. En particulier, nous avons utilisé une technique polarimétrique afin de renforcer encore le contraste et faire apparaître une signature possible du tore, élément essentiel du modèle unifié des NAG. Le travail de thèse porte également sur l'analyse d'images infrarouges de galaxies à flambée d'étoiles afin de contraindre les paramètres décrivant les super amas stellaires, jeunes cocons de poussière très massifs abritant une formation d'étoiles très soutenue.

La première partie de ce travail de thèse porte sur les observations de ces deux types d'objets, depuis la réduction des données combinant diverses techniques à leur

analyse à travers les différentes images obtenues. Ainsi, dans le cas des noyaux actifs, nous avons pu interpréter le signal polarimétrique observé à travers des cartes de degré et d'angle de polarisation. Ces cartes décrivent en effet le double cône d'ionisation, lié aux jets de l'objet central, mais également une région au centre, d'une extension d'environ 60 pc, où le signal trace une polarisation d'orientation constante associée à un degré de polarisation variant, de très faible sur le bord vers assez élevé (autour de 15 %) au centre même de la luminosité du noyau. L'analyse des amas s'est faite, elle, par comparaison des images à différentes longueur d'onde de ces amas, en reliant leur couleur à leurs propriétés.

La seconde partie, la plus conséquente en terme de temps et de volume de travail, a consisté à modéliser ces structures analysées afin de chercher à en reproduire le signal, notamment en polarisation. Un code de transfert radiatif a ainsi été développé, à partir d'une première version créée lors d'un stage, à travers une amélioration et une inclusion de la polarisation. Le code ainsi finalisé permet de simuler des spectres et des images, à la résolution choisie, de sources de lumières entourées de structures variées (tore, disque, cône) contenant poussières et électrons. Nous avons programmé plusieurs simulations, de façon à étudier les épaisseurs et densités des poussières des différentes structures supposées, et avons pu contraindre les dimensions et densité de plusieurs d'entre eux. Nous proposons une interprétation cohérente de la carte de polarisation observée, en terme de double diffusion. Une épaisseur minimale de tore de poussière a ainsi été trouvée, de même qu'une estimation de la densité en électron dans le cône, en accord avec les études précédentes, et en poussière dans les régions externes du tore, dans le cas d'un modèle de noyau actif en accord avec le modèle unifié.

Mots-clés : Galaxies : Seyfert, amas d'étoiles, Techniques : photométrie, polarimétrie, Haute résolution angulaire, Méthodes : observations, numériques, Transfert radiatif.

Contents

List of Figures

List of Tables

List of acronyms

ACS	Advanced Camera for Surveys
AGN	Active Galactic Nucleus
ALMA	Atacama Large Millimeter/submillimeter Array
AO	Adaptive Optics
ASCII	American Standard Code for Information Interchange
AU	Astronomical Unit
BB	Broad Band
BLR	Broad Line Region
CCD	Coupled Charge Device
CE	Central Engine
CFHT	Canada France Hawaii Telescope
CI	Classical Imaging
CMC	Carlsberg Meridian Catalogue
COME-ON	**C**GE **O**bservatoire de **M**eudon **E**SO **ON**ERA
CONICA	COude Near-Infrared Camera
CPU	Computer Processor Unit
DEC	Declination
DM	Deformable Mirror
DPI	Dual Polarisation Imager
ELT	Extremely Large Telescope
ESO	European Southern Observatory
FITS	Flexible Image Transport System
FOV	Field Of View
FWHM	Full Width at Half Maximum
GALEV	GALaxy EVolutionary synthesis models
GC	Globular Cluster
GOALS	Great Observatory All sky LIRG Survey
GPU	Graphical Processor Unit

GTO	Guarantee Time Observation
H-G	Henyey-Greenstein
HAR	High Angular Resolution
HST	Hubble Space Telescope
HWP	Half Wave Plate
IAU	International Astronomical Union
IFS	(infrared) Integral Field Spectrograph
IR	InfraRed
IRAS	InfraRed Astronomical Satellite
IRDIS	InfraRed Dual-beam Imager and Spectrograph
ISM	InterStellar Medium
JD	Julian Date
JWST	James Webb Space Telescope
LESIA	Laboratoire d'Études Spatiales et d'Instrumentation en Astrophysique
LGS	Laser Guide Star
LIRG	Luminous in InfraRed Galaxy
LTE	Local Thermodynamic Equilibrium
MC	Monte-Carlo
MIR	Mid InfraRed
MOAO	Multi-Object Adaptive Optics
MontAGN	Monte-Carlo for Active Galactic Nuclei
MOSAIC	Multi-Object Spectrograph for Astrophysics, Intergalactic-medium studies and Cosmology
MRN	Mathis, Rumpl and Nordsieck
MTF	Modulation Transfer Function
NaCo	NAOS + CONICA
NAOS	Nasmyth Adaptive Optics System
NB	Narrow Band
NED	NASA/IPAC Extragalactic Database
NGC	New General Catalogue
NGS	Natural Guide Star

NICMOS	Near Infrared Camera and Multi-Object Spectrometer
NIR	Near InfraRed
NIRC2	Near InfraRed Camera (2^{nd} generation)
NLR	Narrow Line Region
OB	Observation Block
OC	Open Cluster
OHP	Obervatoire de Haute Provence
OPC	Observing Programmes Committee
PA	Position Angle
PAH	Polycyclic Aromatic Hydrocarbon
PSF	Point Spread Function
PUEO	Probing the Universe with Enhanced Optics (and an Hawaii owl)
RA	Right Ascension
RMS	Root Mean Square
SED	Spectral Energy Distribution
SFR	Star Formation Rate
SINFONI	Spectrograph for INtegral Field Observations in the Near Infrared
SNR	Signal to Noise Ratio
SPHERE	Spectro-Polarimetric High-contrast Exoplanet REsearch instrument
SSC	Super Stellar Cluster
SV	Science Verification
ULIRG	Ultra-Luminous in InfraRed Galaxy
UV	Ultra Violet
VLA	Very Large Array
VLT	Very Large Telescope
WHT	William Herschel Telescope
YSO	Young Stellar Object
ZIMPOL	Zurich IMaging POLarimeter

Chapter 1

Introduction to Extragalactic Observations at High Angular Resolution

Contents

Since the birth of instrumental astronomy with first refractor observations **being conducted around 1610 (by Galileo)**, many extragalactic objects have been observed. Among the first targets, the Andromeda galaxy, was observed short after the development of the refractors, in the first half of the XVIIth century. The Magellanic Clouds, two small irregular galaxies close to the Galaxy, visible with naked eyes, have been observed for even a longer time from the Southern hemisphere likely for thousands of years. In the first catalogue of nebulae, listed by Messier (1781), we find an important number of objects located outside of the border of the Galaxy. However all these extragalactic objects were not known as such and all astronomical bodies were for long considered as belonging to our Galaxy. All non stellar (not observed as point-like and fixed) objects were classified into the "nebulae" category, but were not assumed to be located further away from the Earth than the stars.

This situation lasted until the great debate about the scale of the Universe that occurred around 1920, outlined by Shapley & Curtis (1921). The question was about

the exact dimensions of the galactic system and **about understanding** whether the so-called "spirals" nebulae were intra or extra-galactic objects. These were later designated as "island universes" by Curtis. More clues were brought few years later by Hubble (1925), using Cepheids to measure distances of few of these objects, thanks to the relationship between period and magnitude of Cepheids, discovered by Leavitt & Pickering (1912). Cepheids are a particular type of stars, reasonably close to the end of their "life" and that are pulsating at a frequency precisely measurable. This led to the paper of Hubble (1926) on extra-galactic nebulae, namely galaxies, much more distant than previously thought, introducing what will become the Hubble sequence. Starting from this paper, extragalactic objects became a new domain of research. Note that the term "nebula" is today only attributed to **extended gaseous (non-galaxy) objects**, mainly situated inside our Galaxy. However, "nebula" was still used after the publication of the Hubble seminal paper of 1925 **also** to designate galaxies, like for example in Seyfert (1943) twenty years later.

This chapter aims at introducing different concepts of extragalactic objects which this thesis' work focused on. We will present the benefits of high angular resolution (HAR) and give the main limitations for the observation of extragalactic sources. **Since this thesis work is based on observation in the Near InfraRed (NIR), we will focus particularly on optical and NIR instruments even though some of the concepts developed here could also be applied to instruments dedicated to other wavelength domains observations.** We will detail in a second part some basics on the fields that will be investigated in this work: luminous young star clusters and active nuclei of galaxies.

1.1 Introduction to High Angular Resolution

A lot of information can be brought using the light collected over the entire objects. On extended targets, large aperture photometry, spectroscopy or polarimetry can be used to provide critical evidences to better understand the physics in astronomical objects. However it is sometimes required to have access to more details on the spatial extent of the brightness distribution of the sources in order to understand better their organisation, their components and the physics taking place on specific locations of these particular objects. And this is especially true for extragalactic sources, which are highly structured (arms, bulge, halo, Active Galactic Nucleus (AGN)...).

The angular resolution of an optical system **(in the optical and NIR at least)** is characterised by its Point Spread Function (PSF), representing the instrument response to a point-like source. In the case of circular apertures, like ideal telescopes (refractors or reflectors), the response is well known and is given by the Airy disk, induced by the diffraction of light on the circular aperture and represented in figure 1.1. The position of the first dark ring is defined through the diameter of the aperture D and the wavelength λ as:

$$\theta = 1.22\ \lambda/D. \tag{1.1}$$

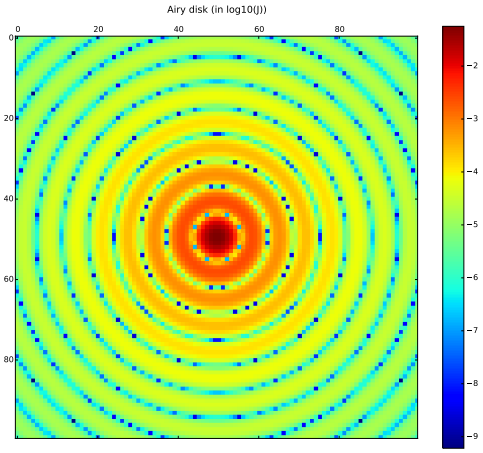

Figure 1.1 – Example of an Airy disk, in logarithmic scale.

This, or the Full Width at Half Maximum (FWHM) of the central peak (there is a factor 1.22 between these two values), is often used as the resolution limit of a telescope [1] and called the "diffraction limit". When represented in the Fourier domain, this limitation can be expressed as the cut-off frequency corresponding the maximal spatial frequency that the telescope is able to give access to. This limits the highest frequency of the Modulation Transfer Function (MTF) to λ/D. We will detail the shape of the MTF and its characteristics when using Adaptive Optics (AO) in section 2.5.1. One immediate conclusion is that the larger the telescope is (in diameter), the higher the angular resolution will be. Real-life experiments always bring other limitations, degrading this ideal resolution. HAR observations are conducted as close as possible to this theoretical resolution.

1.2 Adaptive Optics

After the first morphological studies of Hubble (1926), part of the research on galaxies was dedicated to studying the signal arising from small regions of these galaxies, to better understand the physics at smaller scales. This was achieved thanks to imaging, photometry or spectroscopy, but on apertures or resolution often limited to $1''$. This limitation in aperture is intrinsically due to the atmosphere's turbulence.

1. Note that even without the atmosphere limitations, the PSF of an instrument will never be a perfect Airy disk. The optics are not perfect and in case of reflectors, obstruction or fragmentation will change the instrument's response.

1.2.1 Impact of Turbulence

When the light travels through the atmosphere, the turbulence induces small local temperature variations that in turn induce a proportional variation of the optical index, modifying slightly the phase so that the wavefront is no longer plane but becomes bumpy. When deformed wavefronts are observed through telescopes, they will be translated in the focal plane into speckles with a typical scale of the order of the diffraction limit λ/D, but scattered on a scale of about one arc-second, as shown in figure 1.2. Long exposures will then produce images at a resolution of this typical value of $1''$.

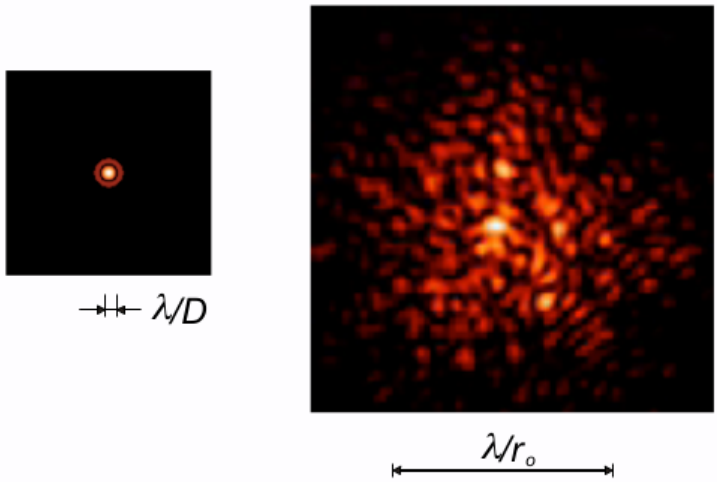

Figure 1.2 – Two examples of PSF, diffraction limited and turbulence limited. D refers to the telescope diameter and r_0 to the Fried parameter, defined in the following text. Image from G. Rousset.

Turbulence in the atmosphere is the current main limiting factor for the resolution in astronomy from the ground. Despite the growing diameter of telescopes [2], bringing theoretically a larger resolving power, the effect of turbulence does not allow to reach it. This effect depends on the quality of the site, measured through a quantity called seeing. The seeing is defined as the typical FWHM of the PSF only due to the atmosphere, integrated over a time larger than typically 100 ms. The corresponding PSF is not an Airy function nor a Gaussian and the value gives an estimate of the maximum angular resolution achievable with a perfect instrument under these atmospheric and dome conditions. Seeing can be linked to the Fried parameter r_0, often seen as the equivalent telescope diameter giving a similar resolution as the one allowed by the atmosphere. Seeing typically has a value of about 0.5–$1''$ in the best observing conditions. These correspond to $r_0 \approx$ 10–20 cm in the visible, meaning that increasing the diameter of a telescope beyond 20 cm will not improve the angular resolution.

2. A larger telescope diameter will allow to receive an increased quantity of light, which still is an important improvement by itself

Note that the Fried parameter and the seeing depend on the wavelength. r_0 varies in $\lambda^{6/5}$ and the seeing therefore depends on

$$\alpha_{\text{seeing}} \propto \frac{\lambda}{r_0} \propto \lambda^{-1/5}. \tag{1.2}$$

Because of this dependency, observations at longer wavelength will have a better image quality as long as $\lambda/D >$ seeing and aberration in the NIR can get closer to the diffraction limit than in the visible for a given telescope.

This atmospheric limitation is critical when trying to map the light distribution of astronomical objects. This is especially true in the extragalactic domain where objects are very extended, typically on the order of the thousands or millions of parsecs. However, these objects are distant (the Magellanic clouds, roughly separating the intra and extra-galactic objects are located at 100 kpc) and at these distances, even such large objects do have a small angular diameter. Andromeda galaxy is an exception. Standing at about 2 Mpc, it has a diameter of few degrees, which is by far the largest angular diameter for any extragalactic object. Most of the galaxies are observable under an angular diameter under $1'$, and it is therefore challenging to achieve high spatial resolution on some of their features, hundreds or thousands times smaller than the whole galaxy.

1.2.2 Methods for Achieving High Angular Resolution

As an answer, observers have been trying to develop and implement instrumental techniques to overcome this limitation in resolution caused by the atmosphere. The first two ideas were interferometry and lucky imaging. Interferometry, consists in recombining beams from different apertures (from two or several telescopes, from holes in a mask, from antennae...) to produce interferences and obtain spatial information with a resolution defined by the length of the base and not by the diameter of the aperture. With this technique, it is possible to reach a similar resolution to that of a unique aperture with a diameter of the scale of the base. It is however still sensitive to atmospheric turbulence when the aperture diameter is larger than the Fried parameter, limiting the amount of targets observable with this technique to bright sources. Lucky imaging corresponds to the strategy of observing with very short exposure times in order to try to catch the short periods during which the turbulence has the smallest amplitude on the surface of the pupil. It is not often the case, but by taking a long series of short images, some of them will have a resolution closer to the diffraction limit. This technique must be combined with shift-and-add processing. In this case as well, bright targets are required to receive enough photons on the detector at each exposure.

Another alternative, started during the 1970's, is to send telescopes to space. In this case, image quality is directly limited by the diffraction of the telescope and by the quality of the optics. The Hubble Space Telescope (HST) is a good illustration of the advantages of spatial telescopes upon ground based telescopes. From 1994,

images obtained through its cameras (once the optics has been corrected of strong aberrations) improved hugely the resolution of images on many extragalactic targets in the visible and NIR. Such space instruments are however limited in size. They are expensive to build and launch, and rockets have limited capacities in size. Note that this limit is challenged thanks to new techniques developed in order to bring to space larger telescopes. One major example is the James Webb Space Telescope (JWST) with an unfolding primary mirror that should be launched in the following year and that will have a diameter of 6.5 m. Furthermore, once in space, fixing errors or problems is difficult (if even possible) and expensive, as demonstrated by the HST. Note that in other wavelength bands, in particular for those which are not observable from the ground because of atmospheric absorptions bands (e.g. the Ultra Violet (UV) or parts of the InfraRed (IR)), space telescopes are still the only way to conduct observations and have proven to be very important facilities.

At the same epoch as the HST, the idea to directly correct the effect of turbulence on ground telescopes has been made possible using AO systems in which the wavefront is measured using a camera to compute the difference between this wavefront and a perfect wavefront and correct it by sending commands to a Deformable Mirror (DM). The system is working in closed-loop where the wavefront analysis is done after the DM. The first AO systems were available on sky around 1990, with for instance COME-ON (CGE Observatoire de Meudon ESO ONERA) in 1989 on the 1.5 m of the Obervatoire de Haute Provence (OHP), see Kern et al. (1989). After what AO was installed on a growing number of telescopes, most of the large telescopes being currently equipped.

1.2.3 Principle of Adaptive Optics

The basic principle of AO is to split the beam into two components, as late as possible in the optical path, as shown in figure 1.3. The first sub-beam is sent toward the science instrument. The second sub-beam goes to a sensor, measuring the wavefront. The most common device for this part of the system is the Shack-Hartmann wavefront sensor, splitting the beam into several sub-pupils, all focused on the same detector plane (see figure 1.4). The difference between the sub-pupil optical axis, precisely calibrated, and the position of the spot from the guide star is proportional to the local slope of the wavefront in this sub-aperture and is therefore used to reconstruct the complete wavefront. Note that other wavefront sensors are growing in maturity and are used to equip large telescope as an alternative to the Shack-Hartmann sensor. Pyramid sensor is one example of such devices (describing their operation is beyond the scope of this work since only instruments with Shack-Hartmann sensors have been used in the context of this thesis, for more information, refer to Ragazzoni & Farinato (1999)).

AO does have some limitations because most wavefront sensor concepts require a point-like guide source to perform the wavefront measurements. Stars, if they are bright enough, provide an excellent reference for turbulence estimation and wavefront

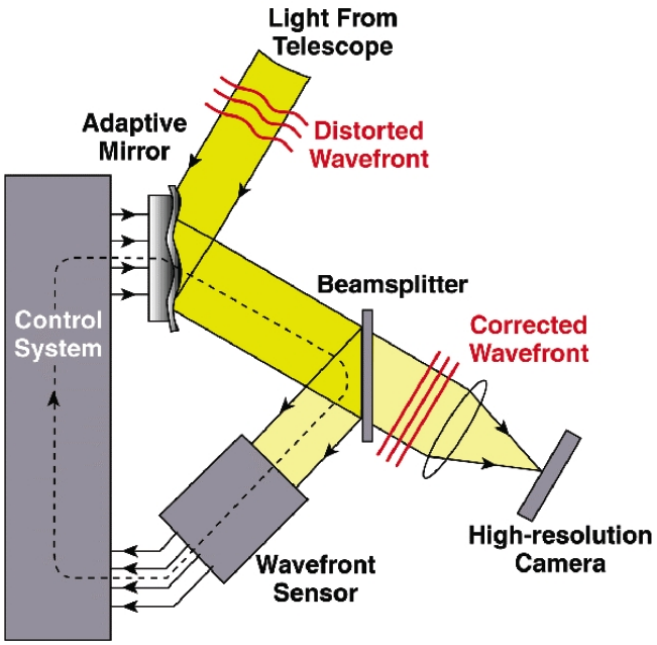

Figure 1.3 – Basics Adaptive Optics principle. Image credits: Lawrence Livermore National Laboratory and NSF Center for Adaptive Optics.

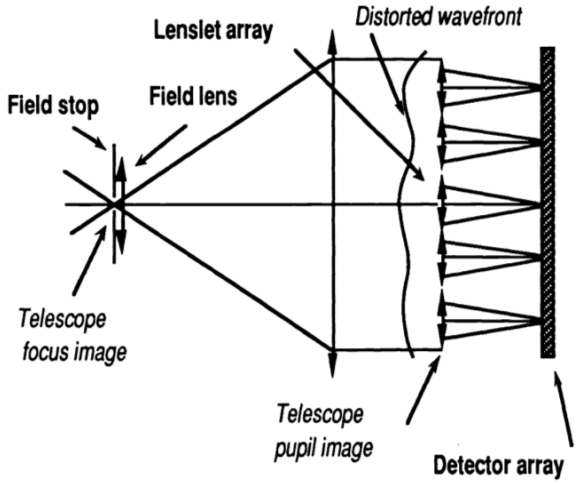

Figure 1.4 – Principle of a Shack Hartmann wavefront sensor, from Kern et al. (1989).

correction.

As the turbulence is measured in the particular direction of this guide source, the more off-axis we go from the star in the field of view, the lower the quality of the correction level is. Indeed, the portion of atmosphere crossed by the light from the guide star will be common with the one crossed by the light coming from the scientific target only if the later is close enough to the guide star. The dependence

of the PSF with respect to the spatial position in the Field Of View (FOV), called anisoplanatism, has been studied since Fried (1982). For more information on its effect on Multi-Object Adaptive Optics (MOAO) or on Extremely Large Telescopes (ELT), see for instance Neichel et al. (2008) and Clénet et al. (2015) respectively. On extended targets, this appears to be limiting the usability of AO and especially on extragalactic observations where stars density at high galactic latitude is generally low. More complex AO systems have been developed to correct the wavefront in a peculiar direction, on a larger field (Multi-Conjugate AO, see Beckers 1989 for example), or on multiple objects (MOAO, presented in section 2.1). These AO systems are particularly relevant to extragalactic observations.

In any case, the corrected field will always be limited to the availability of bright stars. For this reason, the Laser Guide Star (LGS) mode, where lasers are used to create artificial point sources in the upper atmosphere (usually in the sodium layer, around 90 km above the ground) was developed. The two main ways of creating such artificial stars are to use Rayleigh backscattering (see sections 3.2.2.1 and 3.2.3 for details on scattering) or to excite sodium atoms, that will emit light by deexcitation. By using this source as the reference for turbulence measurements, AO can correct the wavefront on any direction. The only limitation is the tip/tilt error, linked to the first order motion of the image of the targets (due to turbulence), which is not accessible using this method, thus requiring a Natural Guide Star (NGS) to be fully operational. The NGS can however be fainter and selected farther away due to the larger isoplanatic patch of the tip/tilt mode, extending the sky coverage of the AO systems.

All these improvements to the AO concept provide access to an increased number of targets. The last generation of AO allowed the 8-meter class telescopes to achieve better resolution, mostly in the NIR, than the HST, thanks to very efficient correction levels. In particular, SPHERE (Spectro-Polarimetric High-contrast Exoplanet REsearch instrument) on the Very Large Telescope (VLT), used in this work, uses an extreme AO system in order to reach a high contrast to reveal exoplanets and disks around bright stars with a resolution better than 50 mas in the NIR, close to the diffraction limit at these wavelengths (about 40 mas in K band).

This thesis work is based on the use of these new AO facilities. The first part of this work focused on Super Stellar Cluster (SSC) while the second and main part targets AGN.

1.3 Super Stellar Clusters

According to their name, SSC are the largest and most massive young stellar clusters, therefore often called YMC for Young Massive Clusters. Star clusters are groups of newly born stars with a local star density much higher than in the surrounding media, often bound by self gravitation and whose stars share an approximately identical age. They are thought to be created by the collapse of large and dusty clouds,

due to a strong gravitational perturbation, triggering locally a high star formation rate when the gas collapses into stars. Some very young clusters are still embedded inside their dust cocoon while the older ones, populated with lower mass stars with a longer life time than the more massive ones, have consumed and/or expelled most of the original gas and dust and are no longer hidden.

To be considered as a SSC, stellar clusters should have a mass within the upper range of cluster masses, typically 10^3–10^6 $M_\odot$, comparable to Globular Clusters (GC). Their age is often estimated to be less than 100 Myr, which is much younger than the minimal age estimated for GC about 10 Gyr (Portegies Zwart et al. 2010), but the limit depends on authors. Some of them estimate the limit at nearly 10 Myr, because at this age most of the massive stars have already reach the supernova stage (as discussed in Johnson 2001). Because of the high concentration of gas embedded within such a small volume, below 5–15 pc of radius (Bastian 2016), SSCs feature among the largest ever measured Star Formation Rate (SFR) with typically $\approx$ 20 $M_\odot$ yr^{-1} (Bastian 2016). Such a high concentration of matter requires some particular conditions, able to trigger collapses of large amount of gas. For this reason, SSCs are often associated to interacting starburst galaxies or to Ultra-Luminous in InfraRed Galaxies (ULIRG) (Johnson 2001; Bastian 2016, described in the next section).

Properties of SSC have been described by many excellent reviews. In particular, for a precise description and discussion about the properties of SSC mass functions, refer to Johnson (2001), O'Connell (2004) or Turner (2009). One can also find a list of the whole zoology of clusters, including SSCs, in Moraux et al. (2016) where most of these definitions come from.

1.3.1 Host Galaxies

Starburst galaxies is an ambiguous term, but corresponds roughly to galaxies showing a SFR about 1 $M_\odot$ yr^{-1} kpc^{-2} or greater, according to Johnson (2001). Usual SFR within a galaxy would be in the range 0.001–0.01 $M_\odot$ yr^{-1} kpc^{-2}. ULIRG are characterised by their luminosity, much larger in the IR than in the visible $L_{IR} \geqslant 10^{12} L_\odot$. They are an extreme category of Luminous in InfraRed Galaxy (LIRG), often defined by $L_{IR} \geqslant 10^{11} L_\odot$ (see Turner 2009). Such IR luminosity requires large concentrations of dust within the galaxy to explain that the essential of the stellar luminosity of young stars is absorbed by grains and converted in thermal IR. Both starburst and (U)LIRG are generally thought to be the consequence of an interaction between galaxies (with mergers being the stronger example), the gravitational torque inducing the falling matter toward the centre of the galaxy.

1.3.2 Short History

It was first noticed (for example by Sargent & Searle 1970) that some galaxies were undergoing larger star formation than average. Stellar clusters were known for long, but the first use of the term SSC to designate particularly massive star cluster is found in van den Bergh (1971) for the starburst galaxy M 82. Schweizer (1982) made

the hypothesis that such massive stellar clusters were present in NGC 7252 (from the New General Catalogue) and triggered by the recent merger event undergone by the galaxy. The term SSC was then formally re-used by Arp & Sandage (1985) for two clusters in NGC 1569 and by Melnick et al. (1985) for the clusters in NGC 1705.

The understanding of SSCs increased significantly thanks to InfraRed Astronomical Satellite (IRAS, launched in 1983) observations, according to Turner (2009). HAR imaging brought in particular by the HST was also critical, as shown for example by the observation of NGC 1275 by Holtzman et al. (1992), confirming that these objects are extremely compact (< 15 pc, see also Bastian 2016).

Later, Heckman (1998) identified that a significant fraction (about 25 %) of the massive stars in the local universe were formed in a few number of starburst galaxies, underlining the importance of starburst galaxies and of SSCs in the process of birth of massive stars.

1.3.3 Evolution of Super Stellar Clusters

The first discovered clusters were Open Clusters (OC) and GCs. Because they are very different, we had to wait for the first observations of SSC to better understand the link between the different types of known clusters.

The evolution of clusters in general, and SSCs in particular is still a matter of debate. It is mostly understood that SSCs are associated to ultra dense H II regions. Since the discovery of SSCs and because of their mass, close to those of GCs, there has been discussions about whether they are the precursors of GCs, which would be their final evolution stage or if they were formed different (Bastian 2016). It appears now that OCs are not fundamentally different from SSCs, whose they represent the lower mass branch. It seems also unlikely that all these massive clusters survive more than 100 Myr or 1 Gyr. The number of GCs would be much higher if it was the case, and we expect the dissolution of most of these clusters, in particular because of the supernova stage of the most massive stars of the clusters, potentially creating strong winds thought to be able to disrupt clusters (Whitmore et al. 2007).

Furthermore, GCs and SSCs do not show the same luminosity functions. The luminosity of SSCs follows a power-law distribution which is not consistent with the GCs which appear to exhibit luminosity distribution according to a log-normal (Johnson 2001). Many studies (e.g. van den Bergh 1971) were dedicated to understand what may have caused such turn-overs, however because of the various effects that need to be included, as selection bias for example, no clear result is up to now largely accepted.

The fields of clusters and those of SSCs in particular may benefit strongly from the HAR. Improvements of the angular resolution clearly triggered this field and allowed true advances. HAR is therefore a choice tool for SSCs studies.

1.4 Active Galactic Nuclei

Active galaxies are a peculiar type of galaxies, harbouring a very bright nucleus with strong emission lines. The high, non thermal luminosity of an AGN is assumed to be emitted by a hot accretion disk, surrounding a super massive black hole, located at the very centre of the nucleus. The basic definition of AGN states that the luminosity of its nucleus should be stronger than the total luminosity of the rest of the host galaxy. This general feature is then split into several subgroups. One famous classification is the distinction by Seyfert (1943) between AGNs showing broad emission lines, and those which only show narrow emission lines. Other differences are used to classify the nuclei as for example their radio emission allowing to distinguish the radio loud and radio quiet AGNs (see e.g. Urry & Padovani 1995).

Interestingly, first identification of the particular properties of AGNs happened before the formal separation between galaxies and nebulae. Fath (1909) discovered bright emission lines, detailed later by Slipher (1917) in NGC 1068 (which will be presented in Chapter 4 as the central target of this thesis work). As mentioned, Seyfert (1943) proposed the first classification of galaxies with intense emission lines, differentiating nuclei showing or not broad lines, what will later become Seyfert galaxies, of type 1 and type 2 respectively.

1.4.1 Toward an Unified Theory

These very different characteristics pushed to the setting of an unified scheme, able to produce the very different features observed in this panel of objects.

Based on observations of different type of AGNs (see, e.g., Rowan-Robinson 1977, Neugebauer et al. 1980, Lawrence & Elvis 1982, Antonucci 1984), it was proposed that a circumnuclear obscuring region was responsible for the lack of a broad line region in Seyfert 2, only revealed in AGNs for which the line of sight was close to the polar axis (type-1 view). This was strengthened by the study of Antonucci (1984) on optical polarisation of radio-loud AGNs and Antonucci & Miller (1985) who discovered broad Balmer and Fe II emission lines in the polarised light of NGC 1068, the archetypal Seyfert 2 galaxy. Following this idea, Antonucci (1993) proposed the unified model for radio-quiet AGNs, stating that Seyfert 1 or 2 were the same type of object harbouring a luminous accretion disk surrounded by a thick torus, but seen under different viewing angles. This model was extended to the radio-loud AGNs by Urry & Padovani (1995) a couple of years later.

According to this model, as represented in sketch of figure 1.5 from Marin et al. (2016a), an AGN would be constituted of:

— a Central Engine (CE), more likely to be a super massive black hole with a hot accretion (with its innermost regions being estimated around 10^7 K by Pringle & Rees 1972) disk emitting through unpolarised thermal emission most of the luminosity from ultraviolet to NIR;

— an optically thick dusty torus, of typical size 10 to 100 pc, surrounding the

CE and blocking the light in the equatorial plane, with its innermost border at sublimation temperature. This hot dust is the main source in the near/mid-infrared and appears as quasi-unresolved source. The cavity inside the torus is assumed to be the region where the broad emission lines are formed, called Broad Line Region (BLR);

— an ionisation cone in the polar directions would be directly illuminated by the CE, connecting with the interstellar medium to create the Narrow Line Region (NLR) after few tens of parsecs.

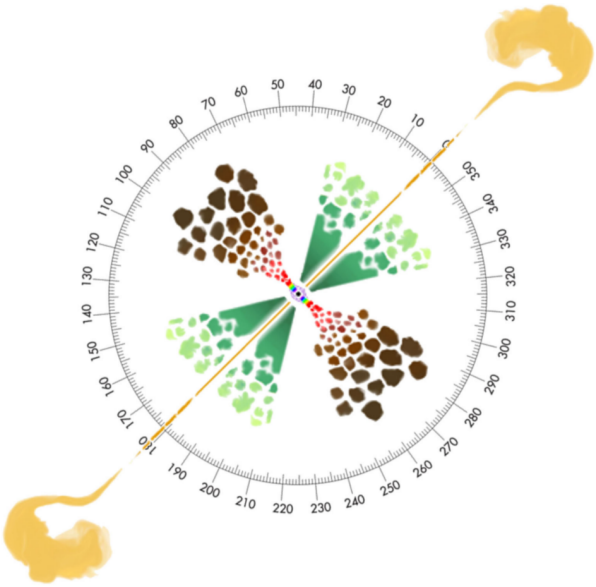

Figure 1.5 – Unscaled sketch of the AGNs unification theory. A type 1 AGN is seen at inclinations 0–60° while a type 2 AGN is seen at 60–90°, approximately. Colour code: the central super massive black hole is in black, the surrounding X-ray corona is in violet, the multi-temperature accretion disc is shown with the colour pattern of a rainbow, the BLR is in red and light brown, the circumnuclear dust is in dark brown, the polar ionized winds are in dark green and the final extension of the NLR is in yellow-green. A double-sided, kilo-parsec jet is added to account for radio-loud AGN. From Marin et al. (2016a).

1.4.2 Validation, Tests and Limitations of the Unified Model

This model has been thoroughly tested for many years by several observers. A significant part of the constraints on these different regions were brought thanks to observations of NGC 1068 and a more detailed picture on the proposed structure and the limits of the interfaces between theses areas can be found in the NGC 1068 description, in section 4.1.1.

More statistical studies were also conducted on the populations of Seyfert galaxies.

For example, Ramos Almeida et al. (2016) examined a sample of Seyfert 2 galaxies, aiming at observing the hidden broad emission lines, thanks to spectro-polarimetry. They detected these hidden emissions in a significant fraction of the sample (about 73 %), correcting misclassification of some of these objects, supporting the unified model.

Observations were compared to many simulations, trying to reproduce the main features (see for example Wolf & Henning 1999; Marin 2014, 2016), with the result that a zeroth-order agreement was found with measures.

Thus, the unified model of AGNs is currently largely accepted, but the initial scheme has evolved thanks to new constraints and to the influence of other models. The torus extension is now assumed to be smaller than the hundred of parsecs predicted by Antonucci (1993), for example a recent estimate by García-Burillo et al. (2016) is about 5 to 10 pc . Furthermore, some components (in particular the torus, but also for example the NLR) are now envisaged as a fragmented media, more physically in line with the fractal structure of the InterStellar Medium (ISM), see for example Elmegreen (1991) and the AGN study of Marin et al. (2015). Furthermore, the BLR and the torus, initially described as two different entities by Antonucci (1993) are now considered as a unique structure, with a temperature gradient inducing the properties of the two regions (see for example Elitzur & Ho 2009). This feature is for instance more related to the disk-wind model proposed by Emmering et al. (1992).

One can note that among the techniques used to increase our understanding of AGNs, polarimetric observations are one of the key methodologies as demonstrated 30 years ago by the studies of Antonucci (1984) and Antonucci & Miller (1985), providing the angular stones for the definition of the unified model of AGNs, extended more recently by Ramos Almeida et al. (2016). We can also underline the growing use of AO on extragalactic sources, starting from Lai et al. (1998), to reach the most hidden inner structures of extension of only few parsecs.

1.4.3 Current Investigations

As demonstrated by the most recent papers still updating the features observed in some Seyfert galaxies, like the new broad lines detections of Ramos Almeida et al. (2016), our understanding of AGNs is continuously evolving. Concerning the torus especially, one of the most important pieces of the model, we still lack informations due to its limited extension and to the high contrast required to observe it. Indeed, with an extension of few tens of parsecs of cold matter, optically thick, close to the very bright CE and the core of hot dust, detecting the signature of this dusty torus is particularly challenging.

1.5 Goal of this Research Work

This thesis will focus on the use of two of the most recent AO systems described in section 1.2.3 in order to go deeper in the understanding of AGNs and of SSCs.

The main part of this work is dedicated to polarimetric observations of an AGN and their interpretation through the use of radiative transfer simulations. With this study, we aim at constraining the geometry, composition and density of different AGN structures.

The first part is dedicated to SSCs and we will describe in Chapter 2 one of the first set of MOAO scientific images obtained on two galaxies, one being out of reach for other AO systems. In particular, our goal is to constrain the properties, as age and metallicity of the clusters newly observed. The second and main part will focus on AGNs, with a polarimetric point of view. We will present in Chapter 3 will introduce and detail the physics of polarisation and in Chapter 4, we will describe the new polarimetric observation conducted on one archetypal Seyfert 2 nucleus. Chapter 5 presents the radiative transfer code developed in the frame of this thesis work to interpret the AGN data and the corresponding analysis will be discussed in Chapter 6, before concluding (Chapter 7).

Chapter 2

Super Stellar Clusters

Contents

As presented in section 1.3, SSCs are key targets to understand the extreme star formation episodes and to constrain SFR evolution at different ages of the Universe. These massive and young star clusters are indeed the best examples of regions with extreme star formation. Understanding their properties is key to understanding the evolution of galaxies. However, up to now the number of accessible galaxies featuring SSCs is still limited. As technology is progressing, more and more targets are becoming reachable for HAR observations. This is one of the main objectives of the future instrument MOSAIC (Multi-Object Spectrograph for Astrophysics, Intergalactic-medium studies and Cosmology), planned for the European-ELT. Such new instruments, requiring significant technological breakthrough rely on demonstrators, allowing to develop and verify the different concepts that will be introduced. CANARY was built with the purpose of testing the performance of new AO concepts on sky, some of which are planned for MOSAIC. We will focus on MOAO in the following.

2.1 The CANARY Instrument and MOAO

Extragalactic science often requires to get access to the best possible resolution on a maximum number of targets simultaneously. As opposed to wide field AO systems, MOAO does not aim at correcting a large field but to only compensate the turbulence perturbations in particular directions, in order to have turbulence corrected images on some small regions of the field instead of the entire FOV. The main difference here is that the turbulence measurements are not conducted in the direction of the targets and that the AO loop is in that case "open": turbulence is measured thanks to other references, and deformation is applied to various DM to correct the wavefront for another line of sight. MOAO can use LGS in order to measure the perturbations, however at least one NGS is still required for tip/tilt correction.

CANARY was designed to be installed on the Nasmyth focus of the 4.2 m diameter William Herschel Telescope (WHT), located at Roque de los Muchachos in La Palma, Canary Islands (in Spain). It has been installed for its phase A on 2010. It has followed several phases, each one dedicated to a particular evolution of the AO strategy until the summer 2017. Initially, CANARY was designed to be able to perform MOAO correction using four NGSs, one on-axis and three off-axis, between 10 and 60″ . All four sensors were 7×7 sub-pupils Shack-Hartmann (see section 1.2.3 and Vidal et al. 2014) and the central beam is separated thanks to a dichroic plate, part of the flux being redirected toward a dedicated NIR camera. A detailed review of the instrument can be found in Gendron et al. (2011).

It has then been evolving for 7 years and after 2012 it had been equipped with four additional wavefront sensors, allowing the AO system to use four LGS as well as NGS farther from the scientific target, up to 1′ Gendron et al. (2011). These LGSs used Rayleigh backscattering. Being a demonstrator, CANARY is designed to compute and correct the wavefront in one particular direction, in a limited FOV ($8'' \times 8''$), but further away from the on axis NGS than what would be possible with other AO systems.

The purpose of CANARY was mainly performances tests and characterisation of new AO concepts. It was not designed for performing scientific programs on astronomical sources, however the team tried after a particularly successful run to observe two galaxies in MOAO mode. These two targets, NGC 6240 and IRAS 21101+5810 were observed during summer 2013 thanks to the LGSs constellation and one NGS. For the first target, NGC 6240, the NGS was located at 30″ away from the centre of the galaxy. It is close enough to allow classical AO systems to give access to this target and it was already observed by Pollack et al. (2007) using Keck. This was however not the case for the second galaxy, IRAS 21101+5810, for which the closest star, bright enough to be used as a guide source is situated 50″ away. CANARY observations are therefore the only AO corrected ground observation of this galaxy up to now, the only previous HAR images were obtained with the HST (Armus et al. 2009). CANARY was furthermore one of the first instruments able to obtain scientific data on astronomical targets in MOAO mode (Gendron et al. 2011).

2.2 Observed Systems

Both galaxies observed with CANARY, NGC 6240 and IRAS 21101+5810, are in mergers at different stages. NGC 6240 is composed of two nuclei, bulges without disks, remnants of the two initial galaxies, currently merging at an advanced stage, with tidal tails. The formation of a disk is even expected in this system in less than 10 Myr according to Tacconi et al. (1999). On the other hand, IRAS 21101+5810 is likely to be at the beginning of a merging process, its two components showing asymmetries due to their first gravitational interaction but being mostly intact (see Haan et al. 2011). As opposed to NGC 6240, the time scale for the merging process was not determined for this second couple of galaxies. Both systems belong to a sample of (U)LIRG: the Great Observatories All-Sky LIRG Survey (GOALS) (eg. Armus et al. 2009).

NGC 6240 is a well known galaxy and has been studied extensively, but this is not the case of IRAS 21101+5810, only examined through GOALS statistical studies. These galaxies are situated at $z = 0.0245$ and $z = 0.0390$ respectively, which corresponds to 116 and 174 Mpc for $H_0 = 70$ km/s/Mpc, according to Iwasawa et al. (2011) using data from the NASA/IPAC Extragalactic Database (NED) based on measurements by Strauss et al. (1992).

SSCs were already detected in NGC 6240 by Pollack et al. (2007) and we expect to find SSCs in the IRAS 21101+5810 system because of the gravitational interaction undergoing by the galaxy. We therefore took advantage of these new CANARY observations to conduct a photometric study of the SSCs present in these systems. This provides new insights on IRAS 21101+5810 and brings new elements to confirm the detection of Pollack et al. (2007) on NGC 6240. Our work is also a good assessment of CANARY performances through the comparison with the NIRC2 (Near InfraRed Camera - 2nd generation) data.

2.2.1 NGC 6240

According to Armus et al. (2009), NGC 6240 has a IR luminosity of $\log_{10}(L_{IR}/L_{\odot}) = 11.93$, and is therefore at the frontier between LIRG and ULIRG. Its two components, shown in figure 2.1, have a magnitude in the I band of 11.75 and 14.56 respectively (Kim et al. 2013) and both nuclei would be active according to Komossa et al. (2003). 20 to 24 % of the bolometric luminosity of the AGN would come from the contribution of dust, and the Spectral Energy Distribution (SED) fitting required hot gas, estimated at $T = 700$ K by Armus et al. (2006). Its distribution studied thanks to CO emission, is concentrated in a 4 kpc region surrounding the two nuclei. This gas shows indication of disk rotation around the Northern nucleus, with a peak of emission in the central kilo-parsec between the nuclei where motions are more turbulent, as discussed by Iono et al. (2007), measurements of stellar velocities shows a large dispersion. This would be explained by the existence of two different stellar populations with the younger and more recently formed would superimpose on an older stellar

populations from the two progenitor galaxies, inducing this apparent wide dispersion in velocities according to Engel et al. (2010).

In NGC 6240, a precise study of the SSCs was conducted by Pollack et al. (2007). The authors identified about 32 clusters, as shown in figure 2.1. They estimated their masses using photometry, obtaining between 7×10^5 and 4×10^7 $M_\odot$ and estimated their age to approximately 15 Myr. This would correspond to the end of the starburst episode as evaluated by Tecza et al. (2000) which occurred 15 to 25 Myr ago. The starburst would have happened when the two nuclei were at the closest distance from each other, estimated to nearly 1.4 kpc. According to the same study of Tecza et al. (2000), the K band luminosity of the two nuclei would be dominated by red supergiants that should have been formed during the aforementioned starburst.

Haan et al. (2011) estimated their luminosity to $L_{South} = 10^{11.29}$ $L_\odot$ [1] and $L_{North} = 10^{10.81}$ $L_\odot$ respectively. They also measured their radius to $R_{South} = 0.23 \pm 0.0$ kpc and $R_{North} = 0.2 \pm 0.01$ kpc, leading to estimates of the mass of their assumed supermassive black holes of $M_{BH,S} = 10^{8.76 \pm 0.1}$ $M_\odot$ and $M_{BH,N} = 10^{8.2 \pm 0.07}$ $M_\odot$, using the relation of Marconi & Hunt (2003). Another estimate, by Medling et al. (2011) for the largest nucleus, gave a mass between 8.3×10^8 and 2.0×10^9 $M_\odot$, consistent with the previous value. Medling et al. (2014) estimated the dynamical mass of the two nuclei to $M_{dyn,S} = 3.2 \pm 2.8 \times 10^9$ $M_\odot$ and $M_{dyn,N} = 0.2 \pm 0.01 \times 10^9$ $M_\odot$ respectively.

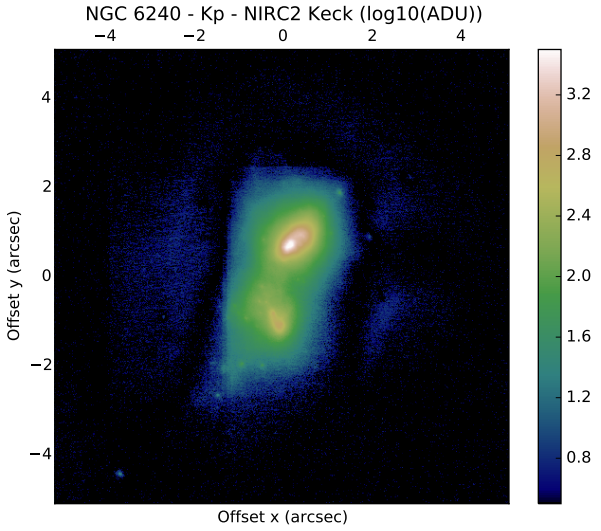

Figure 2.1 – NGC 6240 in Kp band by NIRC2 - Keck. Many SSC are distinguishable on this image as small clouds spread around the two nuclei. The angle between y axis and North is about 160°.

1. These authors also estimated the errors on these measurements, but these are very likely to be overestimated as they are typically of the same magnitude of the measurements themselves, $L_{South} = 10^{11.29 \pm 9.38}$ $L_\odot$ for example.

2.2.2 IRAS 21101+5810

As for NGC 6240, Armus et al. (2009) estimated the IR luminosity of IRAS 21101+5810 to be $\log_{10}(L_{IR}/L_{\odot}) = 11.81$, once again close to the ULIRG limit. The largest component of IRAS 21101+5810, the only one visible in figure 2.2, has I and H band magnitudes of 14.57 and 12.54 respectively, while the other component was measured to $m_I = 16.59$ and $m_H = 14.21$ by Kim et al. (2013). These authors also estimated the FWHM of the luminosity profile of these components, obtaining for I and H bands respectively 9.1 and 3.9 kpc for the first one and 1.0 et 1.1 kpc for the second one, both components being separated by 7.5 kpc. The study by Haan et al. (2011) also includes measurements at H to assess the mass of the assumed central black hole of the principal component. They measured a luminosity of $L_{bulge} = 10^{10.42}$ $L_{\odot}$ with a radius of $R_{bulge} = 0.39 \pm 0.01$ kpc. This led to a black hole mass estimation $M_{BH} = 10^{7.75\pm0.08}$ $M_{\odot}$.

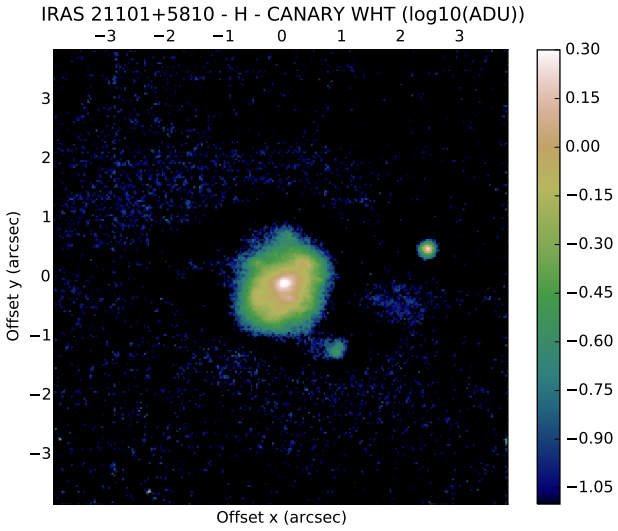

Figure 2.2 – IRAS 21101+5810 in H band by CANARY - WHT. The angle between y axis and North is about 130°.

2.3 Data Reduction

In Addition to the data obtained with CANARY, we also retrieved images of the same two targets from the Keck observatory and from the HST through the dedicated archive, with the purpose of comparing the photometry of the identified SSCs in different bands, from NIR to visible and analyse their properties through colour dependency. NGC 6240 and IRAS 21101+5810 were observed with the HST using ACS (Advanced Camera for Surveys), with the F814W and F435W filters, and NICMOS (Near Infrared Camera and Multi-Object Spectrometer) with the F160W filter. The

NIRC2 instrument, installed on the Keck 10 m diameter telescope, was also used to observe NGC 6240 at Kp using AO correction.

CANARY observations were conducted on three consecutive nights, starting on the 22nd of July 2013. During the last two nights, the standard calibration star CMC 513807 (from the Carlsberg Meridian Catalogue) was observed at H and Kp to perform photometric calibration. In total, 40 images were recorded in H band, 28 in Kp band for NGC 6240 ; 96 images were obtained in H band and 62 in Kp band for IRAS 21101+5810. Seeing during this period was measured between 0.4″ and 0.6″ at 500 nm.

Exposure time per image was set to 20 s for NGC 6240 and to 40 s for IRAS 21101+5810. Those of CMC 513807 were varying between 0.5 and 5 s. On the CANARY IR camera, the plate scale is 0.03″ per pixel for a detector of 256 × 256 pixels.

NIRC2 data were used by Pollack et al. (2007) for their detection of SSCs in NGC 6240 in Kp band, with an exposure time of 30 s. All the observation parameters are given in table 2.1.

2.3.1 CANARY Reduction

As a demonstrator, dedicated to performances studies, no standard scientific data reduction pipeline is available for CANARY. A dedicated pipeline was developed to process the data used in this work. Data were reduced using classical reduction methods:

— Computation of a sky image through a median of science images, acquired following a dithering process on the camera;
— Subtraction of this sky to all images;
— Bad pixel correction;
— Stack of subsets of few images through median;
— Images registration;
— Final images stacking using a clipped average.

The star photometry shows very few variations from one night to the other, below 0.05 magnitude. The measurements are outlined on table 2.2. The zero point (ZP) was then computed from the known magnitude m (from Cutri et al. 2003) and the measured flux F thanks to:

$$ZP = m + 2.5 \log_{10}(F). \tag{2.1}$$

2.3.2 HST - Nicmos

Archives data were already reduced. However, in order to be able to compare these images to the CANARY sets, we needed to convert their photometry to the Vega magnitude system.

Table 2.1 – Summary of data used in our study.

Object and band	Instrument	Exp. time (s)	Plate scale ($''$/pixel)	Field (pixels)	Date
NGC 6240					
H	CANARY	800	0.03	256×256	22-25/07/2013
Kp	CANARY	560	0.03	256×256	22-25/07/2013
F814W (I)	ACS	720	0.05	4228×4358	11/02/2006
F435W (B)	ACS	1260	0.05	4228×4358	11/02/2006
F160W (H)	Nicmos	192	0.075948×0.075355	387×322	12/02/1998
Kp	NIRC2	660	0.009952	1024×1024	03/08/2001
IRAS 21101+5810					
H	CANARY	3840	0.03	256×256	22-25/07/2013
Kp	CANARY	2480	0.03	256×256	22-25/07/2013
F814W (I)	ACS	830	0.05	4228×4358	03/11/2005
F435W (B)	ACS	1425	0.05	4228×4358	03/11/2005
F160W (H)	Nicmos	2496	0.075948×0.075355	387×322	10/06/2008
CMC 513807					
H	CANARY	0.5×2	0.03	256×256	24/07/2013
Kp	CANARY	5×2	0.03	256×256	24/07/2013
H	CANARY	1×2	0.03	256×256	25/07/2013
Kp	CANARY	5×2	0.03	256×256	25/07/2013

Table 2.2 – Calibration star photometry.

Band - Night date	H - 24^{th}	H - 25^{th}	Kp - 24^{th}	Kp - 25^{th}
Intensity (ADU)	33 313.5	64 412.6	195 522	188 927
Flux (ADU/s)	66 627	64 412.6	39 104.5	37 785.4
Magnitude	9.973 ± 0.035	9.973 ± 0.035	9.955 ± 0.022	9.955 ± 0.022
ZP	22.03	22.00	21.44	21.40

Nicmos images were converted thanks to header keyword PHOTFNU. It corresponds to flux density per unit of frequency F_ν, for a source that would produce 1 ADU per second. It is expressed in Jy.s/ADU. This allows to translate these ADU fluxes (F) in the images onto AB magnitudes, according to the Nicmos manual:

$$m_{AB} = -2.5 \log_{10}(PHOTFNU \times F) + 8.9. \tag{2.2}$$

We then applied the AB to Johnson translation $m_J = m_{AB} - 1.39$ in H band, from Blanton & Roweis (2007).

2.3.3 HST - ACS

the reduction of ACS data is analogous to what was done on Nicmos data. The keywords used are however different and we used PHOTFLAM (Inverse sensitivity in erg/cm^2/s/Å) combined with PHOTPLAM (which is the central wavelength of the filter passband) in order to compute the zero point in AB magnitude:

$$ZP_{AB} = -2.5 \log_{10}(PHOTFLAM) - 5 \log_{10}(PHOTPLAM) - 2.408, \tag{2.3}$$

which is then used to convert onto magnitude the flux F measured in the images:

$$m_{AB} = -2.5 \log_{10}(F) + ZP_{AB}, \tag{2.4}$$

and convert to Johnson magnitudes, with $m_J = m_{AB} - 0.45$ in I band and $m_J = m_{AB} + 0.09$ in B band (the two closest Johnson filters to F814W and F435W respectively, see Blanton & Roweis 2007).

Note that these corrections are given for filters H, I et B, different from filters F160W, F814W et F435W. The induced absolute photometric error is thus of the order of 0.05 in magnitude.

2.3.4 Keck - NIRC2

NIRC2 handbook gives a zero point value of 24.80 ± 0.07 in Kp band, depending on the Strehl ratio [2] (this value is of 24.74 in Kp band for a Strehl ratio of 1). Assuming

2. Strehl ratio is used to assess the quality of the seeing, defined in section 1.2.1. A value of 1 would indicate a perfect diffraction limited observation.

small Strehl variations during the observations, we used the same value for all images and therefore converted NIRC2 images using:

$$m_J = -2.5 \log_{10}(I/t) + 24.80, \tag{2.5}$$

with t the exposure time (in s) and I the intensity (in ADU).

2.3.5 Images Registration

The last processing to obtain comparable data sets is to interpolate the images to a same plate scale, and to rotate them to obtain the same orientation.

We used linear interpolation, with a scale factor deduced from plate scales respective values and used CANARY images orientation as a reference. As the exact orientation of CANARY images according to the North is not known, rotations were conducted using reference position in the field of view. This was more precise for IRAS 21101+5810 thanks to a star in the field of view (visible on the upper right corner of figure 2.2), than for NGC 6240, especially between images with very different morphological features at various wavelength.

To cope with the resolution difference between NIRC2 images (obtained with Keck - 10 m) and CANARY images (obtained with the WHT - 4.2 m), we convolved NIRC2 images with a 2D Gaussian representing the CANARY PSF (see section 2.5.1 for details) in order to be able to superimpose images sets.

2.4 Final Images

Final reduced images are shown for NGC 6240 in figure 2.3 and for IRAS 21101+5810 in figure 2.4. Displayed images were rotated, cropped to the same field of view and convolved in the case of NGC 6240 with NIRC2.

2.5 Photometry

With the images shown in figure 2.3, it appears that CANARY data do not bring an improved resolution on NGC 6240. This is fully expected from two instruments with very different diameters but allowed to characterise on sky the performance of CANARY. Furthermore, images of IRAS 21101+5810 (see figure 2.4) are the only available data for this target in these bands at such a resolution and will therefore provide a unique diagnostic for the study of SSC in this system. We aim in the following at constraining the ages of the clusters, as well as their size, composition, metallicity and extinction.

Concerning photometry, an approach fitting the clusters intensity distributions was implemented as opposed to standard aperture photometry. Because clusters are located close to the bright nucleus and inside the galaxy brightest region, aperture photometry will suffer from contamination by the galaxy background. It is therefore

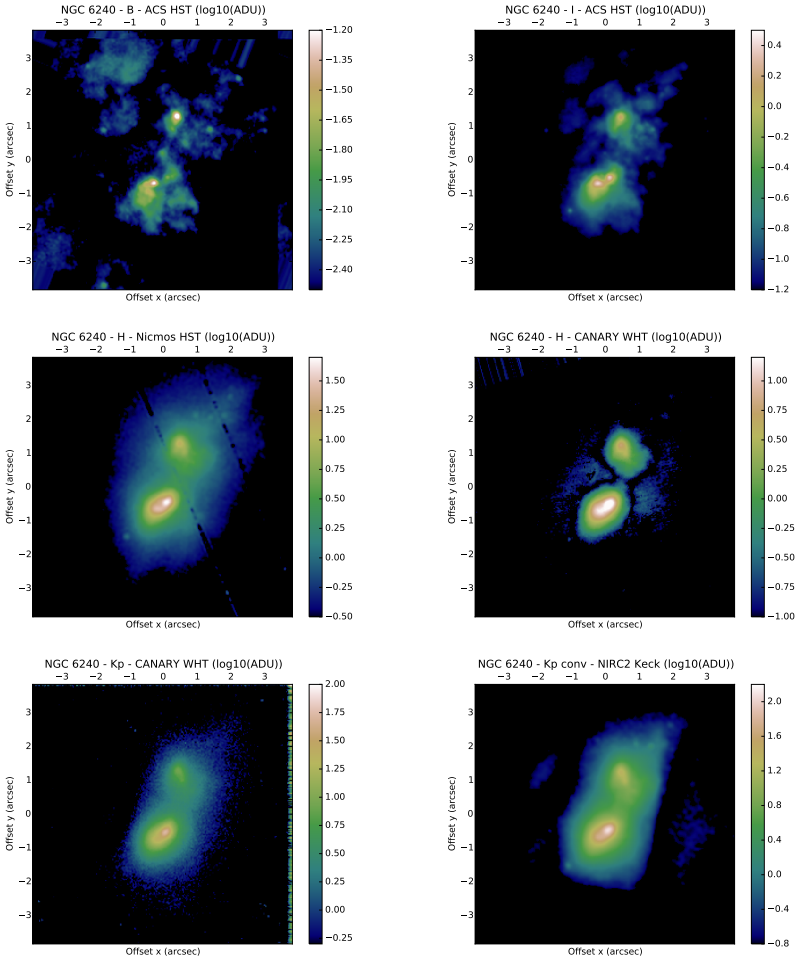

Figure 2.3 – NGC 6240. Images represent intensity maps (in $\log_{10}$(ADU)) obtained in F435W (B) and F814W (I) bands with ACS - HST; F160W (H) band with Nicmos - HST; H and Kp bands with CANARY - WHT; Kp band with NIRC2 - Keck.

necessary to fit a brightness distribution on each cluster, including a proper estimation of the background to achieve a better accuracy.

2.5.1 PSF Estimation

We used the foreground star in the images of IRAS 21101+5810 as an estimate of the instrumental PSF (see figure 2.5). It provides an accurate resolution calibrator for the CANARY observations, to assess whether the clusters are resolved or not. Note that this PSF could be used to fit the clusters intensity distribution.

Efficiency of the AO correction can be evaluated by comparing the FWHM of the PSF to the theoretical resolution. In the case of the WHT, $D = 4.2$ m and we obtain in H band ($\lambda = 1.65$ μm) $\lambda/D \approx 0.081''$ or approximately 2.7 pixels. The FWHM of

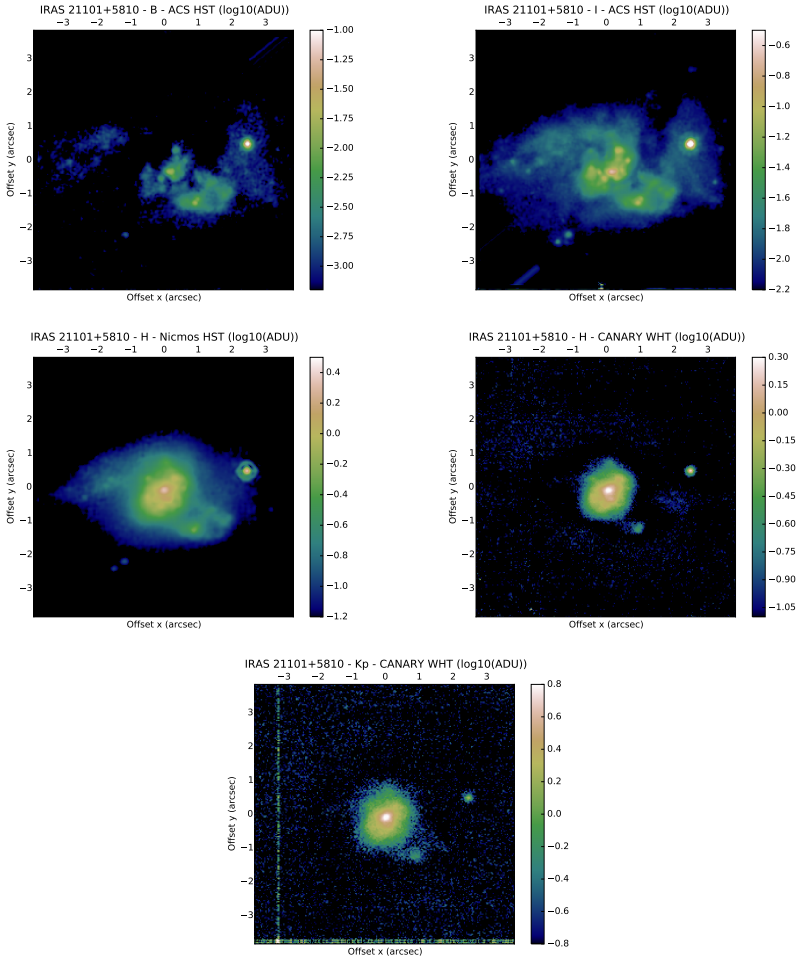

Figure 2.4 – IRAS 21101+5810. Images represent intensity maps (in $\log_{10}$(ADU)) obtained in F435W (B) and F814W (I) bands with ACS - HST; F160W (H) band with Nicmos - HST; H and Kp bands with CANARY - WHT.

the star is 4.5 pixels and we are thus reasonably close to the diffraction limit of the instrument.

Even the best AO system will not be able to compensate fully the higher spatial frequencies of the turbulence induced aberrations (see e.g. Rigaut et al. 1991 and figure 2.6) resulting in a PSF close to the Airy profile (diffraction limit) for the central core, but with stronger wings, as discussed in Moffat (1969) and Rigaut et al. (1991).

To perform photometry fitting, we should use a distribution of Moffat (1969), which has a Gaussian core with wings stronger than those of the Gaussian distribution. However, the wings of the Moffat distribution make it difficult to converge in case of a varying background. It appears that when using Moffat fitting, if the background is not perfectly estimated and subtracted, the fit overestimates the flux or even fails to converge. We therefore used Gaussian fitting, which will likely underestimate

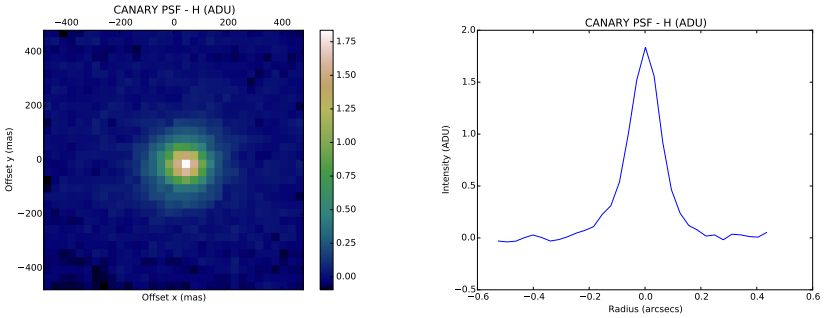

Figure 2.5 – Image and profile of the star in the image of IRAS 21101+5810, with CANARY in H band, a good calibrator for the instrument PSF.

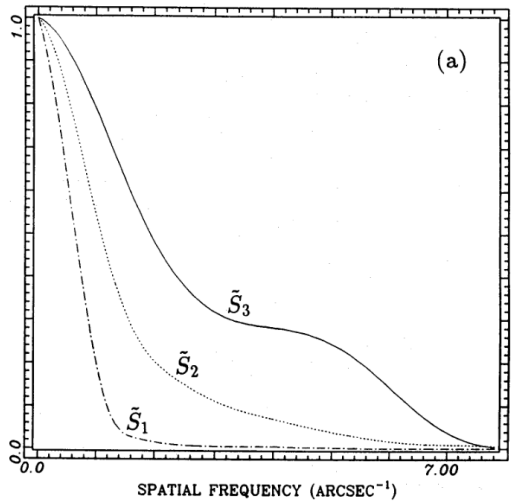

Figure 2.6 – Examples of MTF on a 3.6 m telescope: MTF normalised to 1 in cases without correction: $\tilde{S}1(f)$; with AO correction: $\tilde{S}2(f)$; ideal telescope MTF with central obscuration: $\tilde{S}3(f)$. In K band, Strehl uncorrected of 0.05, Strehl corrected of 0.28, $r_0 = 12$ cm, wind speed of 3 m.s^{-1}. From Rigaut et al. (1991)

slightly the fluxes but will be more reliable and still remains reasonably close to the instrumental PSF (see figure 2.5).

2.5.2 Classical Fitting

Our first fitting algorithm used a second order polynomial to fit the background. Both the cluster and the background were fitted simultaneously with a combination of a second order polynomial and a 2D Gaussian, as shown in figure 2.7.

Despite obtaining better accuracy with a Gaussian than using a Moffat distribution, this fitting procedure was still failing for some clusters, if the background was not reasonably flat or in the case of low luminosity clusters. We therefore tried to imple-

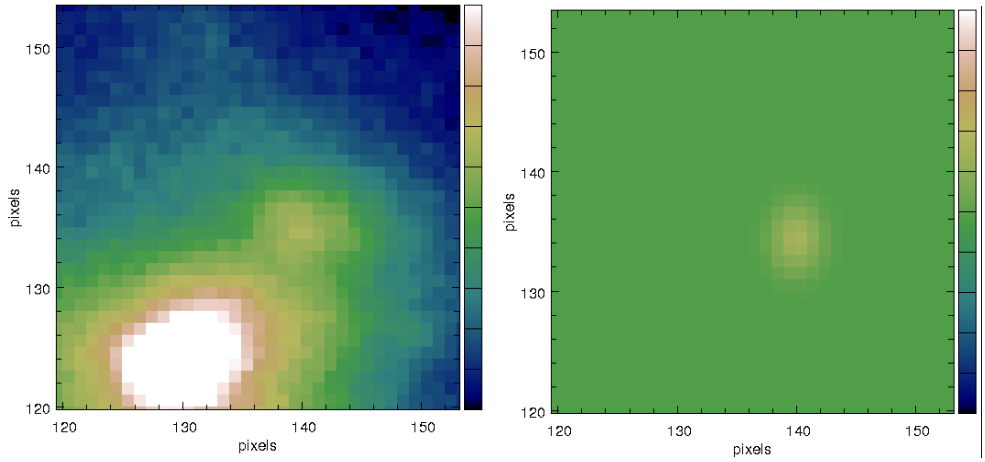

Figure 2.7 – Example of a fit of a 2D Gaussian on one of the clusters in the H band image of IRAS 21101+5810. Left panel shows the initial image, with the cluster to be fitted in the centre, right panel displays the obtained fit, with a colour bar scaled to the previous map (with a constant background).

ment a new procedure, using the resolution of the Poisson's equation inside a contour around the source, to evaluate the background, in order to have a better estimate of its contribution.

2.5.3 Fitting using Poisson's Equation Resolution

This algorithm was initially proposed by Daniel Rouan, based on Dirichlet problem. It consists in a first determination of the cluster's limit on the initial image, using a rough detection procedure. The basic idea here is just to identify both the peak location and the radius, by estimation of the radius where the flux stops to decrease. All the inner pixels are replaced by interpolation of a Green function (ϕ) whose values are constrained on the contour which is equivalent to solving the Poisson's equation $\nabla^2\phi = 0$. The principle here is simply to find the surface with the lowest possible curvature to replace the missing part. This newly estimated background is then subtracted to the initial image, and the 2D Gaussian could then be precisely fitted to the cluster. A test of the method on simulated data is shown in figure 2.8 and an example of the process on the image of IRAS 21101+5810 is displayed on figure 2.9.

Following this last method, we fitted the SSCs present in the IRAS 21101+5810 image. Results are shown in table 2.3. Identification of the cluster numbering can be found in figure 2.10. To estimate the errors made on the photometry, we ran a series of Gaussian fit on simulated images, including background, the source and noise (see figure 2.8). By comparing the obtained photometry to the theoretical one, we have relative incertitude on the photometry of 10–15 %. We will use in the following a conservative incertitude of 15 %.

Table 2.3 – Photometry of the detected SSC in the intensity maps of IRAS 21101+5810. Values are given in apparent unit of $10^{-9} F_{Vega,Band}$. If a "x" is indicated, photometry could not have been obtained with a proper fit. Relative incertitude is 15 %. For SSC location, see figure 2.10.

Object	F435W (B)	F814W (I)	F160W (H)	H	Kp
A	≈ 0	≈ 0	35.3203	42.1078	159.846
B	0.198861	1.40011	12.3392	11.3307	22.2334
SSC1	0.0783366	2.05192	14.2731	14.4328	22.6999
SSC2	<0.01	0.191088	3.14487	3.31517	9.59219
SSC3	<0.01	0.239019	2.50334	3.81237	8.24234
SSC4	0.445026	5.73229	13.0449	8.4024	28.3546
SSC5	0.017639	0.996541	10.803	8.56428	13.2121
SSC6	0.0603434	1.06526	6.55562	6.58728	2.58787
SSC7	x	x	x	x	x
SSC8	x	x	x	x	x
SSC9	x	x	x	x	x
SSC10	x	x	x	x	x
SSC11	x	x	x	x	x
Star	2.29142	19.2562	47.5067	27.956	41.8263

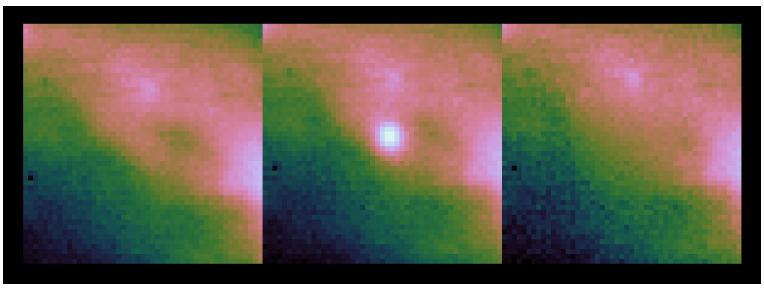

Figure 2.8 – Example of a fit using the Poisson Equation Solving with a 2D Gaussian on simulated data. First panel shows the initial image with varying backgound. We added on the second panel a point-like source, with a Gausian distribution. Last panel shows the resulting background estimation from our fitting method. Image from Daniel Rouan.

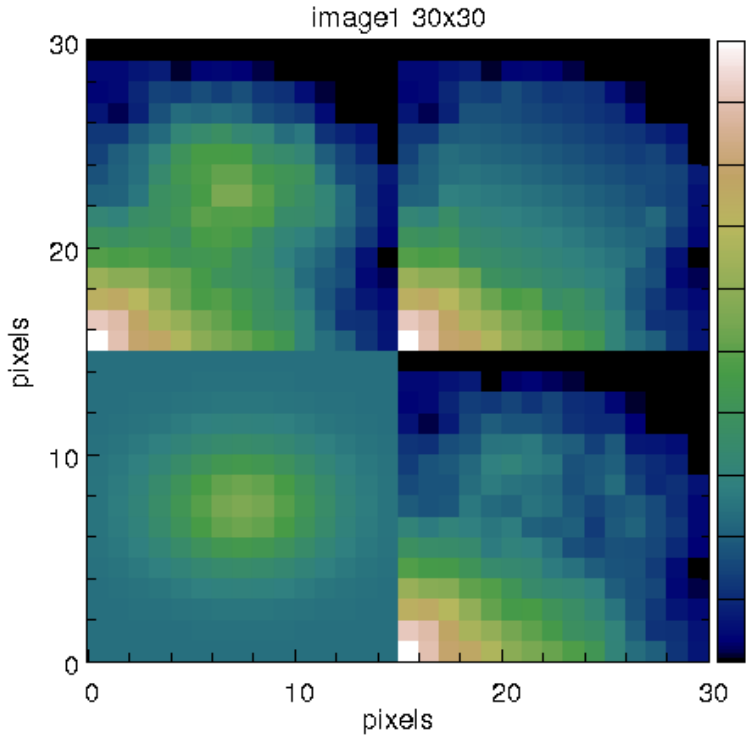

Figure 2.9 – Example of a fit of a SSC thanks to Poisson Equation Solving with a 2D Gaussian. Upper left panel shows the initial image, upper right displays the image with the background estimation through the Green function, bottom left shows the final cluster fitted and bottom right panel correspond to the image subtracted from the fitted cluster.

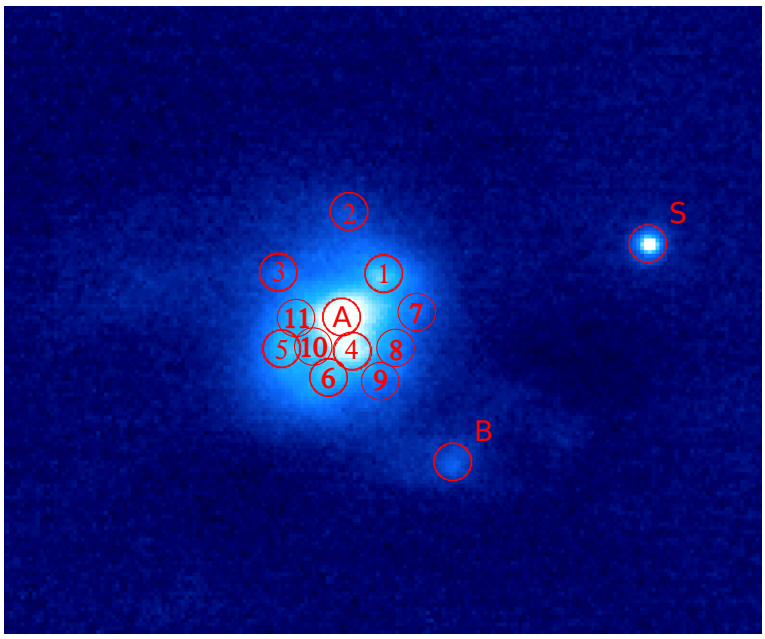

Figure 2.10 – Reference location of the detected SSC in IRAS 21101+5810 on H CANARY image (see figure 2.4). Positions of the centre of the galaxy and of the major clump component are marked A and B respectively. The star (S) is also indicated. Circles only indicate the position of the SSC and their size has no photometric significance.

2.5.4 Colour Maps

Another way of studying the photometric of the clusters is to combine the different images obtained a various wavelength into colour maps. It requires accurate registration of the different images, but provides colour indices for the different clusters in a single shot. This combination strategy can be used to compare with the photometric results obtained through the previous method, for a more robust estimation of the errors, and to have access to fainter SSCs (SSCs 7 to 11 were more difficult to fit properly).

Images were first converted into magnitude maps, using the process described in section 2.3. All images were clipped to a given threshold, to avoid floating overflow. Images were then combined to create maps of magnitude difference between two given observing bands. Colour maps are shown on figure 2.11

Thanks to these maps and using the H band image to identify the clusters, it is possible to obtain colour indices for all of the clusters. Table 2.4 summarises all the results, including the colour indices obtained through photometry.

Note that the given error ranges include only the photometric errors, not the calibration errors.

Table 2.4 – Colour indices of detected SSC in IRAS 21101+5810. For SSC position references, see figure 2.10.

Object	From colour maps			From photometry		
	F814W-F160W	F435W-F814W	H-K	F814W-F160W	F435W-F814W	H-K
A	4.16 ± 0.13	4.03 ± 0.22	1.04 ± 0.09	x	x	1.64 ± 0.33
B	1.99 ± 0.15	2.17 ± 0.12	0.33 ± 0.12	2.27 ± 0.33	2.12 ± 0.33	0.64 ± 0.33
SSC1	2.73 ± 0.16	3.70 ± 0.15	0.54 ± 0.02	2.12 ± 0.33	3.55 ± 0.33	0.50 ± 0.33
SSC2	3.10 ± 0.20	4.50 ± 0.5	1.10 ± 0.30	3.10 ± 0.33	$> 3.20 \pm 0.33$	1.21 ± 0.33
SSC3	3.33 ± 0.11	4.50 ± 0.15	0.48 ± 0.04	3.01 ± 0.33	$> 3.45 \pm 0.33$	1.29 ± 0.33
SSC4	2.51 ± 0.18	2.97 ± 0.30	0.67 ± 0.07	0.42 ± 0.33	2.77 ± 0.33	0.84 ± 0.33
SSC5	2.82 ± 0.09	4.05 ± 0.09	0.46 ± 0.05	2.34 ± 0.33	4.38 ± 0.33	0.22 ± 0.33
SSC6	2.74 ± 0.10	3.43 ± 0.06	0.58 ± 0.02	1.98 ± 0.33	3.12 ± 0.33	-1.01 ± 0.33
SSC7	2.58 ± 0.18	3.44 ± 0.09	0.57 ± 0.08	x	x	x
SSC8	2.69 ± 0.07	3.07 ± 0.07	0.45 ± 0.05	x	x	x
SSC9	2.64 ± 0.04	2.87 ± 0.04	0.47 ± 0.03	x	x	x
SSC10	3.06 ± 0.09	4.62 ± 0.16	0.59 ± 0.03	x	x	x
SSC11	2.80 ± 0.07	3.76 ± 0.19	0.34 ± 0.15	x	x	x
Star	0.61 ± 0.13	2.35 ± 0.07	0.10 ± 0.11	0.40 ± 0.33	2.31 ± 0.33	-0.14 ± 0.33

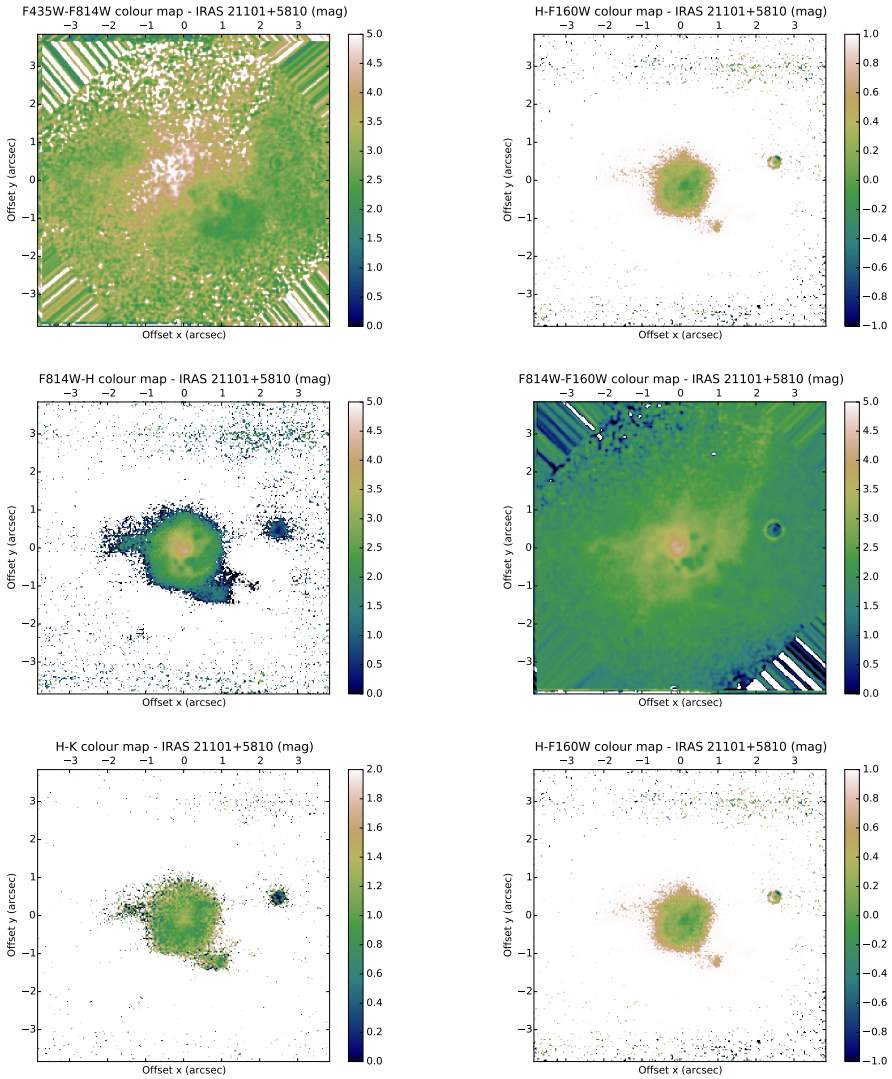

Figure 2.11 – Colour maps for IRAS 21101+5810. F435W-F814W, H-F160W, F814W-H, F814W-F160W, H-K and F160W-K respectively.

2.6 Comparison to Models

2.6.1 GALEV

In order to interpret these results, we simulated the colour indices that clusters would have depending on their age, metallicity and extinction. GALEV (GALaxy EVolution synthesis models) is a code allowing to simulate the evolution of stellar populations in galaxies globally, but which can also be used to model stellar populations in individual SSC. It was developed by Kotulla et al. (2009).

Among the parameters that can be set, we will focus on metallicity and extinction (other parameters were set according to general properties for stellar clusters or by default). Extinction follows the law proposed by Calzetti et al. (1994), for values of E(B-V) between 0.5 and 3 by step of 0.5. Three values of metallicity ([Fe/H] ratio) were tested. The first one takes into account the chemical interaction between the ISM and the stellar populations, simulating the metallicity changes through the galaxy/cluster evolution, the second one is fixed to the Sun metallicity and the third one was set to [Fe/H]=+0.3. The iron content [Fe/H] is related to the metallicity Z (see Bertelli et al. 1994) through:

$$\log_{10}(Z) = 0.977[\mathrm{Fe/H}] - 1.699. \tag{2.6}$$

Therefore [Fe/H]=+0.3 corresponds to $Z \approx 0.04$, a high metallicity, ($Z_\odot$ being 0.02, see Kotulla et al. 2009).

Photometric data were recorded every 4 Myr, with the starburst being set 1 kyr after the beginning of the simulation. The galaxy mass was set to 10^8 $M_\odot$. This is fairly low, but was chosen to constrain the contribution from the galaxy background luminosity in order to remain as close as possible to the intrinsic luminosity of the clusters. Indeed, our measurements on the data will be contaminated by background emission. Comparisons between simulations and observational data should therefore be conducted carefully.

2.6.2 Interpretation

GALEV gives as an output the absolute magnitude, but since we are using the magnitude difference between two bands, this does not have to be taken into account. Our analysis of the simulations results and the comparison with the photometric data through colour-colour diagrams is based on plotting the colour index between two bands versus another colour index, for example I-H magnitude as a function of B-I.

With this tool, it becomes possible to follow the evolutionary path of a simulated cluster, through GALEV. Time will make the luminosity of the cluster to vary, differently for various wavelengths, and its position in the colour-colour diagram will therefore evolve with age.

If all the observed clusters are gathered along a given evolutionary path, this will indicate that clusters probably share roughly the same parameters with different ages. Note that is unlikely because we expect most of the clusters formation to have been triggered by the starburst and therefore the clusters to have similar ages. It is more likely for the SSCs to be aligned along an extinction line, representing the impact of difference in extinction on clusters sharing the exact same parameters (a reddening of their emission distribution). As such, extinction is represented in the diagram, by a segment with a length indicating a change of 1 in extinction. GALEV uses colour excess, $E(B-V)$, instead of extinction A_V and in average, $A_V \approx 3.3\ E(B-V)$ is generally considered as a good approximation (see e.g. Kotulla et al. 2009).

Colour-colour diagrams of observed SSCs (red crosses) superimposed on GALEV tracks are shown on figures 2.12 and 2.13.

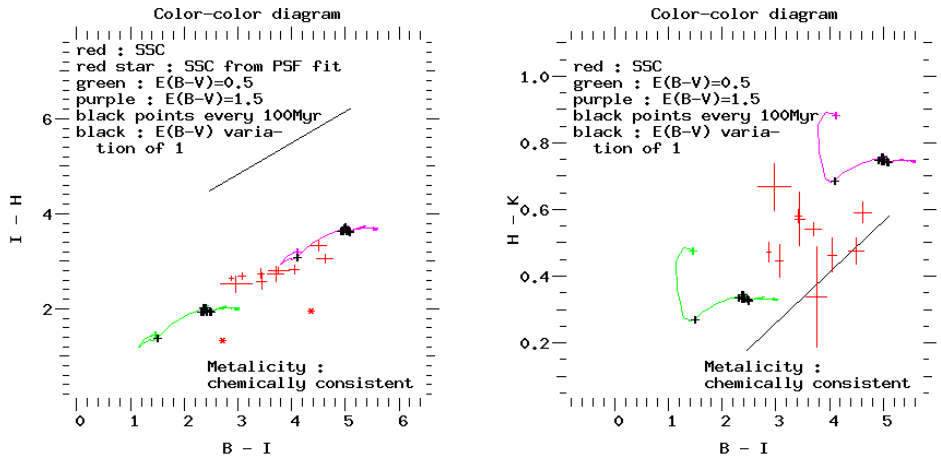

Figure 2.12 – Colour-colour diagrams for IRAS 21101+5810. First panel corresponds to I-H as a function of B-I diagrams and the second one to H-K as a function of B-I, both for a metallicity including chemical evolution. Black crosses represents GALEV simulations data points, spaced every 100 Myr, for two different extinctions, while red crosses shows the measured photometry of the clusters on IRAS 21101+5810, with their associated error bars (through colour maps). The black segment represents the effect of a variation of 1 in E(B-V).

The main parameters impacting the colour of the clusters are their age, their metallicity and extinction: can we disentangle them ?

Extinction could vary from a SSC to another, depending on its geometrical position around the galaxy nucleus. However its impact is mainly a linear translation and therefore can not account for the observed dispersion. All red crosses are consistent with an overall extinction of $E(B-V) \approx 1.0$, with small variations for every cluster. This would mean an averaged extinction of $A_V \approx 3$ for the whole galaxy.

The dispersion of clusters along the direction of the extinction can be explained by extinction. Indeed, as extinction can vary between clusters, we expect the individual clusters position on the diagram to be aligned along the extinction direction. This is particularly striking on the I-H as a function of B-I graph of figure 2.12, where all the clusters are aligned. This would be consistent with position of clusters to be scattered only due to extinction.

However, clusters are not aligned along the extinction direction on the graph of I-H as a function of B-I (second panel of figure 2.12). This extension of the clusters perpendicularly to the extinction direction is consistent with age disparity between the clusters, with all ages smaller than 100–150 Myr. Indeed, the luminosity of clusters after this time scale become more stable and would only results in clusters being aligned along the extinction direction. Because at young ages the clusters colours

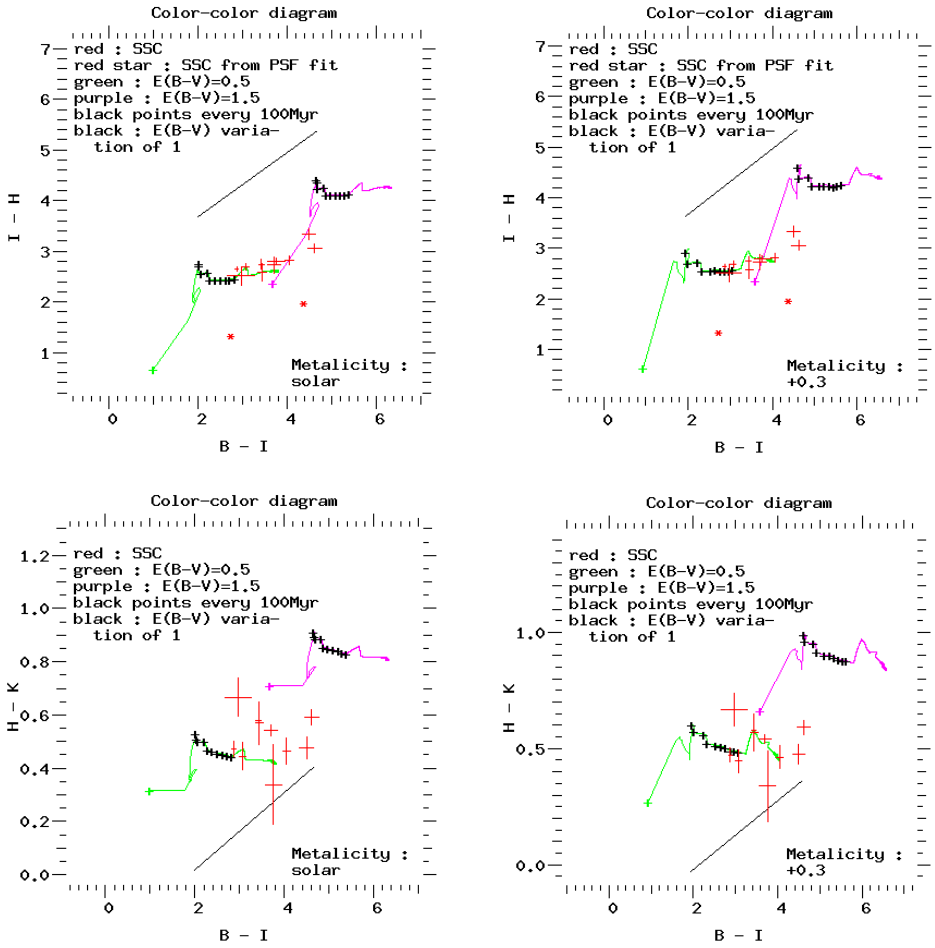

Figure 2.13 – Same as figure 2.12 for solar metallicity (first column) and for a fixed metallicity of [Fe/H]=+0.3 (last column). First row corresponds to I-H as a function of B-I diagrams and the second one to H-K as a function of B-I

vary rapidly, as represented by the large distance between the initial cluster position in these diagrams and the first black cross on figure 2.12, it is likely that all the clusters have ages lower than 100 Myr. This is consistent with the estimation that at 100 Myr, most of the SSCs (up to 90 %) would have been destroyed (see for example Bastian 2016) and that in this case we should not be able to observe this high concentration of clusters. Because of their dispersion, clusters are unlikely to have the exact same age. Note that most of these clusters are also detected on I and B band images and are therefore not as embedded as what is expected for very young clusters and are thus unlikely to be younger than 2–3 Myr (Bastian 2016).

This interpretation is also consistent with different metallicities, as shown in graphs of figure 2.13. In the graph of I-H as a function of B-I, clusters are not as aligned as they were for the chemically consistent metallicity and it is therefore more complicated

to disentangle between the different parameters that can affect the luminosity of the clusters. However, a dependency on the extinction, with an averaged value of $A_V \approx 3$ and an age variation of the clusters, younger than 150 Myr, would still be able to explain the results. It is therefore not possible to clearly disentangle the value of the metallicity in the clusters of IRAS 21101+5810.

2.7 Conclusions

Still in a preliminary state, this study requires further investigations. As we now have an estimate of the distance and the luminosity of each clusters, we should be able to constrain their masses. Recent improvements of the photometric method, involving the resolution of Poisson's equation, will allow us to go further in the analysis. It is also planned to use the radiative transfer code MontAGN, developed in the context of this thesis described in Chapter 5 in order to analyse the effect of dust shells on the luminosity distribution of clusters.

Despite its limits, this study based on data from a demonstrator highlights the interest of new AO concepts for extragalactic astronomy. This capacity to reach resolutions similar to HST observations, from the ground and without bright star close to the target is a major advantage for extragalactic observations and the planned ELTs that will see first light during the next decade should bring the capacity to observe a significant number of new targets, as IRAS 21101+5810. We will therefore be able to detect SSCs on a growing number of galaxies and therefore obtain a more reliable statistics on the SSCs in various environments and ages, so as to better constrain the occurrence of extreme star formation, the conditions of its triggering and its evolution.

Chapter 3

Polarisation

Contents

In optical astronomical observations, only the intensity of the received light is recorded. This is typically the case in standard imaging: each photon that hits a pixel of a Coupled Charge Device (CCD) (or any other type of detector), produces an electron increasing the count number in the pixel. Some detectors are able to count photons one by one, however it is more generally an averaged number of photons over a certain integration time which is recorded and used in the analysis, at least from optical to NIR. This is why a major part of astrophysics at these wavelengths is based on fluxes and intensities. However, there is more information transported by photons than just their energy. Some techniques, such as interferometry or spectroscopy, uses some other properties of the light like its wavelength coherence level for example, and the polarisation of light is one of these additional informations.

From a wave point of view, polarimetry consists in measuring the oscillation direction of electric and magnetic field of the incoming light, giving a more complete description of the received light properties. This can be achieved through classical imaging, with polarimetric images integrated over time, or can be combined with other observing methods to have access to more information at the same time. This can be done for example with some hybrid instrumentation such as spectro-polarimetry

(as used by Antonucci & Miller 1985) or sparse aperture masking combined with polarimetry (available for instance on SPHERE, see e.g. Cheetham et al. 2016).

When a wave packet, composed of a certain quantity of photons, propagates, oscillations of the fields can either be correlated over time or distributed in a fully random orientation. Typically, if from a given source, we receive a fraction of the photons with a privileged direction of oscillation for their electric field, this means that there is a physical process favouring this peculiar oscillation direction in this field of view. This process can be sometimes taking place at the photon emission but can also be a process impacting the light during its propagation.

This chapter will focus on the study of the techniques that allow the observer to measure this oscillation and to disentangle the origin of the polarisation of light.

3.1 Introduction to Polarisation

Polarisation was discovered in the XVII$^{\text{th}}$ century and was studied for example by Christiaan Huygens (around 1670) and Étienne Louis Malus (in 1808). Astronomers have been investigating the polarisation of light from extraterrestrial sources for more than a hundred years. It first began on the Sun and the Moon, which have been known to emit or reflect polarised light. Solar observations particularly benefited from polarisation with about a hundred years of measurements. Zeeman (1899) discovers that magnetic field have an impact on emitted light, separating spectral lines into different components, with particular polarisation. Astronomers then tried to detect it on others sources like Lyot (1924) on Venus or later Hiltner (1949) on three stars, some of the first polarimetric sources outside of the Solar system. Polarisation studies have then been extended to extra galactic observations, leading to one of the most important breakthroughs in AGN science with the polarimetric observation by Antonucci & Miller (1985) of NGC 1068, leading Antonucci (1993) to propose the unified model for AGNs.

Formally, light is a propagation of an oscillation of both an electric and a magnetic field along a direction. Both fields are related through Maxwell's equations, which are defined, for an electric field $\vec{E}$ and magnetic field $\vec{B}$, as:

$$\text{div } \vec{E} = \frac{\rho}{\varepsilon_0} \tag{3.1}$$

$$\text{div } \vec{B} = 0 \tag{3.2}$$

$$\vec{\text{rot}}\ \vec{E} = -\frac{\partial \vec{B}}{\partial t} \tag{3.3}$$

$$\vec{\text{rot}}\ \vec{B} = \mu_0 \vec{j} + \mu_0 \varepsilon_0 \frac{\partial \vec{E}}{\partial t} \tag{3.4}$$

with ρ the electric charge, ε_0 the vacuum permittivity, μ_0 the vacuum permeability and $\vec{j}$ the current density. In the vacuum, $\rho = 0$ and $\vec{j} = \vec{0}$, leading through temporal derivative of equations 3.3 and 3.4 to wave equations for both fields:

$$\frac{1}{c^2}\frac{\partial^2 \vec{E}}{\partial t^2} - \Delta \vec{E} = \vec{0} \tag{3.5}$$

$$\frac{1}{c^2}\frac{\partial^2 \vec{B}}{\partial t^2} - \Delta \vec{B} = \vec{0} \tag{3.6}$$

with c $= 1/\sqrt{\mu_0 \varepsilon_0}$ the speed of light in the vacuum. These two equations have solutions of the form:

$$\vec{E}(\vec{r}, t) = \vec{E_0} \times e^{i(\vec{k}.\vec{r} - \omega t)} \tag{3.7}$$

$$\vec{B}(\vec{r}, t) = \vec{B_0} \times e^{i(\vec{k}.\vec{r} - \omega t)} \tag{3.8}$$

with $\omega = |\vec{k}|c$, the pulsation, $\vec{k}$ the wave vector, indicating the direction of propagation, $\vec{E_0}$ and $\vec{B_0}$ the amplitude of respectively the electric and magnetic field, at a position $\vec{r}$ and a time t.

Both fields therefore oscillates simultaneously, the electric field, the magnetic field and the direction of propagation being all three always orthogonal one to each others, as shown in figure 3.1. This comes from Maxwell's equations. By using equation 3.7 into equation 3.1, we obtain:

$$\text{div } \vec{E} = i\vec{k}.\vec{E} = 0 \tag{3.9}$$

and doing the same thing on equation 3.2 for $\vec{B}$:

$$\text{div } \vec{B} = i\vec{k}.\vec{B} = 0, \tag{3.10}$$

proving that the direction of propagation of the light is orthogonal to both $\vec{E}$ and $\vec{B}$.

Equation 3.3 leads to:

$$i\vec{k} \times \vec{E} = \vec{rot}\vec{E} = -\frac{\partial}{\partial t}\vec{B} = i\omega\vec{B}. \tag{3.11}$$

Therefore:

$$\vec{k} \times \vec{E} = \omega\vec{B}, \tag{3.12}$$

leading to the orthogonality of $\vec{E}$, $\vec{B}$ and $\vec{k}$.

As the oscillation plane of the electric and magnetic fields is always perpendicular to the direction of propagation of the light, we will just need to express the direction of oscillation of the fields to measure polarisation. As their oscillation is synchronous, only one oscillation is required to fully described it. By convention, polarisation is

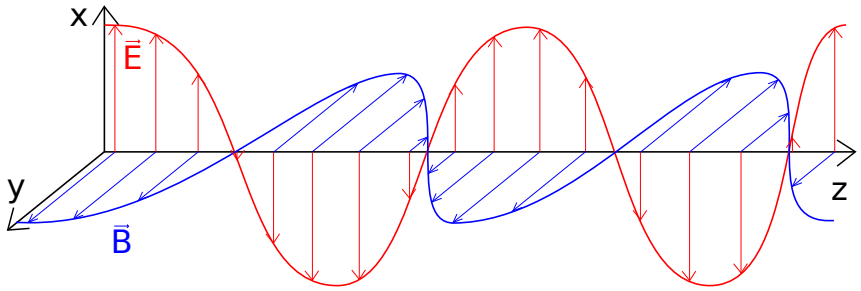

Figure 3.1 – Illustration of light propagation. Here, $\vec{k}$ is along z, while $\vec{E}$ is along x and $\vec{B}$ along y. Note that the illustration represent a precise photon propagating and that therefore the z axis also corresponds to an evolution of time.

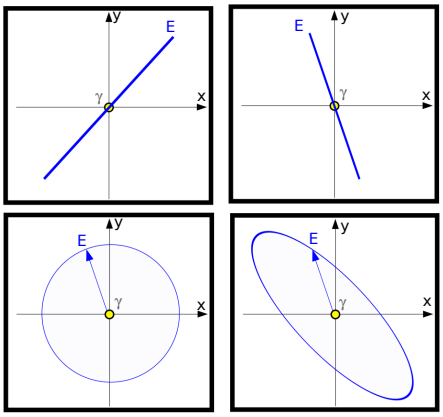

Figure 3.2 – Different type of polarisations: top: two different linear polarisation; bottom left: circular polarisation; bottom right elliptical polarisation (all viewed from the observer). The electric field's vector moves along the traced curves.

related to the electric field. Figure 3.2 gives some examples of patterns of the electric field vector depending on the polarisation of light.

One should note that fields $\vec{E}$ and $\vec{B}$ are conveniently described by complex numbers, carrying some information about the amplitude and the phase of the wave. We also need to consider that these electromagnetic waves are not monochromatic, but correspond to a wave packet, with a minimum bandwidth $\Delta\lambda$. The correlation time of this packet will be $\frac{\Delta\lambda}{c}$ and this is the time scale we must consider to determine whether the two components of the electric field ($E_{\parallel}$ and $E_{\perp}$ that will be detailed in section 3.2.1) are correlated or not. The level of such a correlation determine the degree of polarisation of the wave.

How can we measure this orientation of the electric field ? One simple way is to use a polariser. It often consists in a metal grating, constituted of thin bars along a certain direction. Oscillations in this direction will be absorbed by the polariser

as the electrons of the metal will be able to move in this direction in response to the incoming wave. This is the principle of reflection of light on metal, used in many fields of Physics, like radio astronomy.

A polariser therefore allows to select the polarisation of the absorbed light, and by consequence to the light going through it. The polariser will have a transmission of 0 % for a given direction of the electric field and 100 % for the one at 90°. Note that what is selected is the direction axis of the oscillation, the orientation of the instantaneous field along this direction, whether it is vertical up or vertical down for instance, is not relevant (and actually could not be disentangled). Because of this particularity, all values of the polarisation orientation are given with a range of only 180°, and not 360°. This thesis will use for convention the range −90° and +90° for polarisation values.

For an incoming intensity I_0 of a fully linearly polarised light and an angle of θ in between the polarisation of the light and the polariser, the received intensity I follows the Malus' law (see figure 3.3):

$$I = I_0 \times \cos^2\theta. \tag{3.13}$$

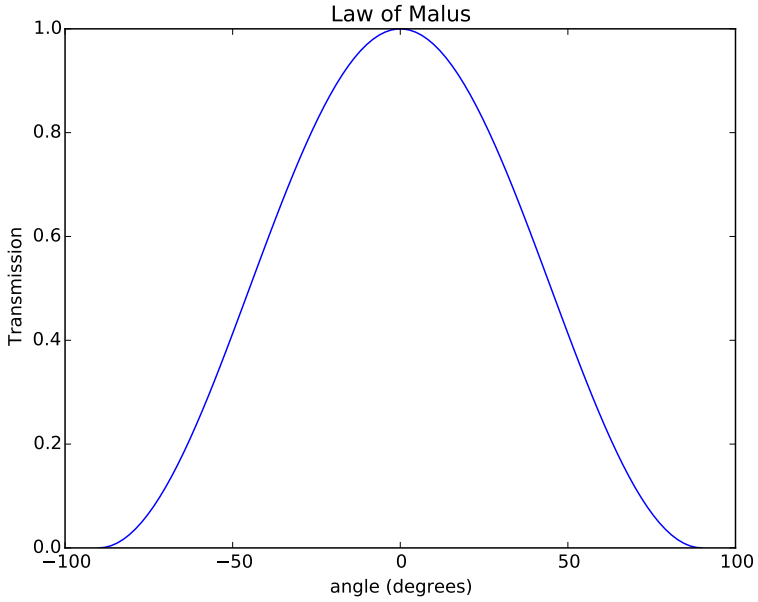

Figure 3.3 – Malus' law

This is where things become slightly more complicated: light with polarisation at +/− 45° from the polariser have a transmission of 50 % and is therefore far from being cancelled. Measuring intensity with only two position of the polariser, 0° and 90° for example, will not be enough to estimate the direction of the polarisation as we will have no information on the −45/+45 direction.

In order to fully characterise the polarisation, four measurements are required. If we restrict ourselves to linear polarisation, we need to obtain measurements in at least three directions, but in fact, generally one uses four measurements, for instance at 0°, 45°, 90° and −45° (corresponding to 135°). Stokes formalism is particularly adapted to describe polarisation in this context.

Note that most (if not all) polarimetric instruments are based on this scheme, despite they are often more complicated than just a rotating polariser. Different methods are used, like Wollaston prisms (described in more details in section 3.3) which spatially separate light into two components with different polarisation instead of blocking one of them.

3.2 Stokes Formalism and Scatterings

3.2.1 Measuring Polarisation with Stokes Vector

The Stokes formalism has been introduced by George Gabriel Stokes around 1852, giving his name to the four parameters he used to describe any polarisation state. Polarisation would be intuitively described by the four parameters of the pattern of the electric field on its ellipse: the ellipse's major and minor axes, the inclination of its major axis and the phase of the vector along this pattern. However these parameters are not measurable as such and this is why George G. Stokes proposed this alternative way of representing the polarisation.

In order to describe the electric field we need a reference direction. In the case of scattering, this reference will be the intersection of the scattering plane with the polarisation plane (orthogonal to the direction of propagation of light). In cases of polarisation maps of regions of the sky, the reference will be the North direction, according to I.A.U. (1973) (International Astronomical Union).

Let us call $E_\parallel$ the value of the projected $\vec{E}$ on this reference direction, and $E_\perp$ its projection on the orthogonal axis. Stokes formalism describes the polarisation of light thanks to four parameters, I, Q, U and V. These parameters are averaged quantity over time of a particular intensity of the electric field. I corresponds to the total intensity and is computed with:

$$I = \langle E_\parallel \overline{E_\parallel} + E_\perp \overline{E_\perp} \rangle. \tag{3.14}$$

The three other components are defined as following:

$$Q = \langle E_\parallel \overline{E_\parallel} - E_\perp \overline{E_\perp} \rangle \tag{3.15}$$

$$U = \langle E_\parallel \overline{E_\perp} + E_\perp \overline{E_\parallel} \rangle = 2\ Re\langle E_\parallel \overline{E_\perp} \rangle \tag{3.16}$$

$$V = i\langle E_\parallel \overline{E_\perp} - E_\perp \overline{E_\parallel} \rangle = 2\ Im\langle E_\parallel \overline{E_\perp} \rangle. \tag{3.17}$$

Thus, Q measures positively the intensity of light with a polarisation along the reference direction and negatively along 90°. U is the same measure but for directions at 45° and -45°. V measures the circular polarisation intensity thanks to a de-phasing of π between the two polarisers. A positive V indicates a direct circular polarisation while a negative V corresponds to an indirect one.

If a wave is totally polarised, we will measure $I^2 = Q^2 + U^2 + V^2$. If it is not polarised, we will have $I > 0$ and $Q = U = V = 0$. In any other case, the wave will be partially polarised and the parameters will satisfy $I^2 > Q^2 + U^2 + V^2$. Table 3.1 shows some particular polarisation states.

Table 3.1 – Examples of Stokes parameters for some polarisation states

Polarisation state	I	Q	U	V
Not polarised	I	0	0	0
Fully linear vertical	I	I	0	0
Fully linear horizontal	I	-I	0	0
Fully linear along +45°	I	0	I	0
Fully linear along -45°	I	0	-I	0
Fully circular direct	I	0	0	I
Fully circular indirect	I	0	0	-I

We often represent Stokes parameters in the form of a vector, called the Stokes vector with symbol S:

$$S = \begin{bmatrix} I \\ Q \\ U \\ V \end{bmatrix} \tag{3.18}$$

Note that Stokes parameters can also be defined from the polarisation ellipse described by the electric field movement as a function of time. Let us call a the maximum amplitude of the electric field (the amplitude in case of linear polarisation), θ the polarisation angle and χ the opening angle of the ellipse ($\tan(\chi)$ being therefore the axial ratio of the ellipse), as illustrated by figure 3.4, following Tinbergen (1996) with different notations to avoid confusions with scattering angles. Stokes parameters can also be expressed as:

$$S = \begin{bmatrix} I \\ Q \\ U \\ V \end{bmatrix} = \begin{bmatrix} a^2 \\ a^2 \cos(2\chi)\cos(2\theta) \\ a^2 \cos(2\chi)\sin(2\theta) \\ a^2 \sin(2\chi) \end{bmatrix} \tag{3.19}$$

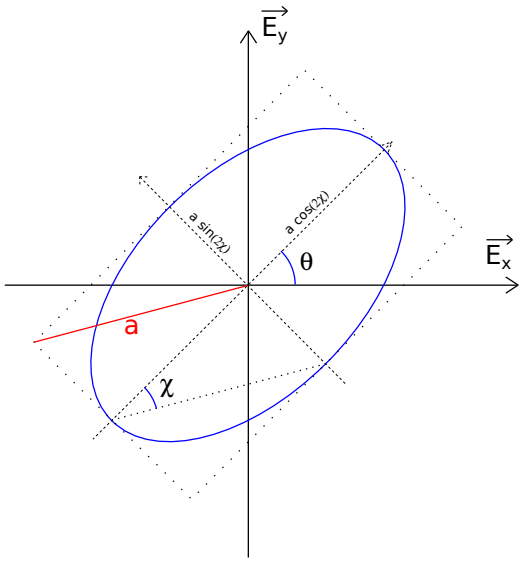

Figure 3.4 – Determination of Stokes parameters from ellipse parameters.

3.2.2 Scattering: Grain Properties

If one wants to model polarimetric observations of any type of source, as long as there is some dust around the source or somewhere between the source and the observer, one needs to take into account the scattering which is one of the most important polarising mechanism. Stokes vector formalism is very useful in polarimetric observations as it allows to fully describe the polarisation with only observable quantities, however it will also reveal itself as being well adapted at describing what happens with the scattering of light on dust grains.

We are now examining the various kinds of scatterings a photon can undergo. In AGN environments, scattering can mostly happen on dust grains, whether spherical or not, and aligned or not and on electrons.

3.2.2.1 Spherical Grains

Scattering on a homogeneous dielectric sphere is analytically solvable using Maxwell's equations and this was first achieved by Mie (1908). Not only this computation takes into account the polarisation, but it also depicts how initial polarisation will affect the resulting scattering geometry. The phase function of the scattering describes the angular dependence of the scattered intensity ; it only depends on two parameters, the form factor x and the complex refractive index of the medium m. Before Mie, John Rayleigh developed around 1871 a theory of scattering which is applicable to cases where $x \ll 1$ and is therefore a boundary case of Mie scattering.

— The form factor x is defined as follow:

$$x = 2\pi a/\lambda \tag{3.20}$$

with λ the incoming wavelength and a the radius of the dust grain.

— The complex refractive index of the medium is composed of the characteristic ratio of the speed of light in vacuum to the velocity of light in the medium (constituting the grain) as its real part $n = c/v$ and the characteristic dissipation of the wave k as its imaginary part:

$$m = n + ik \tag{3.21}$$

We can use Rayleigh scattering if $x \ll 1$, which is the case if the wavelength is much larger than the grain radius. Rayleigh scattering is still used because it offers the advantage of being independent of the form factor (as long as it is below 0.2) and require therefore less computing time for very similar results.

Mie theory gives from x and m the values of the parameters S_1, S_2, Q_{ext} Q_{sca} and Q_{back}.

— S_1 links the incoming wave and the scattered one through their perpendicular component to the scattering plane for every scattering angle.

— S_2 links the incoming wave and the scattered one through their parallel component to the scattering plane for every scattering angle.

— Q_{ext} is the efficiency factor of extinction.

— Q_{sca} is the efficiency factor of scattering.

— Q_{back} is the efficiency factor of backscattering.

— Q_{abs}, the efficiency factor of absorption, is computed thanks to: $Q_{abs} = Q_{ext} - Q_{sca}$.

All these quantities depend on the grain type, the wavelength and the grain radius through the form factor. S_1 and S_2 also depend on the scattering angle. In the following, we will not write all the dependences of these quantities in term of form factor and grain type.

Note that the efficiency factors are linked to the cross sections as following:

$$Q_{ext} = \frac{C_{ext}}{\pi a^2} \tag{3.22}$$

$$Q_{sca} = \frac{C_{sca}}{\pi a^2} \tag{3.23}$$

$$Q_{back} = \frac{\mathrm{d}C_{sca}}{\pi a^2 \mathrm{d}\Omega}. \tag{3.24}$$

We can compute the albedo from these quantities using:

$$\text{albedo} = \frac{Q_{sca}}{Q_{ext}}. \tag{3.25}$$

3.2.2.2 Non Spherical Grains

Generally, grains do not have a spherical shape. Oblong grains are for example proposed in the torus of AGNs where they may explain some properties. However, we do

not have a rigorous theory as the Mie theory to compute the scattering characteristic of non spherical grains.

The model presented in this thesis does not yet allow to take into account non spherical grains. Doing it is however one of the goals in the near future. One proposed way to include non spherical grains would be to have two populations of the same type of grains, with different spherical radius ranges, to stand for grains with different cross-section depending on the angle of incidence. This becomes however more complex if we want the grains to be aligned as in the case of oblong grains aligned by a magnetic field for instance. For these reasons, we will not enter in the details for non spherical grains in the following.

3.2.2.3 Electrons

Scattering of light not only happens on dust, but also on electrons as discovered by Thomson (1906). Thomson scattering is also a peculiar case of a more complete description of scattering on electrons proposed by Compton (1923). Compton scattering is required when the energy of photons is close to the mass energy of particles, electrons in our case and therefore $\lambda \approx \frac{h}{m_e c}$ with h the Planck constant and m_e the electron mass. This correspond to high energy photons ($\lambda \leqslant 10^{-12}$ m). We will only restrict our models to Thomson scattering since we deal with infrared and visible photons only.

In term of phase functions, Thomson scattering on electrons is very similar to Rayleigh scattering. There is however a significant difference as there is no absorption of light with Thomson scattering. We will therefore adopt here the same description as previously used to describe scattering on spherical grains, with particular values corresponding to Rayleigh phase function without absorption:

$$S_1(\alpha) = 1.0 \tag{3.26}$$

$$S_2(\alpha) = \cos(\alpha) \tag{3.27}$$

$$Q_{sca} = Q_{ext} \tag{3.28}$$

$$\text{albedo} = 1. \tag{3.29}$$

α is here the principal scattering angle (see section 3.2.3 for description of the angles).

3.2.3 Scattering: Geometry

With the quantities derived from Mie theory, we are able to fully characterise the scattering geometry, through the two phase functions for the two scattering angles. To describe this geometry, we will use the following convention (illustrated on figure 3.5):

— $\vec{p}$ is the direction of propagation of the light.

— $\vec{u}$ is the orthogonal to the last scattering plane.

— α is the principal scattering angle, between the old and the new direction of propagation
— β correspond to the azimuthal scattering angle. It describes the variation of the vector $\vec{u}$ from a scattering event to the next one.

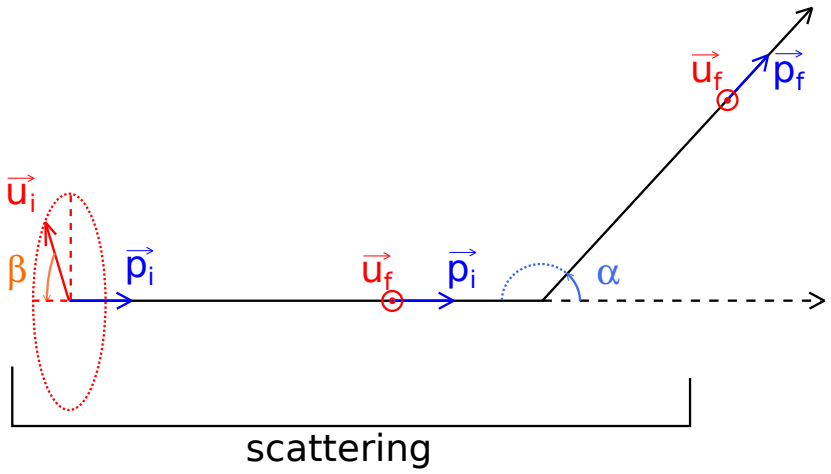

Figure 3.5 – Illustration of the scattering angles α and β on vectors $\vec{p}$ (indicating the direction of propagation) and $\vec{u}$ (normal to the last scattering plane) before and after scattering. Note that changes of vectors $\vec{u}$ and $\vec{p}$ are simultaneous and are only separated here for a better understanding.

$\vec{p}$ and $\vec{u}$ are known from the previous propagation of the light, however α and β are determined thanks to the grain properties through S_1 and S_2. We can show that the probability density function of the principal scattering angle α follows:

$$f_{\cos(\alpha)}(\cos(\alpha)) = \frac{2}{x^2 Q_{sca}} \frac{1}{2} \left(|S_2(\alpha)|^2 + |S_1(\alpha)|^2 \right). \tag{3.30}$$

The second scattering angle β depends on the polarisation of light before the scattering occurs (given in term of the Stokes parameters I, Q and U) and on α. We can express the probability density function of β knowing α:

$$f_\beta(\beta|\alpha) = \frac{1}{2\pi} \left(1 + \frac{\frac{1}{2}(|S_2(\alpha)|^2 - |S_1(\alpha)|^2)}{\frac{1}{2}(|S_2(\alpha)|^2 + |S_1(\alpha)|^2) I} (Q\cos(2\beta) + U\sin(2\beta)) \right). \tag{3.31}$$

Figure 3.6 shows examples of phase functions of the scattering angle α for different values of the form factor. We can see that by increasing the form factor we collimate the scattering forward, with more complex geometry. Because the grain properties depend on the wavelength, we get all the figures with the same grain radius, only changing the wavelength to control the form factor.

Note that the phase functions and the probability densities computed before are related through a $\sin(\alpha)$ factor as shown on figure 3.7. This is related to the spherical geometry where the solid angle is larger toward the equator than in the direction of the pole.

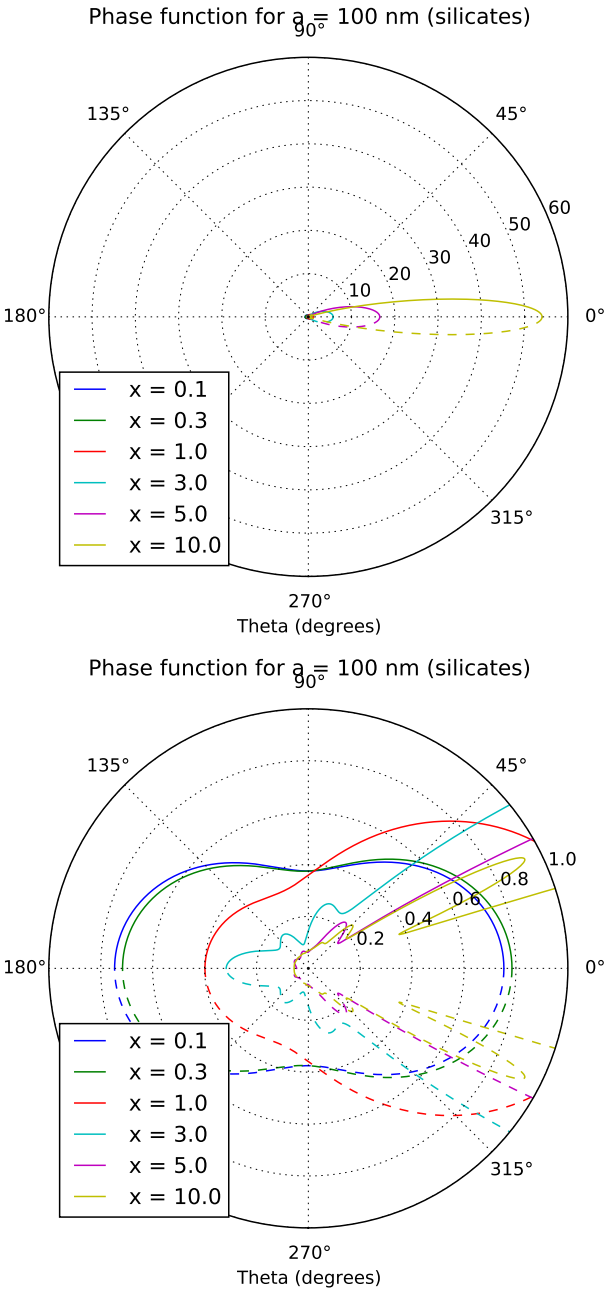

Figure 3.6 – Examples of α phase functions in the case of Mie scattering, for $x = [0.1, 0.3, 1.0, 3.0, 5.0, 10.0]$. Second image is a zoom on the central part.

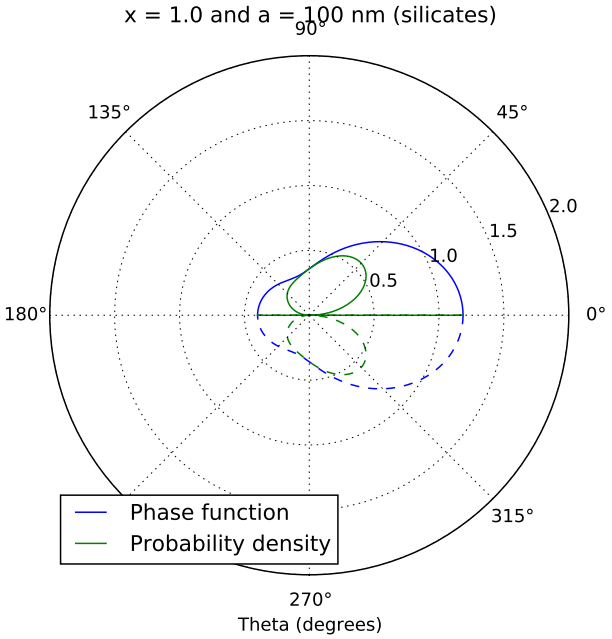

Figure 3.7 – Examples of α phase functions and the corresponding probability density function in the case of Mie scattering, for $x = 1.0$

On the same way, we can display the phase function of scattering angle β, depending on both the initial polarisation and α. Figure 3.8 shows a typical measurements of β angle distribution with a form factor of 1 and without restriction on α, which therefore follows the above phase function. Note that in this case, the distribution is isotropic, as expected for unpolarised incoming light.

3.2.4 Scattering: Mueller Matrix

In order to compute the evolution of polarisation through scattering with Stokes formalism, we can use the Mueller matrix combined with a rotation matrix. Indeed, two matrices are required to compute the new Stokes vector after the scattering event. The Mie theory gives the values of S_1 and S_2 which are determined for each wavelength, grain type, grain radius and scattering angle. Once again we will not specify all these dependences for each matrix element. S_1 and S_2 are used to compute the elements of the Mueller matrix:

$$S_{11} = \frac{1}{2}(|S_2|^2 + |S_1|^2) \tag{3.32}$$

$$S_{12} = \frac{1}{2}(|S_2|^2 - |S_1|^2) \tag{3.33}$$

$$S_{33} = Re(S_2\overline{S_1}) \tag{3.34}$$

$$S_{34} = Im(S_2\overline{S_1}), \tag{3.35}$$

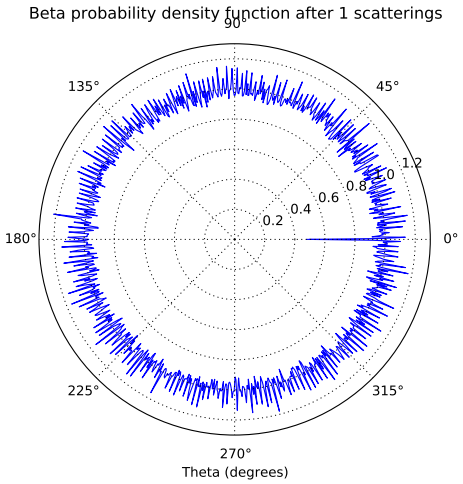

Figure 3.8 – Examples of β phase function in the case of Mie scattering, for $x = 1.0$. Note that this is not the conditional probability density function because there are no knowledges about α.

with the Mueller matrix being define as:

$$M = \begin{pmatrix} S_{11} & S_{12} & 0 & 0 \\ S_{12} & S_{11} & 0 & 0 \\ 0 & 0 & S_{33} & S_{34} \\ 0 & 0 & -S_{34} & S_{33} \end{pmatrix}. \tag{3.36}$$

Note that with this notation, the repartition functions of the scattering angles can be rewrite in a simpler way:

$$f_{\cos(\alpha)}(\cos(\alpha)) = \frac{2}{x^2 Q_{sca}} S_{11}(\alpha) \tag{3.37}$$

$$f_{\beta}(\beta|\alpha) = \frac{1}{2\pi}\left(1 + \frac{S_{12}(\alpha)}{S_{11}(\alpha)I}(Q\cos(2\beta) + U\sin(2\beta))\right). \tag{3.38}$$

By applying the Mueller matrix to the Stokes vector, we take into account the change in polarisation introduced by the main scattering angle (α) between the incoming ray and the new direction of propagation:

$$S_{final} = M \times S_{inter}, \tag{3.39}$$

which gives:

$$\begin{bmatrix} I_f \\ Q_f \\ U_f \\ V_f \end{bmatrix} = \begin{pmatrix} S_{11} & S_{12} & 0 & 0 \\ S_{12} & S_{11} & 0 & 0 \\ 0 & 0 & S_{33} & S_{34} \\ 0 & 0 & -S_{34} & S_{33} \end{pmatrix} \begin{bmatrix} I_{inter} \\ Q_{inter} \\ U_{inter} \\ V_{inter} \end{bmatrix}. \tag{3.40}$$

However, as the scattering is not in the previous polarisation plane of the photon, we need to translate the old photon's polarisation into the new frame used for the scattering. We use for this purpose a rotation matrix defined as follow:

$$R(\beta) = \begin{pmatrix} 1 & 0 & 0 & 0 \\ 0 & \cos(2\beta) & \sin(2\beta) & 0 \\ 0 & -\sin(2\beta) & \cos(2\beta) & 0 \\ 0 & 0 & 0 & 1 \end{pmatrix}. \tag{3.41}$$

The rotation matrix is mandatory to modify the polarisation plane according to the scattering geometry and depend on β, the azimuthal scattering angle. We then switch to S_{final} from S_{init} by applying both matrices:

$$S_{final} = M \times R(\beta) \times S_{init} \tag{3.42}$$

and in detailed form:

$$\begin{bmatrix} I_f \\ Q_f \\ U_f \\ V_f \end{bmatrix} = \begin{pmatrix} S_{11} & S_{12} & 0 & 0 \\ S_{12} & S_{11} & 0 & 0 \\ 0 & 0 & S_{33} & S_{34} \\ 0 & 0 & -S_{34} & S_{33} \end{pmatrix} \begin{pmatrix} 1 & 0 & 0 & 0 \\ 0 & \cos(2\beta) & \sin(2\beta) & 0 \\ 0 & -\sin(2\beta) & \cos(2\beta) & 0 \\ 0 & 0 & 0 & 1 \end{pmatrix} \begin{bmatrix} I_i \\ Q_i \\ U_i \\ V_i \end{bmatrix}. \tag{3.43}$$

If the incident ray is unpolarised, we have in the Mueller matrix computation $I_f = S_{11}I_i$ and $Q_f = S_{12}I_i$ because Q_i, U_i and V_i are null. Therefore, whatever the rotation matrix, the polarisation degree will always be $p = Q_f/I_f = S_{12}/S_{11}$ (see section 3.3.2). The polarisation induced by scattering therefore only depends on scattering angle α for a given form factor as long as the initial photon is not polarised. As we displayed the phase function on previous section, we can also indicate on polar diagrams the polarisation of packets as shown in figure 3.9.

One can note that the maximum of polarisation is obtained in cases of scattering angles close to 90°. This configuration is not the most likely as it generally corresponds to a minimum in the phase functions as seen in figure 3.6, but it is one of the most important point in many analysis of observed polarisation in astrophysics. As the understanding of polarisation becomes really difficult in cases of multiple scatterings, one of the most studied polarisation signal is the one coming from single scatterings, and therefore following the above relation to the scattering angle, as will be seen in the centro-symmetric polarisation patterns of section 3.3.3 for example.

3.3 Polarimetric Observations

When observing with **optical and NIR instruments featuring** polarimetric capacities, one logical way is to use a polariser and to make it rotate between two exposures. It is however possible to separate the beam into two beams of different direction of the electric field. This can be achieved thanks to birefringent materials,

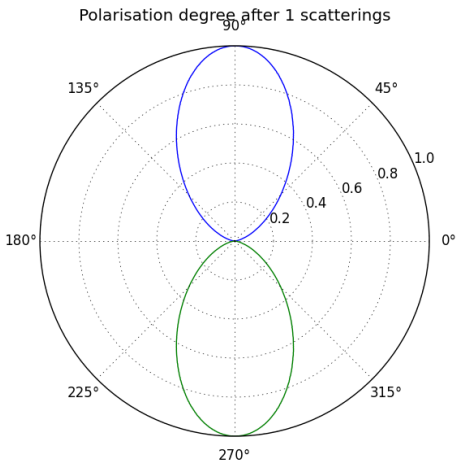

Figure 3.9 – Examples of polarisation (S_{12}/S_{11}) depending on the scattering angle α in the case of Mie scattering, for $x = 1.0$

like Wollaston prism. If so, it is possible to record with a unique device the two perpendicular polarisations at the same time. This still needs a rotation if we want a complete description of the polarisation (remember that we need four measurements) but it is faster than the previous method.

With these methods, what we measure is not directly the Stokes parameters, but the averaged modulus of the component of the electric field transmitted by the polariser. There are few methods allowing to display polarimetric measurements from the measured quantities and we will introduce some of them in the following. As this work mainly consists in polarimetric imaging, we will mostly base our explanations on 2D images. However the same techniques can be applied to any polarimetric measurement.

3.3.1 Q, U and V maps

Translating polarimetric imaging data in term of Stokes parameters corresponds to creating Q and U maps. These maps are comparable to the I maps, the "classical" intensity maps. Following the same method, it is also possible to create V maps to display the circular polarisation, however instruments with circular polarisation capacities are rare (at least in visible and NIR), because it requires to measure the phase difference between the two orthogonal components of the electric vector.

The way to link the observable quantities to the Stokes parameters depends on the instruments, but follows generally the same method, whether observations are obtained at a given angle of polariser, or with ordinary and extraordinary beams. The definitions of Q and U previously used are not the only ones, (see equation 3.15 and 3.16), and we can also define Stokes parameters in a way linked to the components of the electric field (more commonly used in radio astronomy, see Tinbergen 1996):

$$I = \langle E_{\parallel}\overline{E_{\parallel}} + E_{\perp}\overline{E_{\perp}}\rangle = Q_+ + Q_- = I_0 + I_{90} \tag{3.44}$$

$$Q = \langle E_{\parallel}\overline{E_{\parallel}} - E_{\perp}\overline{E_{\perp}}\rangle = Q_+ - Q_- = I_0 - I_{90} \tag{3.45}$$

$$U = \langle E_{\parallel}\overline{E_{\perp}} + E_{\perp}\overline{E_{\parallel}}\rangle = 2Re\langle E_{\parallel}\overline{E_{\perp}}\rangle = U_+ - U_- = I_{45} - I_{-45} \tag{3.46}$$

$$V = i\langle E_{\parallel}\overline{E_{\perp}} - E_{\perp}\overline{E_{\parallel}}\rangle = 2Im\langle E_{\parallel}\overline{E_{\perp}}\rangle. \tag{3.47}$$

Q_+, Q_-, U_+ and U_- are equivalent to I_0, I_{90}, I_{45} and I_{-45} and are the measured intensities depending on the polariser angle. The corresponding positions are shown on figure 3.10. V is not easily translated into a sum of measured intensities. It requires two measurements with a phase introduced between the two components, to measure the positive and negative circular polarisation.

We then group the observations of the same Stokes parameter and stack them together. There are different ways to do so, some common ones will be presented in section 3.4.

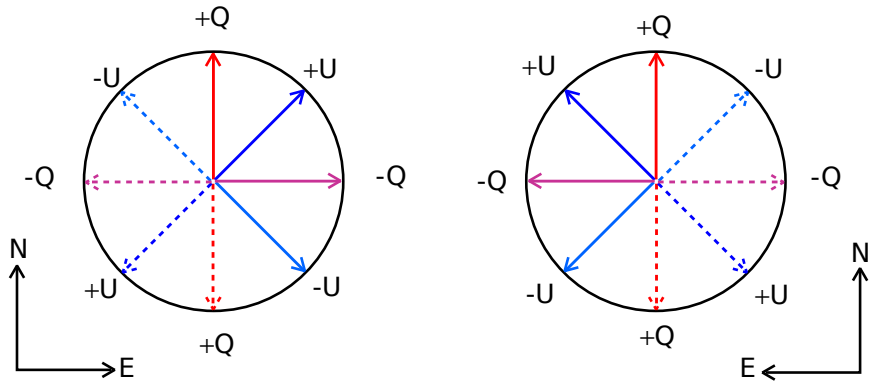

Figure 3.10 – Example of measured Stokes parameters depending on the position of a polariser, first image from a source point of view and second image as viewed by a detector.

3.3.2 Degree and Angle of Polarisation

Once the I, Q, U and V maps are created, it is useful to describe the polarisation measurements more explicitly in a way easier to interpret. One classical method is to represent the degree and angle of polarisation. The polarisation degree, noted p, indicates the fraction of the received light which is polarised. $p = 1$ corresponds to a fully polarised light: the oscillation direction is always the same for all the received photons. $p = 0$ indicates that the light is unpolarised and that the oscillation direction

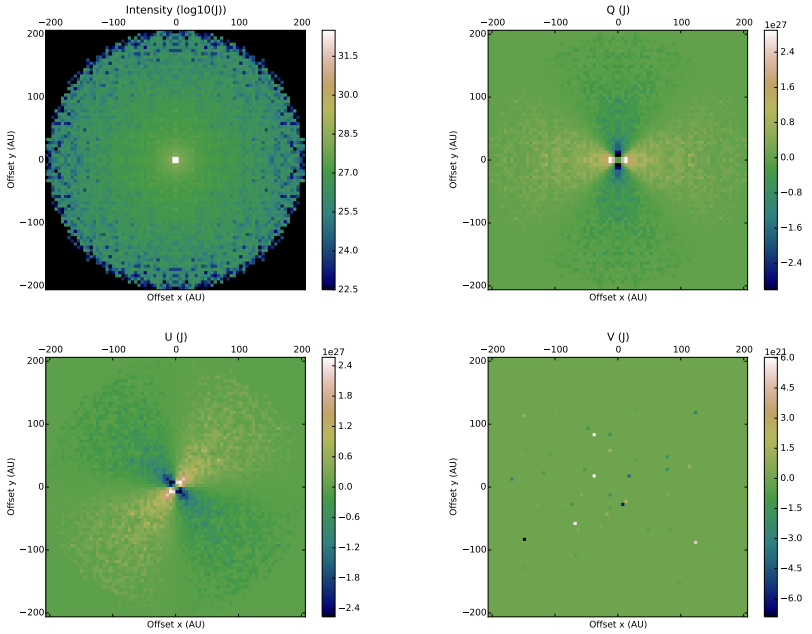

Figure 3.11 – Maps of I, Q, U and V in the case of a star surrounded by a dust shell of $\tau_K = 0.05$ simulated in K band.

of the fields is completely randomly distributed. The polarisation angle, θ, indicates the dominant direction of oscillation of the electric field. This corresponds to the major axis of the ellipse described by the electric field (see figure 3.4 for an illustration). Degree and angle of polarisation are derived from Stokes parameters as:

$$p = \frac{\sqrt{Q^2 + U^2 + V^2}}{I} \tag{3.48}$$

$$\theta = \frac{1}{2} \operatorname{atan2}(U, Q). \tag{3.49}$$

Note that this definition of θ is consistent with the expression of the Stokes parameters in equation 3.19. We can also define the linear and circular degree of polarisation:

$$p_{lin} = \frac{\sqrt{Q^2 + U^2}}{I} \tag{3.50}$$

$$p_{circ} = \frac{V}{I}. \tag{3.51}$$

The degree of linear polarisation is the most commonly used and the term "degree of polarisation" often refers to this quantity instead of the real degree polarisation (once again because it is difficult to measure circular polarisation).

Following I.A.U. (1973) convention, the reference of the angle of polarisation is the position angle of the electric-vector maximum, θ, starting from North and increasing through East. Q and U were defined in this work to be compatible with this convention, every polarisation maps are displayed as such.

An important fact is that all operations on polarimetric data have to be executed **before** computing the degree and angle of polarisation. This includes for instance binning, convolution/deconvolution by a PSF, sum of different observations, flat field or dark corrections. Indeed, Stokes parameters are intensity quantities, and (usually) follow Gaussian distributions, which is not the case of neither the degree of polarisation nor the angle of polarisation. Even the reduced Stokes parameters, Q/I or U/I do not necessary follow such Gaussian distribution as investigated by Tinbergen (1996). We therefore have to perform all operations on Q and U parameters but not on the final product of the processing.

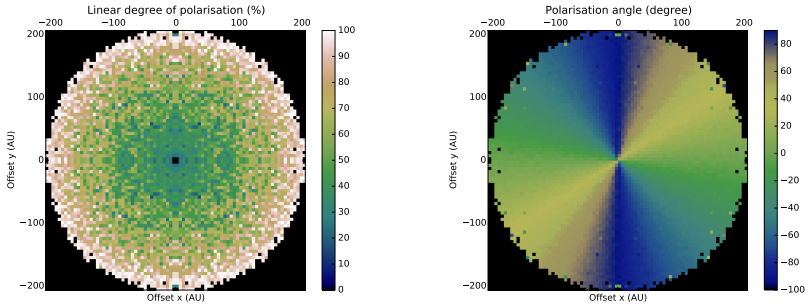

Figure 3.12 – Maps of p_{lin} and θ in the case of a star surrounded by a dust shell of $\tau_K = 0.05$ simulated in K band.

In the case of maps, it is possible to combine these two informations into short segments representing the polarisation vectors to be superimposed to any other maps, their length being proportional to the degree of polarisation in the selected zone (pixel or group of pixels) and the orientation corresponding to the angle of polarisation.

3.3.3 Q Tangential and Centro-symmetric Patterns

One of the most commonly used alternative, especially in the field of exoplanets and disks around young stars, is the polarisation representation by Q tangential maps. Q and U maps represent the intensity of light oscillating along a particular direction, respectively vertical/horizontal and $\pm 45°$ of this pattern. However we may not be interested on the absolute angle but on the angle relative to the direction of a central source. We introduce in the following the concept of centro-symmetric polarisation, Q tangential representation being used to separate the centro-symmetric polarisation from the radial one.

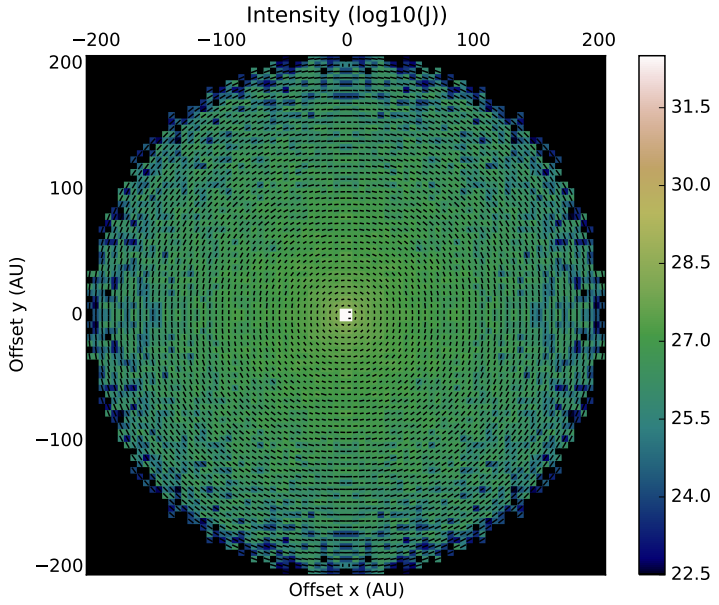

Figure 3.13 – Maps of I with polarisation vectors in the case of a star surrounded by a dust shell of $\tau_K = 0.05$ simulated in K band.

Light of a central source scattered once [1] by a circum-central medium (dust, electrons) exhibits a characteristic polarisation pattern, symmetric according to the central source. In particular, each scattering plane will contain the observer, the source, and the location of the scattering event. The position angle of the polarisation vector will therefore rotate according to the position angle of the scatterer and produces a peculiar pattern of vectors rotating around the central source, as discussed by Fischer et al. (1996) and Whitney & Hartmann (1993) for instance. This pattern is the one observed on figures 3.11,3.12 and 3.13.

Q tangential (we will adopt the notation Q_ϕ in this work but there are other popular notations) is a parameter computed from Q and U, with a rotation according to the position angle ϕ of the observed position with respect to the central source. It is defined as (see for example Avenhaus et al. 2014):

$$Q_\phi = Q\cos(2\phi) + U\sin(2\phi). \tag{3.52}$$

The other Stokes parameter can as well be transformed into a radial quantity:

$$U_\phi = -Q\sin(2\phi) + U\cos(2\phi), \tag{3.53}$$

with ϕ being defined from the position of the observation (x,y) and of the central source (x_0,y_0) as:

1. We assume here that there is only one scattering. This is a particularly common case when the dust is optically thin. In case of multiple scattering, the pattern will be more complex

$$\phi = \arctan \frac{x - x_0}{y - y_0}. \tag{3.54}$$

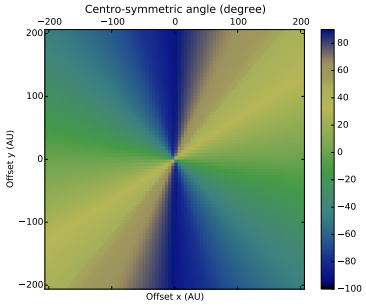

Figure 3.14 – Centro-symmetric map of ϕ.

Q_ϕ and U_ϕ maps trace intensity with polarisation respectively tangential and radial. In the case of a fully centro-symmetric pattern, we should observe a Q_ϕ map very close to the intensity map and a null U_ϕ map, a situation close to the one presented previously with an optically thin dust shell, where most of the photons are scattered only once, and displayed in figure 3.15. This is equivalent to the maps of the difference angle between the observed pattern and a purely centro-symmetric pattern, obtained by subtracting ϕ to the θ map [2], as showed in figure 3.16.

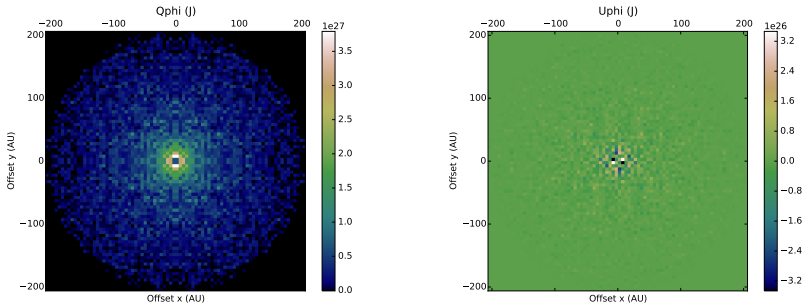

Figure 3.15 – Maps of Q_ϕ, U_ϕ in the case of a star surrounded by a dust shell of $\tau_K = 0.05$ simulated in K band.

3.3.4 Polarimetric Instruments

To map the polarisation, techniques have been developed to decrease the required observation time. Two devices are commonly used, the Half Wave Plate (HWP) and the Wollaston prism (named after William Hyde Wollaston). The HWP provides a way to transform the polarisation vector by introducing a phase of π on one of the two

2. Note that this subtraction is an exception to the impossibility to execute operation on final polarimetric data because it just changes the reference of the angle.

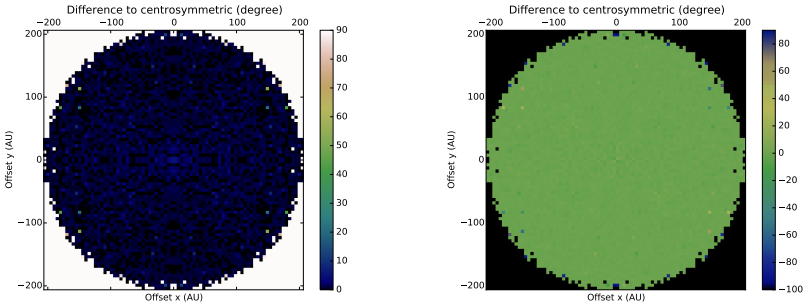

Figure 3.16 – Maps of differences to centro-symmetric pattern, in the case of a star surrounded by a dust shell of $\tau_K = 0.05$ simulated in K band. the first images takes the absolute value of this difference while the second one shows the relative difference.

components of the electric field. Two HWPs are used on instrument SPHERE, the first in order to compensate from the instrumental polarisation offset and the second HWP is used to reverse the sign of the polarisation of the beam and therefore to select the polarisation orientation reaching the camera (see Thalmann et al. 2008).

A Wollaston prism is a birefringent material (so as HWP) which separates the two components of the polarisation into two separate beams. It is therefore possible to record after the prism the two components at the same time, only two exposures are thus required for a complete polarimetric observation. This is for instance the device used in NaCo (NAOS + CONICA), the first AO assisted instrument installed on one unit telescope of the VLT at Cerro Paranal. On these instrument, the two separated components are recorded on the same image (with a field reduction). For more details, see Lenzen et al. (2003) and Rousset et al. (2003).

SPHERE is another AO instrument with polarimetric capacities of the VLT. A detailed description will be given on Chapter 4. We are interested here in the InfraRed Dual-beam Imager and Spectrograph (IRDIS) and Zurich IMaging POLarimeter (ZIMPOL) sub-systems, both using polarimetric modes. IRDIS features a beam splitter which allows to record two images at the same time. This is useful to observe in different filters at the same time, but it can also be combined with polarisers to record simultaneously two different polarisations, with the same advantage than offered by NaCo. ZIMPOL is based on a more original system. Only one detector is used, but a fast periodic transfer of charges in the CCD at the same rhythm than a half-wave modulation by an electro-optic material provides the ability to record one of the polarisation component in half of the pixels and the other one on the other halve. This still requires four measurements, but allows the observer to measure the polarisation simultaneously, with the same optical path at a time-scale much shorter than the atmospheric turbulence and conducts therefore polarisation measurements at very high precision.

3.4 Data Reduction Methods

In section 3.3 we explained the relationship of Q and U maps with the recorded images. There are however different techniques to compute these maps and we describe some of them in the following. In the case of images obtained using a birefringent material splitting the beam, one of the most used nomenclature is to distinguish images by their ordinary or extraordinary properties. Ordinary beam will for instance correspond to the Q_+ polarisation, and the extraordinary one to Q_-. We will keep in the following a description under the names Q_+, Q_-, U_+ and U_-, assuming that there is more than one image taken under the same conditions to keep a general description.

Note that before applying any of these methods, images should have been reduced following standard astronomical procedures (sky subtraction, flat field correction and realignment are the basics). Because polarimetry consists in combining intensity images, it very sensitive to the different instrumental noises and bias. In particular, offsets or differential transmission introduced between two polarisation measurements will alter the resulting measured polarisation. For that reason, different reduction methods were developed, each optimised with particular instruments.

3.4.1 Double Differences Method

The double differences method is the mathematically simplest one. Starting with the quantities Q_+, Q_-, U_+ and U_-, it consists in reconstructing through addition/subtraction the quantities Q and U. Therefore the operations are:

$$I = \Sigma Q_+ + \Sigma Q_- \tag{3.55}$$

$$Q = \Sigma Q_+ - \Sigma Q_- \tag{3.56}$$

$$U = \Sigma U_+ - \Sigma U_-. \tag{3.57}$$

It has the advantage not to be sensitive to precise sky background estimation as only intensity differences are considered.

3.4.2 Double Ratio Method

Another method uses ratio instead of subtraction. Dividing images is less sensitive to imperfect instrumental and associated bias calibrations, if used on images recorded on very close conditions (see Avenhaus et al. 2014) and is therefore commonly used for instruments with two beams. It is thus particularly adequate to SPHERE data reduction. This method is well described in Tinbergen (1996) and Quanz et al. (2011) and compute Q and U through:

$$I = \frac{1}{2}(\Sigma Q_+ + \Sigma Q_-) \tag{3.58}$$

$$R_Q = \sqrt{\frac{\Pi Q_+}{\Pi Q_-}} \tag{3.59}$$

$$R_U = \sqrt{\frac{\Pi U_+}{\Pi U_-}}, \tag{3.60}$$

with

$$Q = I * \frac{R_Q - 1}{R_Q + 1} \tag{3.61}$$

$$U = I * \frac{R_U - 1}{R_U + 1}. \tag{3.62}$$

3.4.3 Matrix Inversion

The last method described here uses matrix inversion to compute I, U and Q maps, inspired by polarization state analysers methodologies, see Zallat & Heinrich (2007) for instance. Indeed, by observing with a polariser, we apply to the initial Stokes parameters on the incoming light the following transformation matrix W to get the measured intensities:

$$I_{meas} = W \times S, \tag{3.63}$$

with

$$S = \begin{bmatrix} I \\ Q \\ U \end{bmatrix} \tag{3.64}$$

$$I_{meas} = \begin{bmatrix} I_1 \\ I_2 \\ ... \\ I_n \end{bmatrix}. \tag{3.65}$$

W depends on the angles θ_n of the polariser for each image recorded:

$$W = \begin{pmatrix} \cos^2(\theta_1) & \cos(\theta_1) & \sin(\theta_1) \\ \cos^2(\theta_2) & \cos(\theta_2) & \sin(\theta_2) \\ & ... & \\ \cos^2(\theta_n) & \cos(\theta_n) & \sin(\theta_n) \end{pmatrix}. \tag{3.66}$$

Because W may not be a square matrix, it is not always invertible. In practice, it will never be the case (having only three polarimetric measurements/images is rare because of the symmetry of measurements) and we apply the pseudo-inverse $(W^T W)$. Therefore, by applying $(W^T W)^{-1} W^T$ on both sides, we can compute S directly:

$$S = (W^T W)^{-1} W^T I_{meas}. \tag{3.67}$$

We will illustrate this method with a simple setup. If we have eight measurements with the four following positions of the polariser:

$$I_{meas} = \begin{bmatrix} Q_+ \\ Q_- \\ U_+ \\ U_- \\ Q_+ \\ Q_- \\ U_+ \\ U_- \end{bmatrix}. \tag{3.68}$$

We then get the W matrix as following

$$W = \begin{pmatrix} 1 & 1 & 0 \\ 1 & -1 & 0 \\ 0 & 0 & 1 \\ 0 & 0 & -1 \\ 1 & 1 & 0 \\ 1 & -1 & 0 \\ 0 & 0 & 1 \\ 0 & 0 & -1 \end{pmatrix}. \tag{3.69}$$

With this method, it is possible to introduce properly the instrumental effects in the matrix W.

Chapter 4

Observation of Active Galactic Nuclei

Contents

As a branch of the study of galaxies studies, AGN is a quite recent field. First evidence for the existence of these galaxies with strong luminosity and bright emission lines are dated to the first half of XX$^{\text{th}}$ century, as introduced in section 1.4. But because of the distance of these objects, very few pieces of information were obtained until the 70's. Most of our current understanding on their properties comes from more recent observations and the establishment of the unified model of AGNs by Antonucci (1993).

As one of the closest and brightest, NGC 1068 is one of the most studied AGN. This galaxy is located at about 14 Mpc corresponding to an angular scale of roughly 72 pc for 1″ , giving the possibility to reach higher resolution than with other AGNs. Furthermore, the galaxy is bright, and its nucleus is luminous enough to be used as a decent guide source for wavefront sensors. For these reasons, NGC 1068 was the first target of our polarimetric high angular resolution study of AGN.

4.1 Context of NGC 1068

NGC 1068 was one of the early observed galaxies. It was indeed included in the first addition to the Messier (1781) *Catalog of Nebulae & clusters of Stars* in 1783. It was therefore first known has M 77 (these are the two main identifiers of the galaxy, it now has 81 of them). According to Messier (1781), it would have been first observed

around 1780 by Méchain, and first classified into the "nebulae" category, before galaxies were known and the separation between galaxies and actual nebulae.

As mentioned in section 1.4, NGC 1068 played a central role for many breakthrough in research on AGN. When Seyfert (1943) established the first classification of galaxies (still called "nebulae") with intense emission lines, what will later become Seyfert galaxies, NGC 1068 was among the first galaxies in the list. Fath (1909) was the first to discover some bright emission lines, detailed later by Slipher (1917) in NGC 1068. Later, new observations of this AGN by Antonucci & Miller (1985) leaded Antonucci (1993) to propose the unified model of AGNs, explaining the apparent subcategories of Seyfert galaxies and of other kinds of radio-quiet AGNs discovered in between.

If NGC 1068 has been the main target of all these observations and triggered these important discoveries, it is because it is one of the closest and brightest AGN. Bland-Hawthorn et al. (1997) listed and discussed the typical standard parameters we should use for NGC 1068. Concerning the distance, they relied on a previous study by Tully & Fisher (1988) giving a value of 14.4 Mpc. Table 4.1 lists basic characteristics of NGC 1068.

Table 4.1 – Basic informations about NGC 1068 (from Bland-Hawthorn et al. 1997)

Main names	M 77 / NGC 1068
Right ascension α	02 h 42 min 40.771 s
Declination δ	-00° 00′ 47.84″
Distance	14.4 Mpc
Inclination of the galaxy	40°
Galaxy type	Sb
Nuclear type	Seyfert 2 (direct light)
	Seyfert 1 (if observed through polarised light)
Bolometric luminosity	$2 \times 10^{11} L_{\odot}$

4.1.1 General Presentation

Trying to model AGNs structure has been an important work since the Seyfert (1943) classification to understand the observed differences among the various species of AGNs. As one of the ideal laboratory to test assumptions on the unified model of AGNs, the development of instrumentation since the early 90's has brought new constraints on the structure of the central region of NGC 1068.

One of the first well detected structure related to the unified model is the radio jet. NGC 1068 shows a bipolar radio jet, associated to radio emission extending over 500 pc from the centre, as shown in figure 4.1 from Wilson & Ulvestad (1983).

Along the jet path, several components were identified (see for example Alloin et al. 2000 or Gallimore et al. 2004). The jet is bent at the location of a cloud (the component C of Gallimore et al. 1996b), located about 25 pc north of the centre, where various authors found evidences for a shock between the jet and the surrounding

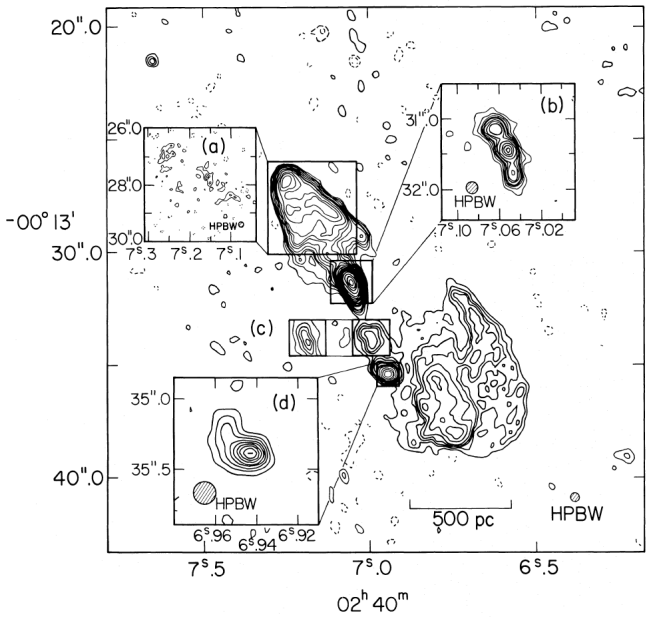

Figure 4.1 – VLA (Very Large Array) maps of the central region of NGC 1068 at 4.9 GHz with resolution $0.4'' \times 0.4''$. Contours plotted are at -0.1 %(dotted), 0.1 %, 0.2 %, 0.3 %, 0.4 %, 0.6 %, 1 %, 1.5 %, 2 %, 3 %, 5 %, 7 %, 10 %, 15 %, 20 %, 30 %, 50 %, 70 % and 90 % of the peak brightness of 0.273 Jy (beam area)$^{-1}$. Insets (a), (b) and (d) show details of the brighter regions at 15.0 GHz. From Wilson & Ulvestad (1983)

media, detected in Mid InfraRed (MIR). Bock et al. (2000) superimposed radio and MIR detections, showing that the jet is surrounded by different clouds. The central radio component S1 (see Gallimore et al. 1996b) would be close to the centre of the AGN, defined here as the brightest UV source. Because it is hidden behind what we expect to be the dusty torus, the exact location of the centre was unclear until the end of the 90's, according to Kishimoto (1999). It is currently accepted that the centre is located at S1 because the H_2O maser emissions detected by Gallimore et al. (1996b) are centred on this location (Das et al. 2006). Because of the inclination of the galaxy on the line of sight (estimated to be around 40°, see Packham et al. 1997 and Bland-Hawthorn et al. 1997), most of the maser detections are on the North side, more visible than in the south, hidden behind the galactic plane. This is for instance visible in the radio map of figure 4.1 at 4.9 GHz ($\lambda \approx 61$ mm), but will also be observable on the NIR images.

A sketch of these regions was drawn by Lopez-Rodriguez et al. (2016) and is displayed on the right panel of figure 4.2.

The region surrounding the jet in the few central arc seconds corresponds to the NLR. This region was named after the detection of strong narrow emission lines in the spectra of Seyfert 2 galaxies, as opposed to the broad lines detected in Seyfert 1,

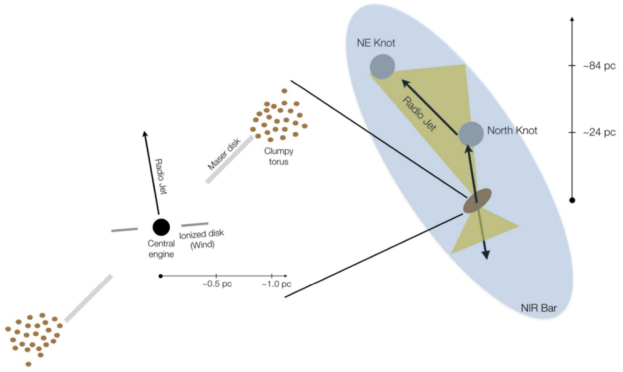

Figure 4.2 – Sketch of the central 100 × 100 pc (right panel) with a zoom-in of the central few parsecs (left panel) of NGC 1068 (both panels are not on linear scale). In the central few parsecs (left panel): the central engine (central black dot), the ionised disk/wind (dark grey region), the maser disk (light grey region), the obscuring dusty material (brown dots) and the radio jet (black solid arrow) are shown. In the 100 × 100 pc scale (right panel): the central few parsecs are represented as a brown ellipsoid with the Position Angle (PA) of the obscuring dusty material. The inner radio jet is shown as a black arrow, bending after the interaction with the North knot (grey circle), towards the NW knot (grey circle). The [OIII] ionization cones (yellow polygons) and the NIR bar (light-blue ellipse) are shown. North is up and East is left. From Lopez-Rodriguez et al. (2016)

originating from the BLR. The NLR is a highly ionised region, with a conical shape as revealed by HST images (Macchetto et al. 1994, see also figure 4.4). The core of the NLR is a polar outflow of ionised matter (Marin et al. 2016a). It is prolonged by an extended NLR of about 7″ (about 500 pc) according to [OIII] line detections by Macchetto et al. (1994). Capetti et al. (1997) revealed that the morphology of this region and its ionisation properties are dominated by the interaction with the radio jet, regions of lines emission and radio lobes being spatially concomitant. According to various studies (see e.g. Axon et al. 1998 and Lutz et al. 2000), the electrons density in this region would be about 10^8 to 10^{11} m^{-3}. The inclination of the axis of the bicone according to the line of sight was investigated by Das et al. (2006), who found an inclination of 85° (North is closer). Thanks to the first AO observations of NGC 1068 with NaCo, Rouan et al. (2004) resolved the nucleus centre in K and L bands into a core of hot dust of diameter of 5 and 8.5 pc respectively. With the same instrument, Gratadour et al. (2006) were able to map and deconvolve the inner parsecs in IR, revealing structures in the NLR, at the source location corresponding to features detected in the optical and MIR. The hot core was resolved at Ks with a FWHM of 2.2 pc, confirming the previous detection, and an upper limit of 5.5 pc in the FWHM of the core in L' and M' bands was found.

The torus and the inner parsecs of NGC 1068, hidden behind the torus, are difficult to detect. The H_2O and OH maser emissions detected by Gallimore et al. (1996a)

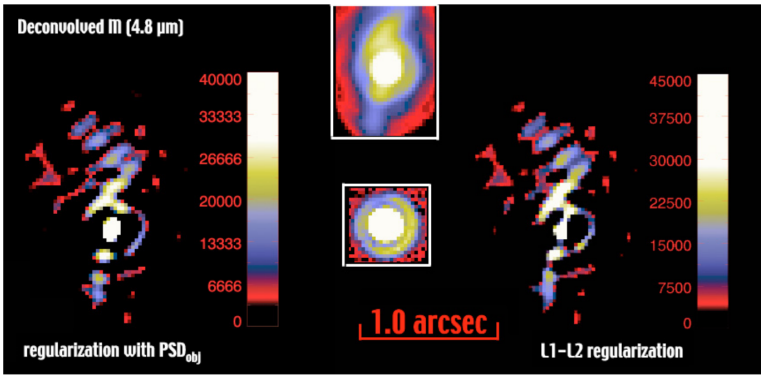

Figure 4.3 – M band deconvolved images of NGC 1068 with two different deconvolution techniques from Gratadour et al. (2006).

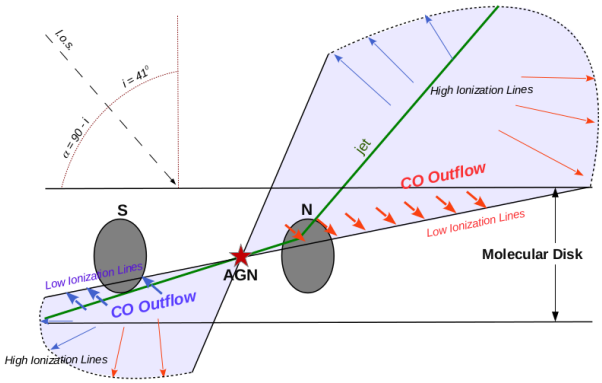

Figure 4.4 – A revised version of the kinematic model of the NLR by García-Burillo et al. (2014), which accounts for the molecular outflow (denoted in figure as CO outflow) detected by Atacama Large Millimeter/submillimeter Array (ALMA) in the CND (seen in projection at N and S, for northern and southern knots) and farther north in the molecular disk. The figure shows a cross-cut of the NLR as viewed from inside the galaxy disk along the projected direction of the radio jet (PA ≈30°; shown by the green line).

were linked to a maser disk, which would stand between 1 and 2 pc from the centre, surrounded by the BLR (see also Gallimore et al. 2001 and sketch of figure 4.2). This disk has to be different from the accretion disk, closer to the CE. However, according to Elitzur & Ho (2009), the transition between the BLR and the maser disk is likely to be mainly associated to the sublimation limit. They suggested that the outer boundary of the maser disk is the sublimation radius, which is the inner bound of BLR. The same idea would apply to the transition with the torus, which would be a colder and thicker continuation of the maser disk (see Elitzur & Ho 2009 and Marin et al. 2016a).

At the very centre, would stand a very compact and luminous object, likely a

super massive black hole, surrounded by an accretion disk. This disk would emit light from NIR to UV. Inverse Compton scattering would occur in a corona in the polar directions, close to the accretion disk, emitting in the X-ray domain (Marin et al. 2016a). All these elements are illustrated in figure 1.5 and detailed in Chapter 1.

Finally, an accretion phenomenon seems to occur on larger scales. Infalling gas was detected by Müller Sánchez et al. (2009a) thanks to integral field spectroscopy in the NIR in the inner 30 pc, streaming toward the nucleus.

4.1.2 Torus

Most of the components of the archetype AGN structure are observable and detected at a particular wavelength. As the coldest piece of the model, the dusty torus, surrounding and hiding the CE and the BLR is poorly constrained. It is far less luminous at shorter wavelengths than in MIR, especially when compared to the surrounding components like the very bright CE. Its extent is another concern and is still a matter of debate. Its typical size would be less than a hundred of parsecs (e.g. Packham et al. 2007), which corresponds to an angular size of approximately $1.3''$. It therefore requires very high contrast and high resolution for this signature to be detect.

The estimated torus size has significantly decreased over years. Planesas et al. (1991) detected 8×10^7 $M_\odot$ of H_2 gas within a range of 130 pc to the centre, but did not formally identify this with the torus. Using optically thick HCN emission detection, Jackson et al. (1993) studied the velocity of the gas, leading to a velocity gradient compatible with a torus of 180 pc radius, rotating around an axis inclined at 33°. Young et al. (1996) obtained polarised images in J and H bands and estimated the torus to be larger than 200 pc. They found similar results about the torus axis with an estimate of inclination of $32 \pm 3°$. Packham et al. (1997) interpret polarisation as arising from dichroic absorption through the torus and obtained a size of 220 pc, from a several series of polarimetric imaging observations in the NIR. A 100 pc structure was resolved by Alloin et al. (2000) in the NIR, compatible with the torus. However, current estimate is much smaller. Gratadour et al. (2003) performed spectroscopy of the nucleus of NGC 1068 with the Canada France Hawaii Telescope (CFHT) and instrument PUEO [1]-GriF (see Clénet et al. 2002) in K band. When compared to radiative transfer simulations, it leads to results consistent with the supposed toroidal geometry and a torus radius smaller than 30 pc. A 22 pc upper limit was determined by Packham et al. (2007) (again from polarimetric observations) and a size smaller than 7 pc was derived by Alonso-Herrero et al. (2011) using MIR spectrometry and SED fitting. Raban et al. (2009) detected two components in the centre of NGC 1068 using mid-infrared interferometry. Their first measured signature is consistent with an emission from a compact region of 0.45×1.35 pc that they interpret as the obscuring regions, composed from silicate dust at $T \approx 800$ K and their modelling required a second component, colder ($T \approx 300$ K) extension of the torus (3×4 pc). García-Burillo et al. (2016) observed with ALMA a 10 pc diameter molecular disk, which

1. PUEO stand for Probing the Universe with Enhanced Optics and is an Hawaii owl

they interpret as the submillimeter counterpart to the torus, they estimated the torus to have a radius of 3.5 ± 0.5 pc. Note that the distance used for NGC 1068 has varied from 18 to 14 Mpc between the oldest and most recent papers, playing a small role in these variations.

The morphology of the torus has also changed. From the uniform constant density of the first models, as for example the one by Antonucci (1993), it is now commonly accepted that the torus has a more complex geometry. It is likely to be clumpy, as the hydrodynamic stability of structures on a scale of tens of parsecs is unlikely (see for example work of Elmegreen 1991). Furthermore, fragmentation has been invoked to explain some observations according to recent work (Mason et al. 2009; Müller Sánchez et al. 2009b; Nikutta et al. 2009; Alonso-Herrero et al. 2011). Current sketchs of the torus geometry and shape can be seen in figures 4.2 and 1.5.

Because the geometry is not well known, the estimations of the optical depth show large variations. Gratadour et al. (2003) estimated a likely $\tau_V = 40$ in the mid plane, while Marin et al. (2012) used $\tau_V = 750$. Note that fragmentation even complicate the estimation, because optical depth of individual clouds and their number along the line of sight need to be constrained. Most studies (see e.g. Marin et al. 2015) argue for clouds with optical depth of nearly 50 in the visible, but the number of clouds is uncertain so is the integrated optical depth. Lira et al. (2013) estimated a lower limit of 5 clouds. More recently, Audibert et al. (2017) obtained a number of clouds between 5 and 15 (but based on several Seyfert galaxies). Both these studies lead to integrated optical depth on the line of sight of above 200 in visible. Lower limit is set by the non-detection of broad lines in unpolarised light from NGC 1068, see for example Ramos Almeida et al. (2016) who revealed these hidden lines only thanks to polarimetry. This implies for certain that the torus can not be optically thin from UV to K band.

The orientation of the torus is also uncertain. Because we do not detect broad line in unpolarised light from NGC 1068 (Seyfert 2), we expect the inclination to be relatively close to 90° as it should be viewed edge on. Young et al. (1996) derived a torus inclination of 42°, while Alloin et al. (2000) argue for an inclination closer to 65°. However Marin et al. (2016a) warn about the difficulty to have a good inclination estimator.

Magnetic field on the torus was also investigated, for instance by Lopez-Rodriguez et al. (2015) using AO observations to constrain the torus composition and the magnetic field intensity and orientation assuming aligned elongated grains.

4.1.3 Previous Polarimetric Studies

Several polarimetric studies were dedicated to NGC 1068. From the breakthrough spectro-polarimetric observation of Antonucci & Miller (1985) to the more recent polarisation maps of Packham et al. (2007), polarimetry has been able to bring strong constraints.

NGC 1068 is a quite polarised target overall. Its integrated linear degree of polar-

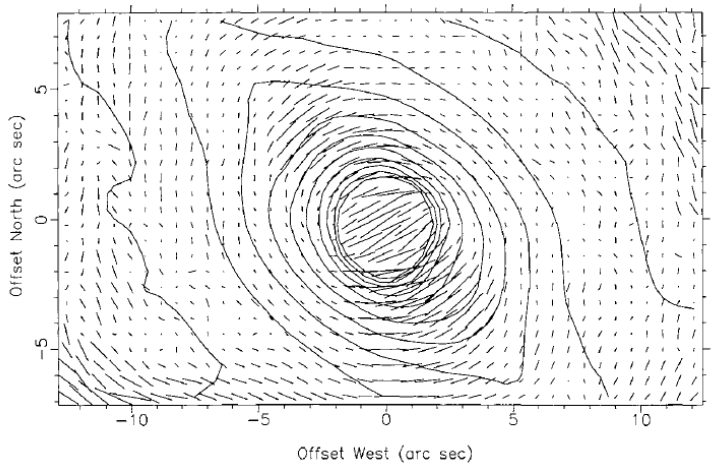

Figure 4.5 – Polarisation image of the central 25 x 15 arcsec^2 in H band. The zero of the coordinates corresponds to the centroid of the nuclear region in this band. A 2.4″ length polarisation vector corresponds to 10 % polarisation. From Packham et al. (1997).

isation is 16.0 ± 2.0 on UV/optical continuum, in the upper range of accessible AGN as listed by Marin (2014) from Miller & Antonucci (1983) data, with a polarisation PA of 95.0°. Packham et al. (2007) used images displayed in figure 4.5 to identify the North-East polarised region as being the scattering cones. Packham et al. (2007) used later polarimetric images at 10 μm to constrain the size of the torus.

Note that polarisation can also be used to constrain the position of the CE. Because it emits the light that will be scattered on the polar directions, leading to a centro-symmetric pattern, we can trace back the location of the source thanks to the polarisation vector PA. This was done by Kishimoto (1999) who derived accurately the location of the nucleus of NGC 1068.

4.2 New Observations with SPHERE

SPHERE (for Spectro-Polarimetric High-contrast Exoplanet REsearch, Beuzit et al. 2008) is an instrument including an extreme AO system installed on the VLT at Cerro Paranal to detect exoplanets and explore the disks around stars. It is composed of three systems, IRDIS, (infrared) Integral Field Spectrograph (IFS) and ZIMPOL. It has been designed to allow polarimetric observations (see Langlois et al. 2014 for IRDIS and Thalmann et al. 2008 for ZIMPOL, the two instruments used in this work). This mode was intended to be used on disk around young stars, to explore the planetary formations, however we thought we could obtain some good results when applied to an AGN.

Our program was based on results of the NaCo observation NGC 1068, deconvolved by Gratadour et al. (2006) (see figure 4.3). We took advantage of the SPHERE Science

Verification (SV) program, at the beginning of this PhD work to propose a follow up of the high angular resolution observation of the core of an AGN. The idea was to take benefit of the high contrast imaging capacities of SPHERE, with a higher AO correction level than NaCo, to obtain a better resolution on the core of NGC 1068. Furthermore, SPHERE can also be used in polarimetric mode. The proposal was accepted and SPHERE and ESO staff carried it, obtaining new images with IRDIS in Broad Band (BB). Based on the results of this observation, we then proposed observations with IRDIS in Narrow Band (NB) as well as an observation with ZIMPOL in R band, during the following periods. Proposal for IRDIS was accepeted for P97 and ZIMPOL observation was executed during P99. Accepeted proposal can be found in Appendix A.

4.2.1 IRDIS Broad Bands

This section details the first observation conducted in the context of this PhD work, using SPHERE-IRDIS during SPHERE SV program in December 2014. I joined the team while the proposal was submitted. I was therefore highly involved on the observation preparation, from the observing time estimation based on our previous NaCo observation to the Observation Block (OB) preparation. We obtained results by the end of 2014 and spent the first half of 2015 reducing and analysing the data, mainly in H and Ks Broad bands (see figure 4.6), leading to the following article (Gratadour et al. 2015). In the context of the initial stage of my PhD work, I participated to the data reduction, going through all the process steps to the final images.

A&A 581, L8 (2015)
DOI: 10.1051/0004-6361/201526554

Astronomy & Astrophysics

Letter to the Editor

Polarimetric imaging of NGC 1068 at high angular resolution in the near infrared

Direct evidence of an extended nuclear torus⋆,⋆⋆

D. Gratadour, D. Rouan, L. Grosset, A. Boccaletti, and Y. Clénet

LESIA, Observatoire de Paris, CNRS, UPMC and Univ. Paris Diderot, France
e-mail: damien.gratadour@obspm.fr

Received 18 May 2015 / Accepted 29 June 2015

ABSTRACT

Aims. One of the main observational challenges for investigating the central regions of active galactic nuclei (AGN) at short wavelengths, using high angular resolution, and high contrast observations, is to directly detect the circumnuclear optically thick material hiding the central core emission when viewed edge-on. The lack of direct evidence is limiting our understanding of AGN, and several scenarios have been proposed to cope for the diverse observed aspects of activity in a unified approach.
Methods. Observations in the near-infrared spectral range have shown themselves to be powerful for providing essential hints to the characterisation of the unified model ingredients because of the reduced optical depth of the obscuring material. Moreover, it is possible to trace this material through light scattered from the central engine's closest environment, so that polarimetric observations are the ideal tool for distinguishing it from purely thermal and stellar emissions.
Results. Here we show strong evidence that there is an extended nuclear torus at the center of NGC 1068 thanks to new adaptive-optics-assisted polarimetric observations in the near-infrared. The orientation of the polarization vectors proves that there is a structured hourglass-shaped bicone and a compact elongated (20×60 pc) nuclear structure perpendicular to the bicone axis. The linearly polarized emission in the bicone is dominated by a centro-symmetric pattern, but the central compact region shows a clear deviation from the latter with linear polarization aligned perpendicular to the bicone axis.

Key words. galaxies: active – galaxies: Seyfert – techniques: polarimetric – techniques: high angular resolution

1. Introduction

The unified model of active galactic nuclei, which has been largely accepted, explains the extreme energy production in a compact region by the presence of a supermassive black hole (a few million to billions of solar masses), which is continuously fueled through an accretion disk and which strongly irradiates its close environment mainly at short wavelengths. To cope with the diverse observed aspects of activity, a key ingredient is the presence of circumnuclear, optically thick material, arranged in an anisotropic manner and hiding the central core emission when viewed edge-on (Antonucci 1993). As one of the closest active galaxies (15 Mpc), NGC 1068 is the ideal laboratory for studying nuclear activity. While indirect evidence has been found in this object, thereby corroborating the unified model (Antonucci & Miller 1985; Raban et al. 2009), many unknowns remain as to the nature and distribution of the obscuring material (Nenkova et al. 2002). Recently, the complexity of the circumnuclear environment has been revealed by high angular resolution broad band observations in the near-IR (Rouan et al. 2004; Gratadour et al. 2006; Exposito et al. 2011). In this Letter, we present the new elements introduced by polarimetry.

2. Observations and data processing

The core of NGC 1068 was observed with the SPHERE instrument on the Very Large Telescope, under the science verification program, using the infrared camera IRDIS (Langlois et al. 2014) in its polarimetric mode. SPHERE has been designed for hunting exoplanets through direct imaging and is equipped with the extreme adaptive optics system SAXO (Beuzit et al. 2008), providing diffraction-limited image quality to IRDIS under nominal atmospheric conditions. It requires an $R < 11$ star for the adaptive optics loop, but bright and compact extragalactic targets can also be used as guide sources as in the case of these observations. NGC 1068 was observed under rather good turbulence conditions (median seeing of about 1″) on 10 and 11 December 2014. The adaptive optics correction quality was fair even though SAXO could not be used at full capacity owing to the faintness of the guide source. The airmass ranged from 1.1 to 1.26 during the observations. The achieved resolution on NGC 1068 (60 mas, i.e. about 4 pc) at H (1.65 μm) and K' (2.2 μm) reveals new details over more than 600 pc around the central engine. We built a data reduction pipeline to produce, for each band, maps with pixels of 0.01225″ (0.9 pc) of the total intensity, the degree of linear polarization, and the linear

⋆ Figure 2 is available in electronic form at http://www.aanda.org

⋆⋆ Data obtained with the SPHERE an instrument designed and built by a consortium consisting of IPAG (France), MPIA (Germany), LAM (France), LESIA (France), Laboratoire Lagrange (France), INAF – Osservatorio di Padova (Italy), Observatoire de Genève (Switzerland), ETH Zurich (Switzerland), NOVA (Netherlands), ONERA (France), and ASTRON (Netherlands) in collaboration with ESO.

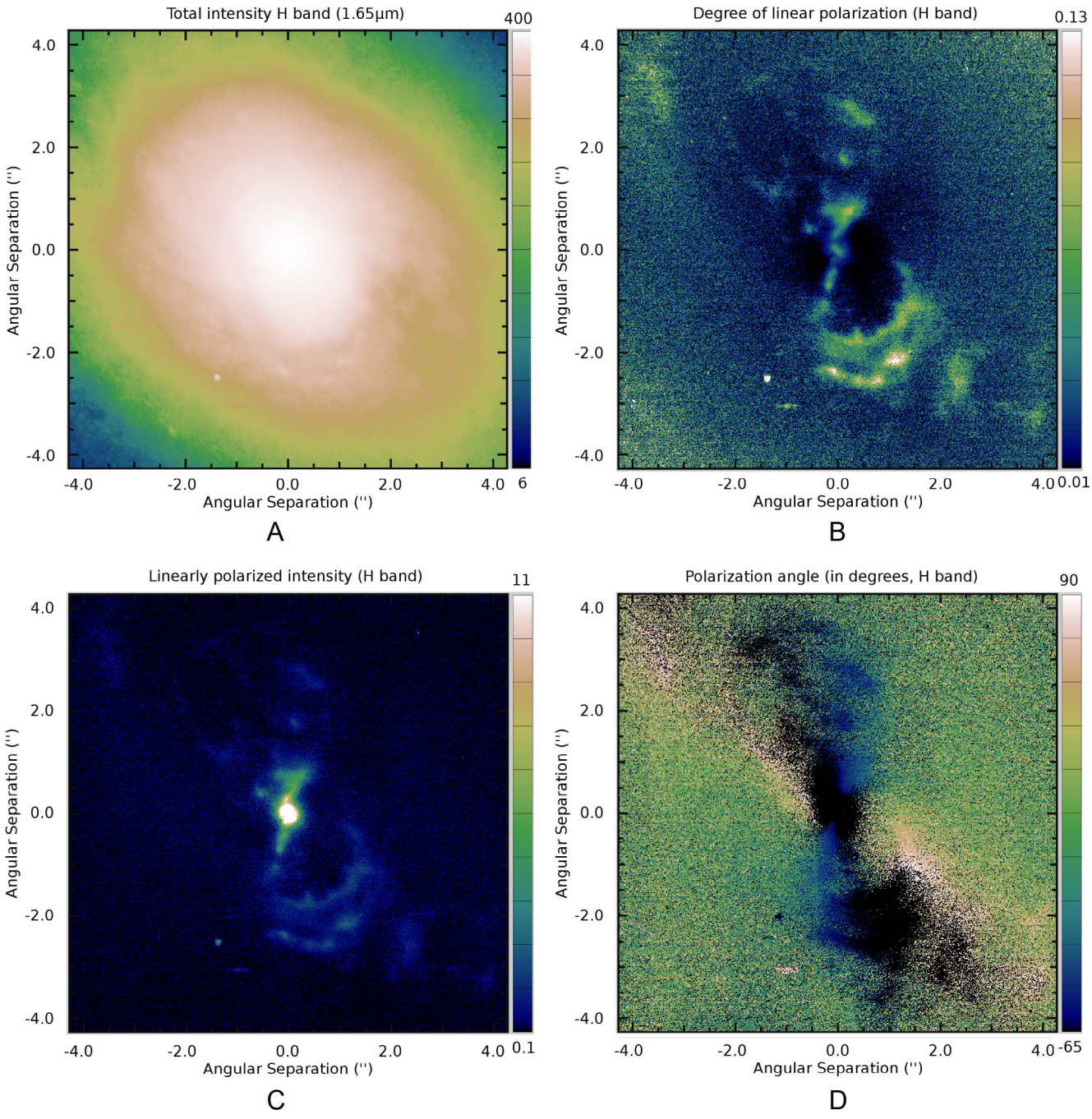

Fig. 1. Output of our data reduction pipeline. North is up, east to the left. **A)** Total intensity image (color bar in arbitrary units); **B)** degree of linear polarization; **C)** polarized intensity (color bar in arbitrary units); **D)** polarization angle (in degrees). The total intensity image has been histogram-equalized between the 2 values in the color bar; i.e., each byte in the color map occurs with equal frequency between the 2 specified values.

polarization angle. This data reduction pipeline includes data pre-processing (detector cosmetics: flat-fielding and bad pixel correction, distortion correction: vertical spatial scale is multiplied by 1.006, sky background subtraction and true north correction as measured on images of 47 Tuc), high accuracy shift-and-add (Gratadour et al. 2005a), and a dedicated polarimetric data reduction procedure. The latter is based on the double-ratio method, which is adequate for dual beam analyzers using half-wave plates (Tinbergen 1996). In such systems the polarization information is contained in the ratio of the two beams but mixed up with the system gain ratio for each pixel. To filter out the latter, Stokes parameters are obtained by computing the ratio of the intensity in one of the beams for two positions of the halfwave plate over the same ratio for the other beam. Four positions of the halfwave plate are thus required to retrieve the degree of polarization and the polarization angle. The total intensity is obtained by summing all the images from both beams. These maps are shown in Fig. 1 for the *H* band with the addition of the polarized intensity image (Panel C), obtained from the product of the total intensity (Panel A) by the degree of polarization (Panel B). The total intensity image has been histogram-equalized to help to show the nice spiral structure of the diffuse

emission at low contrast, it is not representative of the real intensity image entirely dominated by the central source if displayed on a linear or logarithmic scale.

3. Polarization in the ionization bicone

At H and at K', very similar polarized intensity images reveal a bright central source and a distinct bicone, whose axis is at position angle (PA) of about 30°. While the northern cone can be associated to the cloud complex of ionized gas that is extensively studied through optical ionization lines (Groves et al. 2004) and near-IR coronal lines (Barbosa et al. 2014), the southern cone appears as a perfectly symmetrical structure with respect to the central engine location. It shows distinct edges, which are highly polarized close to the base, as well as successive well-defined arcs at 125, 170, and 180 pc from the nucleus to the southwest. The orientation of the bicone with respect to the host galaxy explains that the southern cone is more conspicuous in the near-IR than in the visible (Das et al. 2006): the northern cone is above the disk, while the southern cone, below, is reddened. This is also consistent with the properties of the 21 cm absorption feature observed with the VLA (Gallimore et al. 1994). Highly polarized cone edges is consistent with a simple geometric assumption in which the edge-brightened regions have a scattering angle close to 90° required for maximum polarization (Tadhunter et al. 1999). The southern arcs can be partly associated to patchy clouds detected in the optical with HST/FOC (Macchetto et al. 1994) and to features observed with coronagraphy in the near-IR (Gratadour et al. 2005b). The linearly polarized emission in the bicone is largely dominated by a centro-symmetric component, as shown by the map of polarization angle, and is thus interpreted as scattered emission from the central engine (Simpson et al. 2002). Kinematic models of a global outflow (conical or hourglass shaped) in the narrow line region (NLR), originating in a disk or torus wind, have been successfully compared to spectroscopic data in the optical (Das et al. 2006) and near-IR (Riffel et al. 2014) to explain the observed emission-line velocities in the whole bicone. In these models, the NLR clouds are accelerated to about 1000 km s^{-1} up to a distance of 80 pc from the nucleus, keeping a constant velocity beyond (hourglass model) or decelerating to the galaxy's systemic (conical model), consistent with the location of the arc structure. The sharp and regular circular morphology of the near-IR polarized emission suggests a vast bow shock stemming from the interaction of this outflow with the galactic medium. It could explain the increased degree of polarization in these regions owing to the inescapable accumulation of matter, hence of dust, because of the velocity change at this location, resulting in an increase in Mie scattering efficiency. This interpretation is consistent with the lobe structures observed on radio images (see Wilson & Ulvestad 1982 for instance) and infer the presence of a bow shock.

4. Evidence for an extended nuclear torus

We subtracted a purely centro-symmetric component from the map of polarization angle, assuming the central emitting component to be at the location of the near-IR peak intensity and with the proper reference angle, fit by minimizing the median residual angle over the bicone. Following this method, we find a PA for the bicone axis of 33° ± 2. We are only interested in the absolute value of the difference between the directions of the polarization vectors and the centro-symmetric pattern (hence an angle between 0 and 90°). It is the quantity displayed in the lefthand panel of Fig. 2 for the H band.

The result confirms that the polarized intensity in the bicone is completely dominated by scattered light from the central source. Most importantly, it reveals a compact elongated region in the inner arcsecond around the nucleus, showing a clear deviation from the centro-symmetric pattern with linear polarization aligned perpendicular to the bicone axis and extending over 55 pc perpendicular to this axis and about 20 pc parallel to it. The same result is obtained in both bands as shown by the magnified versions of the difference angle map around the nucleus for both the H (left) and K' (right) bands pictured in the upper part of the right panel of Fig. 2. In addition to the lack of significant residual pattern in the peripheral zones on the difference image at each extremity of the elongated structure, we believe this feature is neither an instrumental artifact nor a shadow effect tracing a region where the polarization is cancelled totally due to multiple scattering in denser material closer to the nucleus. It should be noticed, though, that the bicone shape of this feature is an artefict inherent to the displayed parameter (difference of angle), Indeed for points on the ionization bicone axis, the apparent transverse component becomes parallel to the centro-symmetric vector so that the difference in angles vanishes along this axis. Most important, this subtraction process only enhances a pattern already observable on the polarization angle map without processing as shown by the image at the bottom of the righthand panel of Fig. 2.

In this image, the polarization vectors are displayed as bars overlaid on the degree of the linear polarization map. A transverse polarization angle component crossing the nucleus and extending over about 0.8″ with the same PA can be clearly identified. Such a feature, with a central transverse polarization, has already been observed at lower angular resolution (Packham et al. 1997) and has been interpreted since as dichroic absorption of the central light radiation by aligned non-spherical dust grains. Additionally, it is believed that the transition between dichroic absorption and emission could explain the sudden flip of the polarization angle around 10 μm (Packham et al. 2007) toward the nucleus. However, this interpretation appears incompatible with the observed extension of this feature appearing at high angular resolution because it would require a still undetected extended source of emission in the background to be attenuated by this structure.

This feature is similar to the polarimetric disk effect observed in young stellar objects. An original interpretation of this effect (Bastien & Menard 1988) involves a thick disk or flat torus, on which the radiation from the central engine is scattered twice on average, before reaching the observer: once on the upper (or lower) surface of the disk and then near its external edge. Recently, refined radiative transfer modeling (Murakawa 2010) has supported this interpretation. In this model, grains can be spherical or not, and grain alignment is neither required nor expected to have a significant impact. These simulations show that an extended patch of linear polarization aligned in a direction perpendicular to the bicone axis can appear at its base for a thick disk (thickness parameter greater than 0.3) with rather small dust grains (0.25 μm diameter). The comparison of their Fig. 6 with our data, in the case of double scattering, is particularly convincing. Additionally, this model is able to reproduce the highly polarized bicone edges we observe.

In this simulation, the thickness of the disk, viewed almost edge-on, was taken to be 30% of the diameter, which is consistent with the thickness of 15 pc measured at the outer edges of this feature on our data. For the effect to be efficient, the optical depth of the torus cannot be much larger than 1, otherwise multiple scattering would cancel the polarization: this condition is

compatible with the range generally considered for NGC 1068. An optical depth on the line of sight of 1.25 in K band is inferred, for instance, to cope with high angular resolution spectroscopic observations (Gratadour et al. 2003). We thus believe that this extended patch of linear polarization aligned in a direction perpendicular to the bicone axis is the first direct evidence of an extended torus at the core of NGC 1068.

The derived parameters (radius of 27 pc and thickness of 15 pc) are consistent with recent results using ALMA data that complement a spectral energy distribution analysis (García-Burillo et al. 2014). Additionally, we derive a PA 118° for the uniformly polarized structure that is consistent with the alignment of the two patches of hot molecular hydrogen observed in the near-IR (Müller Sánchez et al. 2009) and the orientation of the extended structure observed with VLBA at 5 GHz (Gallimore et al. 2004). Moreover, the map of degree of polarization seems to suggest that the obscuring complex extends way beyond the elongated feature we detect around the core, with two lobes of extremely low polarization levels on each side of the nucleus showing efficient screening from the central radiation.

While the polarization level in this extended patch is rather low, which agrees with the polarized disk model, one thing the latter cannot reproduce is the ridge of higher linear polarization observed at the location of the nucleus with a PA of 56° (center of bottom right panel in Fig. 2). We propose that this ridge be interpreted as the location at which the linearly polarized emission due to dichroic absorption of the central light originates. While this effect was not included in the other simulations we mentioned, the measured degree of polarization (5–7%) is consistent with such an interpretation. The size of the minor axis of this feature is consistent with the size of the dust sublimation cavity, believed to be the main contributor to the near-IR emission from the core, as it would appear convolved by the instrumental PSF. However, its extension (comparable to the thickness of the previously inferred torus) and exact orientation are questionable.

A deeper analysis of our data, including a close comparison of H and K' bands and numerical simulations, including dichroic absorption, are required for a better understanding of the nature of this ridge.

Acknowledgements. This paper is based on observations at the Very Large Telescope (VLT) of the European Observatory (ESO) in Chile. We thank Julien Girard and Dimitri Mawet for carrying out the observations and Maud Langlois for helpful discussions of how to calibrate polarimetric observations with SPHERE, along with Chris Packham and Enrique Lopez-Rodriguez for very useful and lively discussions regarding data interpretation.

References

Antonucci, R. 1993, ARA&A, 31, 473
Antonucci, R. R. J., & Miller, J. S. 1985, ApJ, 297, 621
Barbosa, F. K. B., Storchi-Bergmann, T., McGregor, P., Vale, T. B., & Rogemar Riffel, A. 2014, MNRAS, 445, 2353
Bastien, P., & Menard, F. 1988, ApJ, 326, 334
Beuzit, J.-L., Feldt, M., Dohlen, K., et al. 2008, in SPIE Conf. Ser., 7014, 18
Das, V., Crenshaw, D. M., Kraemer, S. B., & Deo, R. P. 2006, AJ, 132, 620
Exposito, J., Gratadour, D., Clénet, Y., & Rouan, D. 2011, A&A, 533, A63
Gallimore, J. F., Baum, S. A., O'Dea, C. P., Brinks, E., & Pedlar, A. 1994, ApJ, 422, L13
Gallimore, J. F., Baum, S. A., & O'Dea, C. P. 2004, ApJ, 613, 794
García-Burillo, S., Combes, F., Usero, A., et al. 2014, A&A, 567, A125
Gratadour, D., Clénet, Y., Rouan, D., Lai, O., & Forveille, T. 2003, A&A, 411, 335
Gratadour, D., Mugnier, L. M., & Rouan, D. 2005a, A&A, 443, 357
Gratadour, D., Rouan, D., Boccaletti, A., Riaud, P., & Clénet, Y. 2005b, A&A, 429, 433
Gratadour, D., Rouan, D., Mugnier, L. M., et al. 2006, A&A, 446, 813
Groves, B. A., Cecil, G., Ferruit, P., & Dopita, M. A. 2004, ApJ, 611, 786
Langlois, M., Dohlen, K., Vigan, A., et al. 2014, in SPIE Conf. Ser., 9147, 1
Macchetto, F., Capetti, A., Sparks, W. B., Axon, D. J., & Boksenberg, A. 1994, ApJ, 435, L15
Müller Sánchez, F., Davies, R. I., Genzel, R., et al. 2009, ApJ, 691, 749
Murakawa, K. 2010, A&A, 518, A63
Nenkova, M., Ivezić, Ž., & Elitzur, M. 2002, ApJ, 570, L9
Packham, C., Young, S., Hough, J. H., Axon, D. J., & Bailey, J. A. 1997, MNRAS, 288, 375
Packham, C., Young, S., Fisher, S., et al. 2007, ApJ, 661, L29
Raban, D., Jaffe, W., Röttgering, H., Meisenheimer, K., & Tristram, K. R. W. 2009, MNRAS, 394, 1325
Riffel, R. A., Vale, T. B., Storchi-Bergmann, T., & McGregor, P. J. 2014, MNRAS, 442, 656
Rouan, D., Lacombe, F., Gendron, E., et al. 2004, A&A, 417, L1
Simpson, J. P., Colgan, S. W. J., Erickson, E. F., et al. 2002, ApJ, 574, 95
Tadhunter, C. N., Packham, C., Axon, D. J., et al. 1999, ApJ, 512, L91
Tinbergen, J. 1996, Astronomical Polarimetry (Cambridge, UK: Cambridge University Press)
Wilson, A. S., & Ulvestad, J. S. 1982, ApJ, 263, 576

Page 5 is available in the electronic edition of the journal at http://www.aanda.org

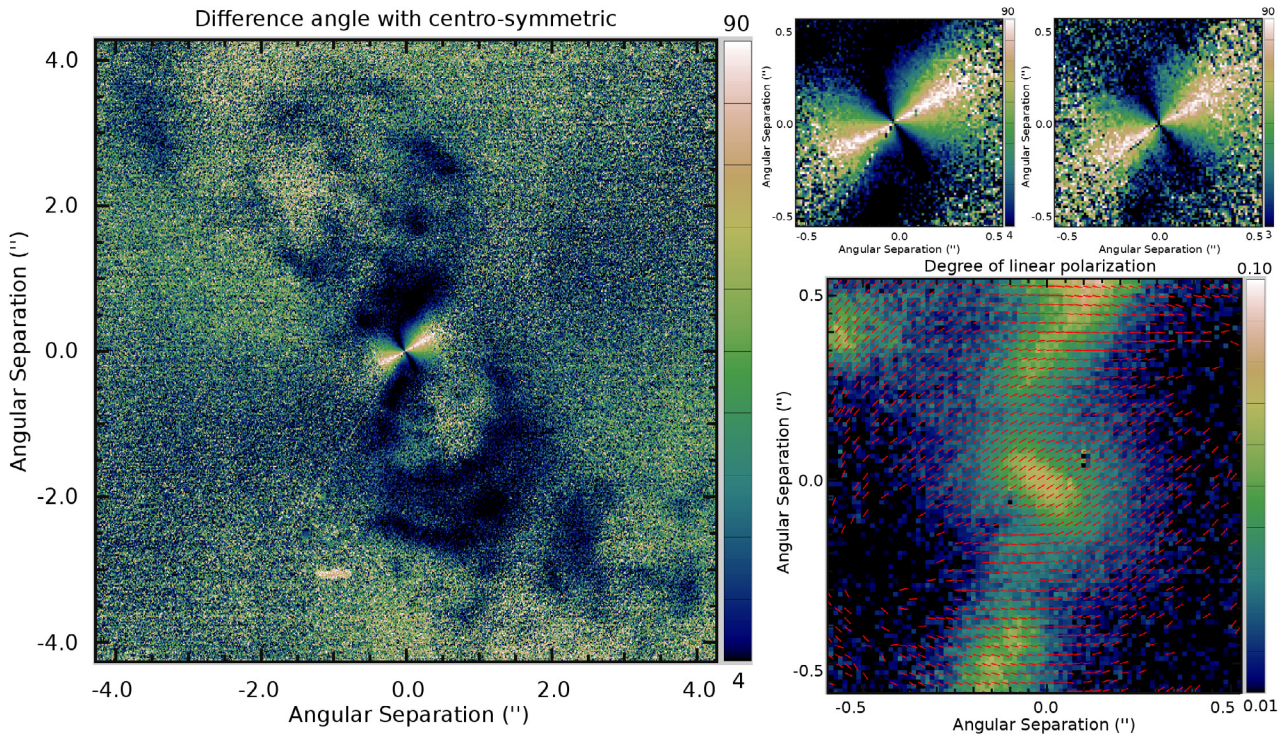

Fig. 2. *Left panel*: result of the difference between the polarization angle map and a purely centro-symmetric pattern. *Right panel*: the *top left image* is a magnified version of the left panel, around the central source and *top right* is the result of the same processing on the K' band angle map. The *bottom right image* is a magnified version of the degree of linear polarization found in Fig. 1, on which we overlaid the direction of the polarization vectors, showing the clear patch of aligned vectors in this region in the data before the subtraction of the centro-symmetric pattern.

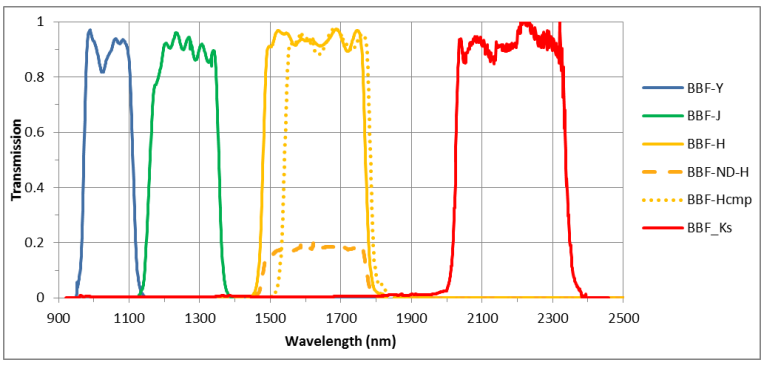

Figure 4.6 – SPHERE-IRDIS BB filters. From SPHERE User Manual.

4.2.1.1 Centro-symmetric Subtraction

A critical point in our final interpretation is the subtraction of the centro-symmetric pattern, showing the central region as having constant polarisation orientation. This subtraction needs to be applied with a centro-symmetric pattern centred on the precise location of the central source of the AGN. However it does not require any hypothesis as it is only a different way of displaying the same data. As discussed in section 3.3.3, this is an operation that can be conducted directly on the final angle map. A similar result can also be obtained by computing Q_ϕ and U_ϕ as explained in section 3.3.3, a usual way of representing such analysis on polarimetric data with SPHERE and in exoplanetary field, but more rarely used with AGNs. After the stimulating discussions that followed the article publication, we derived those maps, displayed for Ks band on figure 4.7.

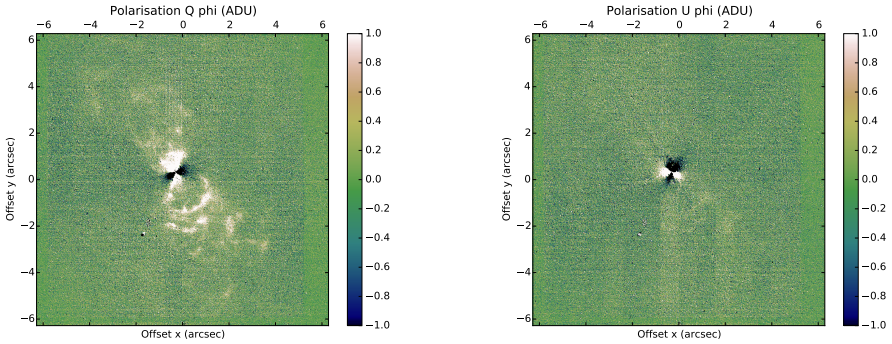

Figure 4.7 – NGC 1068 in Ks band, Q_ϕ and U_ϕ maps.

These images confirm the peculiar polarisation in the centre of NGC 1068 with a central polarimetric signal neither tangential nor radial, consistent with a constant polarisation orientation. Tangential pattern of the polarisation in the bicone is also clearly confirmed. An important new feature brought by these images is the intensity

of these different structures. While the bicone centro-symmetric structures show as expected high fluxes, the very central region where the polarisation orientation is constant also exhibit a significant intensity, making the interpretation of the signal in this region even harder.

4.2.2 IRDIS Narrow Bands

4.2.2.1 Observations

According to Efstathiou et al. (1997), one significant difference between polarisation induced by dichroic absorption/emission by aligned grains and the one created by scattering on more or less spherical grains, is the switch of polarisation angle when looking at different wavelengths. The change from dichroic absorption to emission indeed triggers a 90° change in the polarisation orientation when increasing the wavelength. It would occur around $\lambda = 4$ μm, according to Efstathiou et al. (1997). However, SPHERE can only observe up to the K band (2.2 μm). Our idea was however to obtain SPHERE HAR maps of the core of NGC 1068 at several wavelengths, looking for an evolution of the polarisation. We would not likely observe the switch, but we may catch some modifications of the polarisation with respect to the wavelength. We therefore applied for a follow up observation with SPHERE in the form of a Dual Polarisation Imager (DPI) program of NBs observations in few continuum bands (see proposal in Appendix A and filters `CntH`, `CntK1` and `CntK2` in figure 4.8). The program also included an observation of H_2 very close to the nucleus, with and without coronograph, in Classical imaging (CI).

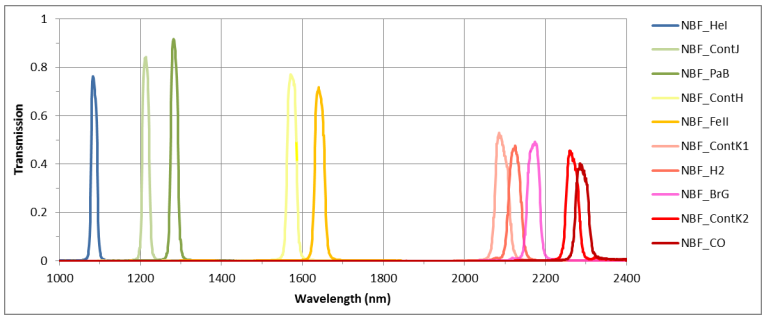

Figure 4.8 – SPHERE-IRDIS NB filters. From SPHERE User Manual.

Observations were conducted in visitor mode, the only mode allowed for polarimetric observations with IRDIS for this period, by Daniel Rouan and me, between the 11th and the 14th of September 2016. Observation log is outlined in table 4.2

4.2.2.2 Data Reduction

Polarimetric images were obtained for four positions of the HWP (1/4 of the observing time per position). All data reduction followed the steps below:

— Sum of the sky images (using median, see section 4.2.2.4)

Table 4.2 – SPHERE-IRDIS observation log, 11th to 14th of September 2016.

Filter	CntH	CntK1	CntK2
Mode	DPI	DPI	DPI
Coronograph	no	no	no
Night	1st night	3rd night	1st night
Observation time (min)	85.33	85.33	106.67
Sky time (min)	32.0	42.67	42.67

Filter	H2	CntK1	H2	CntK1
Mode	CI	CI	CI	CI
Coronograph	yes	yes	no	no
Night	2nd night	2nd night	3rd night	3rd night
Observation time (min)	51.20	51.20	29.60	29.60
Sky time (min)	51.20	51.20	25.60	25.60

— Subtraction of the final sky/skies to scientific images
— Flat-field correction of scientific images
— Image re-centring per HWP position
— Sum of scientific images per HWP position
— Image re-centring

We also applied these steps before the polarimetric reduction. All polarimetric data were then reduced following the three methods described in section 3.4: double subtraction, double ratio and inverse matrix. The final image quality obtained in the various bands are compared in table 4.3 using the pseudo-noise method described in next paragraph. We also tried improved versions of the inverse matrix, allowing elements of the matrix to vary slightly around 1 or -1 to account for instrumental depolarisation, with results very close to the classical inverse matrix. We derived our final images with the inverse matrix method, that gives a slightly lower pseudo-noise (see table 4.3). Note that currently the images are not corrected for aliasing and true North orientation (about 1°). This should be done before publishing final data products, but will not change significantly our analysis.

As discussed in Tinbergen (1996), it is difficult to evaluate the quality of polarimetric maps. Signal to Noise Ratio (SNR) for example is not well defined as a higher intensity will not correspond to higher degree of polarisation. Furthermore, when the degree of polarisation is small, neither the polarisation angle nor the polarisation degree follow Gaussian distributions. In order to evaluate the different generated maps and compare the methods, we based our analysis on the local variations of the degree of polarisation. Thus we ensure to compare the variations on regions were the SNR of the intensity maps is identical which is required since SNR will affect the determination of the degree of polarisation, as detailed in Clarke & Stewart (1986). We subtracted to each pixel a mean of the four closest pixels, creating a "pseudo-noise"

map m_σ and then look at the dispersion of these values on all the maps, as follows:

$$\sigma_{pol} = 1.4826 \times \text{median}(|\sqrt{0.8}\ m_\sigma - \text{median}(\sqrt{0.8}\ m_\sigma)|) \tag{4.1}$$

Table 4.3 – Efficiency of the three polarimetric reduction methods. It shows the measurements of the pseudo-noise σ_{pol} in ADU.

Filter	CntH	CntK1	CntK2
Double differences method	0.05904	0.08924	0.26746
Double ratio method	0.06081	0.09099	0.20141
Inverse Matrix method	0.05751	0.08565	0.20695

4.2.2.3 Derotator

One important parameter for polarimetric observations with SPHERE is the derotator angle. It affects the polarisation measurements and should therefore be carefully planned or taken into account. Figure 4.9 shows the polarimetric efficiency depending on the filter and derotator angle. One can note that NB filters have not been tested and their polarimetric efficiency is therefore unknown. We expect their efficiency to follow the general tends of the other filters, but we have no mean to know exactly what is the efficiency for a given angle. We placed our observations on a graph indicating for each of them the derotator angle (figure 4.10).

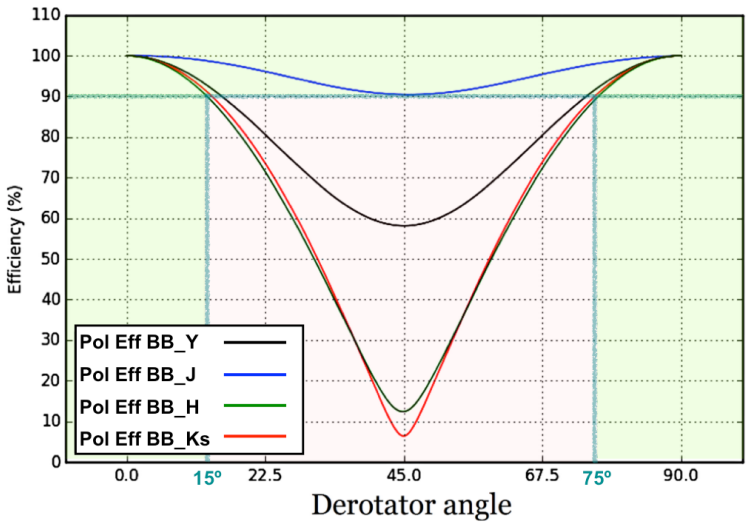

Figure 4.9 – Measurements of the instrumental polarisation efficiency (not accounting the telescope) for four broad band filters. For best use of the DPI mode, one should avoid the pink zone where the efficiency drops below 90° (> 10° loss due to cross-talks). For that, one should make sure the derotator angle stays < 15° or > 75°. From SPHERE User Manual.

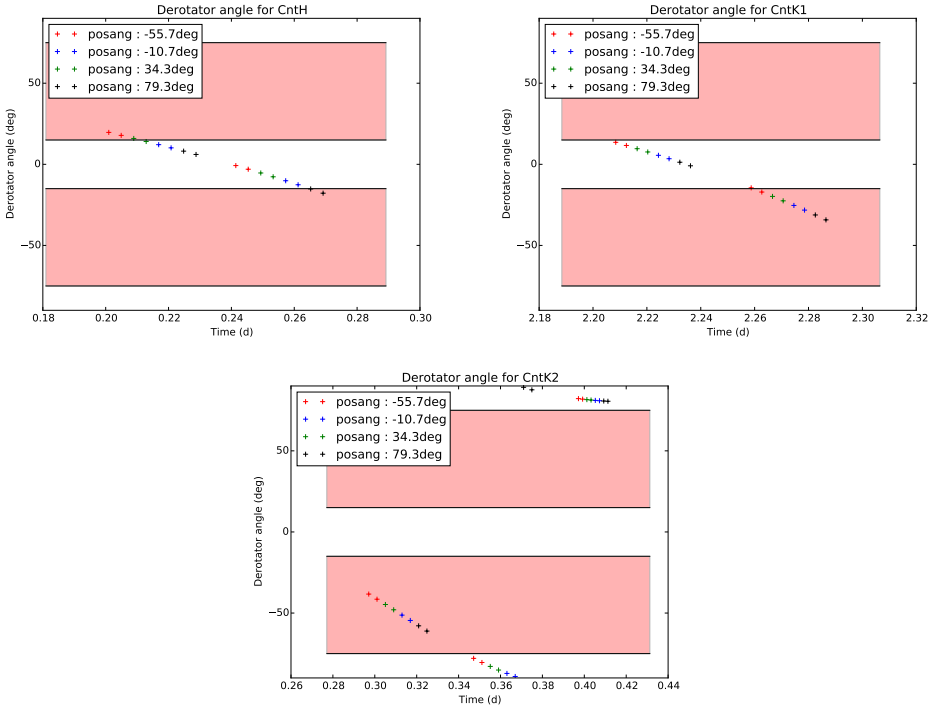

Figure 4.10 – Derotator position for NB observations, `CntH`, `CntK1` and `CntK2`. The red bands indicates the zones that one should avoid.

Most of our observations have been done in the −15°–15° range, i.e. on optimal position for BB filters. However this is not the case for some images taken with the `CntK1` and `CntK2` filters. `CntK2` furthermore shows the lowest polarimetric signal (see fig 4.18 of section 4.2.2.5). We therefore expected this lack of signal to come from the derotator and compared the final maps computed with all raw images, and those obtained with a selection of raw images with an optimised derotator position. Images are shown in figure 4.11, results are shown on table 4.4. Note that despite having some higher polarimetric signal, we also conduct for the same reasons the same experiment on `CntK1` filter with similar results (not shown in this thesis).

Table 4.4 – Impact of derotator position on polarisation degree.

Filter	`CnK2` full	`CntK2` selected
σ (ADU)	0.20695	0.24220

We have no clear improvement by selecting the images in the optimised range of derotator angle. The difference is likely to arise from the exposure time, because it is shorter for the selection therefore inducing a lower SNR. Furthermore, the images look very similar and the low polarisation signal is unlikely to be entirely due to the derotator. We finally used the reduced image obtain with the complete observation,

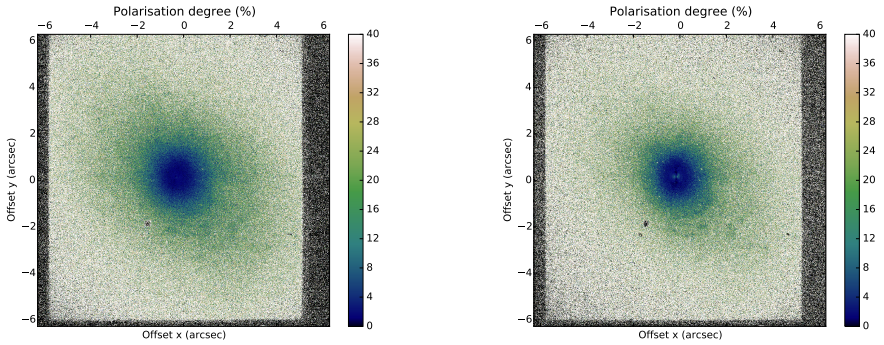

Figure 4.11 – NGC 1068 in `CntK2` NB. First image was created without selection, using all images. Second image was generated from selected images on their derotator angle.

because we can not go further into these comparison without measurements of the NB filters efficiency.

4.2.2.4 Polarimetric Sky Strategy

Preparing the OB, we expected the sky and science acquisitions to match. However it appeared that this is not the case. The SPHERE-IRDIS instrument is set to take sky images with only one HWP position (by default 0°). This is consistent with the fact that the sky should not be highly polarised in the NIR (during night). This difference explains the difference in acquisition time between scientific and sky observations, as shown in table 4.2. We however changed the instrument setup to take skies with the four positions of the HWP. This allowed us to test whether the use of only one polariser position for sky measurement is enough to fully take into account the sky emission in polarimetric measurements. Note that this is not analytically trivial as long as the polarimetric data reduction includes non linear processes (see for example Clarke & Stewart 1986). We tried three combinations of skies: all skies combined, 1/4 of all skies stacked and skies combined by HWP position. The second sky strategy is to be compared to the first method with the same exposure time per created final sky. We compared these three reductions with a fourth final image computed without removing skies, with and without re-centring because the absence of sky subtraction induces an increased amount of bad pixels (see 4^{th} raw of figure 4.12). Final images for `CntK1` filter are displayed in figure 4.12 and results are shown in table 4.5.

One striking fact is that the apparent best final image is the one without sky subtraction. However this image shows polarisation degrees very different from the other three methods. SNR should not affect the value of the resulting polarisation and the values of this map must be rejected. Once again, this is not trivial because it has not been demonstrated analytically so far. We conducted simulations to confirm this: we created some arbitrary maps with some intrinsic polarisation; we added a

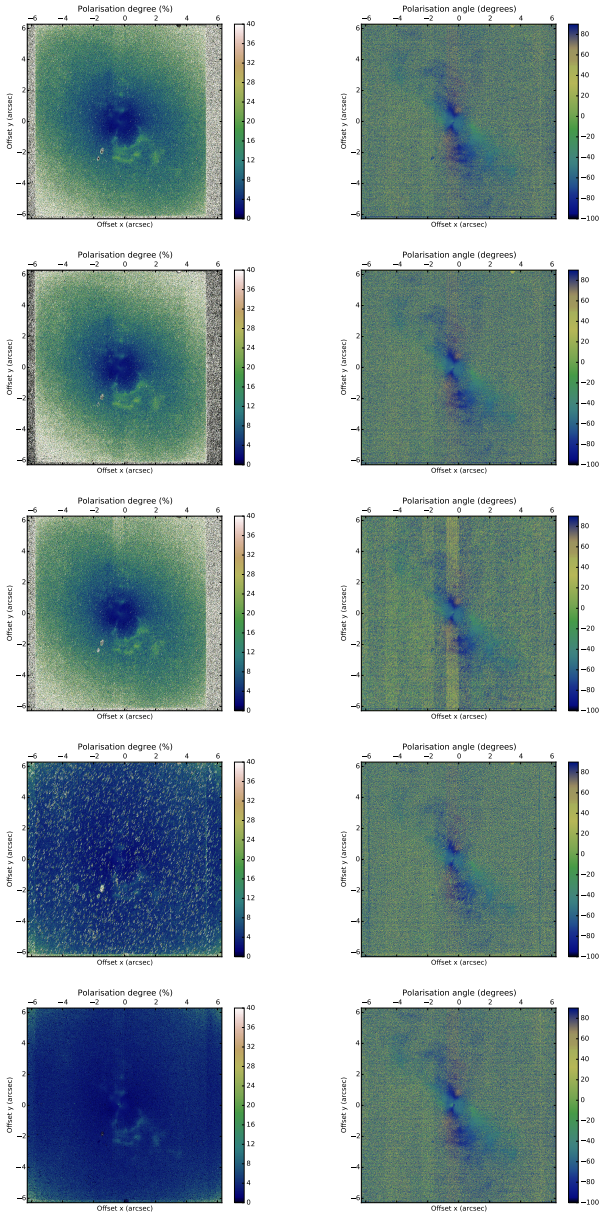

Figure 4.12 – Results of reducing with different sky strategies `CntK1` NB images. First column shows the polarisation degree maps and second the polarisation angle. First row correspond to treatment with all skies combined, second one was obtained using 1/4 of the skies, third with the skies corresponding to the HWP positions, fourth and fifth without sky subtraction. Fifth images were not re-centred.

sky image generated from random Gaussian distribution; reduced these data using another randomly created sky (with the same distribution but another initial seed) or without sky subtraction. Results on the polarisation degree are shown in figure 4.13

Table 4.5 – Impact of the skies used in the polarisation efficiency.

Filter	CntH	CntK1	CntK2
all skies	0.05751	0.08565	0.20695
1/4 skies	0.05417	0.10326	0.21883
HWP skies	0.06890	0.09366	0.21687
no sky	0.05791	0.03216	0.01160
no sky & no centring	-	0.020317	-

while those on polarisation angle are displayed on figure 4.15. Figure 4.14 shows the histogram of the degree of polarisation of these images.

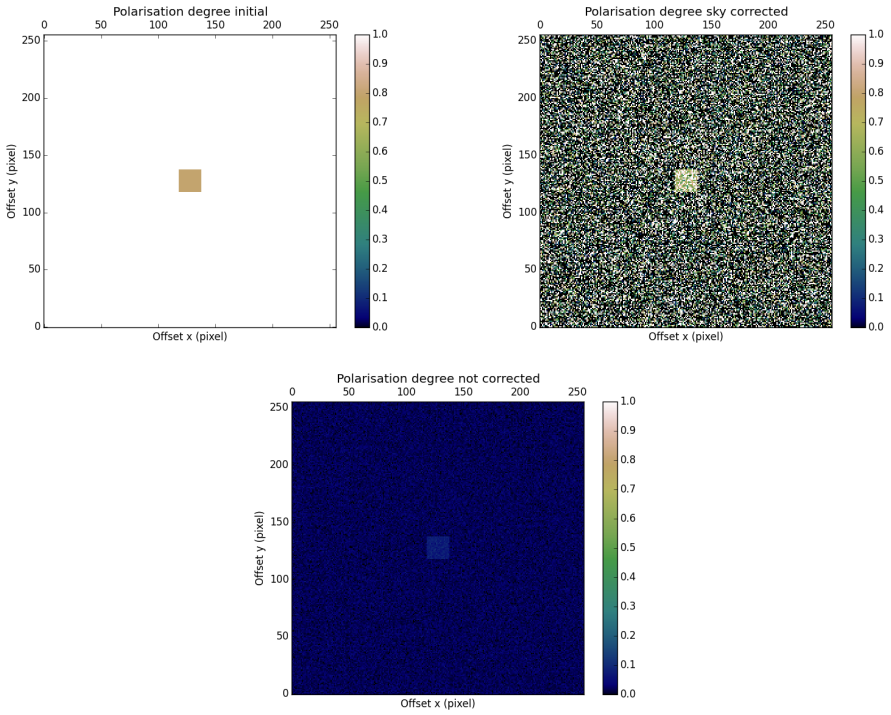

Figure 4.13 – Impact of the sky background on the degree of polarisation. First image is the initial polarisation degree generated, second one represents the polarisation degree observed, with sky subtraction and the third image shows the polarisation degree as measured without subtracting sky.

Figure 4.15 indicates that the sky correction has very little impact on the measured polarisation angle. This is furthermore confirmed by reduced image of figure 4.12. However that is not the case on polarisation degree (figures 4.13 and 4.14). The sky-corrected image has a lowest pseudo-noise, however the uncorrected image has a polarisation degree with an important offset with respect to the initial theoretical value, leading to a wrong estimate. Despite not giving the precise value of expected degree

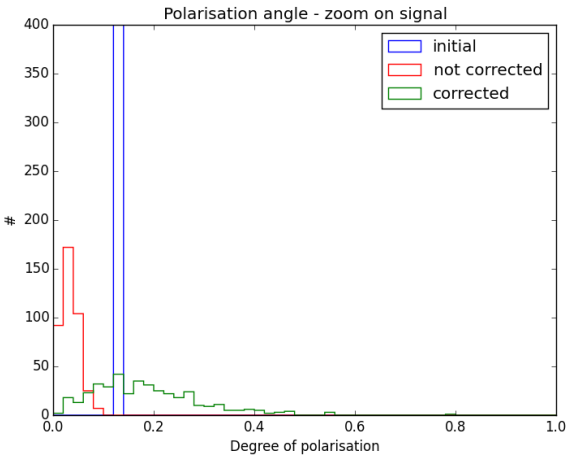

Figure 4.14 – Histogram of the figure 4.13 on impact of the sky background on the degree of polarisation. Blue histogram is the initial polarisation degree generated, the green one one represents the polarisation degree observed, with sky subtraction and the red histogram shows the polarisation degree as measured without subtracting sky.

of polarisation and therefore not being perfect, the sky-subtracted image distribution is almost centred on this value, giving a fair estimate of the true polarisation.

4.2.2.5 Polaro-imaging Results

Following the above remarks, what we consider as the best estimates for the intensity and polarimetric maps of NGC 1068 in the three NB `CntH`, `CntK1` and `CntK2` are shown respectively in figures 4.16, 4.17 and 4.18.

4.2.2.6 Classical Imaging Results

The intensity images of NGC 1068 in the NB `H2` and in the corresponding continuum `CntK1` are shown in figure 4.19. The ratio NB/continuum is shown in figure 4.20. Note that the conspicuous features seen on figure 4.20 are mainly ghosts reflection of light, most likely to occur on the `H2` filter. This unfortunate behaviour has been identified by the SPHERE consortium and does not allow us to go deeper in the analysis of this observation.

4.2.3 ZIMPOL

In order to further investigate the wavelength dependency of the polarisation in NGC 1068, we planed to used the impressive performances of ZIMPOL in the visible to obtain complementary polarimetric maps. The luminosity of NGC 1068 appears to be even more limiting in the visible than in the NIR, restricting to R band observations only. We proposed this program in P99 but had the opportunity to obtain these data

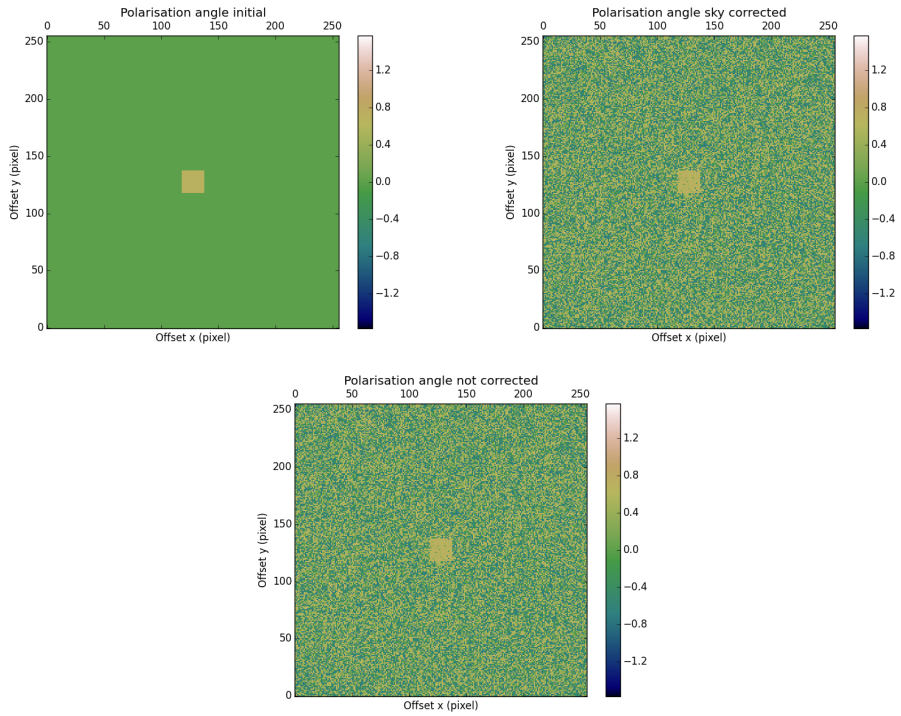

Figure 4.15 – Impact of the sky background on the degree of polarisation. First image is the initial polarisation angle generated, second one represents the polarisation angle observed, with sky subtraction and the third image shows the polarisation angle as measured without subtracting sky.

in the context of the SPHERE Guarantee Time Observation (GTO) thanks to Eric Lagadec and Hans Martin Schmid. Only NB R (see table 4.6) polarimetric imaging were achievable due to the low luminosity of NGC 1068, with the ability to use only the grey beam splitter, that gives access to very few filters. Data were pre-reduced by Eric Lagadec and are shown in figure 4.21.

Table 4.6 – Property of ZIMPOL `N_R` filter, from SPHERE User Manual.

Filter	λ_{min} (nm)	λ_{min} (nm)	FWHM (nm)	λ_0 (nm)
`N_R`	617.5	674.2	56.7	645.9

4.3 Other Targets

With those ZIMPOL observations in R NB conducted in late 2016, we reach the best high resolution polarimetric observations achievable on NGC 1068. The ability to directly trace the torus using polaro-imaging motivated us to push forward our investigations towards other AGN to look for a similar behaviour, or differences that

could be linked to the inclination of the torus on the line of sight. Indeed, observing a similar behaviour of the NIR polarisation in other Seyfert galaxies would bring extremely strong arguments in favour of the unified model and would allow us to build upon the analysis done on NGC 1068.

Three objects, NGC 1097, NGC 1365 and NGC 1808, were selected on the basis of their rather small distances (respectively 16, 18 and 11 Mpc) and of the R-magnitude of the central core, as measured using HST archives. Because of their distance, the resolution that should be obtained is between 0.65 and 1.1 pc/pixel. All sources have been observed using polarimetry at B, B_y, V, R_y and H bands by Brindle et al. (1990, 1991). Furthermore, NGC 1097 has already been observed with NaCo using the nucleus as a guide source for AO (Prieto et al. 2005). The last object, ESO 323-G077, was selected as one of the brightest polar scattering dominated Seyfert 1, a type of AGN which is expected to be observed with a line of sight close to the vertical extend of the torus (Smith et al. 2004), a particularly interesting case in the study of AGNs geometry.

We therefore included these targets in proposals for ESO (European Southern Observatory) P98 and P99, using SPHERE - IRDIS and looking for high resolution on the dusty molecular torus similarly to what we obtained on NGC 1068, with the aim to constrain the extent and opacity of the torus. However, these targets are all fainter in the visible than NGC 1068 and the AO performance will be lower. After the last observation run on NGC 1068 during P97, we decided to propose for P100 to use NaCo instead of SPHERE to guarantee the feasibility of these observations and we are currently discussing about the following of the program.

NaCo would not allow us to reach the same resolution in the inner structure as what was achieved with SPHERE. However, the wave-front sensors allow to close safely the AO loop on fainter targets. Thanks to this trade-off, high enough resolution should be reached to look for the signature of the torus at the tens of parsecs scale on these other targets. Note that we required for that purpose a high precision on the polarisation angle, a condition that is satisfied by NaCo according to Witzel et al. (2011). With the constraint of the previous polarisation observations in the visible and using our radiative transfer model, it will be possible to test the validity of our interpretation or bring new constraints on the geometry and inner structures of those AGNs.

Furthermore, inclination of NGC 1097 and NGC 1365 have been derived with different methods that do not give consistent values (Storchi-Bergmann et al. 1997; Risaliti et al. 2013; Marin et al. 2016a). This issue could be tackled thanks to the additional and independent polarisation observation with NaCo. Prieto et al. (2005) found nuclear spiral structures in NGC 1097 and claimed that a torus should be smaller than 10 pc. Adding the polarisation information at high resolution thanks to NaCo data could confirm or give another perspective on these results. The role of the magnetic field, as discussed in Beck et al. (2005) from radio data, could also be considered in our analysis since aligned grains are expected to affect polarisation through dichroic absorption or emission.

Finally, we also selected in our target list one polar scattering dominated AGN. Despite being further away and therefore observed at a lower spatial resolution, polarisation maps in this type of object could bring strong constraints on the inner geometry of AGNs, especially on the hypothesis of the low range of inclination assumed for these particular Seyfert 1.

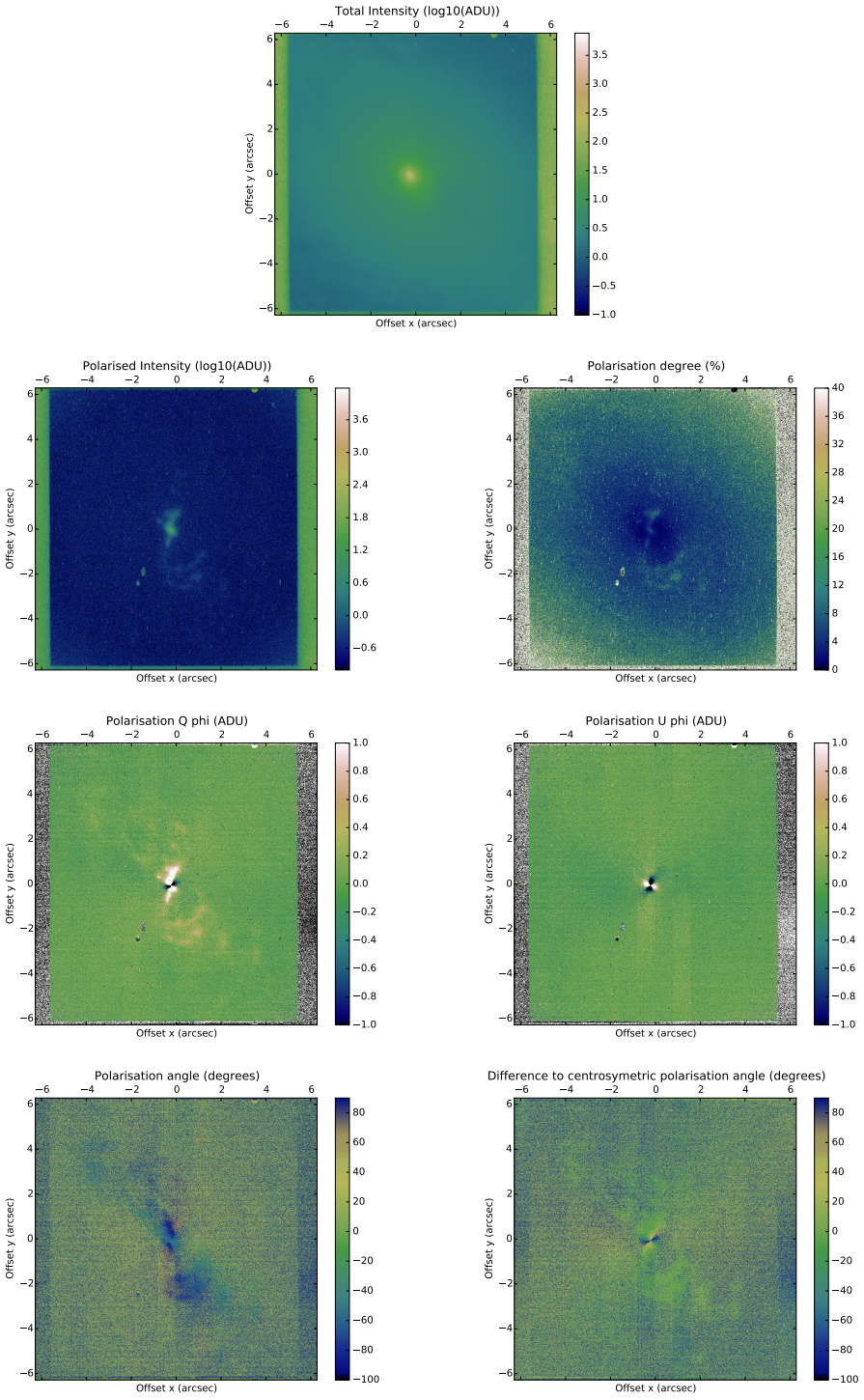

Figure 4.16 – NGC 1068 in `CntH` NB. **1**$^{\text{st}}$ **row** image shows the total intensity recorded (in $\log_{10}$(ADU)); **2**$^{\text{nd}}$ **row**: left shows the polarised intensity (in ADU) and right the degree of polarisation (in %); **3**$^{\text{rd}}$ **row**: left shows the Q_ϕ map and right the U_ϕ map (both in ADU); **4**$^{\text{th}}$ **row**: right shows the polarisation position angle (in °) and right the difference angle to centro-symmetric (in °).

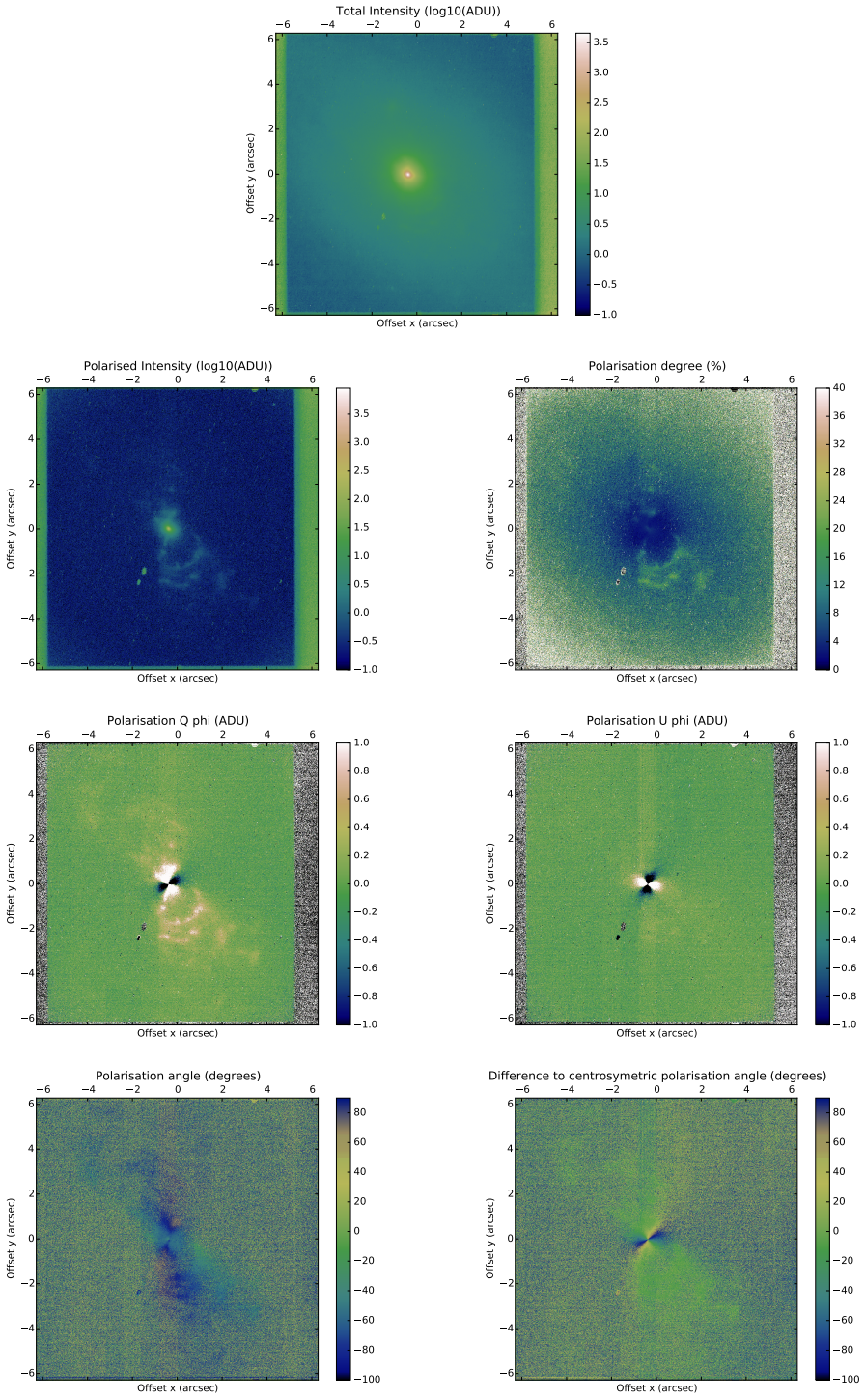

Figure 4.17 – NGC 1068 in `CntK1` NB. **1**$^{\text{st}}$ **row** image shows the total intensity recorded (in $\log_{10}$(ADU)); **2**$^{\text{nd}}$ **row**: left shows the polarised intensity (in ADU) and right the degree of polarisation (in %); **3**$^{\text{rd}}$ **row**: left shows the Q_ϕ map and right the U_ϕ map (both in ADU); **4**$^{\text{th}}$ **row**: right shows the polarisation position angle (in °) and right the difference angle to centro-symmetric (in °).

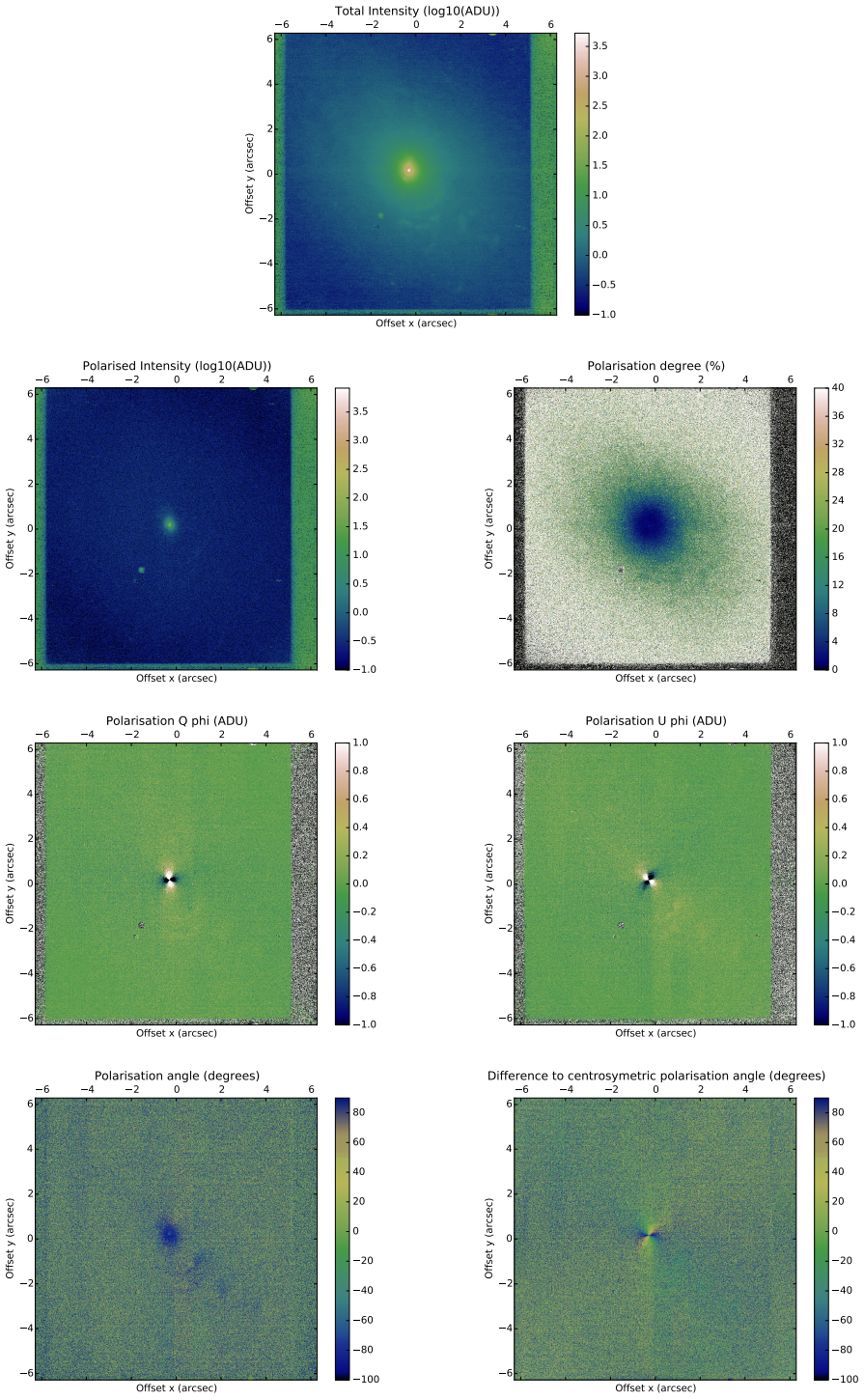

Figure 4.18 – NGC 1068 in `CntK2` NB. **1st row** image shows the total intensity recorded (in $\log_{10}$(ADU)); **2nd row**: left shows the polarised intensity (in ADU) and right the degree of polarisation (in %); **3rd row**: left shows the Q_ϕ map and right the U_ϕ map (both in ADU); **4th row**: right shows the polarisation position angle (in °) and right the difference angle to centro-symmetric (in °).

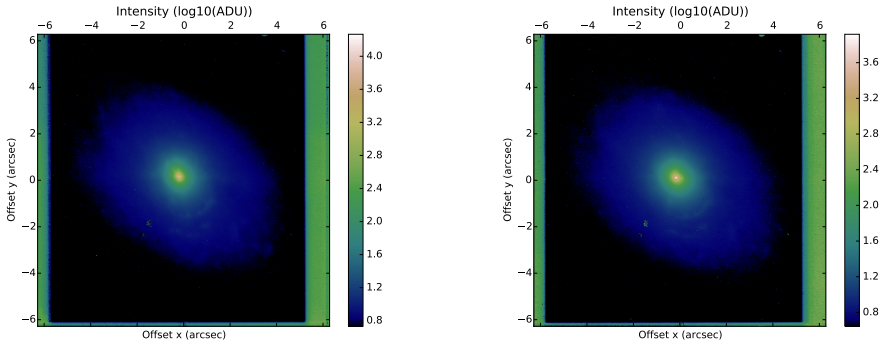

Figure 4.19 – NGC 1068 in NB `H2` and `CntK1`, classical imaging. Total intensity recorded (in $\log_{10}$(ADU)) are shown for `H2` band and for `CntK1` band respectively.

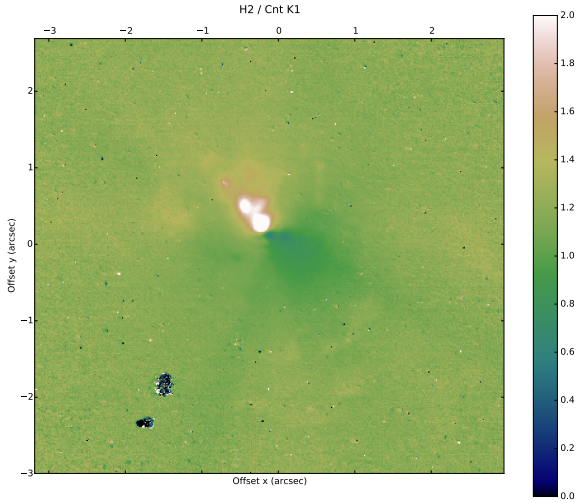

Figure 4.20 – NGC 1068 map of NB `H2` over `CntK1`.

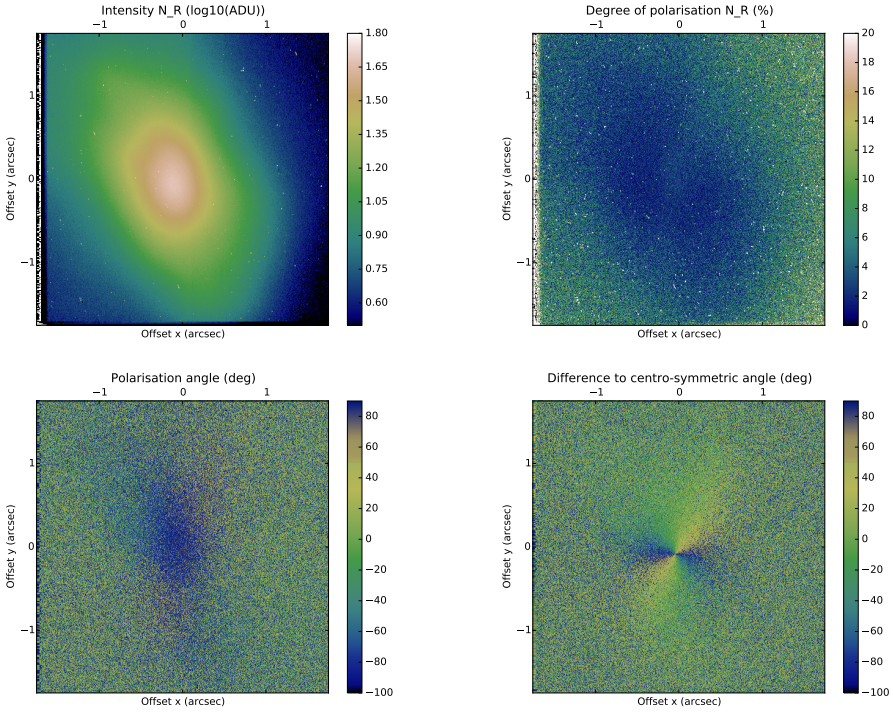

Figure 4.21 – NGC 1068 in R NB. Top left image shows the total intensity recorded (in $\log_{10}$(ADU)), top right shows the degree of polarisation (in %), bottom left shows the polarisation position angle (in °) and bottom right the difference angle to centro-symmetric (in °).

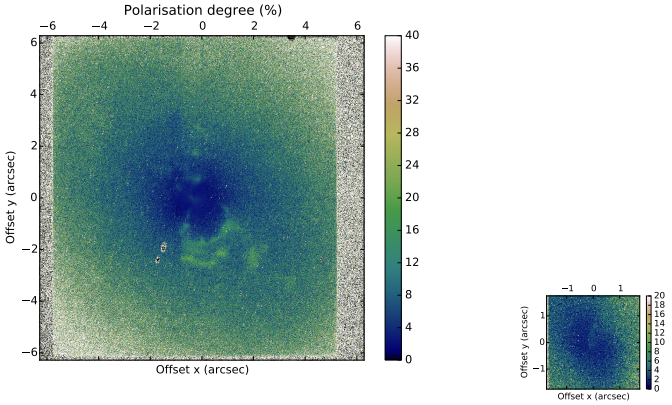

Figure 4.22 – Degree of polarisation (in %) in NGC 1068. The left panel shows image in `CntK1` with IRDIS and the right panel displays the image in R NB by ZIMPOL, corresponding to the centre of the FOV of IRDIS.

Chapter 5

MontAGN

Contents

Because of the difficulty to interpret polarimetric data, radiative transfer codes are essential tools. Several codes have been developed since computational power allowed to envisage such simulations, however as far as we know, there is no radiative transfer code that is able to fulfil the needs of all wavelength ranges. In order to analyse the polarimetric observations presented in Chapter 4, we needed to conduct simulations to assess our interpretations and improve them. For the prospect of this thesis, centred on AGNs observation at high angular resolution in the NIR, we focused on radiative transfer from IR to visible, including the proper treatment of polarisation.

Few codes corresponded at least partly to these criteria at the time we were looking to extend the study in this direction. We identified: RADMC-3D (Dullemond et al. 2012), STOKES (Goosmann & Gaskell 2007; Marin et al. 2012, 2015), SKIRT (Stalevski et al. 2012), MCFost (Pinte et al. 2006) and Hyperion (Robitaille 2011). While RADMC-3D, STOKES, MCFost and Hyperion are available to the community, this was not the case of SKIRT when we started this study (early 2015). Furthermore, RADMC-3D did not include fully usable polarisation at this time. We conducted some short tests on MCFost and Hyperion but it appeared that we needed to spend some time to learn how the codes were working in detail to be able to build the precise cases we would be investigating on.

For our purpose we needed a code able to simulate polarisation in the NIR, especially in the H and K bands, therefore between 1.6 and 2.2 μm and STOKES is only for use under 1.0 μm. However, we have had the opportunity to work in collaboration with the group Hautes Énergies of Observatoire Astronomique de Strasbourg that developed STOKES code and this collaboration allowed to improve the interpretation of the data. Their help was also beneficial on the simulation work where their experience and the common tests we defined allowed to correct bugs and improve several aspects of our simulations.

Because of our particular requirements, we decided to carry on the development of our own simulation code optimised for AGNs observations in the infrared. MontAGN has been developed in the Laboratoire d' Etudes Spatiales et d'Instrumentation en Astrophysique (LESIA), first by Jan Orkisz during an internship from September 2014 to February 2015. Its development started before we obtain our first polarimetric observations (Chapter 4) and its aim was to interpret AGNs HAR observations, however, it was initially without taking into account polarisation. We decided to continue to develop this code and extend it to polarimetry with the goal to make it public, a good way to improve the reliability of results through cross use of codes. This would also allow us to assess whether our assumptions on double scattering with a proper torus geometry were valid. It required an incompressible amount of time to built this code, probably more than getting use to one of the other codes, but with a fully controlled code and with very specific options.

5.1 Overview

MontAGN (acronym for "Monte Carlo for Active Galactic Nuclei") is a radiative transfer simulation code, written entirely in Python 2.7. It uses the libraries Numpy and Matplotlib (Hunter 2007). Its first version only included simple scatterings and no polarisation. It has then been upgraded to its current version as a part of this thesis's work and is aimed to be on open source in a near future.

As a radiative transfer, MontAGN aims at following the evolution of photons, from their emission by one of the sources defined in the simulation to their exit from the volume of the simulation, where they are recorded. This code uses photons packets

instead of propagating single photons. This allows to choose between two propagation techniques, allowing simulations to be run on two modes:

— If re-emission is disabled, the energy of the packet is modified to take into account, at each event, the fraction of the initial packets that continue to propagate in the medium. Therefore at each encounter with a grain, the absorbed fraction of photons is deduced so that just the scattered photons propagate. Murakawa (2010) used the same techniques on Young Stellar Objects (YSO) simulations.

— If enabled, one can takes into account the absorption and re-emission by dust as well as temperature equilibrium adjustment at each absorption. The absorbed photon packet is re-emitted at another wavelength with the same energy but different number of photons to conserve the energy in the cell. The re-emission wavelength is not only dependant on the new cell temperature but also on the temperature difference between the old and the new temperature. By following these steps, we ensure to take into account that the previous re-emissions were not emitted with the final emission function, following the method of Bjorkman & Wood (2001). We therefore uses the differential spectrum between the two emissivities of cell before and after the absorption of the packet to emit the new photon packets at a proper wavelength (see section 5.5.2 and figure 5.6 extracted from the former article).

By disabling re-emission, every packet will propagate until it exits the medium. This disabling allows us to get much more statistics at the end of the simulation as every packet is taken into account [1]. But it also requires to have a significant number of packets in each pixel of final images as we may obtain in one pixel only packets with very few photons (because of several scatterings), a situation that may not be representative of the actual pixel polarisation. This point will be discussed in section 5.7

5.1.1 Pseudo-code

We will give here a general overview of the algorithm of MontAGN. All the non trivial steps will be detailed in the following sections.

General MontAGN algorithm:

— **MontAGN 01**

Read of input parameters and conversion into corresponding class objects:

1. Note that this is only true if the signal in the given wavelength is mainly originating from the centre (hottest dust or CE), it is the opposite when looking at wavelength where emission come mostly from direct dust re-emission (typically in the MIR), see section 5.5.2

General important parameters given as keyword.
Parallelisation if asked.

— **MontAGN 02**
Read of the parameters for dust structures geometry:
Given as keyword, asked or from parameter file.
Dust densities, grains properties and structures associated. Available structures are described in section 5.1.2.

— **MontAGN 03**
Creation of the 3D grid and filling with dust densities:
Compute the density of each grain type for each cell.
Temperature initialisation.

— **MontAGN 04**
Compute of tables of all propagation elements:
Mueller Matrices, albedo, Q_{abs}, Q_{ext}, phase functions,
for each grain type, and different wavelength/grain radius.

— **MontAGN 05**
Start of the simulation:

— **MontAGN 06**
Random selection of one source:
Based on relative luminosity.

— **MontAGN 07**
Determination of the photons wavelength and initial directions of propagation and of polarisation:
Wavelength randomly determined from the source's SED.
Stokes vector initialised.
$\vec{p}$ and $\vec{u}$ computed, in general randomly.
See section 3.2.3 for illustration of $\vec{p}$ and $\vec{u}$.

— **MontAGN 08**
Propagation of the packet until reaching a non empty cell:
Determination of the cell density.
If null, direct determination of the next cell, back to the beginning of MontAGN 08.
If radius smaller than sublimation radius, the cell is considered empty.

— **MontAGN 09**
Draw of a τ that the packet will be able to penetrate:
Computed by inversion from optical depth penetration definition

$P(\tau_x > \tau) = e^{-\tau}$

— **MontAGN 10**

Determination of the next event of the packet:
interaction if τ is too low to allow the packet to exit the cell
or exit from the cell (in that case, decrease of τ of the optical depth of the cell and go to MontAGN 18).

— **MontAGN 11**

Determination of the properties of the encountered grain/electron:
size and therefore albedo, Q_{abs} and Q_{ext}.

— **MontAGN 12**

Case 1 (no re-emission):
decrease of the energy of the packet according to the albedo (and go to MontAGN 16).

Case 2 (re-emission):
determination whether the packet is absorbed from albedo.
If no go to MontAGN 16.

— **MontAGN 13**

Determination of the new temperature of the cell:
Determined from the previous one by balancing incoming and emitted energy.

— **MontAGN 14**

If the new temperature is above the Sublimation temperature of a type of grain:
update of the sublimation radius of this type of grains.

— **MontAGN 15**

Determination of the new wavelength and direction of propagation of the packet:
Directions determined randomly.
Wavelength determined from the cell temperature
and from the difference between new and old temperatures if updated.
Go to MontAGN 18.

— **MontAGN 16**

Determination of the angles of scattering and of the new directions of propagation and polarisation:
From grain properties and wavelength, determination of α, S_1 and S_2.
Determination of β.

Compute of the new vectors $\vec{p}$ and $\vec{u}$
(see figure 3.5).

— **MontAGN 17**
Constructs of the matrices and applies them to the packets Stokes vector:
From the angles, S_1 and S_2, construction of Mueller matrix
and of the rotation matrix (as described in section 3.2.4).
Application to Stokes vector of the packet.

— **MontAGN 18**
Determines if the packet exits:
if the photon is still in the simulation box, go back to MontAGN 10.

— **MontAGN 19**
Computes the packet properties in the observer's frame:
From $\vec{p}$ and $\vec{u}$, determination of the orientation of the polarisation frame
and correction of Stokes parameters using a rotation matrix.

— **MontAGN 20**
Records the packet's properties:
Written in the specified files.

— **MontAGN 21**
Is there other packets to launch ?
If yes go back to MontAGN 06.

— **MontAGN 22**
End of simulation.

— **MontAGN 23**
Computes the displays if asked.

5.1.2 Options Available

MontAGN is usable with many options. This section contains a short description of options available for simulations.

— **Thermal re-emission:** The main option is the enabling or disabling of the re-emission by dust. When disabled, all packets continue to propagate until they exit the medium or they reach the scattering limit. If enabled, packets when absorbed will be re-emitted to another wavelength, with an update of the temperature of the cell. The final model will contain the new adjusted temperature of the grid.

— **Pre-existing model:** It is possible to use already existing models by giving them, as a `model` class object, containing the principal simulation parameters.

— **Force the wavelength:** If the goal of the simulation is to obtain monochromatic images of a source, it is more efficient to emit only the observed wavelength. It is possible to specify it to MontAGN. Note that this should not be used without good reasons together with re-emission mode because the temperature computed might be affected [2]. Also note that even in no-re-emission mode, the final map will only show light coming originally from the sources and not from the dust. This should not be used either in MIR or larger wavelength.

— **Grain properties:** Dust grain have all a default distribution function. All grains are considered as spherical dielectric, with a Mathis, Rumpl and Nordsieck (MRN, see Mathis et al. 1977) distribution, ranging from 0.005 to 0.25 μm with a power law of -3.5. All these parameters are tunable using different keywords, for each type of dust. Up to now, silicate and graphite grains are available, with a distinction between graphite parallel and perpendicular. Note that electrons are also available, using the same parameters despite not being dust.

— **Parallelisation:** As it is based on a repetitive Monte-Carlo process, this radiative transfer code is easy to parallelise. It is possible with MontAGN to specify how many processes should be launched for the simulation. Note that currently this mode is only supported for simulations without dust re-emission.

— **Maximum number of scatterings:** In the case without re-emission, the only way to consider that a packet has finished propagating is by an exit of this packet. However, in the case of high optical depth, this could happen after many scatterings, leading to really long simulations with low energy of the packet at the end. To avoid this configuration, we limit the number of scatterings a packets can undergo. After this number of interaction, the packet is no more considered and we switch to the next packet.

— **Structures available:** When filling the 3D grid with dust densities, some structures already implemented are available: radial and spherical power laws, clouds, shells, constant density cylinders and torus geometries.

A complete list of parameters and keywords, associated to these options or to other functionality is available on section 5.10.

2. the new temperature calculus involve the wavelength through Q_{abs}

5.2 Tools

MontAGN code contains many routines with very different functions. However, some of them have common points and some techniques are often used. Instead of being described in the corresponding sections, they will be introduced here.

5.2.1 Simulation of Random Variables

As a Monte-Carlo code, MontAGN is highly dependant on generation of random numbers. It uses a home-made seed generator created by Guillaume Schworer (`gen_seed`) to initialise the seed, using both the current time and the thread number. This initialisation is particularly critical in the case of parallelised uses of MontAGN, to ensure that every process has a different initial seed.

In order to generate random numbers, one has to know the cumulative distribution function, F of the corresponding random variable X. The cumulative distribution characterise any distribution of random variable by giving for any value x of the variable X the probability for X to be smaller than x:

$$F(x) = P(X \leqslant x). \tag{5.1}$$

As a function indicating a probability and strictly increasing, it starts at 0, its minimum, and increases toward 1 (see figure 5.1 for an example).

The probability density, f, is also an useful function, defined as the derivative of the cumulative distribution. It represents the probability to obtain a random number in a certain range around the targeted value. The greater the probability density goes, the more chance we have to get this value of the random variable.

For example, an uniform distribution between 0 and 1 will have:

$$F(u) = 0 \text{ if } u \leqslant 0 \tag{5.2}$$
$$F(u) = x \text{ if } 0 \leqslant u \leqslant 1 \tag{5.3}$$
$$F(u) = 1 \text{ if } u \geqslant 1, \tag{5.4}$$

$$f(u) = 0 \text{ if } u \leqslant 0 \tag{5.5}$$
$$f(u) = 1 \text{ if } 0 \leqslant u \leqslant 1 \tag{5.6}$$
$$f(u) = 0 \text{ if } u \geqslant 1. \tag{5.7}$$

In order to get a value of a random variable, one simple method is to inverse its cumulative distribution function. If F is the cumulative distribution function of a random variable X, then $F(X)$ is a random variable following a uniform distribution U. We can write:

$$U = F(X) \tag{5.8}$$

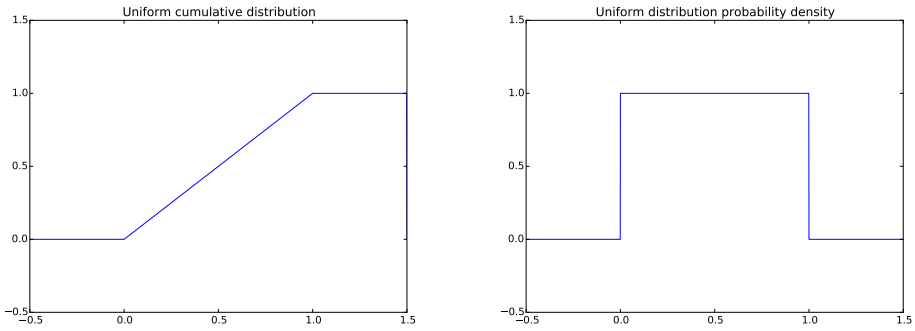

Figure 5.1 – Cumulative distribution (left) and probability density (right) in the case of uniform distribution between 0 and 1.

and therefore:

$$X = F^{(-1)}(U). \tag{5.9}$$

From an uniform distribution random variable, we can obtain a random variable following any distribution as long as its cumulative distribution function can be inverted. This should be achievable in the sense that cumulative functions are strictly monotonic, however there is not always analytic simple expression for this inverse function.

Numerically, an uniform distribution is the basis of the random number generator and we will therefore use this method to simulate some of the distributions. For non-easy invertible distribution, we will prefer the rejection method of von Neumann.

5.2.2 Von Neumann's Rejection Method

This method, first described in von Neumann (1951), consists in finding an envelope g to the function we would like to use as a random generator, f, in the cases where f could not be easily inverted. The envelope must be strictly positive and greater than the function, but the closer it is to the function, the more efficient the method is. The envelope needs to be a simple function so it can be used as a random number generator instead of using the initial function. We have:

$$\forall x,\ g(x) \neq 0,\ \frac{f(x)}{g(x)} \leqslant M. \tag{5.10}$$

From the envelope g, we get a value y of the random variable Y (the random variable associated to g, for example using an inversion method as described on the previous section). Once y obtained, we evaluate for this particular value the difference between the function and the envelope:

$$\frac{1}{M}\frac{f(y)}{g(y)}. \tag{5.11}$$

We then make a test to verify whether the value is accepted or not: we take a number u randomly between 0 and 1 (uniform distribution U), if u is smaller than the ratio function/envelope on the selected abscissa, the value is accepted, of not, it is rejected and we need to take a new random number from the envelope:

$$\text{If } u \leqslant \frac{1}{M}\frac{f(y)}{g(y)}, \text{ then } x = y. \tag{5.12}$$

This is illustrated on figure 5.2.

Von Neumann method ensure to respect the probability density of the function, and only requires to know both the envelope and the function, and to know the inverse of the cumulative distribution of the envelope. Its efficiency, defined as the ratio of the accepted values to the tested ones, is directly related to the matching between the envelope and the function, determined from their relative integral. For example on the case illustrated by figure 5.2, the efficiency would be about 50 %.

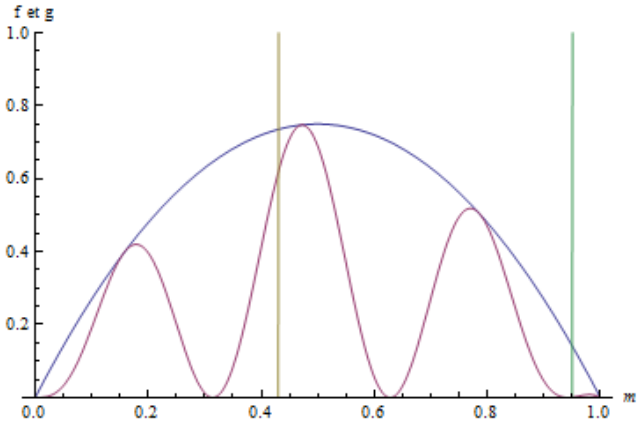

Figure 5.2 – Illustration of the method of Von Neumann. Purple curve is the one we want to use as a probability function, the blue one is the envelope. The yellow line indicate a value of parameter where the envelope is efficient while the green one is placed on a particularly inefficient region of the envelope.

5.3 Initialisation

The first important step in the simulation is the initialisation. It consists in all operations that needed to be executed before entering the main loop of the code, that will launch the photon packets. The largest part consist in organising the different variables into the good class objects for the code to be the most efficient possible. We can notice two critical phases, the first one is the construction of the 3D grid sampling the dust densities. The second one is the pre-computing of all the parameters required for photon propagation. We could compute all this values at each propagation but

this will take a long time. The solution used in MontAGN to have the lowest possible approximation is to compute before the simulation tables of these values for each parameters. These tables can then be interpolated when needed, an operation much faster than processing all the calculi.

5.3.1 Density Grid

MontAGN uses dust particles densities to fill its grid. The grid is composed of cubic cells and a vector in each cell has as many values as the number of dust species plus two. These additional values are the temperature of the cell and the number of packets absorbed within the cell. Currently, the grid has six values stored in each cell for the four available species densities (in particles per cubic metre) corresponding to silicates, graphites ortho and para and Electrons. Despite electrons not being dust, we process them in the same way as explained in section 3.2.2. This number of species can easily be increased if required.

The filling with the proper dust densities is achieved thanks to densities functions, regularly sampled. Several functions are pre-existent, from constant densities to complex power law combinations (see the list in section 5.1.2). It is possible to combine two or more function to construct some complex structures, which is an important advantage of this method. The counterpart is that one needs a good sampling rate to have a fair representation of the dust structures. This often requires to use a grid with a lot of cells, which takes space on the Computer Processor Unit (CPU) memory.

One other geometrical aspect is the concept of sublimation radii in MontAGN. In order to stand for the ionisation sphere surrounding the high luminosity objects, MontAGN allows to set sublimation radii for each dust specie. These radii are adjusted at the occasion of temperature adjustment to match the temperature increase. This guarantees a good physical representation of the path that photons can follow without interaction because of sublimation. In term of algorithm, any cell located before the sublimation radius of a certain dust specie will be considered as empty (if the radius actually crosses the cell, only the inner part will be the object of this procedure).

The last geometrical feature is the ionisation cone. We can define such cones in case of objects with polar jets. In these regions, all packets will propagate directly to the boundary of the cone. This allows to have faster simulations. However in the majority of our simulations, we prefer to use instead a cone constituted of electrons, more physically coherent.

5.3.2 Pre-computed Elements

Before the simulation starts, tables of albedo, phase function, Mueller matrix, absorption and extinction coefficients are generated for a range of grain size and wavelength thanks to Mie theory. For that purpose, we use `bh_mie` modulus initially written by Bohren & Huffman (1983) combined with grain data from Draine (1985).

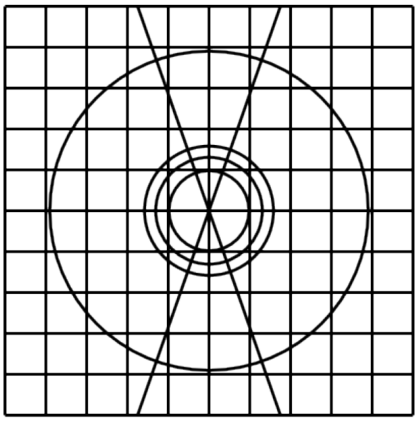

Figure 5.3 – Illustration of the grid used in MontAGN code. It displays the different cubic cells constituting the grid, the different sublimation radii of the dust species and the ionisation cone.

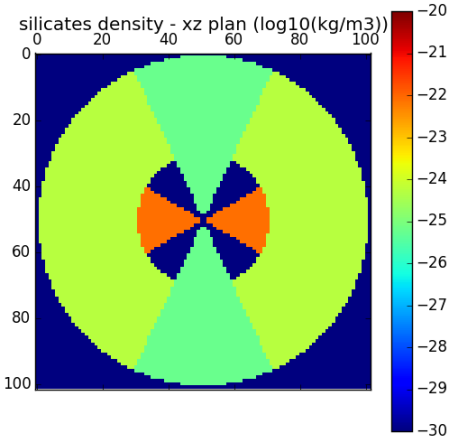

Figure 5.4 – Example of densities grid used in MontAGN simulations. Slice of sampled densities in the cells corresponding to $y = 0$ in a simple AGN model with constant densities in three different structures.

To have a detailed description of the role of each of these elements, see section 3.2.1. These tables then just need to be interpolated to get the precise value for given values of grain size and wavelength during the simulation. This interpolation makes the execution of the code faster and with a fair approximation.

5.4 Emission

At emission, the source is selected according to the respective luminosity of each source. A tag in the packet parameters allows if needed to distinguish which source it comes from. Note that even with a high temperature in the grid, a dust cell will never be considered by the code as a source because its emission is fully integrated on the re-emission process described in section 5.5.2. The inclusion of these dust regions as sources in the other mode of the code, without re-emission, is an interesting point for future implementations.

For photon propagation, MontAGN uses the Stokes vectors formalism to represent polarisation of photons packets:

$$S = \begin{bmatrix} I \\ Q \\ U \\ V \end{bmatrix}, \tag{5.13}$$

with I the intensity, Q and U the two components of linear polarisation and V the circular polarisation (see for more details section 3.2.1). We normalise in MontAGN the Stokes vector ($I = 1$) to simplify the Stokes vector propagation.

The packet's wavelength is determined using the source's spectral energy distribution, initially not polarised (i.e. with Stokes vector of the photon set to [1,0,0,0]). The packet starts to propagate in a direction $\vec{p}$ with a polarisation reference direction $\vec{u}$ both randomly picked. It would technically be possible to change these parameters but it is not yet available as an input parameters. However we can manually impose a particular polarisation at emission, or a particular direction propagation function. This has been achieved in MontAGN for some tests, presented in section 5.8 and should be soon implemented.

5.5 Photons Propagation

Packets propagation is mainly constituted of two distances computing. The algorithm estimates the next crossing of a wall of the current cell (d_{wall}) and the distance that the packet will be able to travel without interaction (d_τ) for a given optical depth τ at the packet's wavelength λ.

In these chapters, we will describe dust and electrons structures thanks to their optical depth. Note that this definition is close but different from extinction A_λ, which is formally defined as:

$$A_\lambda = -2.5 \log_{10}(F_{obs,\lambda}/F_{no\ ext,\lambda}). \tag{5.14}$$

There is therefore a factor $2.5/\log(10)$ between optical depth and extinction:

$$A_\lambda = \frac{2.5}{\log(10)}\ \tau_\lambda \approx 1.0857\ \tau_\lambda. \tag{5.15}$$

What is important for radiative transfer of photons through dust clouds is not the distance travelled but the optical depth of the medium crossed. It is a way to represent the distance in term of "probability of interaction unit". We can compute optical depth τ from a distance d by integrations over the photon path of the number density of particles n times their attenuation cross section σ_{at}:

$$\tau = \int_0^d \sigma_{at}\ n\ \mathrm{d}l. \tag{5.16}$$

In cases of dust MRN distributions (with coefficient α), optical depth can be expressed in function of the extinction coefficient Q_{ext}, the grain geometrical cross-section σ_{cc} and the radius a of a grain as:

$$\tau = \int_0^d \frac{\int_{a_{min}}^{a_{max}} n\ Q_{ext}\ \sigma_{cc}\ a^\alpha\ \mathrm{d}a}{\int_{a_{min}}^{a_{max}} a^\alpha\ \mathrm{d}a}\ \mathrm{d}l = \int_0^d \frac{\int_{a_{min}}^{a_{max}} n\ Q_{ext}\ \pi\ a^2\ a^\alpha\ \mathrm{d}a}{\int_{a_{min}}^{a_{max}} a^\alpha\ \mathrm{d}a}\ \mathrm{d}l. \tag{5.17}$$

As optical depth is directly linked to interaction probability, we will first determine an optical depth τ that the packet will be allowed to travel through. This value is computed at the first encounter of the packet with a non empty cell and will decrease with the travelled distance as long as $\tau > 0$. We derive τ from a random number, U, uniformly distributed between 0 and 1 as follows:

$$\tau = -\log(U). \tag{5.18}$$

Because we use constant dust properties in a cell, the integration of optical depth from equation 5.17 over the packet path is trivial and the corresponding distance can be computed in each crossed cell with number densities n_i of the dust species i using:

$$d_\tau(\lambda) = \tau\ \Sigma_i\ \frac{\int_{a_{min,i}}^{a_{max,i}} a_i^\alpha\ \mathrm{d}a_i}{\int_{a_{min,i}}^{a_{max,i}} n_i\ Q_{ext,i}\ \pi\ a_i^2\ a_i^\alpha\ \mathrm{d}a_i}. \tag{5.19}$$

If the packet is located at a radius smaller than the sublimation radius, or if it is in the funnel, the cells will be considered empty as explained in section 5.3.1.

If the distance to the cell border is the shortest, the packet is moved to this location and the value of τ is decreased according to the distance and the densities of the different dust species:

$$\tau = \tau - d_{wall}\ \Sigma_i\ \frac{\int_{a_{min,i}}^{a_{max,i}} n_i\ Q_{ext,i}\ \pi\ a_i^2\ a_i^\alpha\ \mathrm{d}a_i}{\int_{a_{min,i}}^{a_{max,i}} a_i^\alpha\ \mathrm{d}a_i}. \tag{5.20}$$

If d_τ is the shortest, interaction happens with a grain of the cell. Note that Robitaille (2011) uses the same strategy with the Hyperion code. The grain type is first determined randomly with a probability relative to the value of $n_i \int Q_{ext,i}(\lambda, a_i) a_i^2 \pi \mathrm{d}a_i$. The radius of the grain is obtained using the dust grain size function and from this radius and the wavelength, the albedo is determined by interpolation. Two cases need to be differentiated here, whether the thermal re-emission is enabled or not.

5.5.1 Interaction: Scattering without Re-emission

Without re-emission, we always have a scattering. The phase functions of the scattering, the angles themselves and the Mueller matrix are determined by interpolation from the grain radius and wavelength as described in section 3.2.3. This way of proceeding is a slow solution compared for instance to the use of a direct averaged function on the grain size distribution. However it is more realistic and despite this disadvantage, the simulations still have an acceptable duration for our studies.

In order to obtain the scattering angles from the phase functions, we need to inverse them to be able to generate random numbers. This is fairly easy in the case of Rayleigh scattering, therefore for $x \ll 1$. However this is not possible in other cases and we will use for this purpose the rejection method of von Neumann, described in section 5.2.2. Figure 5.5 gives examples of Mie phase functions and there envelopes used in MontAGN. The normalised phase function is the ratio $\frac{\text{phase function}}{\text{envelope}}$ and corresponds to the test of acceptance of the random variable. The closer this function is to 1, the more efficient the method is.

Envelopes need to be adapted to the phase functions. As these later are highly dependant on the form factor, we need to modify our envelope accordingly. For the low values of the form factor, the phase function is really close to the Rayleigh phase function and we can therefore use this one as an envelope (with an efficiency close to 100 %). For intermediate form factors, we use a third degree polynomial, fitted to the phase function, becoming asymmetric with a higher probability of forward scattering. At high values of the form factor, we prefer a Henyey-Greenstein (H-G) function, a good representation of the main forward lobe of the phase function. Because of the difficulties to reproduce all the secondary lobes, the efficiency decrease for high form factors (see section 5.8).

Table 5.1 – Envelope phase functions used in MontAGN simulations

Envelope function	Form factor
Rayleigh phase function	$x < 0.1$
Polynomial degree 3	$0.1 < x < 2.5$
H-G function	$x > 2.5$

In order to update polarisation properties, we apply to the Stokes vector the Mueller matrix and the rotation matrix:

$$S_{final} = M \times R \times S_{init} \tag{5.21}$$

with M the Mueller matrix constructed from Mie theory and R the rotation matrix, both depending on the scattering angles. A complete description of these matrices, phase functions and Stokes formalism can be found in Chapter 3. We also obtain the new direction of propagation $\vec{p}$ as well as a new polarisation reference $\vec{u}$.

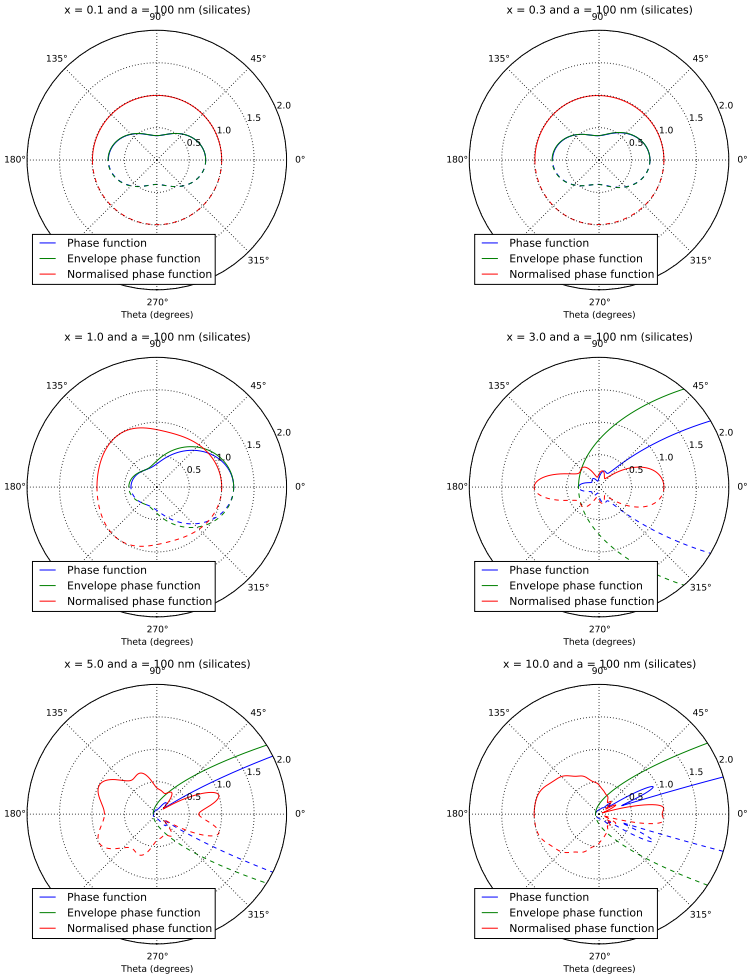

Figure 5.5 – Examples of α phase functions with their corresponding envelope functions, in the case of Mie scattering, for $x = [0.1, 0.3, 1.0, 3.0, 5.0, 10.0]$. The normalised phase function correspond to the ratio envelope over phase function.

We need to take into account that not all the photons of the packets have been scattered during this interaction. Because of the albedo, photons have a probability

$$P(abs) = 1 - \text{albedo} \tag{5.22}$$

to be absorbed. The fraction of scattered photon will therefore be proportional to the albedo. The energy of the packet, also proportional to the number of photons in the packet will be weighted by the albedo:

$$E_{exit} = \text{albedo} \times E_{incoming}. \tag{5.23}$$

A new optical depth is randomly determined after each scattering as explained before and the propagation continue.

5.5.2 Interaction: Temperature Update and Re-emission

If re-emission is enabled, we first need to verify whether the packet is absorbed or not. For that purpose, we take a random number U uniformly between 0 and 1 and if $U >$ albedo, the packet is absorbed, else it is scattered. If scattered, the process is exactly the same as described in the previous section 5.5.1 but without the albedo weighting of the energy (which will therefore always have the same constant value). If absorbed, the packet will contribute to the cell temperature as following.

This temperature update algorithm is described for instance by Lucy (1999) and Bjorkman & Wood (2001). It consists in balancing the received and emitted energy of each cell, assuming therefore a Local Thermodynamic Equilibrium (LTE). The incoming energy is simply for each cell (at the position (i,j,k)) the number of packets absorbed by the cell multiplied by the energy in each packet (a constant for every packets in this mode):

$$E_{in}^{i,j,k} = N^{i,j,k} \times E_{packet}. \tag{5.24}$$

$N^{i,j,k}$ is here the number of absorbed packets in the cell (i,j,k) and E_{packet} is the energy of the packets.

The emitted energy depends on the thermal emissivity of the dust, usually defined as:

$$j_\nu = \kappa_\nu \ \rho \ B_\nu(T) \ \mathrm{d}\lambda, \tag{5.25}$$

where $B_\nu(T)$ is the Planck emission of a black body at temperature T per unit of frequency, κ_ν the dust absorptive opacity and ρ the density of dust.

We will use here an alternative definition, replacing κ_ν by its value in term of Q_{abs} and geometrical cross-section σ_{cc}: $\kappa_\nu = Q_{abs} \ \sigma_{cc} \ n \ / \ \rho$, with n the number density. We get as a function of wavelength:

$$j_\lambda = Q_{abs}(\lambda) \ \sigma_{cc} \ n \ B_\lambda(T) \ \mathrm{d}\lambda, \tag{5.26}$$

with $B_\lambda(T)$ the Planck emission of a black body at temperature T per unit of wavelength. The emitted energy is, for a cell of volume $\mathrm{d}V^{i,j,k}$ during a time Δt:

$$E_{em}^{i,j,k} = 4 \ \pi \ \Delta t \int \mathrm{d}V^{i,j,k} \int Q_{abs}(\lambda) \ \sigma_{cc} \ n \ B_\lambda(T) \ \mathrm{d}\lambda. \tag{5.27}$$

Note that we can also write these two expressions in a different way as the energy of a packet can be expressed in function of the source luminosity L and the total number of packets emitted N_{tot} as:

$$E_{packet} = L \ \Delta t \ / \ N_{tot}. \tag{5.28}$$

Because we are using constant densities and temperature in each cell, the first integral become a simple multiplication by the volume of the cell. The integral over λ can then be numerically integrated and we only need to solve $E_{in}^{i,j,k} - E_{em}^{i,j,k} = 0$:

$$N^{i,j,k}\ E_{packet} - 4\ \pi\ V^{i,j,k}\ \sigma_{cc}\ n^{i,j,k}\ \Delta t \int Q_{abs}(\lambda)\ B_\lambda(T)\ \mathrm{d}\lambda = 0. \tag{5.29}$$

By solving numerically equation 5.29 on T, we get the new temperature T' of the cell after each packet absorption. Note that as absorption number $N^{i,j,k}$ is increasing, the Planck emission function will increase as well. This implies that the new temperature will always increase within a cell (Planck emission is strictly monotonically increasing function with T).

Now that we have computed the new temperature of the cell, we need to correct the emission function of the cell. Of course we will adjust the dust emissivity to the new temperature:

$$j'_\nu = \kappa_\nu\ B_\nu(T'). \tag{5.30}$$

However, all the previous packets have been emitted with different successive emissivities. If we want a correct SED at the end of the simulation, we also need to correct for these offsets in the wavelength selection of re-emitted packets. This can be done by selecting the new wavelength based on the difference of emissivities and not on the new emissivity. We will therefore use for emissivity:

$$\Delta j_\nu = j'_\nu - j_\nu = \kappa_\nu\ (B_\nu(T') - B_\nu(T)). \tag{5.31}$$

Remember that as the temperature is increasing, this difference will always be positive. This corresponds to the shadowed region of figure 5.6. We can now continue our propagation with the new wavelength of the packet determined from this emissivity difference. The direction of propagation and polarisation reference is reset to the initial unpolarised emission and a new optical depth is determined as previously. We also indicate with a flag on the packet that it has undergone a re-emission.

5.6 Output and Recording

When the photon packet exits the simulation box, it is recorded with most of its parameters, whose list is given in table 5.2. Its final direction of propagation is registered in the form of two angles, inclination θ (ranging from 0 to 180°) and azimuthal ϕ (ranging from 0 to 360°) as shown in figure 5.7. Furthermore, we compute from the orientation vectors $\vec{p}$ and $\vec{u}$ the angle to the polarisation reference direction from the Q-U orientation in the frame of the packet:

$$\phi_{QU} = \arctan \frac{u_z}{u_y p_x - u_x p_y}, \tag{5.32}$$

with the u_i and p_i being defined as (with i in [x,y,z]):

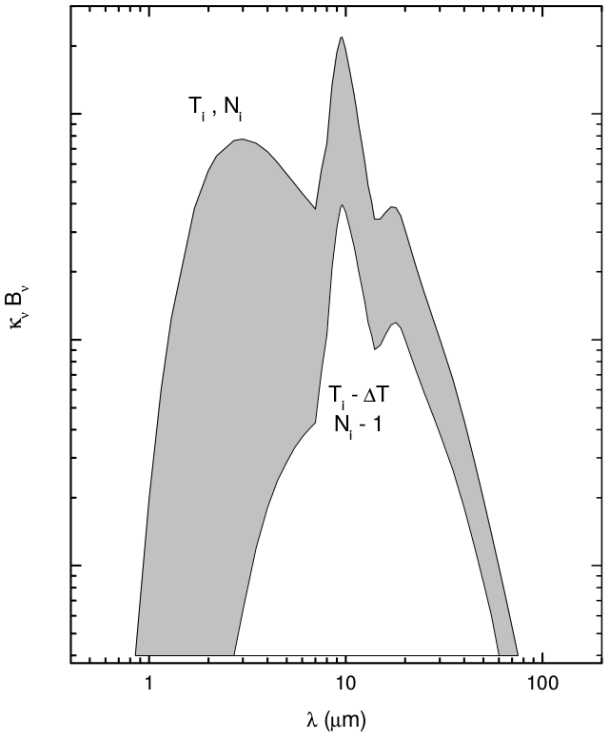

Figure 5.6 – Temperature correction frequency distribution. Shown are the dust emissivities, $j_\nu = \kappa_\nu B_\nu(T)$, prior to and after the absorption of a single photon packet. The spectrum of the previously emitted packets is given by the emissivity at the old cell temperature (bottom curve). To correct the spectrum from the old temperature to the new temperature (upper curve), the photon packet should be re-emitted using the difference spectrum (shaded area), from Bjorkman & Wood (2001).

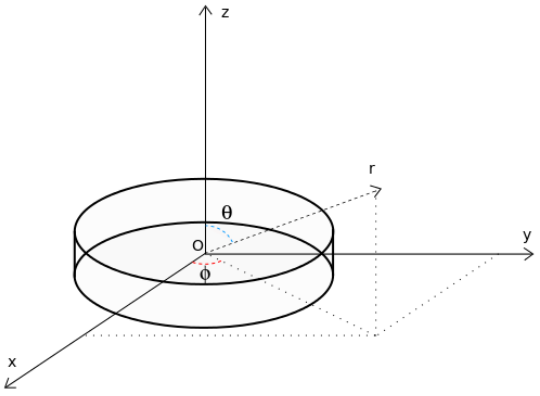

Figure 5.7 – Illustration of the reference angles used in MontAGN code.

$$u_i = \vec{u}.\vec{e_i}. \tag{5.33}$$

We will use this angle to express the Stokes parameters Q and U in the frame of the observer with the proper orientation. This, once again, is achieved thanks to a rotation matrix comparable to those of section 3.2.4:

$$S_{final} = \begin{pmatrix} 1 & 0 & 0 & 0 \\ 0 & \cos(2\phi_{QU}) & -\sin(2\phi_{QU}) & 0 \\ 0 & \sin(2\phi_{QU}) & \cos(2\phi_{QU}) & 0 \\ 0 & 0 & 0 & 1 \end{pmatrix} S_{output}. \tag{5.34}$$

All the packets parameters are currently written in few data files. This allows to limit the used CPU memory while simulations are running. Until now, parameters are recorded in 19 files, each centred on a value of a particular inclination observation angle between 0 and 180°. If a packet has an exit inclination within a range of ±5° to the file's central value, it will be recorded in this file.

Table 5.2 – Output parameters recorded in MontAGN simulations

Output parameter	Symbol	unit
Photon number	i	
Out inclination angle	θ	°
Out azimuthal angle	ϕ	°
Normalised Stokes U parameter	U	%
Normalised Stokes Q parameter	Q	%
Normalised Stokes V parameter	V	%
Out polarisation orientation angle	ϕ_{QU}	°
Last interaction position x	x	pc
Last interaction position y	y	pc
Last interaction position z	z	pc
Number of interaction	n_{inter}	
Number of re-emission	n_{reem}	
Wavelength	λ	m
Label of the packet	label	
Energy of the packet	E	J
Emission time of the packet	δt	s
Total emission time (only if first packet)	Δt	s

From these data, we can extract SED or maps with different selection criteria. The two main routines allowing these will be described in section 5.10. Any polarisation measurement goes through combining all the photons packets into Q and U parameters or maps. All selected packets are summed, pondered by their energy (this point will be detailed in section 5.6.1) and can be combined in polarisation angle and degree maps as presented in section 3.3.2 using:

$$P_{lin} = \frac{\sqrt{U^2 + Q^2}}{I} \tag{5.35}$$

$$P_{circ} = \frac{V}{I} \tag{5.36}$$

$$\theta = \frac{1}{2}\ \mathrm{atan2}(U, Q). \tag{5.37}$$

It is possible to apply any selection on the displayed packets. Altitude and azimuthal angles as well as wavelength are the most used selections, but we can also select only packets at a given number of scatterings, or only the re-emitted ones. In case of maps and once the packets have been selected, the packets' last position of interaction are used to compute their position in the images, according to the observer's inclination angle.

If the model is axi-symmetric, MontAGN allows to increase the signal obtained from simulations by two ways. First, in case of cylindrical symmetries, all the photons exiting the simulation with the same inclination angle θ but different azimuthal angle ϕ can be considered as equivalent. We can therefore extract photons (within a θ range if selected) for all the azimuthal angles ϕ and then apply a rotation around the vertical axis on the position of last interaction of the packet.

If the model is also symmetric according to the equatorial plan, photons recorded above the equatorial plan are equivalent to those below the plan. At the end we can add photons of the four quadrant (up-left, up-right, bottom-left and bottom-right) as long as we correctly change their polarisation properties according to the symmetry. It is however mandatory to observe from an inclination angle of 90° to use this last method.

Note that it is possible to limit the number of absorptions a photons packet undergo in order to only keep the most energetic packets and have faster simulations. As this information is kept, it is also possible to get access to maps of averaged number of interactions undergone in a particular direction.

5.6.1 Summing Packets

As we record packets with different number of photons, we need to take these differences into account when creating the observed maps. The maps referred to as "averaged" (for example averaged number of scatterings) as well as Q and U maps includes a process correcting the relative fraction of photons in packets: all packets i of a given quantity are summed with a factor α_i proportional to the ratio of photons in the given packet, in every pixel. The averaged number of scatterings n will therefore be computed from the number of scatterings of each packet n_i as:

$$n = \frac{\Sigma^i \alpha_i \times n_i}{\Sigma^i \alpha_i}. \tag{5.38}$$

Because this factor is strictly proportional to the energy of the packet, we use directly the recorded energy in the packets to weight the summed quantities.

Note that this difference in photon number should not be considered when looking at different wavelengths. For a same energy in two packets at different wavelengths, the longer the wavelength is, the greater the number of photons should be. However as the number of emitted packets versus wavelength follows the source's SED, they are the ones that one should consider for establishing the final SED (in this case, the packets are equivalent to single photons).

5.7 Packets Significance

One major concern in the simulation strategy without re-emission is the conservation of the photons until they exit the simulation box whatever their number of interactions. We must verify to what extent the detected photons are relevant. As explained before, the energy of each packet, representing the number of photons in the packet, is decreased according to the albedo at each interaction. It is therefore common at the end to record packets of photons with energies 10^4 times lower than the initial energy. However, if a high energy packet reaches a pixel previously populated only with low energy ones, it will totally dominate the pixel so that Q and U values and the polarisation parameters will be essentially linked to this packet. Indeed, most of the photons in the pixel will belong to this packet.

As opposed to simulations including absorption, where all the recorded photons have the same probability, it is not any more the case in the case where re-emission is disabled. A pixel of an output image could have stacked many low energy packets before a high energy one, more representative of the actual polarisation, reach it. But it is also possible that no high power photon reaches this cell, in the course of the simulation leading to a wrong estimate since in the actual case the number of photons emitted by the source is enormous ($> 10^{56}$ s^{-1}) and several will escape after very few scatterings.

To analyse our results, we need first to be sure to disentangle between photons representative of the actual polarisation, and those who are not. Limiting the number of scattering is a good way to ensure that below a given limit on number of photons, packets will stop to be recorded. We also analysed maps of "effective numbers" of packets per pixel, as shown in figure 5.8. These maps are generated by dividing the energy received in each pixel by the highest energy of packets recorded in the pixel. If a single packet dominates the pixel's information, the effective number of packets in the pixel will be close to 1, indicating a non reliable pixel.

As the energy of packets is decreasing with the number of scatterings, regions of low number of scatterings are more likely to be reliable. All regions of single scattered photons, with the exception of the central pixels, are reliable as long as photons can not reach the pixel in this region directly without being scattered. These regions corresponds to the "North and South" regions of images in figure 5.9.

For the same reasons, all the regions with photons scattered twice are very likely to be representative, because only one-time scattered packets have higher energies. For example, the central belt region in figure 5.9 are very unlikely to receive singly

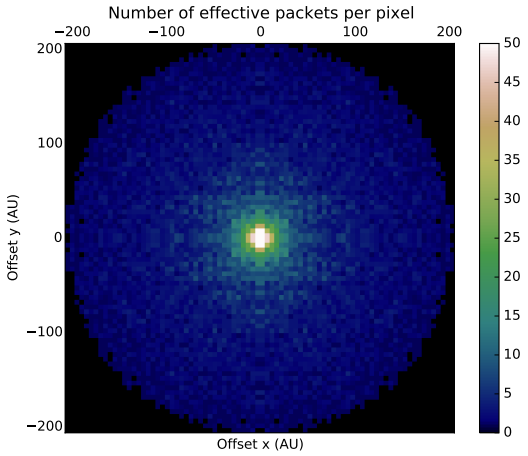

Figure 5.8 – Example of map of effective number of packets in the case of a star at the centre of a dust cocoon.

scattered photons because of the high optical depth of the torus (around 20 at this wavelength). Therefore despite having a fairly low number of effective packets, this region is also quite reliable in terms of intensity and polarisation.

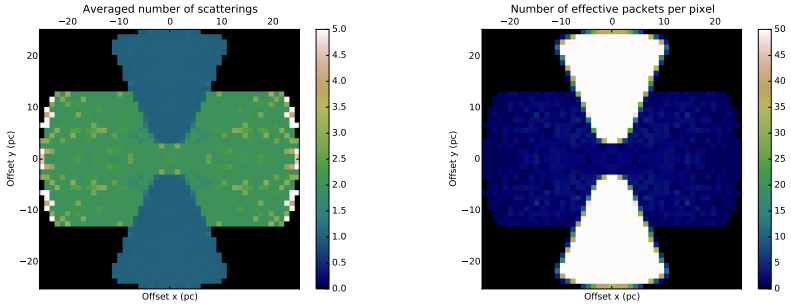

Figure 5.9 – Example of map of averaged number of scattering and the corresponding map of effective number of packets in the case of an AGN surrounded by a dust torus and with an ionisation cone.

5.8 Validity Tests

Before using the code to simulate high angular resolution images of AGN and interpreting the observations according to these simulations, we first conducted tests to verify all the different sub-parts of the code. All tests concerning the temperature update are still under investigation. We have not yet used these capabilities of the code to interpret any data, and we therefore concentrated ourselves on pure scattering/polarisation capacities directly involved in the NGC 1068 SPHERE data analysis

(Chapter 6).

5.8.1 Phase Function

We conducted some tests on the phase functions. We first displayed the averaged phase function of the MontAGN code by adding naively all the different scattering angles given by the scattering routine (on the classical MRN distribution of Silicates, with photons in the visible/NIR leading to form factor below 0.3). This distribution function has been weighted by a factor $\sin(\alpha)$ to correct for the solid angle effect, and is displayed on figure 5.10. We get as expected a function very close to the Rayleigh one.

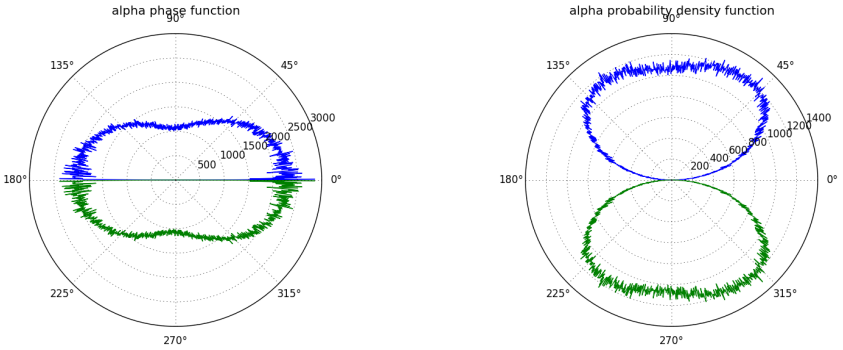

Figure 5.10 – Averaged phase (left) and probability density (right) functions as measured with MontAGN, in the case of Mie scattering on classical MRN distribution of Silicates (not normalised, 4×10^5 photons were sent).

We also measured the phase functions resulting of different form factors, as displayed in figure 5.11. Simulations were achieved through the launch of 10^5 packets for each form factor, with grain radius of 100 nm.

We finally measured the efficiency of the rejection method of von Neumann for a range of form factors using 10^5 packets, and compared them to the measurements of Didier Pelat on his simulation of Mie scattering using the same rejection method. These results correspond to the four middle columns of table 5.3 and have been obtained using water's dielectric characteristic and therefore slightly differs from MontAGN's silicates ones.

MontAGN stops to generate phase functions at form parameters larger than about 2 for grains of radius 10 nm, and at $x = 20$ for grains of 100 nm of radius, because of the wavelength's domain limitations. Table 5.3 shows good agreement until $x = 1$, while beyond the efficiencies diverge. This is likely to be due to the difference of dielectric constants, changing the phase functions and therefore the corresponding envelope efficiency.

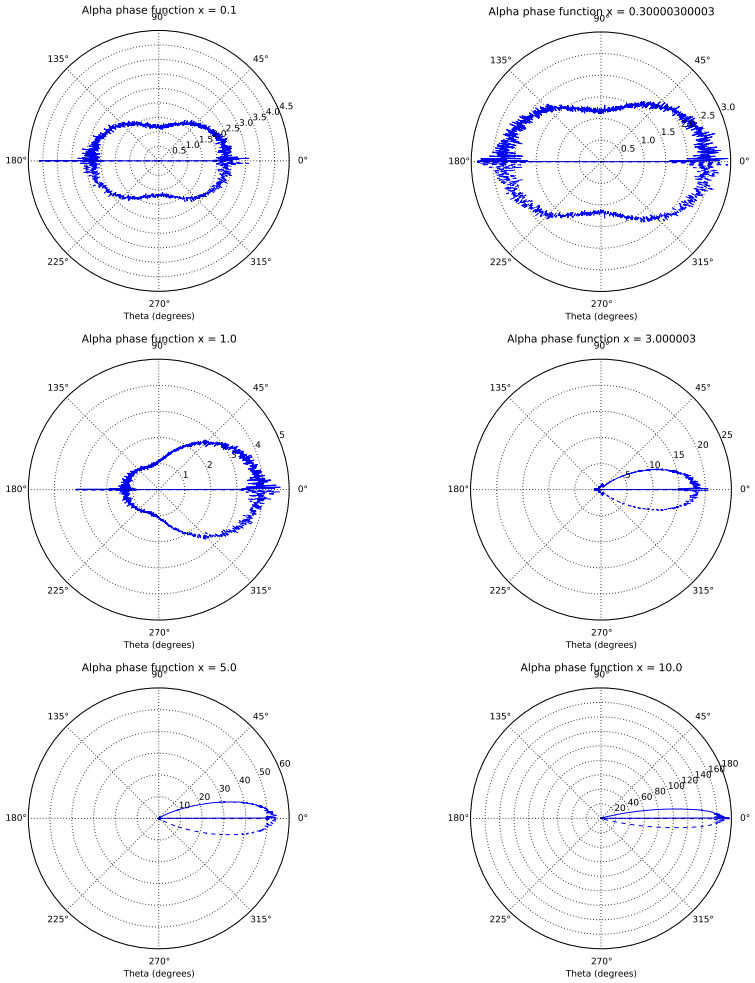

Figure 5.11 – Examples of α phase functions measured with MontAGN, in the case of Mie scattering, for $x = [0.1, 0.3, 1.0, 3.0, 5.0, 10.0]$ on Silicates (based on a grain size of 100 nm). 1×10^6 packets were launched.

5.8.2 Optical Depth

Because of the complexity of the multigrain framework in the estimation of the optical depth, we verify the good behaviour of each of the grain in term of optical depth separately and with the mixture. This later is composed of 25 % of silicates, 25 % of ortho graphites, 25 % of para graphites and 25 % of electrons. In order to conduct the tests, we use a cylinder, whose radius is set to 60 AU (Astronomical Unit). Its height is 20 AU and its density is computed to give particular values of optical depth at 1.6 μm according to this height using equation 5.19. Direction of propagation of photons were set to be initially in direction of the symmetrical axis of the cylinder and therefore to encounter the selected optical depth. It is therefore easy to predict the number of packets N_{out} that should exit without interaction from

Table 5.3 – Efficiency of the von Neumann rejection method applied to envelope phase functions used in MontAGN simulations

x	Rayleigh	Poly. n	n	H-G	MontAGN ($r = 100nm$)	MontAGN ($r = 10nm$)
0.01	**100 %**	100 %	3	66.67 %	99.99 %	99.99 %
0.03	**99.96 %**	99.99 %	3	66.67 %	99.95 %	99.94 %
0.1	**99.57 %**	99.93 %	3	66.67 %	99.93 %	99.92 %
0.3	96.13 %	**99.41 %**	3	66.70 %	99.38 %	99.41 %
1	66.88 %	**92.62 %**	3	71.23 %	89.79 %	88.94 %
2	27.20 %	**89.56 %**	5	72.72 %	51.59 %	50.75 %
3	14.19 %	56.40 %	7	**66.45 %**	39.27 %	-
4	8.56 %	44.04 %	8	**64.92 %**	66.23 %	-
10	2.51 %	13.13 %	9	**21.29 %**	53.06 %	-
30	<1 %	2.69 %	13	**10.86 %**	-	-
100	<1 %	<1 %	18	**5.22 %**	-	-
300	<1 %	<1 %	20	**2.09 %**	-	-
1000	<1 %	<1 %	24	**0.76 %**	-	-

$N_{tot} = 100,000$ packets launched:

$$N_{out} = N_{tot} \times P_{escape}(\tau) = N_{tot}\ e^{-\tau}. \tag{5.39}$$

Results are displayed in table 5.4.

Table 5.4 – Fraction of packets that escaped without interaction through a dust structure of optical depth τ with MontAGN.

τ	N_{out}/N_{tot}	N_{sil}/N_{tot}	N_{gra_o}/N_{tot}	N_{gra_p}/N_{tot}	N_{el}/N_{tot}	N_{mixt}/N_{tot}
0.1	0.90483	0.90590	0.90502	0.90468	0.90535	0.90465
0.2	0.81873	0.82012	0.81974	0.82040	0.82066	0.82045
0.5	0.60653	0.60695	0.60402	0.60964	0.60761	0.60443
1	0.36787	0.36943	0.36946	0.36931	0.36974	0.36682
2	0.13533	0.13594	0.13474	0.13638	0.13608	0.13494
5	0.00673	0.00672	0.00664	0.00725	0.00628	0.00639

Table 5.4 indicate a good correlation between the measured and theoretical escaped fraction of packets, with an error typically below 1 %.

5.8.3 Temperature

As this thesis work does not include studies of the temperature of dust either in AGN or SSC environments by lack of time, we only conducted few tests on the temperature functionalities of MontAGN. Among them, we tried to reproduce the

temperature profile of a cocoon of silicates around a single star, as compared to other computations. MontAGN temperature maps are displayed on figure 5.12 and the temperature profile is shown in figure 5.13.

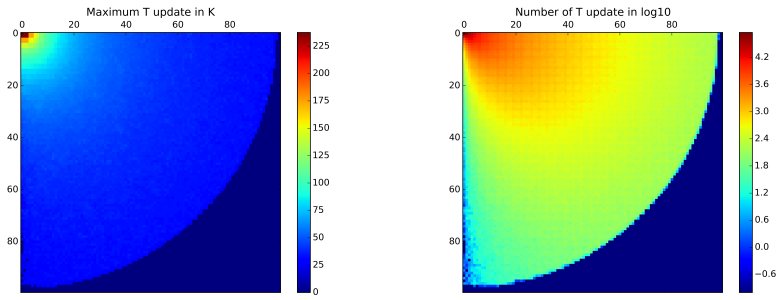

Figure 5.12 – Examples temperature maps generated by montAGN. Left shows the maximum temperature inside a cell, in function of radius and hight. Right shows the number of update that occured in the cells at each position in radius and hight. 5×10^6 packets were launched. Central star has a temperature of 5700 K.

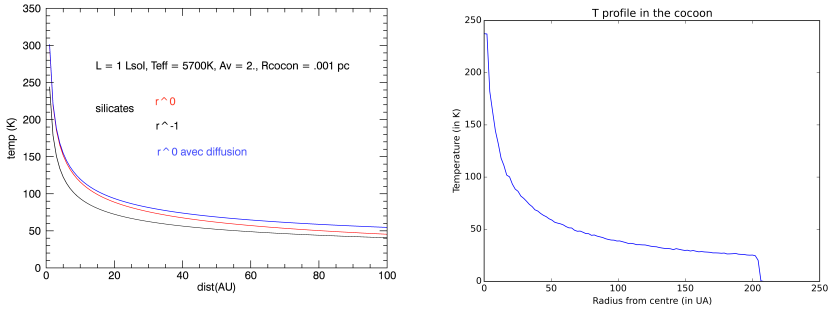

Figure 5.13 – Examples of a temperature profile computed from MontAGN with a constant density structure (r^0, right panel). 5×10^6 packets were launched and central star has a temperature of 5700 K. Left is shown a profile obtain using another computation by Daniel Rouan using comparable parameters. The blue curve corresponds to a case similar to the graph obtained with MontAGN, with a constant density structure (r^0) including scattering.

Many tests concerning the temperature are currently ongoing, however the multiple grain populations complicate the algorithm and this functionality is not yet available.

5.8.4 Angle Corrections and Polarisation Propagation

One major concern in our studies is the orientation of the polarisation vectors. We therefore need to ensure that our simulations correctly reproduces the changes

of polarisation through the scatterings, and that we apply the right rotation matrix correction at the end to translate polarisation into the observer's frame.

Analysing multiple scattering is challenging because it is hardly achievable analytically. This is one of the major motivation for developing MontAGN to simulate polaro-images from AGNs. We will consider for validation tests some more simple cases, mainly with one scattering.

One typical case is a central source surrounding by a dust shell of low optical depth. This imposes to have a low probability of more than one scattering for packets, leading to more predictable polarimetric patterns. We should indeed obtain a perfect centro-symmetric polarisation as shown in the maps of section 3.3. This is a well known feature, studied by Fischer et al. (1996) and Whitney & Hartmann (1993), observed for instance by the HST (Capetti et al. 1995) and reproduced by many simulations as the ones of Murakawa (2010); Marin et al. (2012).

We first try to obtain a similar pattern from simulation of simple dust structure. We consider a star at the centre of this cocoon of radial optical depth τ_V as our source and run a simulation with packets at 2.2 μm. The optical depth is low enough to obtain mainly direct or single scattered photons. Resulting maps are shown in figure 5.14.

We obtained results in excellent agreement with the expected signal of a centro-symmetric polarisation. This is a good indication that the polarisation propagation is occurring accordingly to the physics. Furthermore, it also indicates that the Q-U orientation correction using rotation matrix is working correctly (see section 5.6).

To verify the evolution of polarisation we can also have a look at the local changes on the packets properties during scattering events. Figure 5.15 for example represents the polarisation degree of the packet just after being scattered, in function of the scattering angle α. As expected, the polarisation is maximum at 90° and null for perfect forward and backward scatterings.

Similarly, we can plot the polarisation degree after more than one scattering. In these cases however, the incident light will be polarised after the first scattering and we therefore expect a more complex function, as displayed in figure 5.16. Of course, a scattering of 90° still fully polarises the packets, however, we see a globally increasing polarisation degree for smaller angles with the number of scatterings. This is due to the polarisation already present in the incoming light after a first scattering in case of second scattering, and all the previous scatterings in the other cases.

As explained in section 3.2.3, β the conditional probability density function depends on α and on the incoming polarisation and we can verify that β distributions follow these rules. We measured during a MontAGN simulation β distributions, with imposed α and incoming Q and U. Some results are shown in figure 5.17 which illustrates the effect of both the angle α and the polarisation on the β distribution. We can verify the rotation of the β distribution induced by polarisation. The value of $\alpha = \pi/2$, for which the polarisation is maximum, seems to collimate the values of β toward precise values (depending on the incoming Q and U).

A final test of MontAGN simulation was to create a map of a target seen from

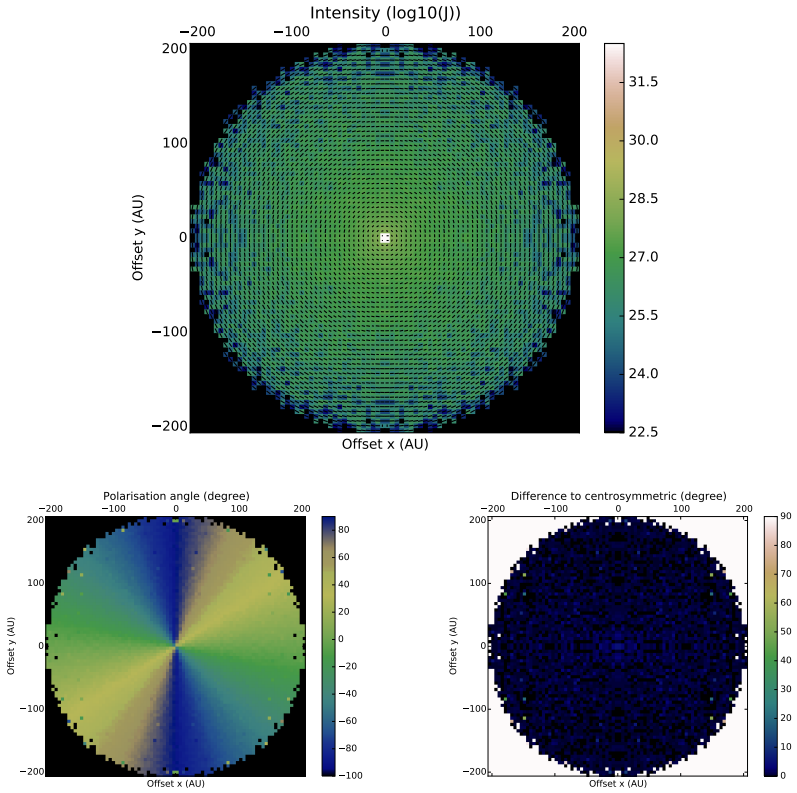

Figure 5.14 – MontAGN centro-symmetric tests maps. First map shows the intensity (in log scale) with polarisation vectors over-plotted. Bottom left image indicate the measured angle of polarisation θ and bottom right shows the difference angle to centro-symmetric pattern. 10^5 packets at 2.2 μm were launched, central star has a temperature of 5700 K and the shell has $\tau_{K_s} \approx 0.05$.

an inclined line of sight. We use for that purpose a model of AGN quite simple, constituted of a torus with a decreasing jump in density beyond 10 pc and of an ionisation cone. This model will be detailed in Chapter 6. We selected an inclination angle of 150°, a line of sight close to but out of the torus outer border. Figure 5.18 shows this simulation.

We can see on this image the direct light from the centre, half hidden by the denser part of the torus, situated above the source. The two ionisation cones are clearly visible, above and under the source, as well as the inner border of the torus, illuminated by the central source. Despite the line of sight is crossing the outer torus, we can see photons from the hidden ionisation cone, because of the low optical depth on this external region of the torus. As this image is consistent with the expectation, we expect reliable results in other situations with a more complex structure.

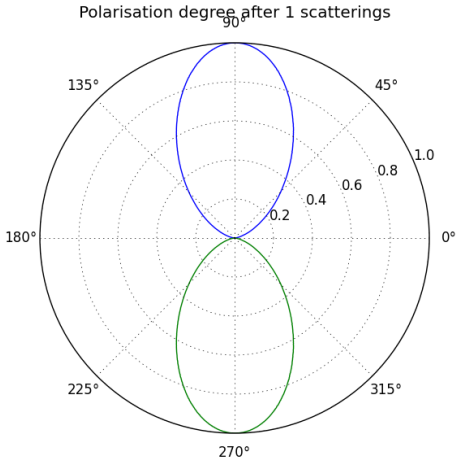

Figure 5.15 – Polarisation degree depending on the main scattering angle α as measured using MontAGN on first scattering. Polarisation degree is obtain through S_{12}/S_{11}, 4×10^5 packets were launched, incoming light is unpolarised.

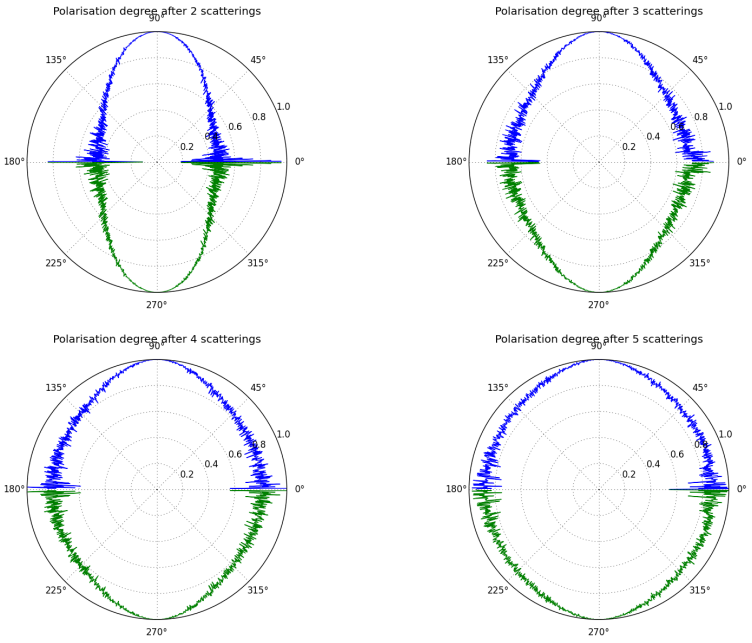

Figure 5.16 – Polarisation degree depending on the main scattering angle α as measured using MontAGN. Polarisation degree is obtain through S_{12}/S_{11}, 4×10^5 packets were launched. The four profiles correspond respectively to second, third, fourth and fifth or more scattering.

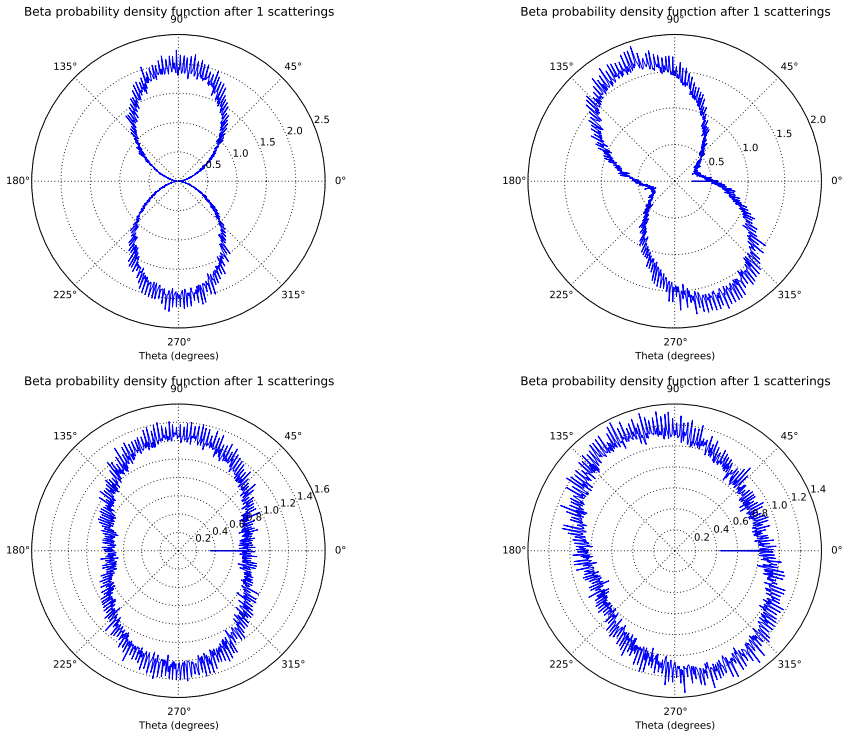

Figure 5.17 – Profiles of distribution of scattering angle β for $x = 1$. First row corresponds to $\alpha = \pi/2$ and second one to $\alpha = \pi/4$. First column was measured with $Q = 1$ and $U = 0$ and second one corresponds to $Q = U = 0.5$. 10^6 packets were launched.

5.9 First Results

As a first experiment using MontAGN, we decided to consider structures with each a constant dust density to represent a simple AGN model. In this way, analysis of the results would be easier and this is critical when using a newborn code. Furthermore, detection of errors is easier. This allows to obtain some first results, guiding our research toward the more complex models of Chapter 6, but also permits to improve the code through comparison to results obtained with the same geometry using the STOKES radiative transfer code. Because both codes were not designed for the same wavelength studies, we selected some intermediate wavelength range to conduct this pre-work: 800 nm to 1 μm.

This need of a comparison to validate our code was the starting point of our collaboration with René Goosmann and Frédéric Marin from the high energy team of Observatoire Astronomique de Strasbourg, developers of STOKES. Indeed, the first comparison allowed to detect some bugs and errors in MontAGN code as well as the need of updating the display function of STOKES. These first steps were the topic of our contributions to the SF2A conference 2016. The two proceedings that arose from

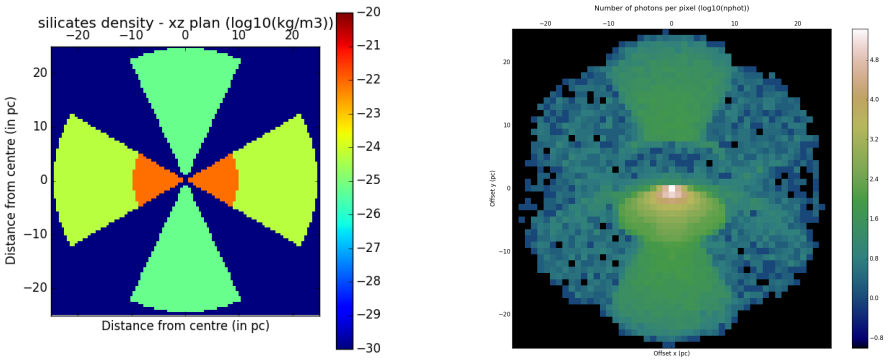

Figure 5.18 – Example of simulation with a viewing angle of 150°. Left map describes the model used, with a torus in orange, with a fainter part starting at 10 pc from the centre. Two ionisation cones are represented in green along the vertical axis. Right image shows the number of received packets per pixel, showing the shapes of the structures. $\approx 5 \times 10^7$ packets were launched.

this conference appear on the next pages, summarizing the work achieved mainly by Frédéric Marin and I, from determining the initial model properties to the first analysis of the outcome.

SF2A 2016
L. Cambrésy, M. Deleuil, E. Pécontal, C. Reylé, J. Richard, L. Tresse and I. Vauglin (eds)

UNDERSTANDING ACTIVE GALACTIC NUCLEI USING NEAR-INFRARED HIGH ANGULAR RESOLUTION POLARIMETRY I : MontAGN - STOKES COMPARISON

L. Grosset[1], F. Marin[2], D. Gratadour[1], R. Goosmann[2], D. Rouan[1], Y. Clénet[1], D. Pelat[3] and P. Andrea Rojas Lobos[2]

Abstract. In this first research note of a series of two, we present a comparison between two Monte Carlo radiative transfer codes: MontAGN and STOKES. Both were developed in order to better understand the observed polarisation of Active Galactic Nuclei (AGN). Our final aim is to use these radiative transfer codes to simulate the polarisation maps of a prototypical type-2 radio-quiet AGN on a wide range of wavelengths, from the infrared band with MontAGN to the X-ray energies with STOKES. Doing so, we aim to analyse in depth the recent SPHERE/IRDIS polarimetric observations conducted on NGC 1068. In order to validate the codes and obtain preliminary results, we set for both codes a common and simple AGN model, and compared their polaro-imaging results.

Keywords: galaxies: active, galaxies: Seyfert, radiative transfer, techniques: polarimetric, techniques: high angular resolution

1 Introduction

Polarimetry is a powerful tool as it gives access to more information than spectroscopy or imaging alone, especially about scattering. In particular, indications on the geometry of the distribution of scatterers, the orientation of the magnetic field or the physical conditions can be revealed thanks to two additional parameters : the polarisation degree and the polarisation position angle. Polarimetry can put constraints on the properties of scatterers, like for example spherical grains or oblate grains (Lopez-Rodriguez et al. 2015) and therefore constrain the magnetic field orientation and optical depth of the medium. The downside is that analysis of polarimetric data is not straightforward. The use of numerical simulations and especially radiative transfer codes is a strong help to understand such data (see for instance Bastien & Menard 1990; Murakawa et al. 2010; Goosmann & Matt 2011). It allows us to assess and verify interpretations by producing polarisation spectra/maps for a given structure, which can then be compared to observations.

STOKES and MontAGN are two numerical simulations of radiative transfer both using a Monte Carlo method built to study polarised light travelling through dusty environments (whether stellar or galactic). In both cases, one of the main goal in developing such codes was to investigate the polarisation in discs or tori around the central engine of AGN. While STOKES was designed to work at high energies, from near infrared (NIR) to X rays, MontAGN is optimised for longer wavelength, typically above 1 μm. Therefore they are covering a large spectral scale with a common band around 0.8 – 1 μm. Both approaches are quite different since STOKES is a geometry-based code using defined constant dust (or electrons, atoms, ions ...) three-dimensional structures while MontAGN uses a Cartesian 3D grid sampling describing dust densities.

In this first research note, we want to present our first comparison between the two codes. We opted for a similar toy model that we implemented in the two simulation tools in order to produce polarisation maps to be compared one to each other. The second proceedings of this series of two will focus on the results of the code when applied to a toy model of NGC 1068.

[1] LESIA, Observatoire de Paris, PSL Research University, CNRS, Sorbonne Universités, UPMC Univ. Paris 06, Univ. Paris Diderot, Sorbonne Paris Cité, 5 place Jules Janssen, 92190 Meudon, France

[2] Observatoire Astronomique de Strasbourg, Université de Strasbourg, CNRS, UMR 7550, 11 rue de lUniversité, 67000 Strasbourg, France

[3] LUTh, Observatoire de Paris, CNRS, Université Paris Diderot, Sorbonne Paris Cité, 5 place Jules Janssen, 92190 Meudon, France

2 The radiative transfer Codes

2.1 STOKES

STOKES was initially developed by R. W. Goosmann and C. M. Gaskell in 2007 in order to understand how reprocessing could alter the optical and ultraviolet radiation of radio-quiet AGN (Goosmann & Gaskell 2007; Goosmann et al. 2007). The code was continuously upgraded to include an imaging routine, a more accurate random number generator and fragmentation (Marin et al. 2012, 2015), until eventually pushing the simulation tool to the X-ray domain (Goosmann & Matt 2011; Marin et al. 2016). STOKES is a radiative transfer code using Mueller Matrices and Stokes vectors to propagate the polarisation information through emission, absorption and scattering. Photons are launched from a source (or a set of sources) and then propagate in the medium until they are eventually absorbed or they exit the simulation sphere. The optical depth is computed based on the geometry given as an input. At each encounter with a scatterer, the photon's absorption is randomly determined from the corresponding albedo; if it is absorbed, another photon is launched from the central source. In a scattering case, the new direction of propagation is determined using phase functions of the scatterer and the Stokes parameters are modified according to the deviation. For a detailed description of the code, see papers of the series (Goosmann & Gaskell 2007; Marin et al. 2012, 2015).

2.2 MontAGN

Following the observation of NGC 1068 in polarimetric mode at high angular resolution conducted by Gratadour et al. (2015), MontAGN (acronym for "Monte Carlo for Active Galactic Nuclei") was developed to study whether our assumptions on the torus geometry were able to reproduce the observed polarisation pattern through simulations in the NIR. MontAGN has many common points with STOKES. Since the two codes were not designed for the same purpose, the main differences originate from the effects that need to be included in the two wavelength domains, which differ between the infrared and the shorter wavelengths. STOKES includes Thomson scattering, not available in MontAGN, while MontAGN takes into account the re-emission by dust as well as temperature equilibrium adjustment at each absorption to keep the cells temperature up to date, not present in STOKES.

In MontAGN photons are launched in the form of frequency-independent photon packets. If absorption is enabled, when a photon packet is absorbed, it is immediately re-emitted at another wavelength, depending on the dust temperature in the cell. The cell temperature is changed to take into account this incoming energy. The re-emission depends on the difference between the new temperature of the cell and the old one to correct the previous photon emissions of the cell at the former temperature (following Bjorkman & Wood 2001). If re-emission is disabled, all photon packets are just scattered, but we apply the dust albedo as a factor to the energy of the packet to solely keep the non-absorbed fraction of photons (see Murakawa et al. 2010). This disabling allows us to get much more statistics at the end of the simulation as every photon is taken into account. But it also requires to have a lot of photons in each pixel at the end as we may obtain in one pixel only photons with weak probability of existence, a situation that is not representative of the actual pixel polarisation.

3 Simulation

We set up a model of dust distribution compatible with the two codes. At the centre of the model, a central, isotropic, point-like source is emitting unpolarised photons at a fixed wavelength (0.8, 0.9 and 1 μm, only images at 0.9 μm are shown in this publication). Around the central engine, is a flared dusty disk with radius ranging from 0.05 pc to 10 pc. It is filled with silicate grains and has an optical depth in the V-band of about 50 along the equatorial plane (see Fig. 1). Along the polar direction, a bi-conical, ionised wind with a 25° half-opening angle with respect to the polar axis flows from the central source up to 25 pc. The wind is filled with electrons in STOKES and silicate grains at much lower density in MontAGN*. The conical winds are optically thin (τ_V = 0.1). We added to these structures a cocoon of silicate grains surrounding the torus, from 10 pc to 25 pc, outside the wind region to account for a simplified interstellar medium in another model. See our second proceedings

*This difference in composition should not affect the polarisation results as the two corresponding phase functions are close, but the flux and polarised flux will be attenuated in the case of dust because of absorption. Thomson scattering should therefore be included in MontAGN to be more realistic.

of this series (Marin, Grosset et al., hereafter Paper II) for more information about the models. Re-emission was disabled for MontAGN in these simulations.

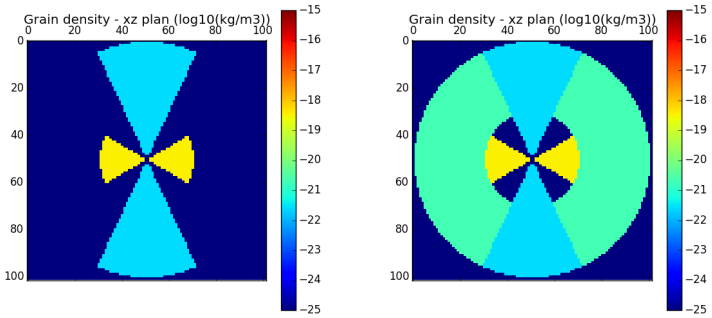

Fig. 1. Grain density (in kg/m^3) set for both models. Note that in STOKES the polar outflow is constituted of electrons, at a density allowing us to have the same optical depth **Left:** first model : "model I" **Right:** second model with the dust shell : "model II".

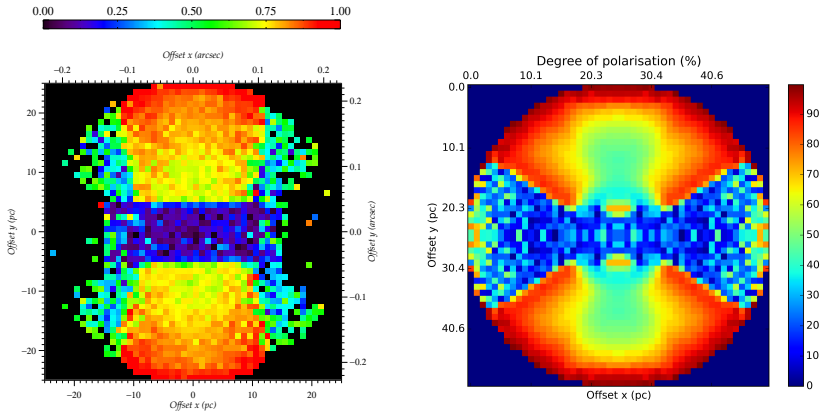

Fig. 2. Polarisation degree for model II at 0.9 μm **Left:** with STOKES **Right:** with MontAGN (in %)

With more than 5×10^6 photons sampled, we obtain for both models an overall good agreement between the two codes. In the polar outflow region, the similarities are high between the two codes, revealing high polarisation degrees (close to 100%) despite the differences in composition (see Fig. 2). This is expected from single scattered light at an angle close to 90° (see Bastien & Menard 1990), which is confirmed from the maps of averaged number of scatterings (see Fig. 3, right). However in the central region, where the torus is blocking the observer's line-of-sight, the results between MontAGN and STOKES slightly differ (see the equatorial detection of polarisation at large distances from the centre in Fig. 2, right). We interpret this polarisation as arising from the differences in the absorption method between the two codes. Because in MontAGN all photons exit the simulation box, we always get some signal even if it may not be representative of photons reaching this peculiar pixel. If inside a pixel only photons with low probability, i.e. with the energy of their photon packets being low after multiple scatterings, are collected, the polarisation parameters reconstructed from these photons will not be reliable. This is why we need to collect an important number of photons per pixel.

Otherwise, the polarisation structure revealed by polaro-imaging is very similar between the two codes and lead to distinctive geometrical highlights that will be discussed in the second research note of this series (Paper II).

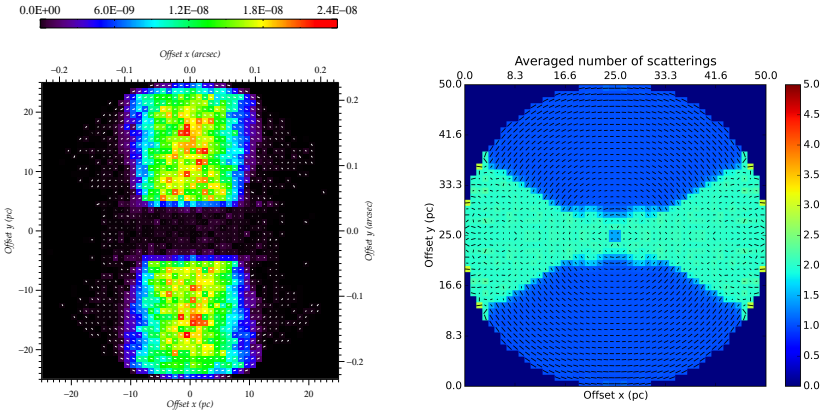

Fig. 3. At 0.9 μm **Left:** Polarised flux (in arbitrary units) with the polarisation position angle superimposed for model II with STOKES. **Right:** Averaged number of scatterings a photon undergo before exiting the medium with polarisation vectors superimposed for model II with MontAGN.

4 Concluding remarks

We compared the MontAGN and STOKES codes between 0.8 and 1 μm for similar distribution of matter and found that many of the polarimetric features expected from one code are reproduced by the second. The only difference so far resides on the detection of polarisation at large distances from the centre of the model, where we need a higher sampling in order for MontAGN to match STOKES results. The next step will be to improve the models, and develop the MontAGN code by including more effects like electron scattering or non spherical grains (ortho- and para-graphite, namely). However we already get a fairly good agreement between the codes which give us confidence to pursue our exploration of the near-infrared signal of AGN together with MontAGN and STOKES. Note that the comparison allowed to detect flaws and bugs, a positive outcome. We intend to explore our first results in Paper II and push the codes towards more complex geometries. Once a complete agreement will be found in the overlapping band (0.8 – 1 μm), we will run a large simulation ranging from the far-infrared to the hard X-rays for a number of selected radio-quiet AGN. Our targets include the seminal type-2 NGC 1068, as well as a couple of other nearby AGN with published polarimetric data. Forthcoming new infrared polarimetric observations using SPHERE will complement our database and be modelled with MontAGN and STOKES.

The authors would like to acknowledge financial support from the Programme National Hautes Energies (PNHE).

References

Bastien, P. & Menard, F. 1990, ApJ, 364, 232

Bjorkman, J. E. & Wood, K. 2001, ApJ, 554, 615

Goosmann, R. W. & Gaskell, C. M. 2007, A&A, 465, 129

Goosmann, R. W., Gaskell, C. M., & Shoji, M. 2007, in IAU Symposium, Vol. 238, Black Holes from Stars to Galaxies – Across the Range of Masses, ed. V. Karas & G. Matt, 375–376

Goosmann, R. W. & Matt, G. 2011, MNRAS, 415, 3119

Gratadour, D., Rouan, D., Grosset, L., Boccaletti, A., & Clénet, Y. 2015, A&A, 581, L8

Lopez-Rodriguez, E., Packham, C., Jones, T. J., et al. 2015, MNRAS, 452, 1902

Marin, F., Goosmann, R. W., & Gaskell, C. M. 2015, A&A, 577, A66

Marin, F., Goosmann, R. W., Gaskell, C. M., Porquet, D., & Dovčiak, M. 2012, A&A, 548, A121

Marin, F., Goosmann, R. W., & Petrucci, P.-O. 2016, A&A, 591, A23

Murakawa, K., Ueta, T., & Meixner, M. 2010, A&A, 510, A30

SF2A 2016
L. Cambrésy, M. Deleuil, E. Pécontal, C. Reylé, J. Richard, L. Tresse and I. Vauglin (eds)

UNDERSTANDING ACTIVE GALACTIC NUCLEI USING NEAR-INFRARED HIGH ANGULAR RESOLUTION POLARIMETRY II: PRELIMINARY RESULTS

F. Marin[1], L. Grosset[2], R. Goosmann[1], D. Gratadour[2], D. Rouan[2], Y. Clénet[2], D. Pelat[3] and P. Andrea Rojas Lobos[1]

Abstract. In this second research note of a series of two, we present the first near-infrared results we obtained when modeling Active Galactic Nuclei (AGN). Our first proceedings showed the comparison between the montAGN and STOKES Monte Carlo codes. No we use our radiative transfer codes to simulate the polarization maps of a prototypical, NGC 1068-like, type-2 radio-quiet AGN. We produced high angular resolution infrared (1 μm) polarization images to be compared with recent observations in this wavelength range. Our preliminary results already show a good agreement between the models and observations but cannot account for the peculiar linear polarization angle of the torus such as observed. Gratadour et al. (2015) found a polarization position angle being perpendicular to the bipolar outflows axis. Further work is needed to improve the models by adding physical phenomena such as dichroism and clumpiness.

Keywords: galaxies: active, galaxies: Seyfert, radiative transfer, techniques: polarimetric, techniques: high angular resolution

1 Introduction

Understanding the role, morphology, composition and history of each AGN component is a non-trivial goal that requires a strong synergy between all observational techniques. The role of polarimetric observations was highlighted in the 80s thanks to the discovery of broad Balmer lines and Fe II emission sharing a very similar polarization degree and position angle with the continuum polarization in NGC 1068, a type-2 AGN (Antonucci & Miller 1985). The resemblance of the polarized flux spectrum with respect to the flux spectrum of typical Seyfert-1s lead to the idea that Seyfert galaxies are all the same, at zeroth-order magnitude (Antonucci 1993). Observational difference would arise from a different orientation of the nuclei between pole-on and edge-on objects; this is due to the presence of an obscuring dusty region situated along the equatorial plane of the AGN that will block the direct radiation from the central engine for observers looking through the optically thick circumnuclear material. This is the concept of the so-called "dusty torus", first conceived by Rowan-Robinson (1977) and later confirmed by (Antonucci & Miller 1985).

Since then, a direct confirmation for the presence and structure of this dusty torus was an important objective for the AGN community. The closest evidence for a dusty torus around the central core of NGC 1068 was first obtained by Jaffe et al. (2004) and Wittkowski et al. (2004), using mid-infrared (MIR) and near-infrared (NIR) interferometric instruments coupled to the European Southern Observatory's (ESO's) Very Large Telescope interferometer (VLTI). Jaffe et al. (2004) were able to spatially resolve the MIR emission from the dusty structure and revealed that 320 K dust grains are confined in a 2.1 $\times$ 3.4 pc region, surrounding a smaller hot structure. The NIR data obtained by Wittkowski et al. (2004) confirm the presence of this region, with the NIR fluxes arising from scales smaller than 0.4 pc. Since then, long-baseline interferometry became a tool used to explore the innermost AGN dusty structure extensively at high angular resolution (typically of the order of milli-arcsec, see e.g., Kishimoto et al. 2009, 2011).

[1] Observatoire Astronomique de Strasbourg, Université de Strasbourg, CNRS, UMR 7550, 11 rue de l'Université, 67000 Strasbourg, France
[2] LESIA, Observatoire de Paris, PSL Research University, CNRS, Sorbonne Universités, UPMC Univ. Paris 06, Univ. Paris Diderot, Sorbonne Paris Cité
[3] LUTH, Observatoire de Paris, CNRS, Universit Paris Diderot, 92190 Meudon, France

Coupling adaptive-optics-assisted polarimetry and high angular resolution observations in the infrared band, Gratadour et al. (2015) exploited the best of the two aforementioned techniques to obtain strong evidence for an extended nuclear torus at the center of NGC 1068. Similarly to previous optical (Capetti et al. 1995) and infrared (Packham et al. 1997; Lumsden et al. 1997) polarimetric observations, Gratadour et al. (2015) revealed an hourglass-shaped biconical structure whose polarization vectors point towards the hidden nucleus. By subtracting a purely centro-symmetric component from the map of polarization angles, an elongated (20×50 pc) region appeared at the assumed location of the dusty torus. If the signal traces the exact torus extension, high angular resolution polarization observations would become a very powerful tool to study the inner core of AGN.

In this lecture note, the second of the series, we will show the preliminary results obtained by running Monte Carlo radiative transfer codes for a NGC 1068-like AGN. Our ultimate goal is to reproduce the existing UV-to-infrared polarimetric observations using a single coherent model in order to constrain the true three-dimensional morphology of the hard-to-resolve components of close-by AGN.

2 Building an NGC 1068 prototype

Our primary model is powered by a central, isotropic, point-like source emitting an unpolarized spectrum with a power-law spectral energy distribution $F_* \propto \nu^{-\alpha}$ and $\alpha = 1$. Along the polar direction, a bi-conical, ionized wind with a 25° half-opening angle* with respect to the polar axis flows from the central source to 25 pc. The wind is assumed to be ionized and therefore filled with electrons. It is optically thin (optical depth in the V-band along polar direction $\tau_V = 0.1$). Along the equatorial plane, a flared disk sets on at 0.05 pc (a typical dust sublimation radius, see Kishimoto et al. 2007) and ends at 10 pc. The half-opening angle of the dust structure is fixed to 30° (Marin et al. 2012) and its V-band optical depth is of the order of 50. The dust is composed of 100 % silicates with grain radii ranging from 0.005 μm to 0.25 μm, together with a size distribution proportional to $a^{-3.5}$ (a being the grain radius).

The observer's viewing angle is set to 90° with respect to the symmetry axis of the model. More than 10^7 photons were sampled to obtain polarimetric images with a pixel resolution of 1 pc (9 milli-arcsec at 14.4 Mpc). For this proceedings note, we selected the images computed at 1 μm and used the Monte Carlo code STOKES.

2.1 Results of our baseline model

The polarimetric maps for our baseline model are shown in Fig. 1. The left image shows the polarization position angle superimposed to the 1 μm polarized flux. The polarization vectors show the orientation of polarization but are not proportional to the polarization degree (which is shown in the right image).

The polar outflows, where electron scattering occurs at a perpendicular angle, shows the strongest polarization degree (up to 90 – 100 %) associated with a centro-symmetric polarization angle pattern. This in perfect agreement with the polarization maps taken by the optical and infrared polarimeters in the 90s and recently upgraded by Gratadour et al. (2015). At the center of the model, the photon flux is heavily suppressed by the optically thick material, but scattered radiation from the cones to the surface of the torus leads to a marginal flux associated with a weak polarization degree† (< 8 %). Such degree of polarization is in very good agreement with the values observed by Gratadour et al. (2015) at the location of the nucleus (5 – 7 %). However, compared to the results of the previous authors, the polarization position angle from the modeling is almost centro-symmetric rather than aligned/anti-aligned with the circumnuclear dusty structure. It is only on the highest point of the torus morphology that a ~ 50 % polarization degree associated with a higher flux can be found, due to a lesser amount of dust facing the wind-scattered photon trajectories. When the whole picture is integrated, the resulting polarization degree is of the order of 60 %.

2.2 Accounting for the ISM

To test multiple configurations, we ran a second series.Based on the previous setup, we included interstellar matter (ISM) around the model. The ISM dust grains share the same composition as the dust in the circum-

*The half-opening angle of our model is smaller than what is observed (Goosmann & Matt 2011). We will change this value when the comparison between montAGN and STOKES will be completed, see Paper I.

†Polarization degrees quoted in the text are for the scattered-induced polarization only. Dilution by the interstellar polarization, host galaxy starlight and starburst light will drastically reduce the observed polarization degree.

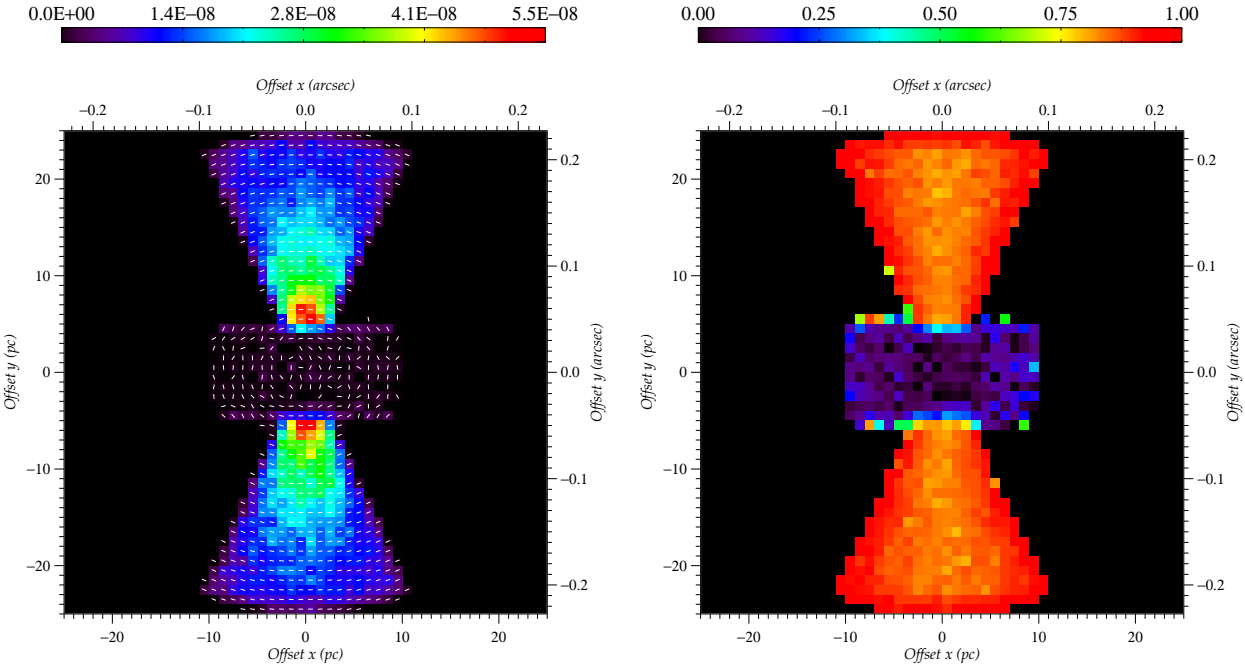

Fig. 1. 1 μm polarimetric simulations of NGC 1068. Left figure shows the color-coded polarized flux in arbitrary units with the polarization position angle superimposed to the image. Right figure shows the color-coded degree of polarization (from 0, unpolarized, to 1, fully polarized).

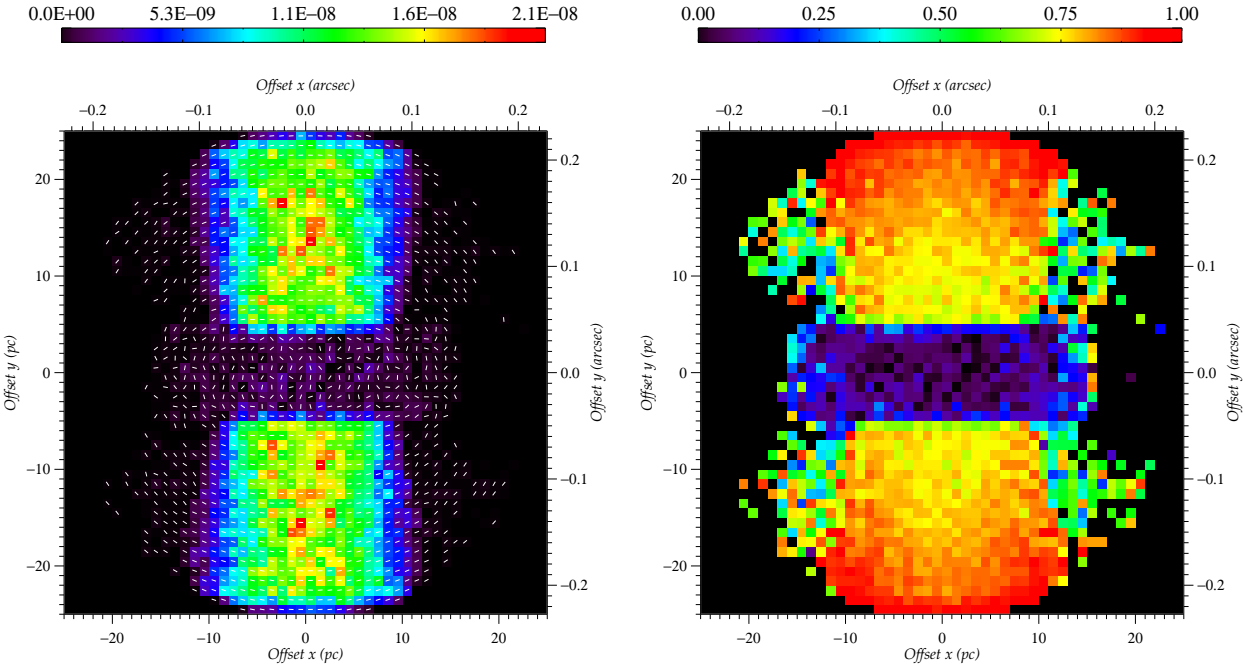

Fig. 2. Same as Fig. 1 with the addition of optically thin interstellar matter around the model

nuclear AGN region and the ISM is optically thin in all directions ($\tau_V = 0.5$). Our new polarimetric images are shown in Fig. 2

A striking difference between the ISM-free (Fig. 1) and the ISM-included (Fig. 2) polarimetric maps is the shape of the outflowing winds seen in transmission through the dust. The perfect hourglass shape observed when the AGN was in vacuum is now disturbed. The global morphology is more similar to a cylinder, with no flux gradient observed as the photons propagate from the central engine to the far edges of the winds. The overall flux distribution is more uniform throughout the winds, which seems to be in better agreement with what has been observed in the same band, at least for sub-arcsec scales (Packham et al. 1997). At better angular resolutions, polarized flux images are still needed. The polarization position angle has retained its centro-symmetric pattern but the polarization angle is more chaotic at the location of the torus, due to additional dust-scattering. The degree of polarization at the center of the AGN is the same as previously but the integrated map shows a slightly smaller polarization degree (58 %) due to depolarization by multiple scattering.

3 Discussion

Running our radiative transfer codes at 1 μm, we found that a NGC 1068-like model produces the centro-symmetric polarization angle pattern already observed in the optical and infrared bands. Disregarding additional dilution by other sources, the polarization position angle pinpoints the source of emission. Including the ISM in the model does not change the results but tends to decrease the final polarization degree. It also changes the flux repartition in the outflowing winds that act like astrophysical mirrors, scattering radiation from the hidden nucleus. Compared to what has been shown in Gratadour et al. (2015) in the H (1.6 μm) and K (2.2 μm) bands, we find very similar levels of linear polarization at the center of the model, where the central engine is heavily obscured by dust. However, we do not retrieve the distinctive polarization position angle of the torus found by the authors. According to our models, the pattern is at best centro-symmetric rather than directed perpendicular to the outflowing wind axis.

Additional work is needed to explore how such a distinctive pattern can arise at the location of the torus. In particular, adopting the most up-to-date morphological and composition constraints from literature is mandatory to built a coherent NGC 1068 model. Including effects such as polarization by absorption (dichroism) will be necessary. Comparing our results with past linear and circular polarization measurements (e.g, Nikulin et al. 1971; Gehrels 1972; Angel et al. 1976) will drive our models towards the right direction. Finally, the broadband coverage of the codes, from the X-rays to the far infrared, will allow us to robustly test our final model against spectroscopic and polarimetric observations in many wavebands.

The authors would like to acknowledge ... PNCG, PNHE ?

References

Angel, J. R. P., Stockman, H. S., Woolf, N. J., Beaver, E. A., & Martin, P. G. 1976, ApJ, 206, L5
Antonucci, R. 1993, ARA&A, 31, 473
Antonucci, R. R. J. & Miller, J. S. 1985, ApJ, 297, 621
Capetti, A., Macchetto, F., Axon, D. J., Sparks, W. B., & Boksenberg, A. 1995, ApJ, 452, L87
Gehrels, T. 1972, ApJ, 173, L23
Goosmann, R. W. & Matt, G. 2011, MNRAS, 415, 3119
Gratadour, D., Rouan, D., Grosset, L., Boccaletti, A., & Clénet, Y. 2015, A&A, 581, L8
Jaffe, W., Meisenheimer, K., Röttgering, H. J. A., et al. 2004, Nature, 429, 47
Kishimoto, M., Hönig, S. F., Antonucci, R., et al. 2011, A&A, 527, A121
Kishimoto, M., Hönig, S. F., Antonucci, R., et al. 2009, A&A, 507, L57
Kishimoto, M., Hönig, S. F., Beckert, T., & Weigelt, G. 2007, A&A, 476, 713
Lumsden, S., Bland-Hawthorn, J., Moore, T., et al. 1997, Ap&SS, 248, 287
Marin, F., Goosmann, R. W., Gaskell, C. M., Porquet, D., & Dovčiak, M. 2012, A&A, 548, A121
Nikulin, N. S., Kuvshinov, V. M., & Severny, A. B. 1971, ApJ, 170, L53
Packham, C., Young, S., Hough, J. H., Axon, D. J., & Bailey, J. A. 1997, MNRAS, 288, 375
Rowan-Robinson, M. 1977, ApJ, 213, 635
Wittkowski, M., Kervella, P., Arsenault, R., et al. 2004, A&A, 418, L39

5.10 MontAGN Manual and Future Improvements

This section gives the required informations to use MontAGN as a simulation tool. The following document describes the main simulation function, as well as some useful functions implemented in the MontAGN code. This is intended to be a first draft of what will be the MontAGN manual when available to community. As the code is continuously evolving, the manual will probably undergo an important number of evolutions before its first release, however it gives already a good vision of how to use the code and the options available.

The final objective is to stabilize the code on a more ergonomic version, easily usable by public. This goal should be reached in the near future. We however started to think about the future developments that could improve MontAGN within a reasonable amount of time.

As one of the main limitation is the execution time, one of the best direction in which improvements are important is to increase the speed of the code. There are different ways to do so, one idea is to export MontAGN toward a code usable on a Graphical Processor Unit (GPU) architecture. As the code is repeating the same calculus a great number of time, its adaptation to GPU should be reasonably easy. Another way is to translate the core of the code from Python to C or Fortran. Doing so, the execution speed should increase sensibly. Because it was from the start thought to need this improvement, the architecture of MontAGN was built closer as possible to a C++ architecture.

One interesting feature which is not yet included in MontAGN is the possibility to use aligned non spherical grains. As two types of graphites are already implemented, the use of elongated grains can be achieved thanks to setting different populations with different sizes of the same dust species. The main limitation is that in order for this grains to have an impact, we need to allow them to be aligned on a particular direction. This is important for AGN studies as it is likely for these grains to exists and to be aligned by magnetic fields (see for example Efstathiou et al. 1997).

Finally, the last fairly accessible amelioration consists in modifying the source selection in order to include the dust thermal emission. This process is already included into the energy equilibrium used in the re-emission routine, however when disabled, these regions are not any more considered as emitters. Thanks to this upgrade, it would be possible to first use the re-emission mode to compute the temperature map and in a second time to conduct faster simulations without re-emission, but including emissions by dust. This improvement would be significant especially when looking at long wavelength.

MontAGN

Quick guide

MontAGN is fully written in `Python 2.7`
`ipython` is recommanded, if not consider using `matplotlib.pyplot.ion`

MontAGN - V 2.5

Manual V 1.0

MontAGN was written by : Lucas Grosset
Jan Orkisz

with the support of :
Lâm Nguyen
Didier Pelat
Daniel Rouan

Manual written by : Lucas Grosset

1 Using MontAGN

1.1 Basic commands

MontAGN can be run by calling the main function of the code :

In [1] : `montAGN()`

(note that there is no caps on the first letter to avoid confusion with the code's name).

It is required however to load the functions into the terminal, using `run`, `import` or `exec` on the file `'montagn.py'` :

In [0] : `run montagn`

The function has no input parameter required but can be use with many keywords as well as a parameter file. Its gives as an output a `model` class object, as defined in section 4.

1.2 Keywords

The keywords available on the main MontAGN function are listed here, following this organisation :

— **keyword** values available (`default value`)
Explanations.

Keywords available for other useful function included in MontAGN will be described in the corresponding sections.

— **paramfile** 'string' ()
Name of the parameter file to be loaded.

— **ask** 0 or 1 (1)
Ask to the user (1) or not (0) the parameters for simulation. If not, one should give the wanted parameters otherwise the default will be used.

— **usemodel** integer from list below (0)
keyword unused if `ask=1`.
0 uses parameters tunable in the file montagn_launch.py
For star models :
1 uses parameters to create a dust cocoon surrounding a central star
2 uses parameters to reproduce the model of Murakawa (2010)
3 uses parameters to reproduce the model of Murakawa (2010) with a lower optical depth
For AGN models :
11 utilise les paramètres du modèle boite de camembert de la simulation de Mie
12 utilise les paramètres du modèle simple d'AGN de NGC 1068
13 utilise les paramètres du modèle de Murakawa 2010 adapté aux AGN
14 utilise les paramètres du modèle commun Stokes de Strasbourg
14.0 pour le modèle complet
14.1 pour le modèle sans ISM
14.2 pour le modèle avec uniquement le tore

— **add** 0 or 1 (0)
Add (1) or not (0) the new data at the end of the output file (if it already exists). If `add=0` and the file exist, it will be replaced.

— **usethermal** 0 or 1 (1)
Enabled (1) or disabled (0) the thermal part of the MontAGN code. If enabled, the simulation will consider temperature adjustment of each cell as well as re-emission by dust, with a slower execution as a downside. If disabled, packet's energy are pondered by the albedo at each scattering to stand for the absorbed part of the packet's photons.

— **nphot** positive integer ( )
number of packets to be launched. If not given, it will be asked to the user at the beginning of the simulation. Some typical execution time is 0.2 s per packet (it depends on the optical depth).

— **filename** 'string' (`'test'`)

root name of the output files (between quotes ") for packets, dust densities and temperature (if `usethermal=1`).

— **ndiffmax** positive integer (`10`)
Maximum number of interaction that a packets will be allowed to undergo. If it reaches this limit, it will stop propagating and will not be considered in the output.

— **modelmont** model class object ( )
Keyword usable to give to MontAGN an already existing model class object (see 4). Allows for example to use a previously computed map temperature, or to avoid to compute again a density grid already existing. If not specified, MontAGN will create a new model class object.

— **thetaobs** [list of integer within the range [0,180]] (`[0,90,180]`)
Keywords that trigger what inclination images to display at the end of the simulation.

— **dthetaobs** positive integer (`5`)
Indicate the angle half-width range recorded in one file. `dthetaobs=5` will therefore create 19 files, each recoding packets with a width of 10, centred on the angle value of the file.

— **force_wvl** float (in m) ( )
Allow if specified to impose a unique wavelength to all the packets launched in the code. Please consider only using wavelength allowed by spectra and grains properties (between 20nm and 2mm currently).

— **grain_to_use** list of 0 or 1 for [sil,gra_o,gra_p,elec] (`[0,0,0,0]`)
Indicate whether grains properties should be computed (1) or not (0). Note that if a grain is used in the simulation, its properties will always be computed.

— **nang** positive odd integer (`999`)
Indicate the angular resolution (number of steps) in the phase functions for scatterings. have to be an odd number !

— **nsize** positive integer (`100`)
Indicate the size resolution (number of steps) for grains. As tables are not well sampled on grain size currently, it is unnecessary to give a high value.

— **rgmin** list of floats for [sil,gra_o,gra_p] (in m) (`[0.005e-6,0.005e-6, 0.005e-6]`)
Minimal radius of grains of different species.

— **rgmax** list of floats for [sil,gra_o,gra_p] (in m) (`[0.25e-6,0.25e-6, 0.25e-6]`)
Maximal radius of grains of different species.

— **alphagrain** list of floats for [sil,gra_o,gra_p] (`[-3.5,-3.5,-3.5]`)
Degree of the power law of MRN dust distribution for grains of different species

— **nsimu** positive integer (`1`)
Indicate the identity of the simulation in term of thread. Mostly used for parallel usages, should be set to `1` otherwise.

— **display** 0 or 1 (`1`)
Allows (1) or not (0) the display of the density maps, final images etc.. Disabling it is recommanded in parallel usages.

— **cluster** 0 or 1 (`0`)
`1` is mandatory when launched on clusters for management of files and directories.

— **cmap** 'string' (`'jet'`)
Determine the colormap to be used for displays.

— **vectormode** 0 or 1 (`0`)
If `display=1`, create some additional final maps with polarisation vectors plotted above.

1.3 Example of execution

1.3.1 Simple launch

Example of launch of MontAGN with a model of dust cocoon around a central star from a `ipython` session :

In [0] : `run montagn`

In [1] : `model=montAGN(ask=0,usemodel=1,add=0,nphot=20000,filename='test')`

Launch a simulation with 20,000 photons packets, with pre-defined model 1 (dust shell, see keyword `usemodel`). Outputs will be saved in `'test_***.dat'` (see output section 2). Will replace the file if existing.

1.3.2 Launch directly from terminal

It is also possible to launch the code directly from a terminal (`bash` or else) by executing file `'montagn_paral.py'` :

> `python montagn_paral.py --usemodel=1 --nphot=20000 --filename='test'`

— Most of the main options described in section 1.2 are also available, see parallelised section 1.5 for more information.
— Launching the code this way automatically disabled the display.
— Filenames will be composed from the root filename, the thread number and the inclination angle : `'filename_001_***.dat'` for the first thread, etc..

1.3.3 Typical execution time

The typical execution time depend on the mode used :
— with temperature computation and dust re-emission : 300 packets <–> 1 min

— without temperature computation and dust re-emission : 100 packets <–> 1 min

1.4 Other parameters

Other parameters are available, especially about the dust structures to be sampled into the 3D grid. These parameters are to be enter into a parameter file (see keyword `paramfile`) :

— **res_map** float ()
Grid resolution (in m).

— **rmax_map** float ()
Grid size (in m).

→ give the total number of cells

— **af** float ()
Ionisation cone half opening angle.

— **enpaq** float ()
Energy in photons packets.

— **fichierspectre** string ()
File containing the spectrum of the central object (Star, AGN...)

— **centrobject** string ()
Label of central source (`'AGN'`, `'star'`...)

— **rsubsilicate** float ()
Estimated sublimation radius of the silicate grains (in m). Be careful, as this radius can only increase, be sure not to choose a value above the actual value.

— **rsubgraphite** float ()
Estimated sublimation radius of the graphite grains (in m). Be careful, as this radius can only increase, be sure not to choose a value above the actual value.

When filling the 3D grid with dust densities, some structures already implemented are available (radial and spherical power laws, clouds, shells, constant density cylinders and torus geometries), through parameters :

— **denspower** [float(col[1]),float(col[2]),float(col[3]),[float(col[4]),float(col[5]),float(col[6]),float(col[7])]] ()
[[Radial power index, Radial typical profile size (in m), Vertical decay size (in m), [Density of grains (in particles / m^3) at radial typical profile size (one for each grain type)]]] .

— **spherepower** [float(col[1]), float(col[2]), [float(col[3]),float(col[4]),float(col[5]),float(col[6])]] ()
[[Radial power index, Radial typical profile size (in m), [Density of grains (in particles / m^3) at radial typical profile size (one for each grain type)]]] .

— **torus** [float(col[1]),[float(col[2]),float(col[3]),float(col[4]),float(col[5])],float(col[6]),float(col[7]),float(col[8])] ()
[[Disc outer radius (in pc),[density coefficent of grains (in kg / m^3)],ratio of the disk height at the disk boundary to the disk outer radius,Envelope mass infall (in Msol / yr),Mass of the star (in Msol)]] .

— **torus_const** [float(col[1]),[float(col[2]),float(col[3]),float(col[4]),float(col[5])],[float(col[6]),float(col[7]),float(col[8]),float(col[9])],[float(col[10]),float(col[11]),float(col[12]),float(col[13])]] ()
[[Disc outer radius (in m),[density coefficent of grains in the torus (in particles / m^3)],[density coefficent of grains in the envelope (in particles / m^3)],[density coefficent of grains in the cone (in particles / m^3)]]] .

— **cylinder** [float(col[1]),float(col[2]),[float(col[3]),float(col[4]),float(col[5]),float(col[6])]] ()
[[cylinder radius (in m),cylinder height (in m),[density of grains (in particles / m^3)]]] .

1.5 Parallel

MontAGN can be launched in parallel. If so, the code will create as many threads as asked, creating as many times the usual number of output files. Of the threads are fully independent in term of seed, insuring to have independent results from one thread to any other.

To launch MontAGN in parallel, the following command should be entered on a terminal in the MontAGN directory, executing file `'montagn_paral.py'` :

> `python montagn_paral.py --options`

- Most of options are the same as the classical `montAGN()` ones. Some of them can not be used in this mode, displays is automatically disabled and a new options can be used (`--nlaunch`).
- As an usual function called from terminal, options should be called using '--', with the corresponding parameter if required.
- The new option `--nlaunch` define the number of thread that will be created and launched in parallel. If it is not given, only one thread will be created, leading to a classical MontAGN simulation.

1.5.1 Example

> `python montagn_paral.py --usemodel=2 --nphot=20000 --filename='test' --nlaunch=2`

will launch two thread, of 20,000 photons packets each, using pre-defined model number 2, and will save the results in files `'test_001_***.dat'` and `'test_002_***.dat'`(see Output section 2)

Available options :

- `ask` can not be used
- `--usemodel=0, 1, 2, ...`
- `--add`
- `--usethermal`
- `--nphot=##`
- `--filename=''`

— `modelmont` can not be used
— `display` can not be used
— `--ndiffmax=##`
— `--tycho`
— `--thetaobs=##`
— `--dthetaobs=##`
— `--nlaunch=##`
— `cmap` can not be used
— `--force_wvl=##`

2 Output

The mains output are the files containing all the exited photons data. There are however some other files than can be created, all starting with the strings set to `filename`. They will all be detailed here :

— `_xxx_phot.dat` files contain all the information about photons, at inclination angle `xxx` (in degrees). The list of all recorded informations is in section 2.1. These files are the one used to reconstruct images, SED...
— `_dust_xy.dat` file contain a density map of `dust` grains in the xy plane.
— `_dust_xz.dat` file contain a density map of `dust` grains in the xz plane.

Furthermore, if the re-emission (`usethermal=1`) is enabled, some additional files are created :

— `_T_update.dat` file contain the list of all the temperature update that occurred, with the corresponding cells.
— `_T_#.dat` file contain a sliced temperature map at a specific time (`#`= 0 for example is for the initial map, `#`= 3 corresponds to the final map).

2.1 Photons files

Table 1 list all the informations recorded in the `_xxx_phot.dat` files with the corresponding unit if needed :

TABLE 1 – Output parameters recorded in MontAGN simulations

Output parameter	Symbol	unit
Photon number	i	
Out inclination angle	θ	°
Out azimuthal angle	ϕ	°
Normalised Stokes U parameter	U	%
Normalised Stokes Q parameter	Q	%
Normalised Stokes V parameter	V	%
Out polarisation orientation angle	ϕ_{QU}	°
Last interaction position x	x	pc
Last interaction position y	y	pc
Last interaction position z	z	pc
Number of interaction	n_{inter}	
Number of re-emission	n_{reem}	
Wavelength	λ	m
Label of the packet	label	
Energy of the packet	E	J
Emission time of the packet	δt	s
Total emission time (only if first packet)	Δt	s

3 Displays

The two main displaying functions included in MontAGN are `display_SED()` and `plot_image()`. Both these functions uses the `_xxx_phot.dat` files to construct their maps or graphs.

The last display function is `plot_Tupdate()` which allows to compute maps of useful informations about the temperature changes within the cells. It therefore uses and requires file `_T_update.dat`.

3.1 `display_SED`

`display_SED()` according to its name is a function allowing to show the SED of packets received under the selected restriction. It gives as an output two maps, a linear and a log scale ones.

In [2] : `display_SED(filename)`

3.2 `plot_image`

The second one, `plot_image()` is the most elaborated display function and compute maps according to requirements. It has one input parameter, `filename`, the name of the file in which load the data to display, and many options, detailed below. Note that if `thethaobs` is set to a particular angle while executing `montAGN`, the code will automatically call `plot_image()` for the corresponding inclination angle.

In [3] : `plot_image(filename)`

will read the data in file `'filename_phot.dat'`
Keywords :

— **outname** 'string' (`'test'`)
Root name of the images that will be recorded (if `rec=1`).

— **suffixe** 'string' (`''`)
Suffix to be placed at the end of the name of recorded files.

— **thetaobs** float within the range [0,180] ( )
Inclination angle selected for the display of maps.

— **dtheta** positive float < 180 (5)
Tolerance interval around the given angle `thetaobs` for photons packets selection. If `[]` is specified, all photons packets within the file will be used.

— **obj** 'AGN' or 'star' (`'AGN'`)
Allows to select have an idea of the final scale (UA ou pc)

— **path** 'string' (`''`)
Indicate the path to find the files to be read. Will read the file `path/filename`.

— **dat** 0 or 1 (1)
If set to `1`, automatically add `'.dat'` at the end of `'filename'`.

— **resimage** integer ( )

Resolution of the final images. Depends on keyword `resunit`. If `resunit` is not given, or set to `'pixel'`, `resimage` gives the number of pixels that will be used on one axis to display the maps (for example `51` for an image of `51x51`). Else, `resimage` determine the resolution of the image in `resunit`.

— **resunit** 'string' (`'pixel'`)
Gives the unit of the value entered with `resimage`.

— **diffn** positive integer or null ( )
If given, uses only packets with this value of number of scatterings.

— **ndiffmax** positive integer ( )
If given, define the maximum value of number of scattering for packets to be used.

— **cmap** 'string' (`'jet'`)
Determine the colormap to be used for displays.

— **enpaq** float (`3.86e26`)
Initial energy in photons packets. Used to compute the probability map.

— **coupe** 0 or 1 (`0`)
Allows to extract cuts of the central lines (`1`) and to compute histograms of polarisation within these cuts.

— **vectormod** 0 or 1 (`0`)
If `display=1`, create some additional final maps with polarisation vectors plotted above.

— **sym** 0, 1, or 2 (`0`)
Uses or not symmetries to compute the Q and U maps.
`0` cylindrical symmetry used
`1` symmetry according to equatorial plane is assumed as well as cylindrical symmetry
`2` symmetry of all four quadrants is assumed as well as cylindrical symmetry

— **rec** 0 ou 1 (0)
If set to 1, will record the displayed images, using 'saveformat' format and 'outname' name for files.

— **saveformat** 'pdf' or 'png' ('pdf')
Define the file format of recorded images.

3.3 plot_Tupdate

In [5] : plot_Tupdate('filename')

Displays the temperature maps extracted from 'filename_T_update.dat'
Keywords :
— **path** 'string' ('')
Indicate the path to find the files to be read. Will read the file path/filename.

— **dat** 0 or 1 (1)
If set to 1, automatically add '.dat' at the end of 'filename'.

— **unity** 'pc' or 'AU' ('pc')
Indicate the unit to be used on the axis.

— **rec** 0 ou 1 (0)
If set to 1, will record the displayed images, using 'saveformat' format and 'outname' name for files.

— **saveformat** 'pdf' or 'png' ('pdf')
Define the file format of recorded images.

— **size** positive integer (100)
Define the number of pixel to be used on each axis to display profiles and maps.

4 MontAGN class objects

MontAGN has a class object called `model` which keeps all the important parameters about the simulation. It is therefore possible to have access to these parameters, at the end of a simulation or before its start. A `model` object contains :

— **sources** ()
list of sources

— **af** ()
aperture of the funnel

— **graininfo** ()
structure containing information about dust species

— **Rsub** ()
list of sublimation radii

— **energy** ()
energy of a packet

— **Dt** (`0`)
time length if the simulation

— **ndiffmax** (`50`)
maximum number of scattering allowed

— **usemodel** ()
indices of model to be used

— **thetaobs** (`[90]`)
inclination of observation, for final plotting

— **thetarec** (`[0,45,90,135,180]`)
list of recorded angles (not used any more)

— **dthetaobs** (`5`)
angle interval for registration into files

— **usethermal** (1)
whether use or not the re-emission

— **Temp_mode** ()
temperature method used

— **nRsub_update** (0)
whether use or not the sublimation radius evolution

— **map.res** ()
resolution of the grid

— **map.Rmax** ()
size of the grid

— **map.N** (int(Rmax/res)+1)
number of cells along an axis (the grid is $8 \times N^3$)

— **map.grid** ([])
grid containing all dust densities as well as temperatures

— **map.dust** ()
list of dust distribution used

Chapter 6

Observation Analysis through Simulations

Contents

In this chapter, we will use simulation tools and especially the MontAGN code, described in Chapter 5, with the goal to go further in the interpretation of the polarimetric observations conducted on NGC 1068 and detailed in Chapter 4 and Gratadour et al. (2015). In particular, we aim at reproducing the central region of low degree of polarisation at a constant position angle with a ridge of higher polarisation degree at the very centre of the AGN.

As said before, polarisation allows us to have access to more information. What is important here is that polarisation gives clues on the history of the successive matter-light interactions. Photons can be emitted already polarised if the source is for instance composed of elongated and aligned grains (see e.g. Efstathiou et al. 1997). But light can also become polarised if scattered or if there is unbalanced absorption by aligned grains. Polarisation is therefore a powerful tool to study the properties of scatterers such as dust grains or electrons in AGN environments. Polarimetric

measurements can also help to disentangle the origin of polarisation between spherical and oblate grains, as discussed in Lopez-Rodriguez et al. (2015) and put constraints on the properties of the magnetic fields around the source, as it is likely to align non spherical dust grains. This would be seen as polarised light through dichroic emission and absorption (see Packham et al. 2007). Differences between oblong and spherical grains will be discussed in section 6.3.

6.1 Observational Constraints for Simulations

We will base our models on the unified model of AGNs, proposed by Antonucci (1993), presented in section 1.4 and detailed in the case of NGC 1068 in section 4.1.1. For such complex environment, simplified models are easier to handle to test basic ideas and we thus approximated the nucleus of NGC 1068 as its essential components: the CE, the ionisation cone and the torus (see section 4.1.1).

Our assumption was that the optically thick torus would block direct light from the hottest dust and that we would see light scattered twice. The first scattering would take place in the ionisation cone, allowing some photons to be redirected toward the outer part of the equatorial plane and then undergo a second scattering (see blue path on figure 6.1 for illustration). If we detect such photons, the signature would be a polarisation pattern aligned with the equatorial plane. This is an analogous phenomenon to the one observed in the envelope of YSOs as proposed by Bastien & Menard (1990) and Murakawa (2010). In this configuration, spherical grains can alone produce these signatures in polarisation images. This should constrain the optical depth of the different components as we will investigate hereafter.

The torus is more likely to be clumpy, as discussed in section 4.1.2, however we will first limit our models to uniform structures, each with a constant density, to ease simulations and analysis. We have tested a range of optical depth between $\tau_V = 20$ and 100 for the torus median plane. We based this choice on the current estimations of about 50 in visible, for example as derived by Gratadour et al. (2003). Note that more recently, Lira et al. (2013) or Audibert et al. (2017) found higher values of optical depth and that both these authors derived them assuming clumpy structures.

The difference in polarisation arising from the choice of uniform or clumpy structures was investigated, in UV - visible, by Marin et al. (2015). Their conclusions was that fragmentation, of the torus mainly, but they also tested it in the NLR, has a significant impact on the observed polarisation (angle and degree). It however becomes much less significant when looking at AGNs with an inclination of about 90°, as shown by their figure 12 in particular. In the case we studied, using or not fragmentation should therefore not affect the overall observed polarisation degree and our results should therefore be also consistent with a fragmented medium. One point that should however be investigated further is whether this could significantly affect the polarisation locally when mapped at high angular resolution.

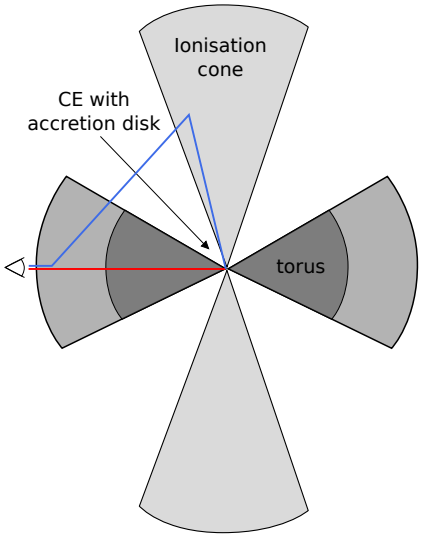

Figure 6.1 – Example of two photon paths on an AGN environment: the blue path will have an integrated optical depth of about 1–4 while the red one will be about 50–200.

6.2 Structures Geometry

6.2.1 First Toy Models

We first developed a set of three models to compare the results of simulations through both the MontAGN and STOKES codes (Goosmann & Gaskell 2007; Marin et al. 2012, 2015) in a simple case. Detailed informations about the comparison of both codes can be found in Grosset et al. (2016) and first analysis and conclusions are also available in Marin et al. (2016b), both shown in section 5.9. As the two codes are not aimed to work in the same spectral range, namely the infrared for MontAGN and the NIR, visible, UV and X-rays for STOKES, we selected intermediate and overlapping wavelengths: 800, 900 and 1000 nm. Our baseline basic models included only silicates grains in the dusty structures and electrons in the ionisation cone. All grains data, including graphites used in other models, come from Draine (1985). In all cases, the grains were set to dielectric spheres with a radius ranging from 0.005 to 0.250 μm and a power law of -3.5, following MRN distribution as defined in Mathis et al. (1977).

The three models are based on simple geometrical features with constant silicates or electrons densities:

— A flared dusty torus, ranging from 0.05 pc to 10 pc, a value typical of what is currently estimated (Antonucci 1993; Kishimoto 1999; García-Burillo et al. 2016). It has a half opening angle of 30° from the equatorial plane and an optical depth of 50 at 500 nm in the equatorial plane.

— An ionised outflow, containing only electrons in a bi-cone with a half opening angle of 25° from the symmetry axis of the model, from 0.05 pc to 25 pc with

an optical depth of 0.1.

— An outer dusty shell ranging from 10 pc to 25 pc, outside of the ionisation cone, with a radial optical depth of 0.5 at 500 nm.

Model 1 is built with these three components, model 2 with only the torus and the outflow and model 3 is reduced to the torus only (model 3). See figure 6.2 for density maps of each model.

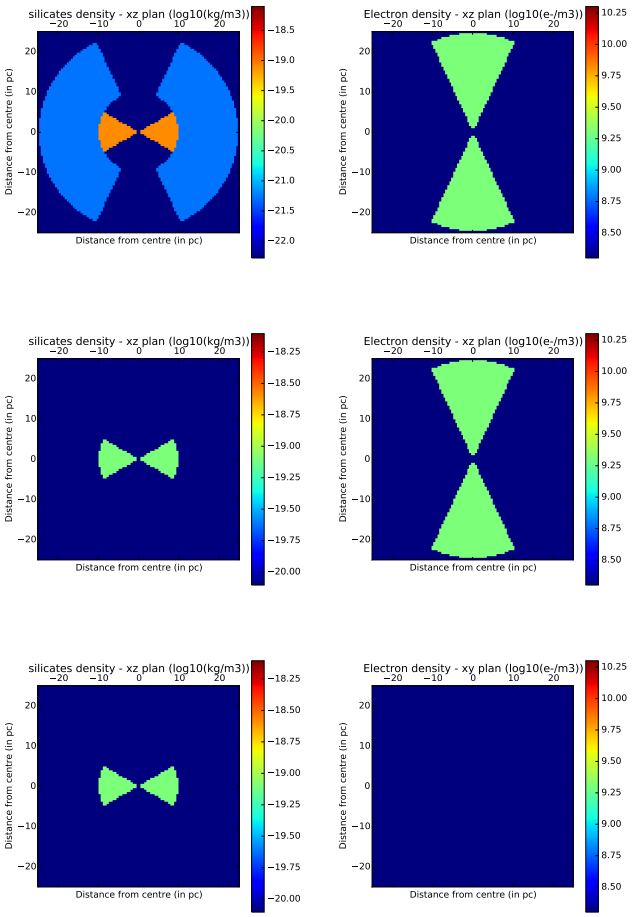

Figure 6.2 – Vertical slices of grain density of silicates (in $\log_{10}(\mathrm{kg/m^3})$, first column) and density of electrons (in $\log_{10}(\mathrm{e\text{-}/m^3})$, second column) set for model 1 (first row), model 2 (second row) and model 3 (third row).

We launched for each of these models 10^7 packets, disabling re-emission and considering only the aforementioned wavelengths. All inclination angles were recorded. We only show in figure 6.3 and 6.4 the $\lambda = 800$ nm maps at an observing angle of 90° (edge on).

Packets are selected for computing the maps on a certain range of inclinations. In this work, we used the range ±5° and the images computed at 90° are therefore

including photons exiting with an inclination in the range [85°,95°].

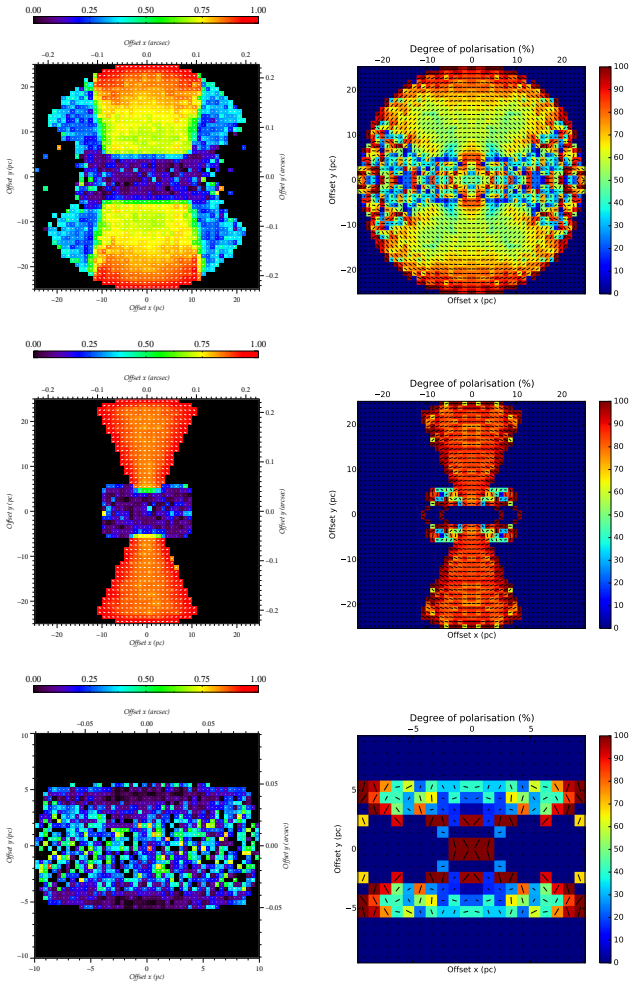

Figure 6.3 – Maps of the polarisation degree with an inclination angle of 90° at 800 nm for model 1, 2 and 3. First column shows maps from STOKES, second column corresponds to MontAGN maps. First row is for model 1, second row for model 2 and third row shows model 3. Polarisation vectors are shown, their length being proportional to the polarisation degree and their position angle representing the polarisation angle

As showed in figure 6.3, results between the two codes are in fairly good agreement, as expected from Grosset et al. (2016) and Marin et al. (2016b). The few observed differences arise likely from the divergence in the simulation strategy. Because MontAGN (in the configuration used here) propagates photons packets sometimes having suffered strong absorption, the pixels with a low number of photons do not contain reliable information (see section 5.7). However, as the packets number increases, the maps converge toward a more realistic result, close to the output of STOKES. In the central regions, we only have few photons recorded. This is expected because photons

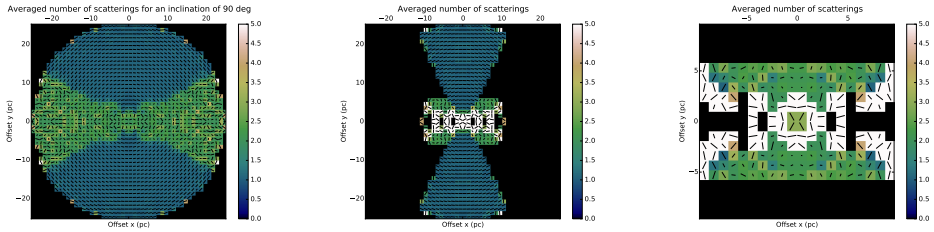

Figure 6.4 – Maps of the observed averaged number of scatterings with an inclination angle of 90° at 800 nm for model 1, 2 and 3 with MontAGN. Polarisation vectors are shown, their length being proportional to the polarisation degree and their position angle representing the polarisation angle ($p = 1$ is represented by a length of a pixel size).

escaping here have been scattered several times, their number decreases strongly at each interaction because of the low albedo. For this reason, the central regions differ slightly between STOKES and MontAGN results, especially in their outer parts.

In model 1, we get two different regions. First a central region mainly composed of photons that have been scattered twice. The second region is separated into two polar areas of single scattering. These appear in blue in the maps of figure 6.4. As it is expected in this configuration (discussed in Fischer et al. 1996 and Whitney & Hartmann 1993 for example), we observe at north and south two well define regions of centro-symmetric polarisation position angle. In these two zones, photons are scattered with an angle close to 90° which ensure a high degree of polarisation and a polarisation position angle orthogonal to the scattering plane, leading to this characteristic pattern (see section 3.3.3 for details).

The central belt is mostly dominated by the photons scattered twice. Therefore it traces the regions that photons can hardly exit without scattering, because of the optical depth of the medium: these are the areas obscured by the torus. However there is no clear privileged direction of polarisation angle in this central band. This is likely to be due to the surrounding medium, allowing the first scattering to take place in any direction around the torus, a conclusion that leads us to define model 5 (described in next section).

Model 2 only differs by the lack of a dust shell surrounding the torus found in the first model. The signal clearly shapes the ionisation cone as a region of single scattering, and the torus region. In this second area, the centre is not tracing photons scattered twice, but photons that undergo multiple scattering (5 or more). The role of the shell is therefore critical for the central signal we observe with model 1. It provides an optically thin region where photons can be scattered, without going through the optically thick torus (see sketch on figure 6.1).

This is confirmed in model 3, which reproduces quite well the results of model 2 in the torus region despite the lack of an ionisation cone in which the photons can undergo their first scattering.

6.2.2 Double Scattering Models

As these simple models were not able to reproduce well enough the observed horizontal polarisation in the central inner parsecs of Gratadour et al. (2015), we then added some features. Namely we increased the density of the torus to an optical depth of nearly 150 at 800 nm (model 4) and replaced in a second model the outer shell by an extension of the torus with lower density (model 5). See figure 6.5 for the density maps.

We used for these models two different dust compositions, only silicates on one hand and a mixture of graphites (parallel and orthogonal) and silicates grains in the other hand. The ionisation cone contains only electrons in both cases. In the case of silicates and graphites, we used the following number ratio: 37.5 % silicates, 41.7 % orthogonal graphites (electric field oscillates in a plane perpendicular to the graphite plane) and 20.8 % parallel graphites (electric field oscillates in a plane parallel to the graphite plane), based on Goosmann & Gaskell (2007). Other ratio could be considered, for example by using the work of Jones et al. (2013). Pure silicate and mixture models share the same τ_R.

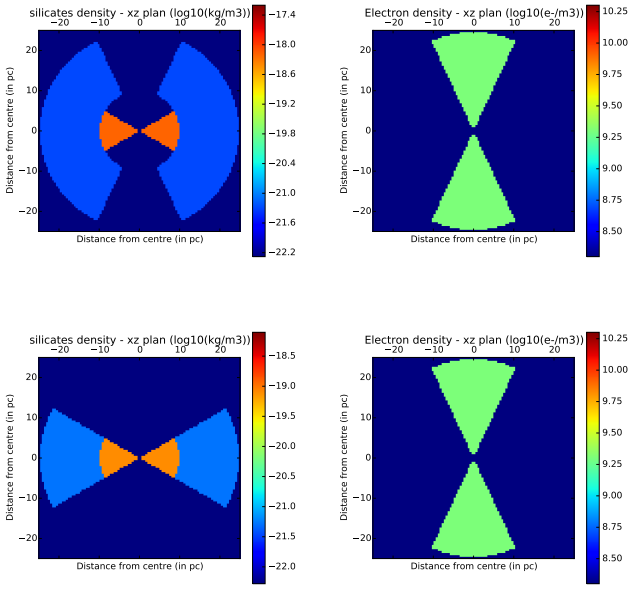

Figure 6.5 – Grain density of silicates (in $\log_{10}(\mathrm{kg/m^3})$, first column) and electron density (in $\log_{10}(\mathrm{e^-/m^3})$, second column) set for model 4 (first row) and model 5 (second row) (shown here for the silicates-electron composition).

We ran each of these models with 10^7 photons packets launched, without re-emission and considering only the wavelengths 800 nm and 1.6 μm. All inclination angles were recorded. We show in figures 6.6 and 6.7 maps derived from the MontAGN simulations. These correspond to maps of averaged number of scatterings with polar-

isation vectors ($p = 1$ is represented by a length of a pixel size), for models with the two dust compositions.

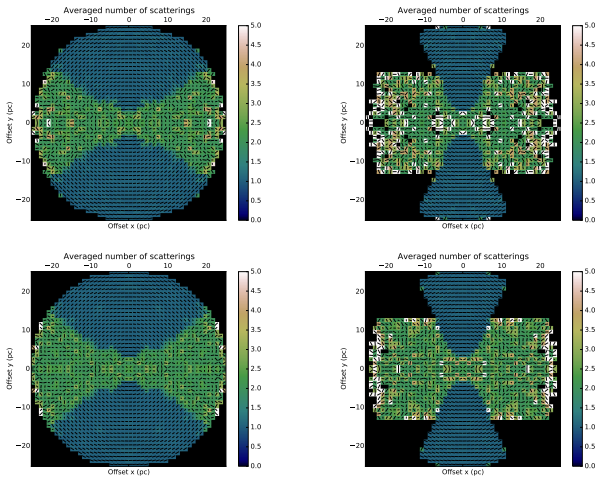

Figure 6.6 – Maps of the observed averaged number of scattering with an inclination angle of 90° at 800 nm with MontAGN. Polarisation vectors are shown, their length being proportional to the polarisation degree and their position angle representing the polarisation angle. The first two images are for models with silicate and electrons, the last two images for models with silicates, graphites and electrons. The first and third images correspond to model 4 and the second and fourth to model 5.

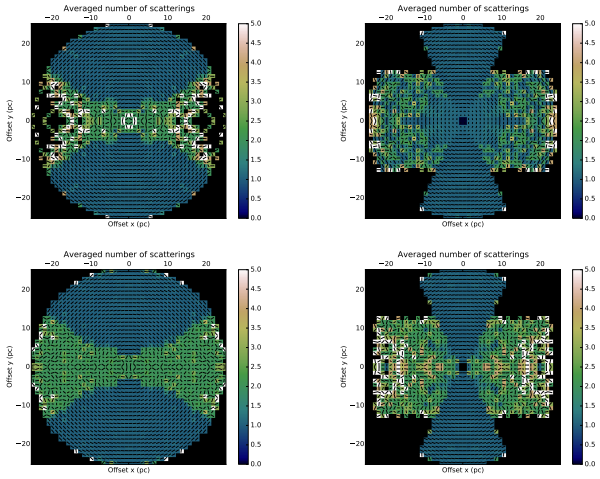

Figure 6.7 – Same as figure 6.6 but at 1.6 μm.

One should first notice that the dust composition slightly affects the results, mostly on maps of figure 6.7. This is likely due to the difference in optical depth introduced

by the difference in composition [1] as it will be discussed later in section 6.3.

The centro-symmetric regions of model 4 are similar for both dust composition at 800 nm and 1.6 μm and are similar to results of model 1. As the optical depth of the torus should not affect this part of the maps, this is consistent. However, the results found with model 4 are very close to those observed with model 1, even in the central belt. In this region, most of the photons undergo two scatterings at 800 nm for model 4, the only difference arises from the model with silicates where we see that a slightly larger fraction of photons have undergone more than two scattering events. At 1.6 μm, there are almost no photon coming from the regions shadowed by the torus on the outer central belt, with the pure silicates model. Again this is an effect of optical depth (see section 6.3)

Model 5 (second and fourth images of figure 6.6 and 6.7) differs more from the previous models. By adding a region, spatially limited, where photons can be scattered a second time, hidden by the torus from the emission of the source, we see a large region of light scattered twice. Polarisation in this area in the 800 nm map shows a clear constant horizontal polarisation. This is not visible on the 1.6 μm map, where the optical depth of the torus is not high enough to block photons coming directly from the AGN centre.

6.2.3 First Interpretations

In the ionisation cone, we are able to reproduce the observed centro-symmetric pattern at large distance from the centre. This is expected from photons scattered only once (see e.g. Marin et al. 2012). The maps of the average number of scatterings confirm that in all these regions, we see mainly photons scattered a single time.

More interesting is the central region. We are able to reproduce with model 5 (figure 6.6) a horizontal polarisation pattern, at least at 800 nm. This is comparable to what was obtained in the case of YSOs by Murakawa (2010) (see for example their figure 6). The case of YSOs is however very different from AGN in terms of optical depth, which is about 6.0x10^5 in K band in the equatorial plane. However the geometry of the dust distribution is somewhat similar, with two jets in the polar directions and a thick dusty environment surrounding the central source. We based our interpretation of the pattern observed in NGC 1068 on the effect called "roundabout effect" by Bastien & Menard (1990) and used by Murakawa (2010) to describe the photons path in YSOs. In AGN environments, despite having an optically thick torus, we do not expect such high optical depth. Studies tend to argue for optical depth lower than 300 in the visible as discussed in section 6.5.2.

As said before, to be able to see horizontal polarisation with only spherical grains, it is necessary to have a region, beyond the torus, with lower optical depth at the considered wavelength (typically under 10), for the photons to be scattered a second time toward the observer. This is realistic because one can expect the external part of the torus to be diluted into the interstellar medium, with a smooth transition. Raban

1. The optical depth is the same in R but evolves differently depending on the dust composition

et al. (2009) used two components with different extension and temperature to fit their observations. Furthermore, the theory of disk wind (Emmering et al. 1992) being at the origin of torus, described for example in Elitzur & Ho (2009), would support such dilution.

The ionisation cone is an important piece as it is required for the first scattering. However, while comparing results of model 1 and 5, it seems important to have a collimated region for this first scattering to happen because all photons will have almost the same scattering plane which therefore leads to a narrow range of polarisation position angle. This is not the case in model 1 where photons could interact not only in the ionisation cone but in all the outer shell.

6.3 Discussion on Composition

6.3.1 Oblong Aligned or Spherical Grains

One major composition difference that has been investigated for nearly 30 years is whether polarisation is due to dichroic absorption or emission through elongated aligned grains, or comes from scattering. Because of their shape, non spherical grains would emit or absorb photons in a non uniform fashion as a function of their polarisation. If they are randomly distributed, one should expect the difference in polarisation to be averaged and not significant. However, if aligned, polarisation can arise directly from absorption or emission of these grains. This model was discussed in Efstathiou et al. (1997), who investigated through simulations the effect of aligned dust grains on polarisation.

A critical feature of dichroism is the switch in polarisation angle induced by the transition from absorption to emission as a function of the wavelength described by Efstathiou et al. (1997). This should theoretically drive a 90° orientation modification of the polarisation angle since the preferred direction of absorption at short wavelengths will become a direction of emission at longer wavelengths. Such a transition was observed on NGC 1068 by Bailey et al. (1988) with a polarisation PA of approximately 120° under 4 μm and a PA of 46±8° above. This was interpreted as arising from the presence of elongated aligned grains by Efstathiou et al. (1997).

In this case, this alignment could be induced by strong magnetic fields around the nucleus (see for example Bailey et al. 1988; Efstathiou et al. 1997). This allowed Aitken et al. (2002) and Lopez-Rodriguez et al. (2015) to constrain this hypothetical magnetic field using polarimetric simulations and observations. However, the precise modality of this alignment process in this configuration on a rather large scale (60 pc as observed in Chapter 4) is still to be established. For instance if it is due to magnetic field, it would require a toroidal component because we expect the polarisation pattern to be parallel to the magnetic field in the case of dichroic absorption as discussed in Aitken et al. (2002) and Lopez-Rodriguez et al. (2015).

Bastien & Menard (1990) and later Murakawa (2010) have shown that scattering on spherical grains can reproduce some of the features attributed to elongated grains.

In particular, the horizontal pattern reproduced thanks to model 5 was also obtained by Murakawa (2010) (see figure 6 of the paper). The wavelength dependency of the scattering on spherical grains is however still to be investigated in the case of multiple scattering, but could hardly reproduce the wavelength switch with simple scattering. For these reasons, the inclusion of aligned elongated grains is an important future improvement for our model.

6.3.2 Dust Composition

Dust composition also has an effect on the polarisation maps. Optical depth evolution as regard to the wavelength is dependent on the dust species. This is triggered by the difference in extinction coefficient shown in figure 6.8. Because we used different dust compositions, despite fixing the optical depth at a given wavelength, optical depths will evolve differently. For instance, with $\tau_V \approx 50$, we have $\tau_H \approx 2.7$ in the pure silicates case and $\tau_H \approx 11.6$ with the mixture of graphites and silicates.

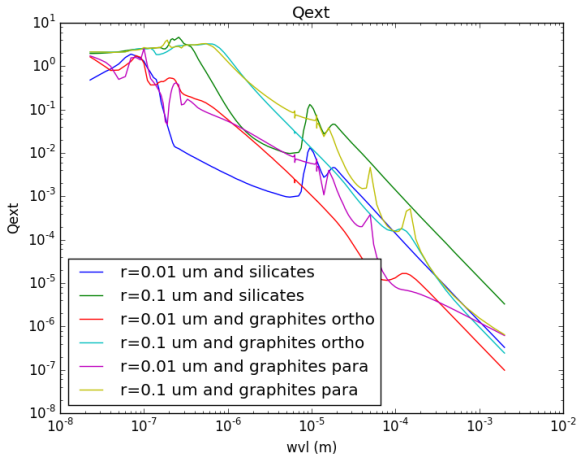

Figure 6.8 – Extinction coefficient Q_{ext} in function of wavelength, grain radius r and grain type (data from Draine 1985).

This also explains why there are almost no photons in the equatorial belt of upper panel of figure 6.7 (pure silicates), as opposed to the case with silicates and graphites. The extended torus region indeed has in the pure silicate model a low optical depth at 1.6 μm and photons have a low interaction probability in this area, making the signal in the equatorial belt hard to detect. This will be discussed and used later to study the role of the optical depth in the outer torus.

6.3.3 NLR Composition

When Antonucci & Miller (1985) first observed broad emission lines in the polarimetric spectra of NGC 1068, they estimated that the scattering was likely to happen on free electrons in the NLR. It was thought before that dust scattering may be the

dominant mechanism as explained by Angel et al. (1976) because of the shape of the spectra. The presence of electrons in a highly ionised gas is currently mostly accepted, with a higher density closer to the centre, despite discussions on the presence of dust components in the NLR as for example by Bailey et al. (1988) and Young et al. (1995), invoked to explain observational features especially in the NIR.

We assessed two versions of our two first models. The first version is the one showed in section 6.2.1 with the densities displayed on 6.2, containing electrons in the ionisation cone. The second version uses the same dust densities in the torus and the outer shell, but we replaced electrons by silicate grains in the ionisation cone, with a density allowing to have the same optical depth in the V band. This provides the ability to evaluate the respective impact of the two types of scatterings. Images generated with these two versions are shown in figure 6.9 for model 1 and 6.10 for model 2.

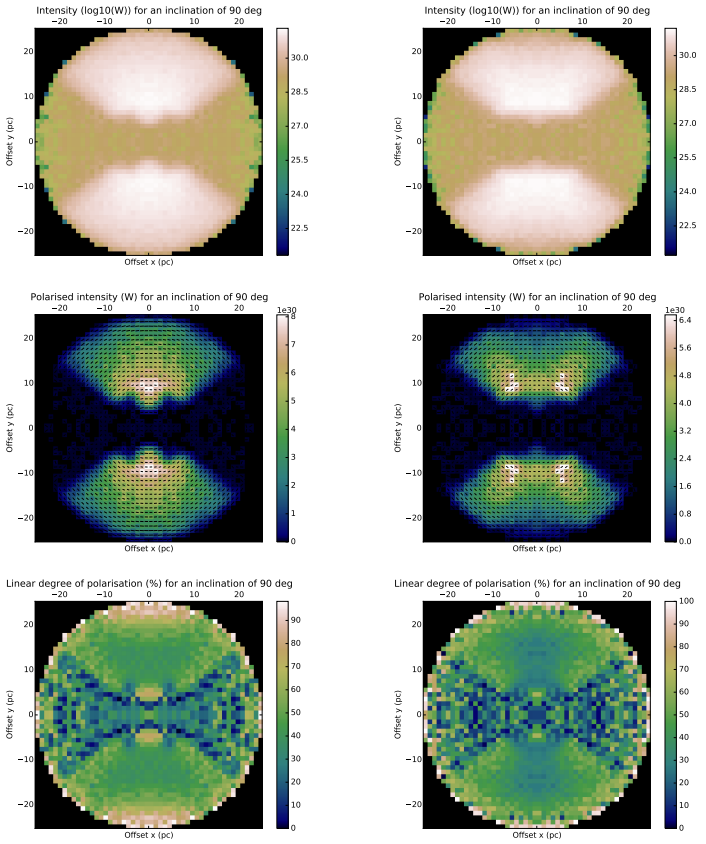

Figure 6.9 – Maps obtained from model 1 with MontAGN with an inclination angle of 90° at 500 nm. The first column corresponds to ionisation cone with electron, the second one with silicates, both after launching 1.5×10^7 packets. The first row shows the total intensity (in $\log_{10}$(J)), the second row the linearly polarised intensity (in J), with polarisation vectors represented, and the last row shows the linear degree of polarisation (in %).

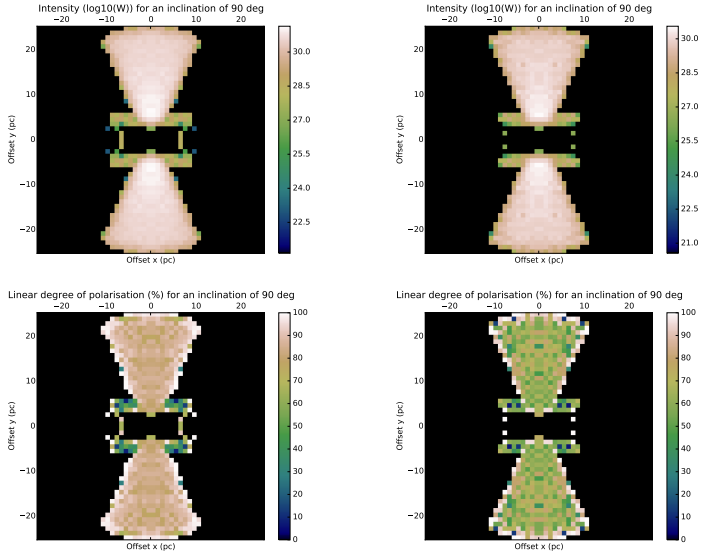

Figure 6.10 – Maps obtained from model 2 with MontAGN with an inclination angle of 90° at 500 nm. First column correspond to ionisation cone with electron, second one with silicates, both after launching 1.5×10^7 packets. First row shows the total intensity (in $\log_{10}$(J)) and second row shows the linear degree of polarisation (in %).

We observe that in the cone, the flux due to scattering on electrons is stronger than the one coming from scattering on silicate grains on both figures 6.9 and 6.10. This difference stems directly from the absorption properties. Silicates through Rayleigh scattering and electrons with Thomson scattering have the same scattering phase functions. However electrons have an absorption coefficient of 0 while silicate's is close to 1 and depends on the wavelength. This increased flux coming from the ionisation cone is the effect that allows photons to be scattered twice on the central belt because it sends more photons toward this region.

Note that the linear degree of polarisation is also slightly lower in the cone if coming from dust scattering. It is however though to compare this feature to observations because we need to include the dilution of polarisation by thermal emission as well as by ISM and galactic influence.

6.4 Optical Depth

6.4.1 Models

In order to measure the impact and significance of the optical depth, we ran a series of models based on model 5, differing only by the optical depth of their components. Among the three main parameters, the ionisation cone, the torus and its extended region, we kept fixed the density of two of them and changed the last one's. First we took models with varying optical depth in the torus. In a second batch, we changed

the optical depth of the cone, and lastly we studied a variation in extended torus. The results are shown in figures 6.11, 6.12 and 6.13, respectively. Polarisation vectors are shown, their length being proportional to the polarisation degree and their position angle representing the polarisation angle. All these models contain the same mixtures of silicates and graphites as in model 4 and 5. 2×10^7 packets were launched per model, all at 1.6 μm where the optical depth is set. Some additional maps are available in figures 6.14 and 6.15. These maps were computed from the same model, at 1.6 μm in which optical depth of the cone is fixed to 0.1, 0.8 in the extended torus and 20 in the torus (in H band).

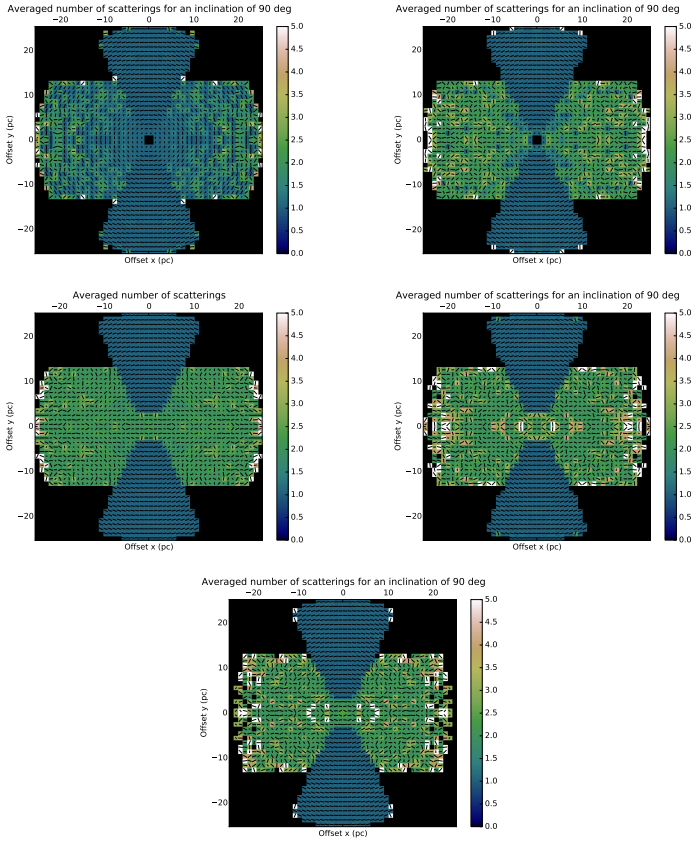

Figure 6.11 – Maps of observed averaged number of scattering with an inclination angle of 90° at 1.6 μm with MontAGN. Optical depth of the cone is fixed to 0.1, those of the extended torus to 0.8 and the torus one is respectively 5, 10, 20, 50 and 100 (in H band)

With the first series of simulation, (figure 6.11), we obtain similar results as in the previous cases. For a low optical depth in the torus, photons can travel without interaction through the torus and produce a centro-symmetric pattern, even in the central region. By increasing the density, the significance of these photons decreases until the double scattering effect becomes predominant (around $\tau \approx 20$). At this

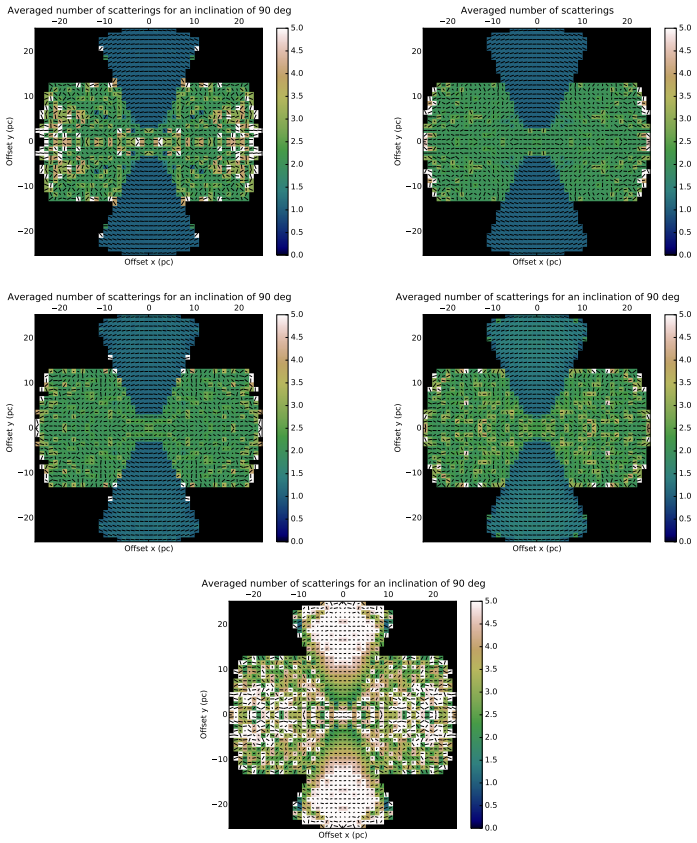

Figure 6.12 – Same as figure 6.11. Optical depth of the cone is respectively 0.05, 0.1, 0.5, 1.0 and 10.0, those of the torus and its extended part are fixed to 20 and 0.8 (in H band)

step, increasing the optical depth does not seem to change significantly the observed features.

With the second and third series, the density of the two other structures must be in a given range to obtain the constant horizontal polarisation pattern we are looking for. If these structures have an optical depth too low or too high, the central belt shows multiple scatterings as seen in both figures 6.12 and 6.13. In extreme cases with very high optical depth in the outer torus, we have no photons in this region, a case close to the simulations of model 2 (see figure 6.4). These two conditions seem to be critical to reproduce the features we are expecting.

A last remark is that the photons detected from the ionisation cone are not any more just scattered once at high optical depth in the cone (figure 6.12). However the centro-symmetric pattern seems to be somewhat similar for double scattering in the cone.

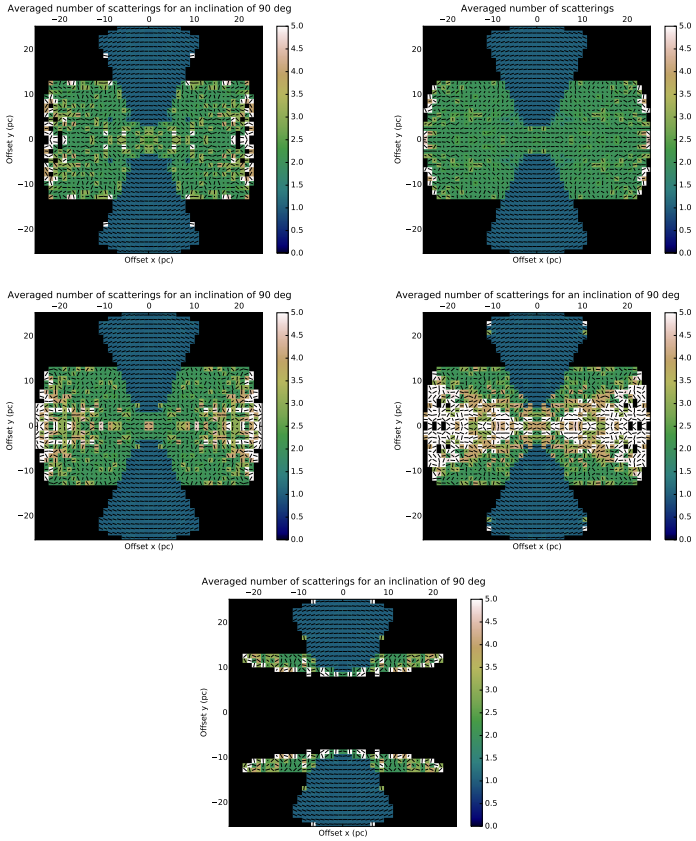

Figure 6.13 – Same as figure 6.11 and 6.12. Optical depth of the cone is 0.1, those of the extended torus respectively 0.4, 0.8, 4.0, 8.0 and 80.0. The torus one is fixed to 20 (in H band)

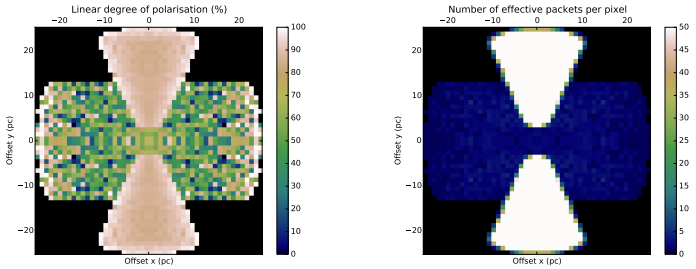

Figure 6.14 – Maps of observed linear polarisation degree (first image) and of effective number of packets (second one, effective number of packets is defined in section 5.7) with an inclination angle of 90° at 1.6 μm.

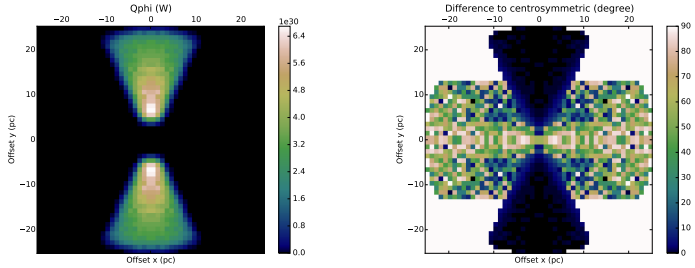

Figure 6.15 – Maps of observed Q_ϕ (tangential, first panel, corresponds to the image of the centro-symmetric polarised intensity), and of difference angle to centro-symmetric pattern so as computed in Gratadour et al. (2015), with an inclination angle of 90° at 1.6 μm.

6.4.2 Thick Torus

In order for the photons scattered twice to be dominant in the central region, it is necessary to have an optical depth high enough in the equatorial plane. If not, photons coming directly from the source, with single or no scattering will contaminate the observed polarisation and even become dominant, as said in section 5.7. The switch from one regime to the other is when the probability for a photon to emerge from the dust having suffered at most one scattering is of the same order as the probability of a photon being scattered twice. Note that because electrons do not absorb photons, they are much more efficient than dust grains for a given optical depth. Even with electrons in the cone, photons have to be redirected in the correct solid angle toward the equatorial plane and be scattered again without being absorbed in the observer's direction. The favourable cases to observe this signal seems to be for optical depth higher than 20 in the equatorial plane, as determined from figure 6.11.

This conclusion is in agreement with the observation that no broad line emission is detected in total flux when the AGN is viewed edge-on. With lower optical depth torus, we would have been able to detect such broad lines directly through the torus. This is not the case as demonstrated for example by Antonucci & Miller (1985) on NGC 1068 and Ramos Almeida et al. (2016) on a larger sample, who revealed these hidden lines only thanks to polarimetry.

6.4.3 Optical Depth of Scattering Regions

Another important parameter is the density of the matter in the cone and in the extended part of the torus. If both areas have low density, photons have a lower probability to follow the roundabout path and are less likely to produce the horizontal pattern, as seen in figure 6.12. But if the optical depth is too high in the cone and/or in the outskirts of the torus, typically of the order of 1–2, photons have a low probability to escape from the central region and will never be observed. We can see on the last two panels of figure 6.12 that the averaged number of scatterings in the cone is larger

than 1, and that the signal arising from the photons scattered twice becomes weaker in the central belt. The range of values which favours the constant polarisation signal in the centre is around 0.1–1.0 in the cone and 0.8–4.0 in the extended region of the torus. This corresponds for the outer torus to a density about 20 times lower than in the torus.

This underlines the significance of these two parameters and especially the extension of the torus. When comparing these results to the previous models, we noticed that on the first panel of figure 6.6 and 6.7, we observed few photons in the centre of the 800 nm image and almost none in the 1.6 μm image. The optical depth of the torus is lower in the second case and this region is therefore more easy to reach for photons in this configuration. The only factor that can explain this lack of photon at 1.6 μm is the optical depth difference in the outer shell, which is of the order of 0.5 at 800 nm and much lower in the NIR, to be compared to the 0.8 lower limit determined previously. The structure, composition and density of the torus (including its outer part) are therefore all intervening to determine the polarisation pattern in the median plane. To be observable, the horizontal polarisation requires a proper combination of the parameters within a rather narrow range.

6.5 Application to NGC 1068 Observations

6.5.1 NGC 1068 Model

Based on previous simulations, we tried to reproduce the SPHERE observations of NGC 1068. As we observed constant polarisation orientation in the core of NGC 1068 both in H and Ks bands, we need in our simulation an optical depth $\tau \geqslant 20$ at 2.2 μm to be able to generate such polarisation features. We changed our previous model 5 to adapt it to these larger wavelengths. Here, the torus has an optical depth $\tau_{Ks} = 19$, which gives $\tau_H = 35$ and $\tau_V = 169$. Note that this is in the range of the current estimation for the density of dust in the torus as it will be discussed in section 6.5.2. We used for this simulation a mixture of silicate and graphite grains to rely on realistic dust composition for an AGN, inspired from Wolf & Henning (1999). We adapted their mass ratio to number ratio according to Guillet (2008) leading to 57 % silicates, 28.4 % parallel graphites, 14.2 % orthogonal graphites.

With these parameters, maps of figure 6.16 are now able to reproduce some of the observed features. Namely, the constant horizontal polarisation in the central part is similar to the one observed on NGC 1068 at 1.6 and 2.2 μm. We are however not able yet to reproduce the ridge that appears on the very centre of the SPHERE observations.

6.5.2 Consequences for Observations

On figure 6.16, one can see that there are very few differences between H band and Ks band images. The optical depth of 169 in V band required for these images is

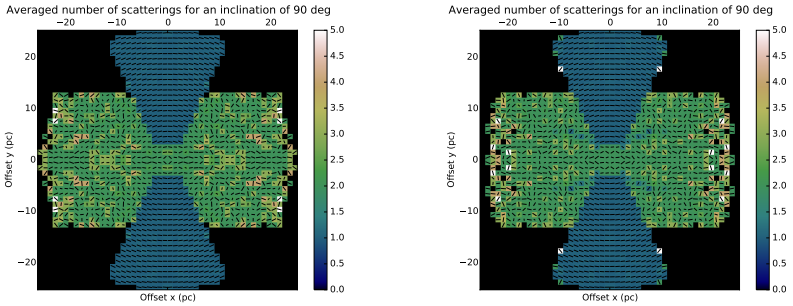

Figure 6.16 – Maps of observed averaged number of scattering with an inclination angle of 90° at 1.6 (top) and 2.2 μm (bottom). Polarisation vectors are shown, their length being proportional to the polarisation degree and their position angle representing the polarisation angle.

acceptable, being in the range of present estimations. Marin et al. (2015) use values of optical depth in the range 150–750 in visible, while Gratadour et al. (2003) derived $\tau_V = 40$. Assuming clumpy structures, Alonso-Herrero et al. (2011) obtained optical depth of about 50 in V per cloud fitting MIR SEDs of NGC 1068. Lira et al. (2013); Audibert et al. (2017) more recently found integrated values of optical depth of about 250, based on fits of the NIR and mid-IR spectral energy distributions of samples of Seyfert 1 and 2 galaxies. We have to keep in mind that all these optical depths are derived assuming a clumpy structure so that we should be careful when comparing them to optical depths of continuous dust distributions, the masses of dust being very different. It is in our plans to explore the effect of a clumpy structure, a capability already implemented in MontAGN.

A part of the polarisation may arise from elongated aligned grains as studied by Efstathiou et al. (1997) and introduced in section 6.3.1. If so, the required optical depth could change. This might explain the observed ridge on the polarimetric images of NGC 1068 and aligned elongated grains are therefore something we should investigate further.

Our interpretation does not require special properties for grains (elongated and/or aligned) and indeed, spherical dust grains in the torus coupled to electrons in the ionisation cone are able to reproduce the polarisation orientation in the central belt. We constrained in this case the optical depth of the structures to a rather narrow range of values. In the cone, the range of optical depth is in between 0.1 to 1. A value of 0.1 gives an electrons density of 2.0×10^9 m^{-3} which is consistent with the estimated range in AGN (10^8–10^{11} m^{-3} for NGC 1068 according to Axon et al. 1998; Lutz et al. 2000).

The only feature that our simulations do not seem to reproduce is the ridge at the very centre of NGC 1068 (Gratadour et al. 2015). Investigating a model with non spherical grains could potentially solve this problem through dichroism.

6.5.3 Wavelength Dependency

As introduced before, the considered scattering effects do not have the same wavelength dependency (scattering on dust, on electrons, dichroic absorption/emission) and observations in different bands can bring strong constraints on the dominant mechanism. This was the motivation of conducting the IRDIS NB observations shown in section 4.2.2.5. From these and the conclusion driven from simulations, we will try here to interpret the wavelength dependency of the features observed on NGC 1068.

Concerning the NLR structures, South-West of the nucleus, the different images from `CntH` to `CntK2` show a rather constant degree of polarisation, about 10–15 %. As demonstrated in section 4.2.2.3, this signal is unlikely to come from the depolarisation induced by the derotator. Furthermore, these structures are also detected on intensity maps and the SNR should therefore be sufficient to have a fair confidence on the obtained values. However we can not drive strong conclusions as long as the filters used have not been tested in polarimetric mode.

Assuming that this lower polarisation is due to physical processes taking place in NCG 1068, we can constrain the composition and temperature of observed structures. `CntK2` is the higher wavelength filter as shown in figure 4.8, centred around 2.275 μm (against 2.100 and 1.575 μm for `CntK1` and `CntH` respectively). For this reason we expect images with this filter to show more thermal emission from dust than in the other filters, potentially accounting for the dilution of the polarised signal. But as we identified these parts of the double hourglass structures in H, Ks, `CntH`, `CntK1` and `CntK2` polarimetric maps with a rather constant polarisation as a function of wavelength, this would be more consistent with electron scattering. This is in agreement with the results obtained on the previous section and with the studies of Axon et al. (1998); Lutz et al. (2000).

As opposed to the hourglass structures, the central feature is varying according to wavelength. Its polarisation degree is rather high on the `CntH` image (about 10–15 %), lower on the `CntK1` map ($<$ 10 %) and is not detected on `CntK2` image. However, this structure at the very centre is visible in the polarised intensity maps from `CntH` to `CntK2`, and are therefore not completely hidden. This would indicate the presence of dust in this region, at a temperature high enough for the dust to become a major emitter at 2.275 μm (roughly above 600 K), or with an optical depth close to 1–2 in the `CntK2` band.

Because emissivity and optical depth at 1.575 and 2.275 μm are close, we could theoretically constrain precisely the dust temperature or the density in this structure. This, however, requires a precise knowledge of the scattered flux and will be conducted later. It would be also risky to drive strong conclusions from data with non characterised filters. Furthermore, ZIMPOL observation in narrow R band brought new constraints, with the central region being detected with a degree of polarisation about 5 %, slightly slower than those obtained with IRDIS.

On these images, obtained in R band with ZIMPOL, we can roughly identify the inner parts of the bicone structures, situated about 1″ from the centre, visible as 5–10 % polarisation degree regions on the R maps.

Despite this low polarisation degree, the polarisation position angle map shows more precise patterns, once again indicating a clear polarising mechanism taking place on very luminous regions and therefore not dominating the total intensity. At large distance (≈ 1″), we seem to observe once again the previously analysed centro-symmetric pattern. In order to further investigate, we are currently simulating images at 646 nm with MontAGN, the first obtained image is shown in figure 6.17.

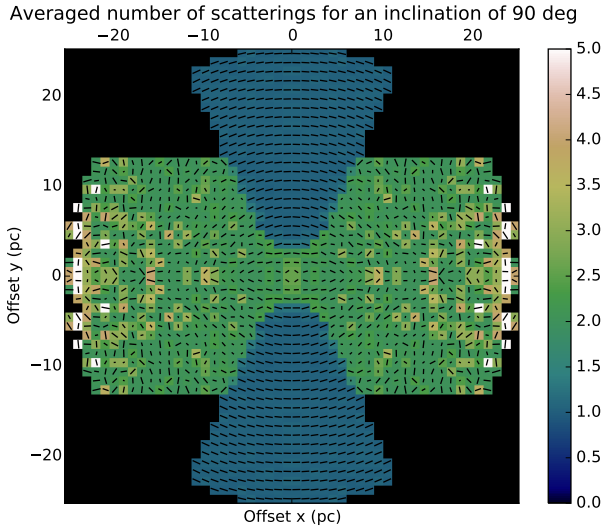

Figure 6.17 – Map of observed averaged number of scatterings with an inclination angle of 90° at 646 nm. Polarisation vectors are shown, their length being proportional to the polarisation degree and their position angle representing the polarisation angle.

Chapter 7

Conclusions and Prospectives

Contents

It will require yet a significant amount of work from committed scientists to fully understand the actual structure of the inner region of an AGN, or to backtrace the proper evolution of SSCs from their birth in extreme star formation regions to their late states, with a clear understanding of the impact of the period of their formation. It is exciting to be facing these unresolved problems and to participate to the construction of the new tools that will hopefully be able to give the answers to these questions, or at least to come closer to the solution.

In this last chapter, we will outline the results obtained in this thesis about two types of extragalactic objects, thanks to new adaptive optics techniques giving access to high angular resolution. In a first section, the preliminary results obtained with MOAO on SSCs will be summarised and in a second section we will present the major results of this work obtained on AGNs, thanks to the comparison between extreme AO corrected polaro-imaging in the NIR and simulations of radiative transfer featuring polarimetric capabilities using the code MontAGN developed in-house. We managed to simulate the inner dust structures of an AGN, with a special focus on NGC 1068, and found that the comparison with observations brings some clear constraints on the geometry and the density of the dust and electron structures. Finally, we will detail the perspectives opened by this work as well as the projected future work to improve the simulations and go further in the understanding of these objects.

At the scale of this work, our starting point on the SSC domain was to constrain the young cluster properties with questions such as: Are the SSCs the progenitors of the GCs ? Are the SSCs a extremely massive version of the OCs ? Do we lack information due to incompleteness of our sample ?

Concerning AGNs, the holy grail would be to build an AGN model which would perfectly reproduce all the observations at all wavelengths and for all type of objects. Obviously, our purpose was less ambitious, and we aimed at constraining the torus geometry on Seyfert 2 galaxies. Would this constrained structure also perfectly stand for other type of AGN ? Would it be possible to determine the composition of the

torus ?

7.1 Observations and Simulations

This work is mostly based on high angular resolution original data obtained thanks to the last generation of AO systems, one being a demonstrator giving a taste of the next generation of instruments. The results obtained here demonstrate the capabilities of these new techniques and illustrate the kind of scientific discoveries achievable thanks to them.

CANARY is a demonstrator of the new MOAO technology and was used on two extragalactic targets: IRAS 21101+5810 and NGC 6240.

While the images of IRAS 21101+5810 brought unprecedented informations, the observation of NGC 6240 with CANARY (on the WHT, a 4.2 m diameter telescope), did not bring improvements to the already existing images by NIRC2 on the Keck telescope (10 m diameter). We however did take advantage of these two sets of images to compare the quality of the data obtained thanks to MOAO with CANARY. This study, lead by Damien Gratadour, shows that despite using a new AO system, still under development and on a smaller aperture telescope, the results are close to the expectations for this system, reaching the same resolution as achieved by SINFONI (Spectrograph for INtegral Field Observations in the Near Infrared) on the VLT (note that SINFONI is an integral field spectrograph and is not optimised to obtain the highest angular resolution through BB imaging). A comparison of these images is shown on figure 7.1.

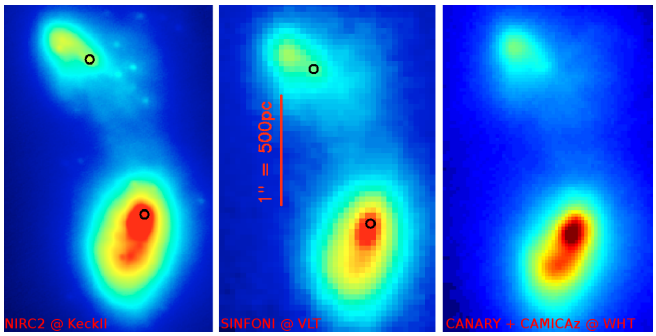

Figure 7.1 – Comparison of CANARY performances on Kp band images of NGC 6240. Left panel shows the Keck - NIRC2 image, at the centre is VLT - SINFONI image and right panel corresponds to the WHT - CANARY map. Image from Damien Gratadour.

These performances give confidence in the future development of MOAO and its ability to achieve on sky an excellent resolution on several targets simultaneously.

SPHERE is the new exoplanet hunter installed since late 2014 on the VLT. It features an extreme AO system, giving access to high contrast capabilities and to a HAR, which are required to image exoplanet or disks around young stars. However, it reveals powerful as well at unveiling the inner region of an AGN.

Our three observing runs of NGC 1068 with SPHERE highlighted the gain brought by very good AO corrections when observing nearby galaxies. This idea is not new as our team already applied this method on NGC 1068 with PUEO-CFHT (Rouan et al. 1998), then with NaCo (Rouan et al. 2004 and Gratadour et al. 2005). The difference between the previous NaCo observations and the new SPHERE data illustrates perfectly the improvements achieved on this 2nd generation of instrument on the VLT. Despite the fact that NGC 1068 was a difficult target because its magnitude was just at the SPHERE sensitivity limit, SPHERE images show a very satisfactory resolution as well as high contrast (weak wings on the PSF), critical for the study of the inner structures. Furthermore, the use of polarimetry revealed an important piece of information, out of reach without this technique. Analysing polarimetric data is more complex, but thanks to modelling, it is possible to derive new conclusions and therefore improve our understanding of AGNs inner regions.

Last but not least, we developed a radiative transfer code to reproduce the observed polarimetric features directly from the inferred geometry of the inner region of the AGN. This simulation code was entirely developed at LESIA, thanks to an initial release by Jan Orkisz and a complete update toward polarimetric capacities in the context of this thesis. Radiative code already revealed themselves as very powerful when trying to interpret complex sets of data, but when applied to the polarimetric studies of this work, MontAGN allowed us to go deeper in the fundamental understanding of an AGN inner parsecs.

7.2 Super Stellar Clusters

Thanks to the other set of data from CANARY, we were able to conduct a preliminary study of the SSCs in IRAS 21101+5810, the first for this galaxy. We implemented a new fitting algorithm, able to provide photometry on targets lying on a complex background. The tests conducted were satisfactory and the routine was able to fit properly most of the clusters, with a significant fraction of them being out of reach to more classical methods. In order to compare the results obtain with this tool, we also created colour maps of IRAS 21101+5810.

We then compared these results with the star formation simulator GALEV, which gave us colour indices for star clusters, at different evolutionary stage and with different sets of parameters.

Thanks to combination of these different tools, we obtained constraints on the extinction, about $A_V \approx 3$ on average for the system, and on the ages of the clusters in the system, which would be more compatible with ages roughly between 3 and 100 Myr, with a small dispersion in ages and in extinction between the clusters. Furthermore, the results are compatible with a metallicity following the evolution of the SSCs through feedback, but we can not exclude other metallicity.

By going deeper in the analysis, we should be able to better constrain the ages of the clusters, that might be linked to the starburst time-scale and therefore to the

dynamical scale of interaction of the two components. We aim also at improving our incertitudes by a better constraints on the algorithm. An improving, for example of the source estimation, would give access to a better background estimation and to an even more reliable photometry. This would also bring more statistics for the SSCs population, still limited in their understanding by the low number of observable systems.

We will be able thanks to these tools to analyse a growing number of SSCs. Indeed, we already obtained images of a third system, IRAS 17138-1017 that we will analyse through the same process. But on longer time-scales, we will have access to a significant larger sample of targets, thanks to the next generation of instruments. The JWST should be launched on newt year, and will provide a turbulence-free 6.5 m telescope that will be able to image with an unprecedented angular resolution on many extragalactic targets, among which several starburst galaxies, likely to feature SSCs. Furthermore, as demonstrated by CANARY, new AO systems will soon be able to increase the sky coverage for such targets. This, combined with the horizon of the ELTs, bringing the telescopes' diameters to almost 40 m, will give us a significant amount of work.

If we can reach SSCs situated in galaxies at larger distance from us, thanks to these new capacities, we will be able to trace the evolution of the characteristics of the SSCs as a function of redshift. With these new pieces of information, we should be able to improve our model of star and cluster formation, toward a model standing for all the different types of clusters.

This would for example help to assess the question of the multiple star populations highlighted by Krause et al. (2016). GCs show evidences of multiple populations, while SSC do not seem to show the same feature (see Moraux et al. 2016). Multiple scenarii were developed to try to explain these observed differences, but so far, no clear answer to this question was found (Bastian 2016). If this point was solved, we could then move to deeper investigations, like for instance precise studies of the impact of the clusters on the evolution of galaxies on long time-scales.

7.3 Active Galactic Nuclei

With our high angular investigation of the inner parsecs of AGN, we were successive in reproducing observed patterns thanks to simulations of a simple model. We applied this on NGC 1068, in which the observed polarisation pattern is compatible with the idea of photons scattered twice proposed by Bastien & Menard (1990) and later validated by Murakawa (2010) on YSOs. This was the basis of our analysis of our observations of NGC 1068 (Gratadour et al. 2015). The code MontAGN allowed us to simulate NIR polarimetric observations of an AGN featuring an ionisation cone, a torus and an extended envelope.

Despite limiting ourselves to a simple case where the various structures have a constant density of dust or electrons, we were able with spherical grains only, to

constrain the optical depth of the different dust structures so that obtaining a similar polarisation pattern as the one observed on NGC 1068.

We highlighted the important role of both the ionisation cone and the dusty torus. The cone allowed photons to be scattered toward the equatorial plane. In order for this redirection to be efficient, we found that electrons are much more satisfactory than dust grains, because they are non absorbing, a hint that these cones are more likely populated by electrons, as suspected by Antonucci & Miller (1985). We estimate the optical depth in the ionisation cone, measured vertically, to be in the range 0.1–1.0 in the first 25 parsecs from the AGN. This is confirmed by the first results from our series of observations from R to K NBs.

We found that for the light directly coming from the central region of the AGN to be blocked, the torus should have an in-plane integrated optical depth greater than 20 in the considered band, so $\tau_{Ks} \geqslant 20$ in the case of NGC 1068. Furthermore, the torus should not only be constituted of an optically thick dense part, but also of an almost optically thin extended part. We find satisfactory results with an outer part with optical depth $0.8 < \tau_H < 4.0$ and an extension ranging from 10 to 25 pc from the centre. We considered structures with constant density, something unrealistic, but we expect similar results for a more continuous torus with a density decreasing with distance to the centre. This is a direction in which we aim at carrying our study in the near future.

This work opens several perspectives as most of the studies conducted here will be investigated further. At short time scales, publication of the simulation code MontAGN will require to work on the input and output management in order to make the code easier to use for non-developers. This work will be the occasion to implement the last short term ameliorations planed. These include for example the setting of new dust geometries, like progressive dust torii or fragmented media, both already partially implemented. With these new tools, we will be able to conduct more realistic simulations and possibly being able to reproduce the few features that we could not observe through our simulations up to now, especially the ridge at the very centre of the observed polarisation maps.

There are other improvements that we will be able to conduct on longer time-scales. One major amelioration will be to include elongated aligned grains and potentially other dust species, like Polycyclic Aromatic Hydrocarbons (PAH) or nano-diamonds for example. This will give us the opportunity to study the polarisation patterns created by spherical grains and elongated grains, in the same conditions. We will therefore assess the question of the mechanism triggering the observed polarisation of the light from AGNs.

One particularly significant limitation to our studies is the time required for the simulations. Thanks to a long experience in GPU usage for scientific computations (in particular on AO systems) of the HAR team of LESIA, we were able to identify that the code MontAGN is possible to translate for GPU usages. Thus, we planed to make this change and we should be able to accelerate the code execution, making it

faster enough to bring new opportunities of usage of the code.

One other work that will be undertaken is the interpretation and publication of the newly obtained data on NGC 1068. Observation from IRDIS in September 2016 and from ZIMPOL conducted in early 2017 are currently analysed and we have already drawn some conclusions from early comparisons to our models.

We also already began to plan some follow-up observing programs. With the collaboration built with the High Energy team of Observatoire Astronomique de Strasbourg, we decided to extend this work toward new targets, to have access to a range of inclinations for AGNs and being able to study in detail the influence of the geometry on the observed polarisation. This program is made difficult by the fact that except for NGC 1068, other AGNs are difficult to targets with AO on ground based telescopes because they are fainter than NGC 1068 and not point-like sources. It is therefore very challenging to obtain polarimetric images of these objects, with a sufficient resolution and without risks.

However, such new observations could help to give strong constraints on the inner structures of AGNs, mostly constrained at HAR through the observations of NGC 1068. We aim for example at assessing the origin location of the polarimetric signal from polar scattering dominated AGNs. These Seyfert 1 galaxies are expected to be observed with a line of sight close to the vertical extend of the torus (Smith et al. 2004).

Appendix A

Proposals

Contents

European Organisation for Astronomical Research in the Southern Hemisphere

OBSERVING PROGRAMMES OFFICE • Karl-Schwarzschild-Straße 2 • D-85748 Garching bei München • e-mail: opo@eso.org • Tel.: +49 89 320 06473

APPLICATION FOR OBSERVING TIME

PERIOD: **97A**

Important Notice:

By submitting this proposal, the PI takes full responsibility for the content of the proposal, in particular with regard to the names of CoIs and the agreement to act according to the ESO policy and regulations, should observing time be granted.

1. Title

Category: **B–9**

Flushing out the nuclear torus of NGC 1068 with the exoplanet hunter

2. Abstract / Total Time Requested

Total Amount of Time: 1.5 nights VM, 0 hours SM

This proposal is the first part of a program of polarimetric observations in near-IR (H to K) at a high angular resolution of nearby Active Galactic Nuclei. AGN studies can take benefit of high contrast polaro-imaging which gives access to the colder part of the dusty torus traced either by Mie scattering or dichroic absorption/emission by dust grains. Broad-band polaro-images of NGC 1068 obtained in K and H during the SPHERE Science Verification last year indeed revealed a compact and elongated structure at a scale of a few tens pc, bracketing the quasi point-like central source. We propose here to complete this measurement by narrow-band polaro-images to look for wavelength dependent effect. We also propose coronagraphic imaging in the 1-0 S(1) H2 line to look for the molecular extension of the torus. In the coming semesters we aim at obtaining polaro-imaging of a sample of few close AGN in order to extend this kind of study to other targets with different characteristics.

3.

Run	Period	Instrument	Time	Month	Moon	Seeing	Sky	Mode	Type
A	97	SPHERE	1.5n=3H2	sep	n	0.8	CLR	v	

4. Number of nights/hours

	Telescope(s)	Amount of time
a) already awarded to this project:	UT3	5.5h in 60.A-9361(A)
b) still required to complete this project:	UT3	15h

5. Special remarks:

This program is an updated and extended form of proposal 60.A-9361(A) for SPHERE SV, which had been granted 5.5h with UT3+SPHERE and was partially executed.

6. Principal Investigator:

Lucas Grosset, lucas.grosset@obspm.fr, F, LESIA,

6a. Co-investigators:

D.	Gratadour	LESIA,,F
D.	Rouan	LESIA,,F
Y.	Clénet	LESIA,,F
A.	Boccaletti	LESIA,,F

Following CoIs moved to the end of the document ...

7. Description of the proposed programme

A – Scientific Rationale: Polarimetric observation is one of the key methodology to investigate the nature of AGN, as demonstrated 30 years ago by Antonucci and Miller who measured a broad line emission in the polarized light of NGC 1068 (Antonucci and Miller 1985), the archetypal Seyfert 2 galaxy which was catalogued as such because its standard spectrum exhibited only narrow lines. Assuming that a dusty torus could hide the broad line region in Seyfert 2, Antonucci (1993) proposed the unified model for AGN, stating that Seyfert 1 or 2 types were the same type of object harboring a luminous accretion disk surrounded by a thick torus, but seen under different viewing angles.

For many years, the AGN unified model has been tested with simulations (Marin et al. 2012) and confronted with a number of observations (see Gratadour et al. 2005 and Packham et al. 2007 for instance). As one of the closest Seyfert 2 galaxy at a distance of 14.4Mpc, NGC 1068 is an ideal laboratory to investigate further this model of AGN and its interactions with its host galaxy. Multi-wavelength observations at a few parsec scale allowed to discover several features close to the Central Engine of this object. This includes a structured radio jet (Gallimore et al. 1996) and a fan-shaped Narrow Line Region seen in UV and visible (Capetti et al., 1997). Near-IR is also very well suited to explore AGN environment because it allows to observe through dense dusty regions and traces the hot dust, especially the one at the internal edge of the torus, directly heated by the luminous accretion disk. Near-IR range also contains several lines of interest, among which are ro-vib lines of H2, recombination lines of H+ (Brγ) and FeII lines, tracing high energy phenomena like jets and accretion disks (Barbosa et al. 2014).

One master piece of the model is the presence of a dusty torus surrounding the central engine. Several hints point to its existence, however no clear imaging have been obtained so far. Last year we took advantage of the SPHERE excellent performances to propose, in the frame of the Science verification program, a polarimetric observation of NGC 1068 at the highest possible angular resolution. The Ks and H images, with and without a coronagraph, showed a very precisely defined hourglass-shaped polarization pattern centered on the bright core that fits very well the visible cone of the NLR and, even more important, the polarization angle maps traced a thin and compact elongated structure perpendicular to the bi-cone axis that we interpreted as the direct signature of the torus (Gratadour et al. 2015): see Figure 1.

The goal of the proposal is to go further in this approach of using polaro-imaging to probe the physical conditions in the torus of NGC1068.

One issue is to disentangle the origin of the peculiar polarization of the putative torus, either due to dichroic absorption/emission by aligned elongated grains or to Rayleigh scattering on more or the less spherical grains. In the first case the magnetic field intensity and orientation could be constrained. In the second case, the pattern we observed is compatible with scattering on spherical grains, as in the case of disks in YSO (Murakawa 2010), if the optical depth is of the order of unity, an important piece of information. The behavior of the polarization (degree and direction) with respect to wavelength could therefore indicate the actual dominant mechanism and give access to important parameters. We thus propose polaro-images in several narrow-band filters (continuum and Brγ). We also wish to benefit from the excellent correction by SPHERE to look for the emission of the hot molecular hydrogen in the very central region, a challenging observation given the important continuum, but it could locate the region where molecular hydrogen is protected enough to survive the intense UV field.

Observing a similar behavior of the near-IR polarization in other Seyfert galaxies would be extremely interesting, so we will propose in P98 a pilot program where a few nearby AGNs will be observed in broad-band polaro-imaging.

B – Immediate Objective: A first aim of the observations is to complete the near-IR polarimetric information in the very central nuclear region of NGC 1068 by obtaining four narrow bands polarimetric images, three in the continuum (filters Cnt H, Cnt K1 and Cnt K2) and one in Brγ. The basic idea is to look for a trend in the degree and direction of the polarization vector that could indicate polarization by dichroic absorption or dichroic emission by elongated grains and even a potential switch from one to the other mechanism (Efstathiou et al. 1997). Indeed, the polarization vector measured at 10 microns by Packham (Packham et al. 2007) is perpendicular to the one we measured at K, an indication of such a possible switch. In the case of the continuum NB filters, the dominant source of photons is the hot dust at the internal edge of the torus, practically a point source, while in the case of the Brγ filter, the ionized gas could fill a much larger volume so that comparison between the different maps could be indicative of the structuration of the medium. Note that we already developed a numerical model of radiative transfer, including scattering, that will be used to interpret the data set.

The second aim is to try to detect and measure the extent of the molecular hydrogen that should be the main component, in mass, of the torus. The difficulty, already faced in previous observations with NACO (Gratadour 2005) and SINFONI (Müller Sànchez et al., 2009) is that the continuum due to very hot dust is extremely high and dilutes the flux of the line. On the image obtained by Müller Sànchez et al. (Fig.2) there is a clear hint of an elongated structure in the H2 v=1-0 S(1) ro-vib line, aligned with the one we delineate in polaro-imaging, however the very central region cannot be mapped because of the high contrast. We expect that thanks to the use of the coronagraph in the 1-0 S(1) line, the most prominent central source of this continuum will be hidden,

Description of the proposed programme (continued)

so that the molecular torus will be detectable. If successful, this observation would bring strong constraints on the mass of molecular gas and on its distribution, two key parameters in the unified model of AGNs.

Attachments (Figures)

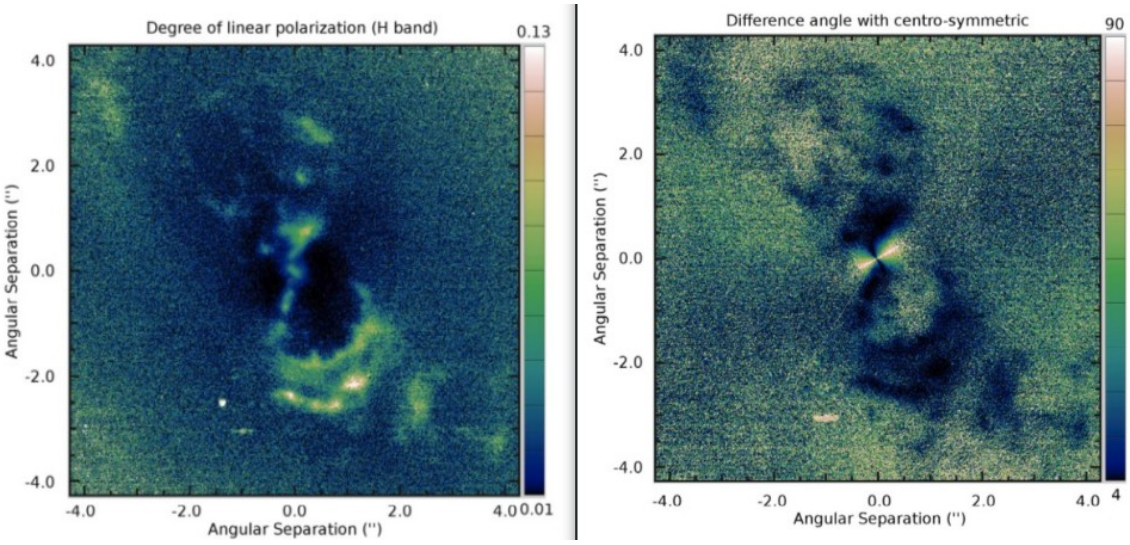

Fig. 1: Left panel : NGC 1068 nucleus, degree of linear polarization in H band. North is up, east to the left. Right panel : result of the difference between the polarization angle map and a purely centro-symmetric pattern in H band.

References:
Antonucci, R., 1993, A&A, 31, 473: Unified models for active galactic nuclei and quasars
Antonucci, R. R. J., & Miller, J. S. 1985, ApJ, 297, 621: Spectropolarimetry and the nature of NGC 1068
Barbosa, F. K. B. et al., 2014, MNRAS, 445, 2353: Modeling the [Fe II]1.644m outflow and comparison with H 2 and H + kinematics in the inner 200 pc of NGC 1068
Capetti, A. et al., 1997, ApJ, 487, 560: The ionization structure of the narrow-line region of NGC 1068 and its relationship to the extended radio emission
Efstathiou, A. et al., 1997, MNRAS, 285, 102: Polarization due tu dichroic absorption and emission by aligned grains in dusty discs
Gallimore, J. F., et al., 1996, ApJ, 458, 136: The subarcsecond radio structure in NGC 1068. I. Observations and results
Gratadour, D., 2005, PhD Thesis Université Paris Diderot
Gratadour, D. et al., 2015, A&A, 581, L8: Polarimetric imaging of NGC 1068 at high angular resolution in the near infrared. Direct evidence of an extended nuclear torus
Marin, F. et al., 2012, A&A, 548, A121: Modeling optical and UV polarization of AGNs II. Polarization imaging and complex reprocessing
Müller Sànchez, F. et al., 2009, ApJ, 691, 749: Molecular gas streamers feeding and obscuring the active nucleus of NGC1068
Murakawa, K., 2010, A&A 518, A63: Polarization disks in near-infrared high-resolution imaging
Packham, C. et al., 2007, Apj, 661, L29, Gemini mid-IR polarimetry of NGC 1068: polarized structures around the nucleus

8. Justification of requested observing time and observing conditions

Lunar Phase Justification: The Lunar phase requirement is linked to the VLT active optics which could encounter problems, according to the SPHERE manual, when the Moon is less than 30 degrees from the targets.

Time Justification: (including seeing overhead) ESO Exposure Time Calculators is not available for DPI mode of SPHERE. However, it is offered for the CI mode and the corresponding output can be used as an estimator for the DPI mode. Furthermore, as the same target has been observed with success during SPHERE SV, we were able to refine this estimate using available broad band polarimetric data and narrow band filters specifications.

To meet the strong SNR requirements, critical in polarimetric imaging, we request 3200s on target per band in DPI mode (DIT=16 x NDIT=20 x NEXPO=5 x 2 positions of the Half-Wave Plate) and 3072s in CI mode (DIT=64 x NDIT=16 x NEXPO=3). This should allow us to reach a SNR of about 100 (i.e. 1 percent error on the polarization angle) on the extended emission close to the central source along the torus axis. As we aim at measuring a small variation (few percents) in polarization angle from one narrow band to another, reaching this SNR is critical to our program. Since one of our main goals is to look for a trend in the degree and direction of the polarization vector on the very central source and its close environment, we need to avoid saturation on the core which explains the rather low DIT in our DPI mode observations as compared to the one calculated for the CI mode for which the DIT can be larger thanks to the use of the coronagraph.

Using the overhead formula given in the SPHERE Manual leads to 3200s per band in DPI mode and 3072s in CI mode which means a total of 6810s per band in DPI mode and 6258s in CI mode including skyes and overheads. Hence assuming 4 narrow bands filters in DPI mode and two filters in CI mode, we obtain a total time of about 11h. We thus request 3 half nights to complete this program and adding 6 acquisition templates (6x1320s) leads to a total observing time request of 13.3h.

8a. Telescope Justification:

SPHERE, with its extreme AO system, has already proven to be the only instrument allowing us to reach the required contrast close to the very central source of NGC 1068. While SPHERE has been designed to hunt for exoplanets, it shows excellent results on NGC 1068 because of the rather limited extension of the core (used as the guide source for the AO system) which dominates completely the extended emission at R. The performance achieved during SV significantly surpasses what was obtained with NaCO in the past decade which completely justifies the use of SPHERE for this program.

8b. Observing Mode Justification (visitor or service):

For SPHERE DPI observations, only visitor mode is offered. Additionally, several AO experts are involved in the team and will be able to provide critical advises for efficiently closing the AO loops on this extended target and optimizing AO performance to reach maximum contrast.

8c. Calibration Request:

Standard Calibration

9. Report on the use of ESO facilities during the last 2 years

SPHERE SV programme 60.A-9361(A) completed (P.I. D. Gratadour). Data published in D. Gratadour et al. 2015 (A&A, 581, L8).

9a. ESO Archive - Are the data requested by this proposal in the ESO Archive (http://archive.eso.org)? If so, explain the need for new data.

Data requested in this proposal are not available in the ESO Archive in polarimetric mode at this resolution.

9b. GTO/Public Survey Duplications:

10. Applicant's publications related to the subject of this application during the last 2 years

Gratadour D. et al., 2015, A&A, 581, L8: Polarimetric imaging of NGC 1068 at high angular resolution in the near infrared. Direct evidence of an extended nuclear torus

11. List of targets proposed in this programme

Run	Target/Field	α(J2000)	δ(J2000)	ToT	Mag.	Diam.	Additional info	Reference star
A	NGC 1068	02 42 40.771	-00 00 47.84	15.0	12.66	2 min		alt

Target Notes: The core of NGC 1068 will be used as the guide for Adaptive Optics

12. Scheduling requirements

13. Instrument configuration

Period	Instrument	Run ID	Parameter	Value or list
97	SPHERE	A	Field	IRDIS-CI
97	SPHERE	A	IRDIS-CI	N-ALC-Ks/NB-H2
97	SPHERE	A	IRDIS-CI	N-ALC-Ks/NB-CntK1
97	SPHERE	A	IRDIS-DPI	None/NB-CntK1
97	SPHERE	A	IRDIS-DPI	None/NB-CntK2
97	SPHERE	A	IRDIS-DPI	None/NB-CntH
97	SPHERE	A	IRDIS-DPI	None/NB-BrG

6b. Co-investigators:

...continued from Box 6a.

F.	Marin	Observatoire Astronomique de Strasbourg,F
R.	Goosmann	Observatoire Astronomique de Strasbourg,F
P.	Andrea Rojas Lobos	Observatoire Astronomique de Strasbourg,F

Bibliography

Aitken, D. K., Efstathiou, A., McCall, A., & Hough, J. H. 2002, MNRAS, 329, 647 (cited on page 162)

Alloin, D., Pantin, E., Lagage, P. O., & Granato, G. L. 2000, A&A, 363, 926 (cited on pages 64, 68 and 69)

Alonso-Herrero, A., Ramos Almeida, C., Mason, R., et al. 2011, ApJ, 736, 82 (cited on pages 68, 69 and 171)

Angel, J. R. P., Stockman, H. S., Woolf, N. J., Beaver, E. A., & Martin, P. G. 1976, ApJ, 206, L5 (cited on page 164)

Antonucci, R. 1993, ARA&A, 31, 473 (cited on pages 11, 13, 38, 63, 64, 69, 154 and 155)

Antonucci, R. R. J. 1984, ApJ, 278, 499 (cited on pages 11 and 13)

Antonucci, R. R. J. & Miller, J. S. 1985, ApJ, 297, 621 (cited on pages 11, 13, 38, 64, 69, 163, 169 and 179)

Armus, L., Bernard-Salas, J., Spoon, H. W. W., et al. 2006, ApJ, 640, 204 (cited on page 17)

Armus, L., Mazzarella, J. M., Evans, A. S., et al. 2009, PASP, 121, 559 (cited on pages 16, 17 and 19)

Arp, H. & Sandage, A. 1985, AJ, 90, 1163 (cited on page 10)

Audibert, A., Riffel, R., Sales, D. A., Pastoriza, M. G., & Ruschel-Dutra, D. 2017, MNRAS, 464, 2139 (cited on pages 69, 154 and 171)

Avenhaus, H., Quanz, S. P., Schmid, H. M., et al. 2014, ApJ, 781, 87 (cited on pages 56 and 59)

Axon, D. J., Marconi, A., Capetti, A., et al. 1998, ApJ, 496, L75 (cited on pages 66, 171 and 172)

Bailey, J., Axon, D. J., Hough, J. H., et al. 1988, MNRAS, 234, 899 (cited on pages 162 and 164)

Bastian, N. 2016, in EAS Publications Series, Vol. 80, EAS Publications Series, ed. E. Moraux, Y. Lebreton, & C. Charbonnel, 5–37 (cited on pages 9, 10, 35 and 178)

Bastien, P. & Menard, F. 1990, ApJ, 364, 232 (cited on pages 154, 161, 162 and 178)

Beck, R., Fletcher, A., Shukurov, A., et al. 2005, A&A, 444, 739 (cited on page 87)

Beckers, J. M. 1989, in Proc. SPIE, Vol. 1114, Active telescope systems, ed. F. J. Roddier, 215–217 (cited on page 8)

Bertelli, G., Bressan, A., Chiosi, C., Fagotto, F., & Nasi, E. 1994, A&AS, 106 (cited on page 33)

Beuzit, J.-L., Feldt, M., Dohlen, K., et al. 2008, in Proc. SPIE, Vol. 7014, Ground-based and Airborne Instrumentation for Astronomy II, 701418 (cited on page 70)

Bjorkman, J. E. & Wood, K. 2001, ApJ, 554, 615 (cited on pages 97, 111 and 113)

Bland-Hawthorn, J., Gallimore, J. F., Tacconi, L. J., et al. 1997, Ap&SS, 248, 9 (cited on pages 64 and 65)

Blanton, M. R. & Roweis, S. 2007, AJ, 133, 734 (cited on page 22)

Bock, J. J., Neugebauer, G., Matthews, K., et al. 2000, AJ, 120, 2904 (cited on page 65)

Bohren, C. F. & Huffman, D. R. 1983, Absorption and scattering of light by small particles (cited on page 105)

Brindle, C., Hough, J. H., Bailey, J. A., Axon, D. J., & Sparks, W. B. 1991, MNRAS, 252, 288 (cited on page 87)

Brindle, C., Hough, J. H., Bailey, J. A., et al. 1990, MNRAS, 244, 577 (cited on page 87)

Calzetti, D., Kinney, A. L., & Storchi-Bergmann, T. 1994, ApJ, 429, 582 (cited on page 33)

Capetti, A., Axon, D. J., Macchetto, F., Sparks, W. B., & Boksenberg, A. 1995, ApJ, 446, 155 (cited on page 122)

Capetti, A., Axon, D. J., & Macchetto, F. D. 1997, ApJ, 487, 560 (cited on page 66)

Cheetham, A. C., Girard, J., Lacour, S., et al. 2016, in Proc. SPIE, Vol. 9907, Optical and Infrared Interferometry and Imaging V, 99072T (cited on page 38)

Clarke, D. & Stewart, B. G. 1986, Vistas in Astronomy, 29, 27 (cited on pages 79 and 82)

Clénet, Y., Gendron, E., Gratadour, D., Rousset, G., & Vidal, F. 2015, A&A, 583, A102 (cited on page 8)

Clénet, Y., Le Coarer, E., Joncas, G., et al. 2002, PASP, 114, 563 (cited on page 68)

Compton, A. H. 1923, Physical Review, 21, 483 (cited on page 46)

Cutri, R. M., Skrutskie, M. F., van Dyk, S., et al. 2003, VizieR Online Data Catalog, 2246 (cited on page 20)

Das, V., Crenshaw, D. M., Kraemer, S. B., & Deo, R. P. 2006, AJ, 132, 620 (cited on pages 65 and 66)

Draine, B. T. 1985, ApJS, 57, 587 (cited on pages 105, 155 and 163)

Dullemond, C. P., Juhasz, A., Pohl, A., et al. 2012, RADMC-3D: A multi-purpose radiative transfer tool, Astrophysics Source Code Library (cited on page 96)

Efstathiou, A., McCall, A., & Hough, J. H. 1997, MNRAS, 285, 102 (cited on pages 78, 135, 153, 162 and 171)

Elitzur, M. & Ho, L. C. 2009, ApJ, 701, L91 (cited on pages 13, 67 and 162)

Elmegreen, B. G. 1991, ApJ, 378, 139 (cited on pages 13 and 69)

Emmering, R. T., Blandford, R. D., & Shlosman, I. 1992, ApJ, 385, 460 (cited on pages 13 and 162)

Engel, H., Davies, R. I., Genzel, R., et al. 2010, A&A, 524, A56 (cited on page 18)

Fath, E. A. 1909, Popular Astronomy, 17, 504 (cited on pages 11 and 64)

Fischer, O., Henning, T., & Yorke, H. W. 1996, A&A, 308, 863 (cited on pages 56, 122 and 158)

Fried, D. L. 1982, Journal of the Optical Society of America (1917-1983), 72, 52 (cited on page 8)

Gallimore, J. F., Baum, S. A., & O'Dea, C. P. 2004, ApJ, 613, 794 (cited on page 64)

Gallimore, J. F., Baum, S. A., O'Dea, C. P., Brinks, E., & Pedlar, A. 1996a, ApJ, 462, 740 (cited on page 66)

Gallimore, J. F., Baum, S. A., O'Dea, C. P., & Pedlar, A. 1996b, ApJ, 458, 136 (cited on pages 64 and 65)

Gallimore, J. F., Henkel, C., Baum, S. A., et al. 2001, ApJ, 556, 694 (cited on page 67)

García-Burillo, S., Combes, F., Ramos Almeida, C., et al. 2016, ApJ, 823, L12 (cited on pages 13, 68 and 155)

García-Burillo, S., Combes, F., Usero, A., et al. 2014, A&A, 567, A125 (cited on page 67)

Gendron, E., Vidal, F., Brangier, M., et al. 2011, A&A, 529, L2 (cited on page 16)

Goosmann, R. W. & Gaskell, C. M. 2007, A&A, 465, 129 (cited on pages 96, 155 and 159)

Gratadour, D., Clénet, Y., Rouan, D., Lai, O., & Forveille, T. 2003, A&A, 411, 335 (cited on pages 68, 69, 154 and 171)

Gratadour, D., Rouan, D., Boccaletti, A., Riaud, P., & Clénet, Y. 2005, A&A, 429, 433 (cited on page 177)

Gratadour, D., Rouan, D., Grosset, L., Boccaletti, A., & Clénet, Y. 2015, A&A, 581, L8 (cited on pages 71, 153, 159, 169, 171 and 178)

Gratadour, D., Rouan, D., Mugnier, L. M., et al. 2006, A&A, 446, 813 (cited on pages 66, 67 and 70)

Grosset, L., Marin, F., Gratadour, D., et al. 2016, in SF2A-2016: Proceedings of the Annual meeting of the French Society of Astronomy and Astrophysics, ed. C. Reylé, J. Richard, L. Cambrésy, M. Deleuil, E. Pécontal, L. Tresse, & I. Vauglin, 57–60 (cited on pages 155 and 157)

Guillet, V. 2008, Theses, Université Paris Sud - Paris XI (cited on page 170)

Haan, S., Surace, J. A., Armus, L., et al. 2011, AJ, 141, 100 (cited on pages 17, 18 and 19)

Heckman, T. M. 1998, in Astronomical Society of the Pacific Conference Series, Vol. 148, Origins, ed. C. E. Woodward, J. M. Shull, & H. A. Thronson, Jr., 127 (cited on page 10)

Hiltner, W. A. 1949, Nature, 163, 283 (cited on page 38)

Holtzman, J. A., Faber, S. M., Shaya, E. J., et al. 1992, AJ, 103, 691 (cited on page 10)

Hubble, E. P. 1925, The Observatory, 48, 139 (cited on page 2)

Hubble, E. P. 1926, ApJ, 64 (cited on pages 2 and 3)

Hunter, J. D. 2007, Computing in Science and Engineering, 9, 90 (cited on page 96)

I.A.U. 1973, XVth General Assembly, Sydney, Australia. (cited on pages 42 and 55)

Iono, D., Wilson, C. D., Takakuwa, S., et al. 2007, ApJ, 659, 283 (cited on page 17)

Iwasawa, K., Sanders, D. B., Teng, S. H., et al. 2011, A&A, 529, A106 (cited on page 17)

Jackson, J. M., Paglione, T. A. D., Ishizuki, S., & Nguyen-Q-Rieu. 1993, ApJ, 418, L13 (cited on page 68)

Johnson, K. E. 2001, PhD thesis, University of Colorado at Boulder (cited on pages 9 and 10)

Jones, A. P., Fanciullo, L., Köhler, M., et al. 2013, A&A, 558, A62 (cited on page 159)

Kern, P., Lena, P., Gigan, P., Fontanella, J.-C., & Rousset, G. 1989, in Proc. SPIE, Vol. 1114, Active telescope systems, ed. F. J. Roddier, 54–64 (cited on pages 6 and 7)

Kim, D.-C., Evans, A. S., Vavilkin, T., et al. 2013, ApJ, 768, 102 (cited on pages 17 and 19)

Kishimoto, M. 1999, ApJ, 518, 676 (cited on pages 65, 70 and 155)

Komossa, S., Burwitz, V., Hasinger, G., et al. 2003, ApJ, 582, L15 (cited on page 17)

Kotulla, R., Fritze, U., Weilbacher, P., & Anders, P. 2009, MNRAS, 396, 462 (cited on pages 32 and 33)

Krause, M. G. H., Charbonnel, C., Bastian, N., & Diehl, R. 2016, A&A, 587, A53 (cited on page 178)

Lai, O., Rouan, D., Rigaut, F., Arsenault, R., & Gendron, E. 1998, A&A, 334, 783 (cited on page 13)

Langlois, M., Dohlen, K., Vigan, A., et al. 2014, in Proc. SPIE, Vol. 9147, Ground-based and Airborne Instrumentation for Astronomy V, 91471R (cited on page 70)

Lawrence, A. & Elvis, M. 1982, ApJ, 256, 410 (cited on page 11)

Leavitt, H. S. & Pickering, E. C. 1912, Harvard College Observatory Circular, 173, 1 (cited on page 2)

Lenzen, R., Hartung, M., Brandner, W., et al. 2003, in Proc. SPIE, Vol. 4841, Instrument Design and Performance for Optical/Infrared Ground-based Telescopes, ed. M. Iye & A. F. M. Moorwood, 944–952 (cited on page 58)

Lira, P., Videla, L., Wu, Y., et al. 2013, ApJ, 764, 159 (cited on pages 69, 154 and 171)

Lopez-Rodriguez, E., Packham, C., Jones, T. J., et al. 2015, MNRAS, 452, 1902 (cited on pages 69, 154 and 162)

Lopez-Rodriguez, E., Packham, C., Roche, P. F., et al. 2016, MNRAS, 458, 3851 (cited on pages 65 and 66)

Lucy, L. B. 1999, A&A, 344, 282 (cited on page 111)

Lutz, D., Sturm, E., Genzel, R., et al. 2000, ApJ, 536, 697 (cited on pages 66, 171 and 172)

Lyot, B. 1924, L'Astronomie, 38, 102 (cited on page 38)

Macchetto, F., Capetti, A., Sparks, W. B., Axon, D. J., & Boksenberg, A. 1994, ApJ, 435, L15 (cited on page 66)

Marconi, A. & Hunt, L. K. 2003, ApJ, 589, L21 (cited on page 18)

Marin, F. 2014, MNRAS, 441, 551 (cited on pages 13 and 70)

Marin, F. 2016, MNRAS, 460, 3679 (cited on page 13)

Marin, F., Goosmann, R. W., & Gaskell, C. M. 2015, A&A, 577, A66 (cited on pages 13, 69, 96, 154, 155 and 171)

Marin, F., Goosmann, R. W., Gaskell, C. M., Porquet, D., & Dovčiak, M. 2012, A&A, 548, A121 (cited on pages 69, 96, 122, 155 and 161)

Marin, F., Goosmann, R. W., & Petrucci, P.-O. 2016a, A&A, 591, A23 (cited on pages 11, 12, 66, 67, 68, 69 and 87)

Marin, F., Grosset, L., Goosmann, R., et al. 2016b, in SF2A-2016: Proceedings of the Annual meeting of the French Society of Astronomy and Astrophysics, ed. C. Reylé, J. Richard, L. Cambrésy, M. Deleuil, E. Pécontal, L. Tresse, & I. Vauglin, 103–106 (cited on pages 155 and 157)

Mason, R. E., Levenson, N. A., Shi, Y., et al. 2009, ApJ, 693, L136 (cited on page 69)

Mathis, J. S., Rumpl, W., & Nordsieck, K. H. 1977, ApJ, 217, 425 (cited on pages 101 and 155)

Medling, A. M., Ammons, S. M., Max, C. E., et al. 2011, ApJ, 743, 32 (cited on page 18)

Medling, A. M., U, V., Guedes, J., et al. 2014, ApJ, 784, 70 (cited on page 18)

Melnick, J., Moles, M., & Terlevich, R. 1985, A&A, 149, L24 (cited on page 10)

Messier, C. 1781, Catalogue des Nébuleuses & des amas d'Étoiles (Catalog of Nebulae and Star Clusters), Tech. rep. (cited on pages 1 and 63)

Mie, G. 1908, Annalen der Physik, 330, 377 (cited on page 44)

Miller, J. S. & Antonucci, R. R. J. 1983, ApJ, 271, L7 (cited on page 70)

Moffat, A. F. J. 1969, A&A, 3, 455 (cited on page 25)

Moraux, E., Lebreton, Y., & Charbonnel, C., eds. 2016, EAS Publications Series, Vol. 80, Stellar Clusters: Benchmarks of Stellar Physics and Galactic Evolution - EES2015 (cited on pages 9 and 178)

Müller Sánchez, F., Davies, R. I., Genzel, R., et al. 2009a, ApJ, 691, 749 (cited on page 68)

Müller Sánchez, F., Davies, R. I., Genzel, R., et al. 2009b, ApJ, 691, 749 (cited on page 69)

Murakawa, K. 2010, A&A, 518, A63 (cited on pages 97, 122, 154, 161, 162, 163 and 178)

Neichel, B., Fusco, T., Conan, J.-M., Petit, C., & Rousset, G. 2008, in Proc. SPIE, Vol. 7015, Adaptive Optics Systems, 701573 (cited on page 8)

Neugebauer, G., Morton, D., Oke, J. B., et al. 1980, ApJ, 238, 502 (cited on page 11)

Nikutta, R., Elitzur, M., & Lacy, M. 2009, ApJ, 707, 1550 (cited on page 69)

O'Connell, R. W. 2004, in Astronomical Society of the Pacific Conference Series, Vol. 322, The Formation and Evolution of Massive Young Star Clusters, ed. H. J. G. L. M. Lamers, L. J. Smith, & A. Nota, 551 (cited on page 9)

Packham, C., Young, S., Fisher, S., et al. 2007, ApJ, 661, L29 (cited on pages 68, 69, 70 and 154)

Packham, C., Young, S., Hough, J. H., Axon, D. J., & Bailey, J. A. 1997, MNRAS, 288, 375 (cited on pages 65, 68 and 70)

Pinte, C., Ménard, F., Duchêne, G., & Bastien, P. 2006, A&A, 459, 797 (cited on page 96)

Planesas, P., Scoville, N., & Myers, S. T. 1991, ApJ, 369, 364 (cited on page 68)

Pollack, L. K., Max, C. E., & Schneider, G. 2007, ApJ, 660, 288 (cited on pages 16, 17, 18 and 20)

Portegies Zwart, S. F., McMillan, S. L. W., & Gieles, M. 2010, ARA&A, 48, 431 (cited on page 9)

Prieto, M. A., Maciejewski, W., & Reunanen, J. 2005, AJ, 130, 1472 (cited on page 87)

Pringle, J. E. & Rees, M. J. 1972, A&A, 21, 1 (cited on page 11)

Quanz, S. P., Schmid, H. M., Geissler, K., et al. 2011, ApJ, 738, 23 (cited on page 59)

Raban, D., Jaffe, W., Röttgering, H., Meisenheimer, K., & Tristram, K. R. W. 2009, MNRAS, 394, 1325 (cited on pages 68 and 161)

Ragazzoni, R. & Farinato, J. 1999, A&A, 350, L23 (cited on page 6)

Ramos Almeida, C., Martínez González, M. J., Asensio Ramos, A., et al. 2016, MNRAS, 461, 1387 (cited on pages 13, 69 and 169)

Rigaut, F., Rousset, G., Kern, P., et al. 1991, A&A, 250, 280 (cited on pages 25 and 26)

Risaliti, G., Harrison, F. A., Madsen, K. K., et al. 2013, Nature, 494, 449 (cited on page 87)

Robitaille, T. P. 2011, A&A, 536, A79 (cited on pages 96 and 108)

Rouan, D., Lacombe, F., Gendron, E., et al. 2004, A&A, 417, L1 (cited on pages 66 and 177)

Rouan, D., Rigaut, F., Alloin, D., et al. 1998, A&A, 339, 687 (cited on page 177)

Rousset, G., Lacombe, F., Puget, P., et al. 2003, in Proc. SPIE, Vol. 4839, Adaptive Optical System Technologies II, ed. P. L. Wizinowich & D. Bonaccini, 140–149 (cited on page 58)

Rowan-Robinson, M. 1977, ApJ, 213, 635 (cited on page 11)

Sargent, W. L. W. & Searle, L. 1970, ApJ, 162, L155 (cited on page 9)

Schweizer, F. 1982, ApJ, 252, 455 (cited on page 9)

Seyfert, C. K. 1943, ApJ, 97, 28 (cited on pages 2, 11 and 64)

Shapley, H. & Curtis, H. D. 1921, Bulletin of the National Research Council, Vol. 2, Part 3, No. 11, p. 171-217, 2, 171 (cited on page 1)

Slipher, V. M. 1917, Lowell Observatory Bulletin, 3, 59 (cited on pages 11 and 64)

Smith, J. E., Robinson, A., Alexander, D. M., et al. 2004, MNRAS, 350, 140 (cited on pages 87 and 180)

Stalevski, M., Fritz, J., Baes, M., Nakos, T., & Popović, L. Č. 2012, MNRAS, 420, 2756 (cited on page 96)

Storchi-Bergmann, T., Eracleous, M., Teresa Ruiz, M., et al. 1997, ApJ, 489, 87 (cited on page 87)

Strauss, M. A., Huchra, J. P., Davis, M., et al. 1992, ApJS, 83, 29 (cited on page 17)

Tacconi, L. J., Genzel, R., Tecza, M., et al. 1999, ApJ, 524, 732 (cited on page 17)

Tecza, M., Genzel, R., Tacconi, L. J., et al. 2000, ApJ, 537, 178 (cited on page 18)

Thalmann, C., Schmid, H. M., Boccaletti, A., et al. 2008, in Proc. SPIE, Vol. 7014, Ground-based and Airborne Instrumentation for Astronomy II, 70143F (cited on pages 58 and 70)

Thomson, J. J. 1906, Conduction of Electricity through Gases (cited on page 46)

Tinbergen, J. 1996, Astronomical Polarimetry, 174 (cited on pages 43, 52, 55, 59 and 79)

Tully, R. B. & Fisher, J. R. 1988, Catalog of Nearby Galaxies (cited on page 64)

Turner, J. L. 2009, Astrophysics and Space Science Proceedings, 10, 215 (cited on pages 9 and 10)

Urry, C. M. & Padovani, P. 1995, PASP, 107, 803 (cited on page 11)

van den Bergh, S. 1971, A&A, 12, 474 (cited on pages 9 and 10)

Vidal, F., Gendron, É., Rousset, G., et al. 2014, A&A, 569, A16 (cited on page 16)

von Neumann, J. 1951, Journal of Research of the National Bureau of Standards, 3, 36 (cited on page 103)

Whitmore, B. C., Chandar, R., & Fall, S. M. 2007, AJ, 133, 1067 (cited on page 10)

Whitney, B. A. & Hartmann, L. 1993, ApJ, 402, 605 (cited on pages 56, 122 and 158)

Wilson, A. S. & Ulvestad, J. S. 1983, ApJ, 275, 8 (cited on pages 64 and 65)

Witzel, G., Eckart, A., Buchholz, R. M., et al. 2011, A&A, 525, A130 (cited on page 87)

Wolf, S. & Henning, T. 1999, A&A, 341, 675 (cited on pages 13 and 170)

Young, S., Hough, J. H., Axon, D. J., Bailey, J. A., & Ward, M. J. 1995, MNRAS, 272, 513 (cited on page 164)

Young, S., Packham, C., Hough, J. H., & Efstathiou, A. 1996, MNRAS, 283, L1 (cited on pages 68 and 69)

Zallat, J. & Heinrich, C. 2007, Optics Express, 15, 83 (cited on page 60)

Zeeman, P. 1899, ApJ, 9, 47 (cited on page 38)

Résumé

Malgré l'existence de modèles précis, notre connaissance des structures à petite échelle des galaxies est toujours limitée par le manque de preuves observationnelles. Les progrès instrumentaux ont permis d'atteindre une haute résolution angulaire à l'aide des nouvelles générations de télescopes, mais celle-ci est restreinte à un faible nombre de cibles extragalactiques à causes des besoins de l'Optique Adaptative (OA). En effet, afin de permettre une mesure efficace du front d'onde, l'OA requiert une source brillante et ponctuelle proche de la cible scientifique, typiquement en dessous de 30″ . La partie principale de cette thèse porte sur l'analyse de la dizaine de parsecs centrale des Galaxies à Noyaux Actifs (NAG) à l'aide de différentes techniques observationnelles et numériques. Nous avons dans ce contexte développé un code de transfert radiatif nous permettant d'analyser les données polarimétriques. La seconde partie de ce travail est dédiée à l'analyse d'images en proche infrarouges de galaxies à flambée d'étoiles afin de contraindre les paramètres décrivant les super amas stellaires, jeunes cocons de poussière très massifs abritant une formation d'étoiles très soutenue, à l'aide de données obtenues avec l'instrument CANARY, démonstrateur de nouvelles technologies d'OA.

Mots Clés

Galaxies: Seyfert, amas d'étoiles, Techniques: photométrie, polarimétrie, Haute résolution angulaire, Méthodes: observations, numériques, Transfert radiatif.

Abstract

Despite having strong theoretical models, the current limitation in our understanding of the small-scale structures of galaxies is linked to the lack of observational evidences. Many powerful telescopes and instruments have been developed in the last decades, however one of these strongest tools, namely Adaptive Optics (AO), can only be used on a very limited number of targets. Indeed, for AO to be efficient, a bright star is required close to the scientific target, typically under 30″ . This is mandatory for the AO systems to be able to measure the atmospheric turbulence and this condition is rarely satisfied for extended extragalactic targets such as galaxies. The main part of this thesis work consisted in going deeper in the analysis of the inner tens of parsecs of Active Nuclei (AGN) by combining different techniques to obtain and to interpret new data. In this context, we developed a new radiative transfer code to analyse the polarimetric data. A second part of my work was dedicated to a high angular resolution study of Super Star Clusters (SSC) in a new system, thanks to data obtained with the AO demonstrator CANARY instrument.

Keywords

Galaxies: Seyfert, star clusters, Techniques: photometric, polarimetric, high angular resolution, Methods: observational, numerical, Radiative transfer.